Lithium-Ion Conducting Thin-Films for Solid-State Batteries prepared by Chemical Solution Deposition

dem Fachbereich Biologie und Chemie

der Justus-Liebig-Universität Gießen

vorgelegte Dissertation zur Erlangung des akademischen Grades

Doktor der Naturwissenschaften

- Dr. rer. nat.-

von

Annika Baumann

geboren am 21. Februar 1989 in Hamburg

Gießen, 2018

Dean : Prof. Dr. Jürgen Janek

1st Reviewer : Prof. Dr. Jürgen Janek
2nd Reviewer : Prof. Dr. Bernd Smarsly

Submission date: Gießen, _____ 2018

EIDESSTATTLICHE ERKLÄRUNG

Die vorliegende Arbeit wurde im Zeitraum vom 01.08.2014 bis 30.04.2018 in der Deutschen Nanoschicht GmbH und am Physikalisch-Chemischen Institut der Justus-Liebig-Universität Gießen unter Betreuung von Prof. Dr. Jürgen Janek angefertigt.

Ich erkläre: Ich habe die vorgelegte Dissertation selbständig und ohne unerlaubte fremde Hilfe und nur mit den Hilfen angefertigt, die ich in der Dissertation angegeben habe. Alle Textstellen, die wörtlich oder sinngemäß aus veröffentlichten Schriften entnommen sind, und alle Angaben, die auf mündlichen Auskünften beruhen, sind als solche kenntlich gemacht. Bei den von mir durchgeführten und in der Dissertation erwähnten Untersuchungen habe ich die Grundsätze guter wissenschaftlicher Praxis, wie sie in der "Satzung der Justus-Liebig-Universität Gießen zur Sicherung guter wissenschaftlicher Praxis" niedergelegt sind, eingehalten.

Gießen, 08.05.2018

_____
Annika Baumann

DANKSAGUNG

ABSTRACT

Lithium (Li) metal anodes could increase the energy density of next generation batteries due to the high specific capacity of Li. However, they are currently not applied in rechargeable lithium-ion batteries (LIB) with liquid electrolytes due to safety concerns ascribed to the inherent reactivity of lithium metal and the growth of dendrites upon cycling that leads to electrical short circuits. Solid-state batteries (SSB) with solid electrolytes could enable safe and dendrite-free operation. One of the main challenges in these systems is the fabrication of thin layers of solid electrolytes with high lithium-ion conductivities and their compatibility with Li metal anodes.

The focus of this thesis is the synthesis of lithium thiophosphate (LPS) solid electrolyte thin-films as separators for SSB by chemical solution deposition.

LPS glasses with different stoichiometries were initially dissolved in *N*-methylformamide (NMF) and used as precursors to formulate suitable coating solutions. Interestingly, X-ray photoelectron spectroscopy (XPS) and energy dispersive X-Ray spectroscopy (EDX) revealed high oxygen contents in the final thin-films. The chemistry of the coating solution was analysed by time-dependant NMR measurements, which confirmed an S-O exchange between the solvent NMF and the LPS precursors. This reaction also leads to ageing of the coating solution.

Coatings derived from balled milled $70Li_2S$-$30P_2S_5$ precursors lead to amorphous LPS thin-films with high oxygen contents, well adjustable thicknesses up to 3 µm, lithium-ion conductivities of $3.2 \cdot 10^{-5}$ S cm^{-1}, and activation energies of 0.38 eV after optimisation of the deposition parameters.

Finally, the electrochemical performance of the LPS thin-films as solid electrolytes and their compatibility with Li metal was investigated in Si/LPS/Li and LTO/LPS/Li half-cells. The formation of a thin solid electrolyte interphase (SEI) between lithium metal and LPS layers was revealed by *In situ* XPS. Stable conductivities and cycling

performance up to 500 cycles of cells composed of Li anode and LPS electrolyte indicate the protecting function of the SEI and demonstrate the excellent electrochemical properties of LPS thin-films as solid electrolyte in microbatteries. Deposition of LPS thin-films on composite cathodes and bulk solid electrolytes show potential application of LPS thin-films in SSB as separator or protective coating, to prevent the reduction of conventional solid electrolytes by Li metal anodes. Solution-prepared LPS thin-films show great potential to be applied as cost-effective separators in SSB.

KURZZUSAMMENFASSUNG

Batterien der nächsten Generation mit Lithiummetallanoden eröffnen die Möglichkeit von höheren Energiedichten, bedingt durch die hohe spezifische Kapazität von Lithium. Gegenwärtig werden Lithiummetallanoden aufgrund von Sicherheitsbedenken jedoch nicht in wieder aufladbaren Lithiumionenbatterien (LIB) mit flüssigen Elektrolyten verwendet. Dies ist zum einen auf die hohe Reaktivität von Lithiummetall und zum anderen auf das Wachstum von Lithiumdendriten beim Zyklisieren zurückzuführen, wodurch es zu elektrischen Kurzschlüssen kommen kann. Festkörperbatterien (SSB) mit Festelektrolyten könnten hingegen einen sicheren und dendritfreien Batteriebetrieb ermöglichen. Einige der größten Herausforderungen bei der Realisierung von SSB sind die Herstellung von dünnen Festelektrolytschichten mit hohen Lithiumionenleitfähigkeiten sowie die Kompatibilität von Festelektrolyt und Lithiummetall.

Der Schwerpunkt dieser Arbeit liegt auf der Synthese von Lithiumthiophosphat (LPS)-Festelektrolytdünnfilmen durch chemische Lösungsabscheidung, die als Separatoren für SSB genutzt werden können.

Zur Formulierung geeigneter Beschichtungslösungen wurden zu Beginn verschiedene LPS-Gläser als Vorläuferverbindungen verwendet und in N-Methylformamid (NMF) gelöst. Die aus diesen Lösungen hergestellten LPS-Schichten weisen interessanterweise hohe Sauerstoffgehalte auf, wie mittels Röntgen-Photoelektronenspektroskopie (XPS) und energiedispersiver Röntgenspektroskopie (EDX) gezeigt wurde. Zur Identifizierung der Sauerstoffquelle wurden die Beschichtungslösungen mittels zeitabhängigen NMR-Messungen analysiert. Die NMR-Messungen zeigten einen S-O-Austausch zwischen dem Lösungsmittel NMF und den LPS-Gläsern, der ebenfalls zu einer Alterung der Beschichtungslösung führt.

Amorphe LPS-Filme mit einer einstellbaren Schichtdicke von bis zu 3 µm wurden aus 70Li$_2$S-30P$_2$S$_5$-Vorläuferverbindungen hergestellt. Nach der Optimierung der Beschichtungsparameter zeigen diese LPS-Dünnschichten – neben einem hohen Sauerstoffgehalt – Lithiumionenleitfähigkeiten von $3.2 \cdot 10^{-5}$ S cm^{-1} und Aktivierungsenergien von 0.38 eV.

Weitere elektrochemische Eigenschaften der LPS-Dünnschichten und die Kompatibilität der LPS-Schichten mit Lithiummetall wurden in Si/LPS/Li- und LTO/LPS/Li-Halbzellen untersucht. Mittels *in situ* XPS wurde die Bildung einer dünnen Festelektrolyt-Grenzschicht (SEI) zwischen Lithiummetall und LPS-Film nachgewiesen. Die Schutzfunktion dieser Grenzfläche konnte in Zellen aus Lithiumanode und LPS-Elektrolyt durch stabile Leitfähigkeiten und Zyklisierungsperformance von bis zu 500 Zyklen demonstriert werden. LPS-Dünnfilme zeigen demnach ausgezeichnete elektrochemische Eigenschaften für die Anwendung als Festelektrolyt in Mikrobatterien. Des Weiteren können LPS-Filme in SSB als Separator oder Schutzschicht integriert werden, um die Reduktion von herkömmlichen Festelektrolyten durch Lithiummetallanoden zu verhindern. Hierfür wurde die Beschichtung von Verbundkathoden und Feststoffelektrolyten mit LPS-Dünnfilmen untersucht. Aus Lösung hergestellte LPS-Dünnschichten zeigen hervorragende Eigenschaften, um als kostengünstige Separatoren oder Schutzschichten in SSB mit Lithiummetallanode eingesetzt zu werden.

TABLE OF CONTENTS

LIST OF ABBREVIATIONS

[70-30]	$70Li_2S\text{-}30P_2S_5$
[75-25]	$75Li_2S\text{-}25P_2S_5$
[80-20]	$80Li_2S\text{-}20P_2S_5$
Ar	Argon
Au	Gold
C	Carbon
CCD	Cyclic charge discharge
CEI	Cathode electrolyte interlayer
Co	Cobalt
CPE	Constant phase element
CR	Capacity retention
CSD	Chemical solution deposition
Cu	Copper
CV	Cyclic voltammetry
CVD	Chemical vapour deposition
DC	Direct current
DMC	Dimethyl carbonate
DME	1,2-Dimethoxyethane
DoD	Depth of discharge
DT	Deposition technique
e-BE	Electron beam evaporation
EC	Ethylene carbonate
EDX	Energy dispersive X-ray spectroscopy
EIS	Electrochemical impedance spectroscopy
emf	Electromotoric force
EPA	Environmental protection agency
Eq.	Equation

EtOH	Ethanol
EV	Electrical vehicle
FIB	Focused ion beam
H	Hydrogen
HEV	Hybrid electrical vehicle
HF	high frequency
Ge	Germanium
ITO	Indium tin oxide
LAGP	$Li_{1+x}Al_xGe_{2-x}(PO_4)_3$
LATP	$Li_{1+x}Al_xTi_{2-x}(PO_4)_3$
Li	Lithium
Li^+	Lithium ions
LiPON	Nitrogen doped lithium phosphate
LISICON	Lithium super ionic conductor
LCO	Lithium cobalt oxide, $LiCoO_2$
LE	Liquid electrolyte
LF	Low frequency
LFP	Lithium iron phosphate, $LiFePO_4$
LGPS	$Li_{10}GeP_2S_{12}$
LIB	Lithium-ion battery
LLTO	$Li_{3x}La_{2/3-x}TiO_3$
LLZO	$Li_7La_3Zr_2O_{12}$
LMO	$LiMnO_2$
LMO spinel	$LiMn_2O_4$
LNMO	$LiNi_{0.5}Mn_{1.5}O_4$
LNO	$LiNiO_2$
LPD	Liquid phase deposition
LPS	Lithium thiophosphate
LTO	lithium titanate, $Li_4Ti_5O_{12}$
MCI	Mixed conducting interphase
MeOH	Methanol
MF	Mid frequency
Mn	Manganese
MO	Metal organic
MS	Magnetron sputtering
N	Nitrogen
NASICON	Sodium super ionic conductor

NCA	$LiNi_{0.8}Co_{0.15}Al_{0.05}O_2$
NCM	$Li_{1+x}(Ni_aCo_bMn_c)_{1-x}O_2$
NEFZ	Neuer Europäischer Fahrzyklus
Ni	Nickel
NMF	*N*-Methylformamide
NMR	Nuclear magnetic resonance spectroscopy
O	Oxygen
O_b	Bridging oxygen
O_{nb}	Non-bridging oxygen
rf	Radio frequeny
P	Phosphorous
PLD	Pulsed laser deposition
PLE	Protected lithium electrode
Pt	Platinum
PVDF	Polyvinylidene fluoride
Ref	Reference
RT	Room temperature
S	Sulphur
S_b	Bridging sulphur
S_{nb}	Non-bridging sulphur
Sn	Tin
SE	Solid electrolyte
SEI	Solid electrolyte interphase
SEM	Scanning electron microscopy
Si	Silicon
SoC	State of charge
SSB	Solid-state battery
TF	Thin-film
Ti	Titan
TR	Thermal runaway
V_{OC}	Open circuit voltage
XPS	X-Ray photoelectron spectroscopy
XRD	X-Ray diffraction
ZRA	Zero resistance ammeter

LIST OF SYMBOLS

A	Contact area
A_D	Pre-exponential factor
CE	Coulombic efficiency
c	Concentration
c_i	Carrier concentration
C	Capacity
C_{ch}	Charge capacity
C_{dis}	Discharge capacity
C_{th}	Theoretical capacity
d	Jump distance:
D_i	Self-diffusion coefficient
e	Electronic charge ($1.602 \cdot 10^{-19}$ C)
E	Open circuit voltage
E_A	Activation energy
ED	Energy density
E_g	Electrochemical stability window
E_{pol}	Non-ohmic polarisation voltage
ε_0	Permittivity of free space ($8.854 \cdot 10^{-12}$ F m^{-1})
ε_r	Dielectric constant
F	Faraday constant (96 485 C mol^{-1}).
$\Delta_R G$	Gibbs Free Energy of Reaction
ΔG_m	Free molar enthalpy
ΔH_m	Molar enthalpy
I	Current
j	Imaginary unit $\left(\sqrt{-1}\right)$

j_i	Ionic current density
l	Electrolyte thickness
M	Molecular weight
μ_A	Chemical potentials of the anode
μ_C	Chemical potentials of the cathode
o	Fractional occupation
P	Power
Q	Constant phase element
R_{Gas}	Ideal gas constant
R	Resistance
R_{int}	Internal cell resistance
ΔS_m	Molar entropy
σ_{el}	Electronic conductivity
σ_i	Ionic conductivity
σ_{Li^+}	Lithium-ion conductivity
t	Time
T	Temperature
u_i	Ionic mobility
U	Cell voltage
V_{OC}	Open circuit voltage
$w_{e,\,max}$	Maximum amount of electrical work
W	Energy
ω_0	Jump attempt frequency
ω	Radial frequency
Y_0	Capacitance of a constant phase element
z_{NN}	Number of nearest neighbours
z	Stoichiometric coefficient of the electrons
Z_C	Impedance of a capacitor
Z_{CPE}	Impedance of a constant phase element
z_i	Charge number

1 INTRODUCTION

Energy generation, transportation and storage are topics of global importance, as energy – in form of thermal, electric or nuclear energy – is required in all areas of daily life. The generation of energy is still largely based on the combustion of fossil fuels such as natural gas, oil or coal. The increasing demand of energy leads to a depletion of these resources and, as a result of the combustion process, to an increase of toxic exhausts and carbon dioxide (CO_2) emissions, which are considered to be responsible for global warming.[1]

In Germany 30% of the total energy consumption and 20% of CO_2 emissions are caused by motorised individual transportation, which highlights the importance of the development of alternatives to conventional combustion engines for cars.[2] Solutions to these serious pollution and emission problems could be provided by vehicles, which are powered either by a hydrogen (H_2) based fuel cell or a battery. Electromobility offers therefore a possible alternative for "greener" transportation to the benefit of society, particularly if the electricity is generated from renewable energy resources such as wind, geothermal or solar energy. The first battery powered all-electric car from a major manufacturer was released in 1996 by General motors.[3] Up to date, several electric drive vehicles, including both hybrid electrical vehicles (HEVs) and complete electrical vehicles (EVs) have been developed and commerzialised. Leading companies in the automobile industry, including Tesla, Nissan, Volkswagen, Ford or Daimler Benz, use lithium-ion batteries (LIBs) as storage system for their EVs.[4,5,6,7] Even though various other battery types exist, LIBs offer the advantages of stable cycling performance and high energy densities, which is related to the low molecular weight of lithium. Energy densities are correlated to the driving range of EVs, while power densities determine how fast a battery can be charged or discharged.

Figure 1-1 summarises the operational range determined by the *Environmental Protection Agency (*EPA) and price of commercially available EVs.[8] The EPA estimated range is a general guideline for consumers, when comparing EVs, and the actual range depends on additional factors such as weather condition or personal driving habits.[9] Taking this reduction into account, even the EVs with the best performances do not reach the driving range of cars with conventional combustion engines.
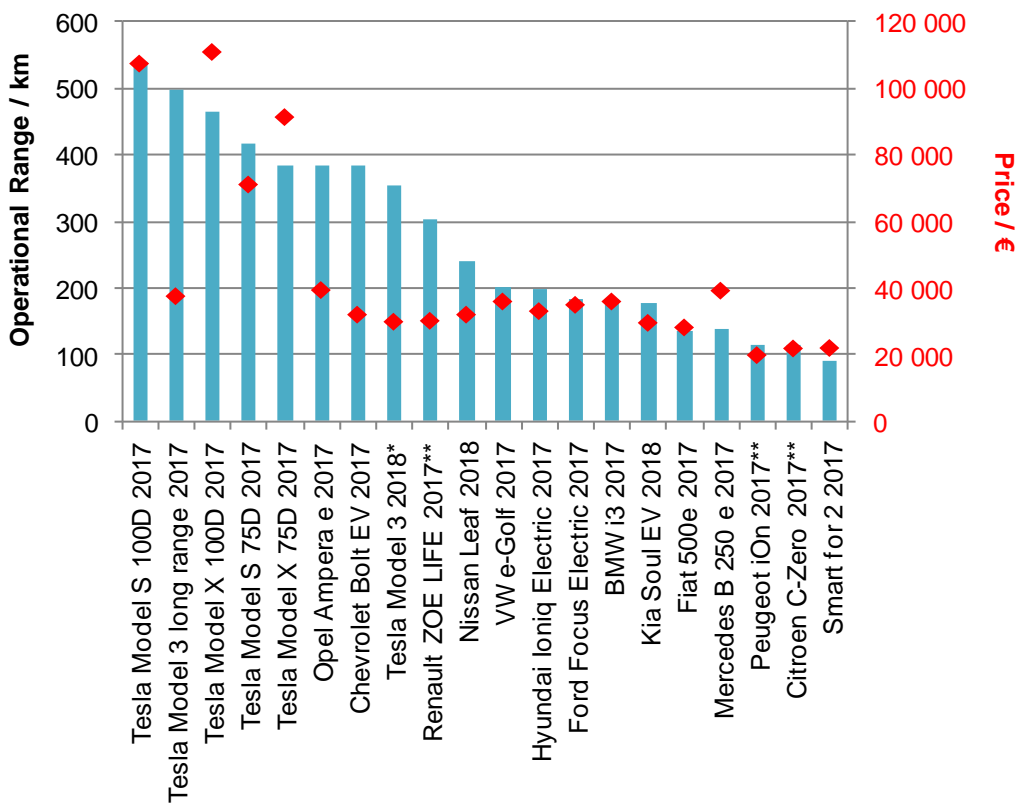
Figure 1-1: Operational range and price of commercially available EVs. The range was determined by EPA.[8] *Operational range provided by supplier (Tesla) not verified by EPA yet[10], **Operational range determined by NEFZ (*Neuer Europäischer Fahrzyklus)* and multiplied with a factor of 0.76 for adequate comparison.[11,12,13] This factor was determined from the average difference between known NEFZ and EPA values of 12 different EVs.

While HEVs are growing in market share, the limited demand for EVs results from high battery costs, limited driving range, insufficient charging station infrastructure, long charging times and safety concerns associated to flammable and toxic liquid electrolytes.[14] Batteries with sufficient driving range (high energy density), fast

charging times (high power density), reduced costs or improved safety are the focus of current research. In order to meet the requirements for the broad market it will be, however, necessary to go beyond present lithium-ion strategies as conventional LIBs have nearly reached their physicochemical energy density limit.[15]. Next-generation batteries such as lithium-sulphur (Li-S), lithium-air (Li-air) or solid-state batteries (SSBs) with lithium (Li) metal anode are currently under intense investigation as they are expected to achieve higher energy densities due to the high specific energy of lithium metal. However, dendrite formation is a major problem in Li based batteries causing performance and safety issues, which still limits their commercial application to non-chargeable batteries.[15,16,17] Figure 1-2 compares the specific energy and power (Ragone plot) of LIBs with several next generation batteries.
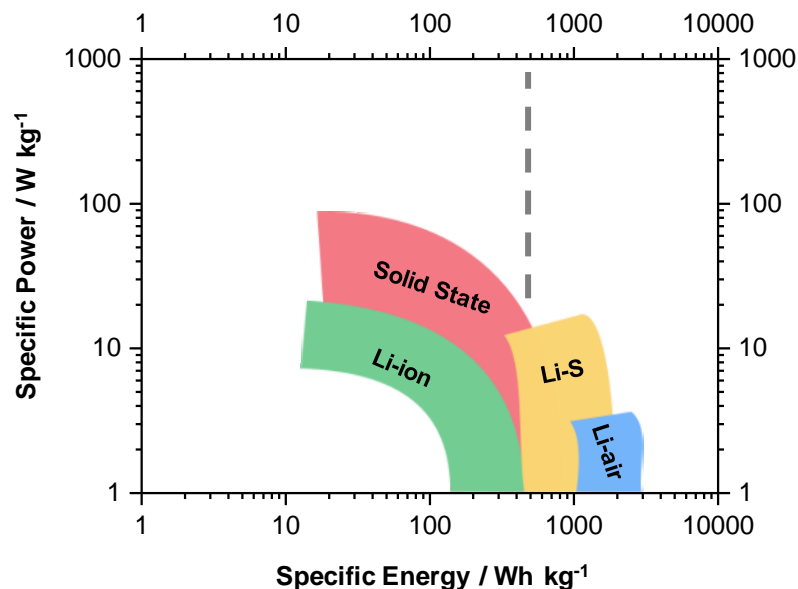
Figure 1-2: Ragone plot of different lithium based next generation batteries compared with state of the art lithium-ion batteries. The dashed line represents the physicochemical energy density limit of LIBs. The diagram is based on the reported gravimetric values by Kato *et. al.*[18]

The specific energy of Li-air and Li-S batteries can theoretically reach 3500 and 2600 Wh kg⁻¹, respectively, which is up to ten times higher than the energy density of conventional LIBs with graphite anode.[19] However, both Li-air and Li-S batteries suffer from high overpotentials and poor cycle life.[19,20,21] In SSBs the flammable and toxic liquid electrolyte is replaced by a solid electrolyte (SE) enabling safer operation

compared to LIBs. Prototype SSBs with conventional anode materials (graphite or lithium titanate) already exhibit excellent performance combined with superior power densities and energy densities comparable to LIBs.[18] Integration of Li anodes into SSBs could significantly increase the energy density of the battery but several challenges related to material research and manufacturing need to be overcome before SSBs could replace state-of-the-art batteries in EVs.[15,22]

The aim of the PhD project was the synthesis and characterisation of lithium-ion conducting thin-films for applications in SSBs with Li anode via chemical solution deposition (CSD). CSD offers the potential to fabricate thin-film SEs at low production costs, which is important for industrial applications. The thin-films might be applied directly as separator in SSBs between cathodes and Li anodes, which would enable a reduction in SE thickness or as protective coating on unstable bulk SEs to prevent their decomposition by Li metal. Both applications require thin-films that are homogeneous, dense and either intrinsically stable or form a stable interphase in contact with Li metal. Therefore, after the formulation of a suitable precursor solution and the optimisation of the coating process, the structural and electrochemical properties of the thin-films and their integration in SSBs have to be studied. SE thin-films prepared by CSD approach might enable the use of Li metal in bulk type SSBs, which would be necessary to achieve a significant increase in energy density.

2 THEORETICAL BACKGROUND

2.1 BATTERIES

Batteries are composed of stacked cells, which convert chemical energy into electrical energy and *vice versa*. This conversion is related to redox reactions at the two different electrodes in the cell, which require the transport of electrons (e^-) and ions (A^{z+}) from one electrode to the other. Upon discharge an oxidation takes place at the negative electrode (anode), while a reduction occurs at the positive electrode (cathode). The electrons are transported via an external circuit from the anode to the cathode, while ions move through an electrolyte in the same direction. The electronic current resulting from the redox reaction can be used for electrical work. The processes occurring upon discharge of a battery cell are displayed in Figure 2-1.
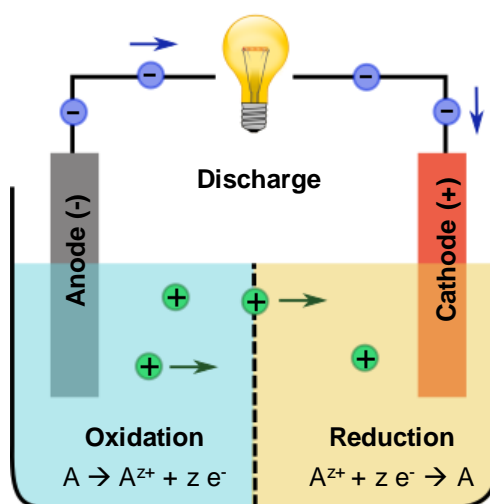
Figure 2-1: Schematic setup of a battery cell including visualisation of redox and transport processes occurring upon discharge of a battery cell. Ions (A^{z+}) are shown in green, electrons (e^-) in blue.

The chemical driving force for the redox reaction is related to the difference in the chemical potentials between the anode μ_A and cathode μ_C.[23] Under open circuit conditions an electric potential difference E arises between both electrodes, historically called electromotoric force (emf) and referred to as open circuit voltage (V_{OC}):

$$E = V_{OC} = \frac{\mu_A - \mu_C}{e}. \tag{2-1}$$

In equation 1, e is the magnitude of the electronic charge ($1.602 \cdot 10^{-19}$ C).

The maximum amount of electrical work $w_{e,\,max}$ provided by the battery is correlated to the Gibbs Free Energy of Reaction $\Delta_R G$, which is a function of V_{OC}:

$$w_{e,\,max} = \Delta_R G = -zFE. \tag{2-2}$$

Here z is the stoichiometric coefficient of the electrons from the cell reaction and F is the Faraday constant ($96\,485$ C mol^{-1}).

Cell thermodynamics and V_{OC} are exclusively determined by the properties of the electrode materials. However, the cell voltage U upon discharge is lower than V_{OC} due to ohmic and various other polarisation effects, which are related to the internal formation of electrostatic potential drops and limitations due to diffusion in the electrodes, transfer across the interfaces, redox processes and other kinetic phenomena:[24]

$$U = E - IR_{int} - E_{pol}. \tag{2-3}$$

In equation 2-3, I is the discharge current, R_{int} the internal cell resistance (without electrode polarisation) and E_{pol} the non-ohmic polarisation.

The internal cell resistance R_{int} is determined by (i) the resistance of current collectors and wires, which can often be neglected as highly conductive materials are commonly used and (ii) the electrolyte resistance.[25] A low electrolyte resistance can be achieved with materials characterised by a high ionic conductivity and a negligible electronic conductivity, as the electrolyte should only be permeable for ions and blocking for electrons.

The power P (in W) or power density (in W kg^{-1}) of the battery determines how fast the stored energy of a battery can be delivered. The output power P is the product of cell voltage and discharge current I:

$$P = I \cdot U. \tag{2-4}$$

The maximum amount of energy W that a battery cell can deliver (in Wh) depends on the discharge current I, the cell voltage U and the time needed for complete discharge of the battery Δt:

$$W = \int_0^{\Delta t} IU(t)\mathrm{d}t. \tag{2-5}$$

The charge transferred by the current I is the capacity C (in Ah) with:

$$C = \int_0^{\Delta t} I\mathrm{d}t. \tag{2-6}$$

The theoretical specific capacity C_{th} (in mAh g^{-1}) of an electrode is determined by the stoichiometric coefficient of the electrons from the cell reaction and the molecular weight M of the electrode:

$$C_{\text{th}} = \frac{zF}{3.6\,M} \cdot \frac{\text{mAh}}{\text{C}}. \tag{2-7}$$

Similar to the cell voltage, the available cell capacity varies with discharge current: when the cell is discharged at high currents the available cell capacity is significantly lower than the theoretical capacity because the rate of ionic transfer across the electrode/ electrolyte interfaces becomes diffusion-limited.[23]

The C-rate (in h^{-1}) is the ratio of discharge current to the maximum cell capacity and specifies how fast a cell is discharged: A 1C rate refers a discharge current that discharges the entire cell in 1 hour; 2C rate refers to a discharge current that discharges the cell in 0.5 h. Thus, higher C-Rates correlate with higher currents and lower available cell capacities.

The specific energy or gravimetric energy density (in Wh kg^{-1}) ED of a battery cell depends on the cell voltage U, the specific capacity C_{sp} (in mAh g^{-1}) and the mass loading of active materials m_A (in g cm^{-2}) relative to the total battery mass $\sum m_i$ including the mass (in g cm^{-2}) of all inactive cell components (packaging, electrolyte, current collectors):[26]

$$ED = \frac{U \cdot m_A \cdot C_{sp}}{\sum m_i}. \tag{2-8}$$

Therefore, the practical energy density of a battery cell can be maximised by (i) enlarging the potential difference E between the two electrodes, (ii) increasing the amount of electrons involved in the cell reaction, (iii) minimalising the molecular weight of the electrodes, (iv) minimalising inactive components, (v) reducing the discharge current or (vi) decreasing the internal cell resistance.

The growing interest in developing cells with lithium anodes is related to a high cell voltage due to the very low electrochemical potential of lithium metal and to the high theoretical capacity (3862 mAh g^{-1}) of lithium metal, which stems from the low molecular weight of lithium and the fact that no inactive elements are included in the electrode.

Another important property of electrochemical cells is self-discharge, which implies a decrease in available capacity over time, even without energy being taken from the cell for electrical work. Self-discharge can result from transport of neutral species or simultaneous transport of ions and electrons through the electrolyte.[27] In addition, chemical reactions between electrode and electrolyte or decomposition can cause a capacity loss over time.[23]

Up to date, different types of batteries are being developed and commercialised. In general, batteries can be divided in primary and secondary cells. A primary battery can only be discharged once and has to be disposed after use, as the electrode materials undergo irreversible changes during discharge. Examples for primary batteries are the alkaline battery or the zinc-air battery used in hearing aids.[28] In a secondary battery the original composition of the electrodes can be restored by reverse current. Upon charge the redox and transport processes occurring upon discharge in the cell are reversed. Therefore, these rechargeable secondary batteries can be cycled multiple times.[29] To reduce battery stress and increase the battery lifetime rechargeable batteries are seldom fully discharged or charged. They are either operated with defined cutoff-potentials or in a defined state of charge (SoC) range. A depth of discharge (DoD) of 80% means for example that only 80% of the available energy is delivered, while 20% remain stored in the battery. The cycle life of a battery defines the number of cycles until the capacity fades to 80% of its initial capacity, while the capacity retention is the ratio of the capacity after a certain amount of cycles to the initial capacity. The capacity fade of a single cycle is given by the Coulombic efficiency *CE,* describing the ratio of the charge gained from the system to the charge introduced to the system.

The capacity loss upon self-discharge is reversible, while electrode and electrolyte reactions or decomposition during cycling lead to an irreversible capacity loss.[23]

The most prominent rechargeable battery is the LIB with applications in portable electronics, EVs and stationary energy storage systems.[30,31] In the following chapter the state-of-the-art LIB and its working mechanism is introduced.

2.1.1 Lithium-Ion Battery (LIB)

Since Sony released the first LIB in 1991, the annual production of LIBs has increased constantly.[32] LIBs are currently the primary energy storage devices in portable electronics such as smartphones or laptops, in EVs or in stationary storage systems for regenerative electricity.

LIBs contain electrode materials that can reversibly store and release lithium ions (Li^+). During operation, lithium ions shuttle between the anode and cathode, thus LIBs are often referred to as 'rocking-chair' batteries. Upon discharge, lithium ions deintercalate from the anode and intercalate into the cathode across a liquid electrolyte, while electrons are transported through an external circuit. Upon charge the direction of all processes is reversed. The working principle of a typical LIB is presented in Figure 2-2 with graphite and lithium cobalt oxide $LiCoO_2$ (LCO) as anode and cathode materials, respectively.
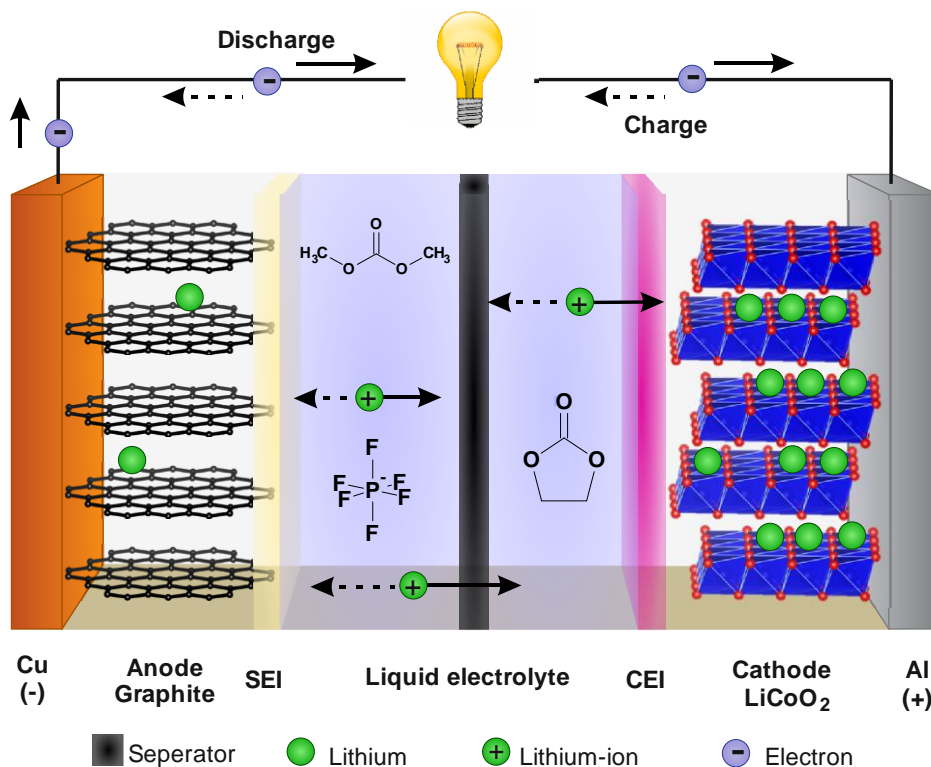
Figure 2-2: Schematic visualisation of the working principle of a typical lithium-ion battery, composed of $LiCoO_2$ and graphite as cathode and anode materials, respectively. The liquid electrolyte contains $LiPF_6$ dissolved in ethylene carbonate and dimethyl carbonate.

The redox reactions occurring upon cycling of the cell shown in Figure 2-2 are given by equation 2-9 and 2-10:

$$\text{Anode:} \qquad Li_xC_6 \underset{\text{Charge}}{\overset{\text{Discharge}}{\rightleftharpoons}} C_6 + x\,e^- + x\,Li^+ \qquad\qquad (2\text{-}9)$$

$$\text{Cathode:} \qquad Li_{1-x}CoO_2 + x\,e^- + x\,Li^+ \underset{\text{Charge}}{\overset{\text{Discharge}}{\rightleftharpoons}} LiCoO_2 \qquad\qquad (2\text{-}10)$$
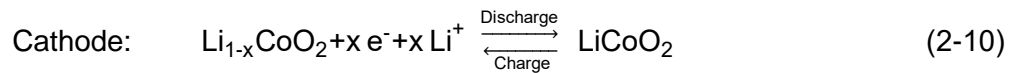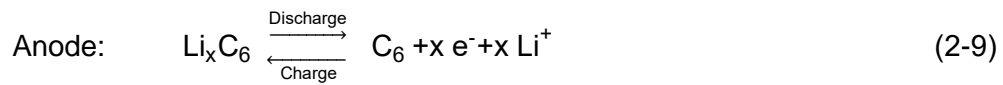
Different cell chemistries with various electrode combinations are used in LIBs. Each material combination exhibits distinct advantages and disadvantages in terms of energy and power density, safety, costs or lifetime.

Graphite is the common material at the anode side in LIB as carbon-based materials exhibit high energy densities.[33] Other anode materials are being further explored, such as silicon (Si) or lithium titanate $Li_4Ti_5O_{12}$ (LTO), to avoid the risk of the thermal runaway of a battery, which will be discussed in more detail below.[33,34,35]

LCO is the predominant cathode material used in LIBs for consumer applications as it is easily synthesised and exhibits stable cyclisation.[36] However, the high costs of cobalt (Co) and safety hazards have led to the substitution of Co by nickel (Ni) or manganese (Mn) and the development of alternative cathodes such as $LiNiO_2$ (LNO), $LiMnO_2$ (LMO), $LiMn_2O_4$ (LMO spinel) $LiNi_{0.5}Mn_{1.5}O_4$ (LNMO) or $Li_{1+x}(Ni_aCo_bMn_c)_{1-x}O_2$ (NCM).[31,37] Ni and Mn instead of Co are advantageous in terms of reversibility and safety, respectively.[38] The most prominent cathodes for automotive applications include $LiNi_{0.8}Co_{0.15}Al_{0.05}O_2$ (NCA), $LiMn_2O_4$ (LMO spinel), $Li_{1+x}(Ni_aCo_bMn_c)_{1-x}O_2$ (NCM) or $LiFePO_4$ (LFP).[39] Figure 2-3 compares the properties of several cathode materials for applications in EVs.
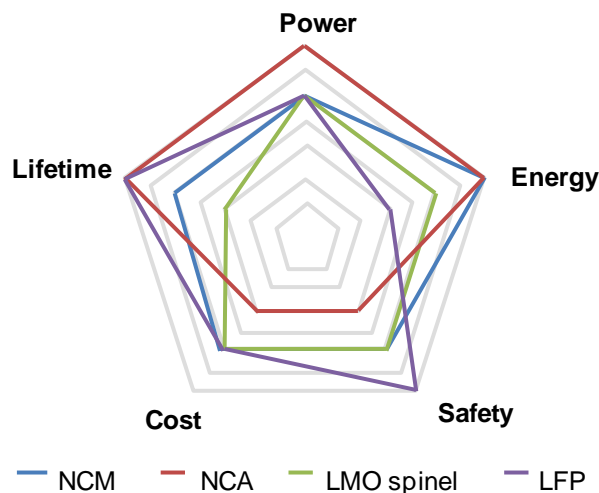
Figure 2-3: Comparison of different cathode materials for applications in EVs. Drawn after Dinger *et al.*[39]

No cathode material reaches maximum performance along all dimensions, *e.g.* NCA or NCM provide high energy density, while LFP possesses a very low electrical conductivity and has to be mixed with conductive carbon, which reduces its energy density. However, LFP exhibits a high chemical stability and provides safe operation.[31]

In conventional LIBs the liquid electrolyte (LE) consists of a lithium salt (*e.g.* lithium hexaflurophosphate $LiPF_6$) dissolved in organic solvents based on carbonates. A synergistic effect is achieved when cyclic and linear carbonates are mixed.[40] The low viscosity of the linear carbonate (*e.g.* dimethyl carbonate (DMC)) promotes the lithium-ion transport, while the cyclic carbonate (*e.g.* ethylene carbonate (EC)) exhibits high anodic stability on cathode surfaces and has a high dielectric constant, which theoretically reduces the formation of ion pairs and increases the mobility of ions in the electric field.[31,40] The LE is characterised by a high lithium-ion conductivity (up to $10^{-2}\,S\,cm^{-1}$) and a low electronical conductivity. Even though conventional LIBs are indispensable in today's electronic market, several LE related challenges remain in LIBs:

(1) The operation of LIBs is limited to a narrow temperature window. At low temperatures the viscosity of the LE increases, reducing the lithium-ion conductivity, while at high temperatures the flammability of the LE is a serious risk.[14]

(2) The charge and discharge potentials of graphite anodes are close to the potential of Li deposition. Therefore, Li metal can be deposited on the graphite under harsh conditions such as overcharging or charging at low temperatures.[41] This process is known as Li plating and leads to a decrease in performance, and poses safety hazards.[42]

(3) The risk of a thermal runaway (TR) during cycling of a LIB results from a series of self-accelerated exothermic reactions causing an increase of the cell temperature. This situation is responsible for many safety incidents and fires associated with battery operations. Once started, a TR is unstoppable until all reactants (electrodes and electrolyte) are consumed.[31] A TR of a fully charged LIB occurs if the temperature exceeds 160 °C.[43]

(4) During initial cycle the LE reacts with the anode or cathode, creating a SEI (solid electrolyte interlayer) or CEI (cathode electrolyte interlayer), respectively. These interlayers lead to an increase of the cell resistance and

decrease of the capacity due to consumption of active Li.[44,45] The continuous formation and dissolution of the SEI on graphite is also considered as an important part of a TR.[46]

(5) The lithium-ion transfer number t_{Li^+} of common liquid organic electrolytes is limited to $0.2 - 0.5$.[40,47] A lithium-ion transfer number significantly lower than 1 indicates undesired anion transport as the lithium-ion transfer number t_{Li^+} equals the ratio of the lithium-ion mobility u_{Li} to the sum of mobilities of all ions $\sum u_i$:

$$t_{Li^+} = \frac{u_{Li^+}}{\sum u_i}.$$

(2-11)

A low transfer number results to an enrichment of anions near the electrode's surfaces causing concentration polarisation during battery operation and an increase in the cell resistance.[40]

(6) The integration of high-voltage cathodes such as LNMO (4.8 V *vs.* Li+/Li) or NCM materials cannot be realised in conventional LIBs as the thermodynamic stability limit of carbonate electrolytes is exceeded.[31] As a result of electrolyte decomposition at high potentials the formation of gaseous degradation productions can be observed.[49]

(7) Transition metal ions from the cathode such as Mn^{2+} in LNMO can dissolve in the LE and migrate from the cathodic to the anodic side resulting in capacity fading as active material is consumed in side reactions.[48,49] For the graphite anode the reduction of Mn^{2+} to nanoscaled metal particles is reported.[50] In principle all electrode side reaction products can diffuse to the opposite electrode, where they can trigger additional degradation reactions.[49]

(8) The integration of Li metal anodes in LIBs can lead to the formation of Li dendrites upon cycling. Li dendrites growing from the anode to the cathode side result in short-circuiting and battery failure.[16] Furthermore, Li dendrites can initiate a TR.[51]

The limits and problems of LEs in LIBs have led to the development of alternative battery concepts including SSBs which will be presented in the following chapter.

2.1.2 Solid-State Battery (SSB)

In solid-state batteries (SSBs) the flammable and toxic liquid electrolyte used in LIBs is replaced by a solid electrolyte (SE), which improves safety and enables operation in a wider temperature window. Anode and cathode materials known from LIBs can be in principle used for construction of SSBs but only lithium metal anodes enable an increase in volumetric and gravimetric energy density up to 70 and 40%, respectively.[15] In contrast to LEs most SEs are single ion conductors, thus undesired anion movement is suppressed in SSBs and, consequently, the cell current is not limited by polarisation effects. Therefore, SSBs could possibly provide higher current densities and faster charging than conventional LIBs. SEs also prevent the undesired dissolution of metal ions from the electrodes in the electrolyte. In addition, SSBs provide the potential advantage of a simplified battery structure with lower weight as all cells could be set in one container, whereas LIBs require individual containers for each cell.[52] The setups of a SSB with lithium anode and a state-of-the-art LIB are compared in Figure 2-4.
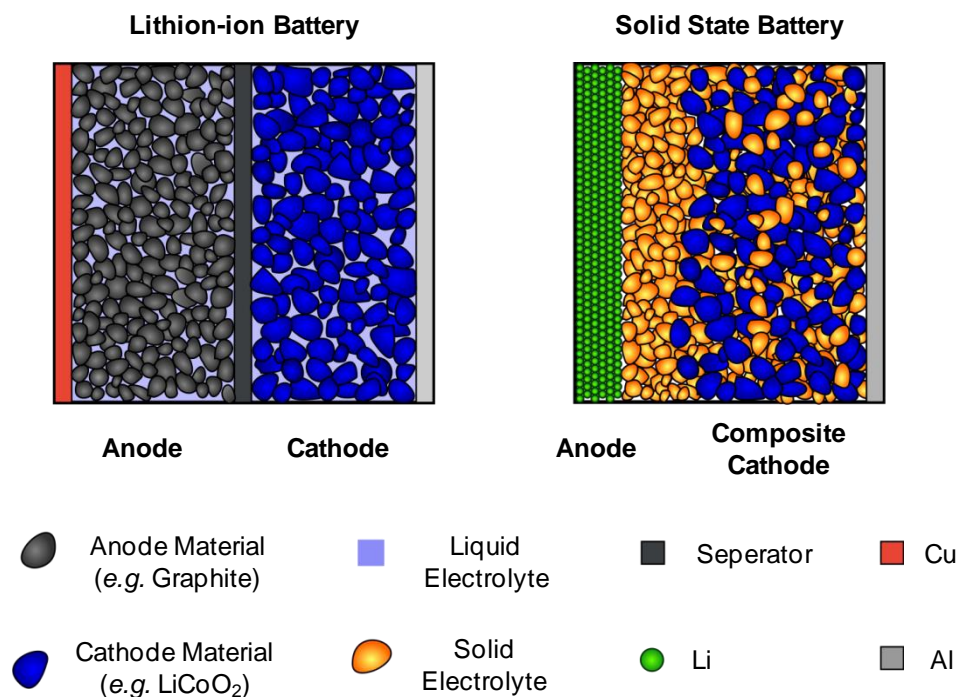
Figure 2-4: Setup of a state-of-the-art lithium-ion battery and a solid-state battery with lithium metal anode.

In LIBs the LE infiltrates the electrodes creating ionic conduction paths, as the electrode materials are often poor ionic conductors. To ensure the electrode connectivity in SSBs, composite cathodes consisting of active cathode particles, solid electrolyte and electronic conductive particles (*e.g.* graphite) are formed, creating an ionic and electronic percolation network.

SEs can be divided into two major groups: (i) inorganic solids including crystalline materials, glasses or glass-ceramics and (ii) organic solid polymers.[15]

Polymer-based electrolytes offer the benefit of elastic and plastic deformation for compensation of volume changes of the electrodes upon cycling. However, SSBs with polymer electrolytes have to be operated with low current densities at elevated temperatures due to the limited rate capability and the low lithium-ion conductivity of polymers.[53] Interestingly, several polymer electrolytes can be combined with lithium metal anodes and cycled safely at these elevated temperatures.[15] However, further research is needed to develop stable polymer electrolytes with higher lithium-ion conductivities, that can be cycled at higher current densities.

In contrast, a number of inorganic solids such as the lithium thiophosphates (LPS) $Li_7P_3S_{11}$ (17 mS cm^{-1})[54], $Li_{10}GeP_2S_{12}$ (LGPS, 12 mS cm^{-1})[55] and $Li_{9.54}Si_{1.74}P_{1.44}S_{11.7}Cl_{0.3}$ (25 mS cm^{-1})[18] exhibit lithium-ion conductivities exceeding the conductivities of liquid electrolytes (10 mS cm^{-1}). The various inorganic SEs and their properties will be discussed in detail in chapter 2.2. The potential of inorganic SEs for enhanced battery performance at high currents has recently been demonstrated by Kato *et al.* The reported SSB is based on $Li_{9.54}Si_{1.74}P_{1.44}S_{11.7}Cl_{0.3}$ as SEs, $LiNbO_3$ coated LCO as cathode, and a composite $Li_4Ti_5O_{12}$ as anode. This SSB was cycled with a high current density (18C) at 100 °C with a capacity retention of 75% after 500 cycles.[18] However, only a lithium metal anode would provide the desired increase in energy density for applications in EVs.

Kerman *et al.* provide an excellent overview about various SSBs that have been described in literature.[56] However, commercialisation of lithium based SSBs have not been achieved so far. Several challenges related to material research and manufacturing still need to be overcome before SSBs can compete with conventional LIBs.[15,56,57]

Figure 2-5 provides an overview about of major challenges in the development of SSBs.
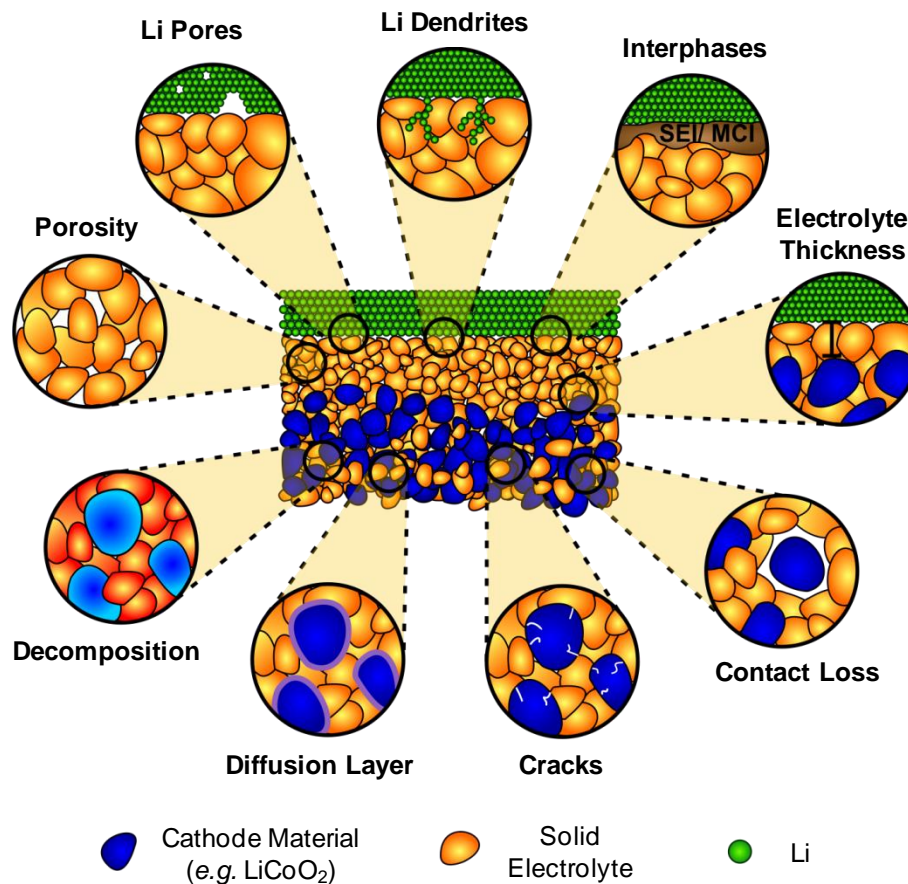
Figure 2-5: Major challenges in the development of SSBs.

(1) At the anode side the formation of Li dendrites can occur, which can grow through the grain boundaries, through pre-existing defects or because of inhomogeneous lithium metal deposition upon charging.[15,56] Li dendrites cause a serious risk of short-circuiting, leading to a failure of the SSB.

(2) Most SEs exhibit a low thermodynamic stability and are reduced or oxidised at low or high potentials, respectively.[58] This low thermodynamic stability leads to a decomposition of the SE or to the formation of interphases between the electrodes and the SEs. Increased interfacial resistances or complete battery failure could possibly be prevented by protective layers at the anode or cathode side or by the formation of stable solid electrolyte interphases (SEI) with sufficient lithium-ion conductivity. A detailed discussion of the electrochemical stability of SEs is provided in chapter 2.2.4.

(3) At the cathode SE interdiffusion of elements could occur, resulting in the formation of a diffusion layer between the cathode and SE. For the LPS/LCO interphase the mutual diffusion of Co, P and S have been reported.[59,60] This problem can be avoided by suitable cathode coating with *e.g.* thin $LiNbO_3$,[61,62] or $Li_4Ti_5O_{12}$ layers.[63,64]

(4) Volume changes upon lithiation and delithiation of both Li anodes and intercalation cathodes could result in cracks, pores or loss of interfacial contact between the SE and the active materials. Increased interfacial resistances and overvoltages as well as capacity fading might be the consequences. Physical delamination and pore formation could be avoided by applying mechanical pressure during cycling, while fractures could be prevented by less brittle SEs.[56] LPS provide the advantage that they are mechanically soft, which is favourable to compensate the volume expansion and contraction of the active materials during cycling. Also they allow cold pressing.[65]

(5) The SE has to be dense and thin enough to reach a total resistance and physical volume comparable to those from separator plus LE in LIBs. The total SE resistance is the sum of the interfacial resistances between SE and electrodes, and the resistance of the bulk material, which depends on the SE thickness and ionic conductivity. SEs with ionic conductivities of $\sim$5 10^{-3} S cm^{-1} have to be thinner than 100 µm to enable SSBs with energy densities competitive with conventional LIBs.[26] However, to achieve higher energy densities the SE thickness has to be further reduced, which still remains a manufacturing challenge.

Further studies are *i.a.* required in the fields of dendrite growth, interfacial and mechanical properties and manufacturing of SSBs.

Interestingly, inorganic SE thin-films and Li metal anodes have also been combined successfully in microbatteries, which were cycled up to 31 000 times.[66]

2.1.4 Microbattery

Microbatteries act as power sources for consumer and medical electronics such as smart cards, sensors, implantable defibrillators, neural simulators, electronic chips and microelectromechanical systems (MEMS).[67] Microbatteries include solid inorganic thin-films instead of liquid electrolytes because they allow device minimalisation and improved safety as no flammable and toxic liquid electrolyte is used.[14,68]

The first thin-film solid-state battery (TF-SSB) – a battery based on lead and silver and their corresponding chlorides – was patented in 1965.[69] Since then, the research focus shifted to lithium based batteries. In 1972 the first lithium based microbattery was reported, consisting of lithium metal as anode, (doped) lithium iodide as electrolyte and metal-iodide as cathode – but it was a non-rechargeable battery.[70] Rechargeable TF-SSBs based on lithium were intensively investigated in the 1990s by Bates *et al.* from Oak Ridge National Laboratory (OGNL).[66,71,72,73,74] The general setup of such microbattery consists of a substrate, a cathode, an anode, their respective current collectors, the thin-film SE and a protective coating on top of the whole system, as is schematically visualised in Figure 2-6.
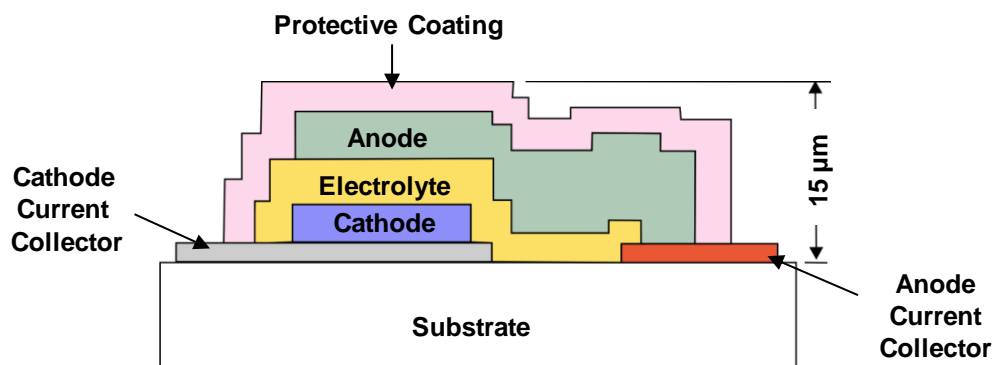
Figure 2-6: Schematic cross-section of a thin-film lithium battery. Drawn after Dudney *et al.*[75]

The various layers of microbatteries are commonly prepared by vacuum deposition techniques such as thermal evaporation (TE) or radio frequency magnetron sputtering (rf-MS).

A large variety of cathode materials such as V_2O_5, $Li_xMn_2O_4$, TiS_2 or $LiCoO_2$ were integrated in thin-film cells with lithium metal as anode and amorphous nitrogen

doped lithium phosphate (LiPON)[1] as SE.[66,74,76,77] LiPON exhibits a lithium-ion conductivity in the range of $2 \cdot 10^{-6}\,\mathrm{S\,cm^{-1}}$ and exceptional electrochemical stability.[78,79] LiPON and Li are most commonly applied as electrolytes and anodes, respectively, in TF-SSBs. However, microbatteries composed of alternative materials such as $Li_2S\text{-}P_2S_5$ (electrolyte) and Zn_3N_2 (anode) have been reported as well.[80,81] Neudecker *et. al* developed a Li-free thin-film battery, where the Li anode is formed *in situ* directly on top of a Copper (Cu) current collector upon charge.[82]

Table 2-1 gives an overview of lithium based microbatteries with at least 100 reported cycles. The microbattery with the highest performance was reported by Wang *et al* and was cycled 31 000 times with a capacity retention (CR) of 97%.[66] This battery consisted of $LiCoO_2$, LiPON and Li metal, which is also the setup used in commercial microbatteries.[83,84,85,86]

All microbatteries listed in Table 2-1 are prepared by expensive vacuum deposition techniques. A cost-effective alternative would consider the preparation of one or several layers by chemical solution deposition (CSD).

---

[1] note that the acronym is not a chemical sum formula

Table 2-1: Overview of reported lithium microbatteries with a minimum of 100 cycles. The deposition method is given in brackets if available.

Anode	Electrolyte	Cathode	U / V	j / µA cm^{-2}	Cycles	CR / %	Year	Ref.
Li (TE)	LiPON (rf-MS) [1 – 2 µm]	LiCoO$_2$ (rf-MS) [0.05 µm]	3.0-4.2	100	31000	97	1996	[66]
Li (TE)// LiI (TE)	6LiI-4Li$_3$PO$_4$-P$_2$S$_s$ (rf-MS)	TiS$_2$ (rf-MS)	1.4-2.8	100	21000	80	1996	[87]
SiTON (rf-MS) [0.01 µm]	LiPON (rf-MS) [1.5 µm]	LiCoO$_2$ (rf-MS) [2 µm]	2.7-4.1	83	13000	77	1999	[88]
Li	LiPON [2.5 µm]	LiNi$_{0.5}$Mn$_{1.5}$O$_4$ [2 µm]	3.5-5.1	5 C	10000	91	2015	[89]
Li$_6$V$_2$O$_5$ (rf-MS) [0.3 µm]	LiPON (rf-MS) [1.0 µm]	V$_2$O$_5$ (rf-MS) [100 nm]	1.0-3.5	10	5800	90	1999	[76]
Li (TE) [3-5 µm]	LiPON (rf-MS) [1 µm]	TiS$_2$ (rf-MS)	1.8-2.45	100	4000		1994	[74]
Li (TE) [3 µm]	LiPON (rf-MS) [1.0-1.5 µm]	Li$_x$Mn$_{2-y}$O$_4$ (rf-MS)	2.5-4.5	20	4000	90	1999	[77]
Li (TE) [4 µm]	Li$_{3.6}$Si$_{0.6}$P$_{0.4}$O$_4$ (rf-S) [2 µm]	TiS$_2$ (CVD) [1 µm]	2.0-2.5	16	2000	80	1983	[90]
Li (TE) [1.0 µm]	LiBON (rf-MS) [1.5 µm]	LiCoO$_2$ (rf-MS) [1.7 µm]	3.0-4.2	84	1000	90	2016	[91]
Li (TE) [1 µm]// Si (TE) [20 nm]	Li$_2$S-P$_2$S$_5$ (PLD) [10 µm]	LiCoO$_2$ (PLD) [1 µm] // LiNbO$_3$ (PLD) [10 nm]	3.0-4.2	100	1000	90	2012	[80]
Zn$_3$N$_2$	LiPON	LiCoO$_2$	2.7-4.2	100	1000	73	2000	[81]
Sn$_3$N$_4$	LiPON	LiCoO$_2$	2.7-4.2	1000	1000	57	2000	[81]
Cu [0.1 µm] (Li-free)	LiPON [2 µm]	LiCoO$_2$ [0.8 µm]	3.0-4.2	1000	1000	80	2000	[82]
Li (TE)	LiPON (rf-MS) [1-2µm]	LiCoO$_2$ (rf-MS) [0.47 µm]	3.8-4.2	100	1000	99	1996	[66]
Li (TE) [3 mm?]	LiPON (rf-MS) [1 µm]	LiMn$_2$O$_4$ (e-BE) [0.3 - 4 µm]	3.8-4.5	40	600		1995	[92]
Li$_x$V$_2$O$_5$ (rf-MS) [0.3 µm]	LiPON (rf-MS) [1.5 µm]	V$_2$O$_5$ (rf-MS) [0.3 µm]	1.0-3.5	10	350	100	1999	[93]
Li	Li$_2$O-V$_2$O$_5$-SiO$_2$ (rf-MS)	MoO$_{3-x}$ (rf-S)	1.0-3.0	20	250		1989	[94]
Li (TE) [3-5 µm]	LiPON (rf-MS) [1 µm]	LiMn$_2$O$_4$ (rf-MS)	3.9-4.2	30	150	85	1994	[74]
Li	Li$_2$O-V$_2$O$_5$-SiO$_2$ (rf-MS)	MnO$_{2-x}$ (rf-S)	1.0-3.0	10	100	78	1996	[95]
SnO (PLD) [0.15 µm]	Li$_2$O-V$_2$O$_5$-SiO$_2$ (Li$_{2.2}$V$_{0.54}$Si$_{0.46}$O$_{3.4}$) (PLD) [1.1 µm]	LiCoO$_2$ (PLD) [0.4 µm]	0.7-3.0	44	100	45	2004	[96]
Li (TE)	LiPON (rf-MS) [1 µm]	LiMn$_2$O$_4$ (rf-MS) [0.3 µm]	3.7-4.3	100	100	96	1999	[97]
Li (TE) [1 µm]	LiPON (rf-MS) [2.5 µm]	LiCr$_{0.05}$Ni$_{0.45}$Mn$_{1.5}$O$_{4-\delta}$ (PLD) [0.06 µm]	3.5-4.9	2C	100	100	2014	[98]

TE: Thermal evaporation, rf: radio frequeny, MS: magnetron sputtering, CVD: chemical vapor deposition, PLD: pulsed laser deposition, e-BE: electron beam evaporation.

2.2 SOLID ELECTROLYTES

In 1899 Walther Nernst discovered ionic conductivity in solid ceramic oxides, suited therefore to be used as solid electrolytes (SEs).[99] Typically, SEs exhibit ionic conductivities in the range of 10^{-1}-10^{-5} S cm^{-1}, which is in the same order of magnitude as those of liquid electrolytes and semiconductors.[100]

Up to date, a huge variety of materials have been described as SEs with different mobile species including protons, halogenides, oxides, lithium, sodium, silver, or copper ions.[101] Especially proton, oxide and lithium-ion conductors are important for technological applications such as water hydrolysis cells, proton exchange membrane fuel cells, solid oxide fuel cells (SOFCs), chemical sensors, electrochromic displays, chemotronic elements, photogalvanic solar cells and solid-state batteries (SSBs).[100]

Sodium and lithium-ion conducting materials are commonly used as electrolytes in SSBs. The most important properties of a solid electrolyte for application in SSBs include:

(1) high ionic conductivity at operational temperature,

(2) negligible electronic conductivity for prevention of self-discharge of the SSB,

(3) negligible grain boundary resistance,

(4) low charge transfer resistance between SE and electrode materials,

(5) prevention of dendrite formation and growth,

(6) chemical and electrochemical stability against electrode materials during cell preparation and operation,

(7) chemical stability against air and moisture,

(8) cost-efficient and easy fabrication, abundant precursors and non-toxic materials.

Recently, several solid lithium-ion electrolytes with ionic conductivities exceeding the conductivities of conventional liquid electrolytes in LIBs have been discovered.[18,54,55] Moreover, most lithium-ion conducting SEs exhibit very low electronic conductivities, resulting in lithium-ion transference numbers close to 1.[55]

As previously discussed high charge transfer resistances between SEs and cathode materials can be reduced by suitable coating of the cathode particles. However, other aspects such as dendrite formation, electrochemical stability and the fabrication process remain challenging.

This section focuses on the principles of ionic conduction in solids, followed by an overview of lithium conducting bulk and thin-film inorganic SEs. In addition, the electrochemical stability of SEs will be discussed.

2.2.1 Ionic Conduction

Ionic transport in a solid requires vacancies in regular lattice positions or only partially occupied interstitial sites. Defects can be formed in crystalline stoichiometric materials *e.g.* (i) by cation migration from their regular lattice position to interstitial sites, or (ii) by both cation and anion migration from their regular positions to the crystal surface, which creates the so-called Frenkel or Schottky defects, respectively. The ionic transport through these defects is visualised in Figure 2-7. Defects can also be introduced into the lattice by nonstochiometry or by doping with aliovalent ions.
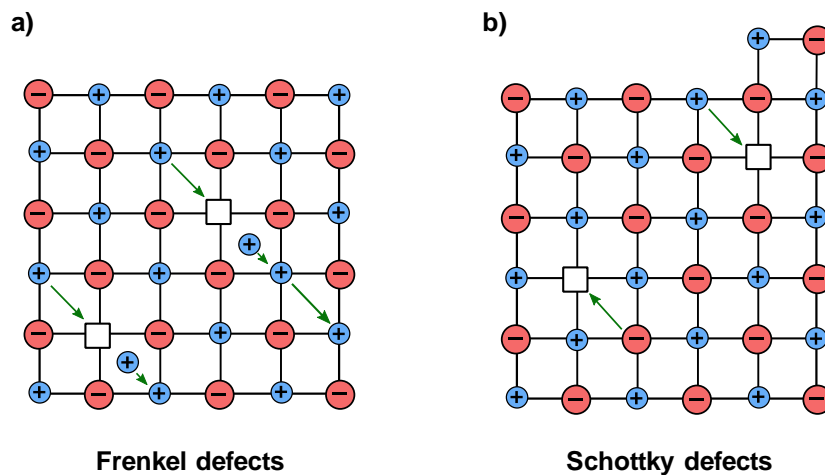
Figure 2-7: Material transport in stoichiometric crystalline solids by defect migration. Frenkel defects (a) and Schottky defects (b) are created by cation migration to interstitial sites (a) or by anion and cation migration to the crystal surface (b) leaving behind vacancies.

Ionic conduction describes the process of ion hopping through interconnected sites under the driving force of an electric field E as described by Eq. 2-12:

$$j_i = \sigma_i E, \tag{2-12}$$

where j_i is the ionic current density and σ_i the specific ionic conductivity. The ionic conductivity σ_i depends on the carrier concentration c_i, the Faraday constant F, the charge number z_i and the ionic mobility u_i:

$$\sigma_i = c_i z_i F u_i. \tag{2-13}$$

A general guideline of SE design is that half of the available mobile ion sites should be filled to reach the maximum conductivity.[102]

Since the ionic motion in a solid electrolyte is diffusive, the Einstein equation can be applied for correlation of the ionic mobility u_i to the self-diffusion coefficient D_i:

$$D_i = \frac{u_i R_{\text{Gas}} T}{z_i F}. \tag{2-14}$$

In Eq. 2-14, R_{Gas} is the ideal gas constant and T the temperature. Insertion of Eq. 2-14 into Eq. 2-13 results in the Nernst-Einstein equation for the ionic conductivity:

$$\sigma_i = \frac{D_i c_i (z_i F)^2}{R_{\text{Gas}} T}. \tag{2-15}$$

The diffusion coefficient D_i shows an Arrhenius behaviour, which is expressed by Eq. 2-16:

$$D_i = D_{i,0} e^{-\frac{\Delta G_m^{\neq}}{R_{\text{Gas}} T}}, \tag{2-16}$$

where $\Delta G_m^{\neq}$ is the free molar enthalpy of migration. $D_{i,0}$ is correlated by the random walk theory to the jump attempt frequency ω_0 and the jump distance d according to Eq. 2-17 for three-dimensional diffusion:

$$D_{i,0} \approx \frac{1}{6} d^2 z_{\text{NN}} (1 - o) \omega_0 f. \tag{2-17}$$

In Eq. 2-17 z_{NN} describes the number of nearest neighbours, o the fractional occupation and f is a geometrical factor. Therefore, the factor $z_{\text{NN}}(1 - o)$ defines the number of unoccupied neighboring sites. Insertion of Eq. 2-17 and 2-16 in Eq. 2-15 leads to Eq. 2-18:

$$\sigma_i = \frac{1}{6} d^2 z_{\text{NN}} (1 - o) \omega_0 f \frac{c_i (z_i F)^2}{R_{\text{Gas}} T} e^{-\frac{\Delta G_m^{\neq}}{R_{\text{Gas}} T}}. \tag{2-18}$$

The free molar enthalpy of migration $\Delta G_{\mathrm{m}}^{\neq}$ is defined as:

$$\Delta G_{\mathrm{m}}^{\neq} = \Delta H_m^{\neq} - T \Delta S_m^{\neq}, \tag{2-19}$$

where $\Delta H_m^{\neq} = E_{\mathrm{A}}$ describes the molar enthalpy of migration or the activation energy and $\Delta S_m^{\neq}$ the molar entropy of migration.

Insertion of Eq. 2-19 into Eq. 2-18 leads to Eq. 2-20:

$$\sigma_{\mathrm{i}} = \frac{A_D}{T} e^{-\frac{E_{\mathrm{A}}}{R_{\mathrm{Gas}} T}}, \tag{2-20}$$

with the pre-exponential factor A_D given by Eq. 2-21:

$$A_D = \frac{1}{6} d^2 z_{\mathrm{NN}} (1 - o) \omega_0 f \frac{c_i (z_i F)^2}{R_{\mathrm{Gas}}} e^{\frac{\Delta S_m^{\neq}}{R_{\mathrm{Gas}}}}. \tag{2-21}$$

Eq. 2-20 and 2-21 lead to the conclusion, that ionic conductivity depends on parameters such as activation energy and entropy, temperature, jump attempt frequency, jump distance, charge carrier concentration, number of unoccupied neighbouring sites and a geometric factor.

2.2.2 Inorganic Lithium-Ion Conductors

In general, inorganic electrolytes for applications in SSBs can be grouped in lithium oxide based SEs and lithium sulphide based SEs. Figure 2-8 compares the lithium-ion conductivities of several inorganic SEs with polymer and liquid electrolytes.
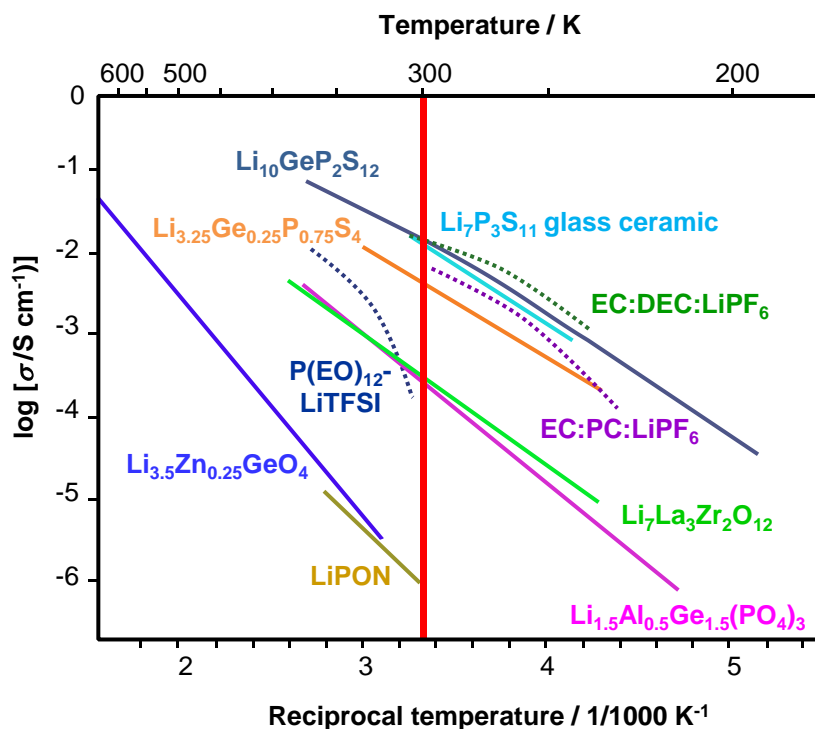
Figure 2-8: Lithium-ion conductivities of inorganic SEs compared to those of commonly used liquid electrolytes (EC:DEC:LiPF$_6$ and EC:PC:LiPF$_6$)[103] in LIBs and a typical polymer electrolyte (P(EO)$_{12}$-LiTFSI).[104] Inorganic SEs includes Li$_{10}$GeP$_2$S$_{12}$,[55] Li$_{3.25}$Ge$_{0.25}$P$_{0.75}$S$_4$,[120] Li$_7$P$_3$S$_{11}$,[54] LiPON,[79] Li$_{3.5}$Zn$_{0.25}$GeO$_4$,[116] Li$_7$La$_3$Zr$_2$O$_{12}$ [105] and Li$_{1.5}$Al$_{0.5}$Ge$_{1.5}$(PO$_4$)$_3$.[106] The vertical red line marks room temperature. The diagram is drawn after Janek *et al*.[15]

Oxide based lithium-ion conductors

Oxide based lithium-ion conductors include *e.g.* perovskite- and garnet type materials as well as materials with NASICON (sodium super ionic conductor) or LISICON (lithium super ionic conductor) structure. Detailed description of the corresponding structures and lithium-ion conduction mechanisms can be found elsewhere.[107,108,109]

Perovskite-type materials (ABO$_3$) include the lithium-ion conductor Li$_{3x}$La$_{2/3-x}$TiO$_3$ (LLTO). Li$_{0.34}$La$_{0.51}$Ti$_{2.94}$ exhibits a high bulk lithium-ion conductivity of 1 mS cm^{-1} but

a low grain boundary conductivity of 0.075 mS cm^{-1},[110] which is characteristic for LLTO.

Garnet-type materials ($C_3A_2D_3O_{12}$) are some of the most prominent lithium-ion conductors especially $Li_7La_3Zr_2O_{12}$ (LLZO). Compared to the general garnet structure LLZO contains a higher proportion of Li. Garnets such as LLZO can crystallise in a tetragonal or a cubic phase, but only cubic LLZO exhibits a lithium-ion conductivity of 0.8 mS cm^{-1}, which is two orders of magnitude higher than its tetragonal phase.[111,112] By doping with metals with higher valences such as Al more lithium vacancies can be created, which enhances the lithium-ion conductivity.[108]

NASICON materials ($AM_2(PO_4)_3$ with A=Na, Li and M= Ge, Ti, Zr, Ta, Hf, Sn) include different sodium and lithium-ion conductors. By partial substitution of the tetravalent metal ion with trivalent ions such as Al^{3+} more lithium ions are incorporated into the structure and new diffusion paths with reduced activation energies are created, enhancing the ionic conductivity.[113] $Li_{1+x}Al_xTi_{2-x}(PO_4)_3$ (LATP)[114] with x=0.3 and $Li_{1+x}Al_xGe_{2-x}(PO_4)_3$ (LAGP)[115] with x=0.5 exhibit lithium-ion conductivities of up to 0.7 mS cm^{-1} and 5 mS cm^{-1}, respectively. LISICON ($Li_{2+2x}Zn_{1-x}GeO_4$) materials include *e.g.* the solid solution $Li_{3.5}Zn_{0.25}GeO_4$ with a lithium-ion conductivity of 10^{-7} S cm^{-1}.[116]

Sulphide based lithium-ion conductors

Substitution of oxygen in LISICON materials by sulphur leads to the so-called thio-LISICON material family with various stoichiometries in the Li_2S, GeS_2, ZnS, Ga_2S_3, SiS_2, P_2S_5, Al_2S_3 systems.[117,118,119] Thio-LISICON materials such as $Li_{3.25}Ge_{0.25}P_{0.75}S_4$ exhibit lithium-ion conductivities of 2 mS cm^{-1}.[120] The higher ionic conductivity of thio-LISICON compared to LISICON materials is related to a weaker interaction between the anions and the lithium ions, as sulphur ions show a better polarisation capability than oxygen ions.[121]

Recently, several crystalline materials with different crystal structure from the thio-LISICON phase such as $Li_{10}GeP_2S_{12}$,[55] $Li_7P_3S_{11}$[54] and $Li_{9.54}Si_{1.74}P_{1.44}S_{11.7}Cl_{0.3}$[18] were reported to exhibit extremely high lithium-ionic conductivities of 12 mS cm^{-1}, 17 mS cm^{-1} and 25 mS cm^{-1} at room temperature (RT), respectively. These values are comparable to those of standard liquid electrolytes used in LIBs (10 mS cm^{-1}).[55] Argyrodite-type crystals Li_6PS_5X (X = Cl, Br, I)[122] and the solution processed nanoporous β-Li_3PS_4[123] also exhibit high ionic conductivities of over 1 mS cm^{-1} and 0.1 mS cm^{-1}, respectively.

In addition several amorphous sulphide glasses and glass ceramics based on Li_2S and other oxides or sulphides with high conductivities have been reported. The highest conductivities observed among sulphide glasses, *e.g.* LiI–Li_2S–P_2S_5[124] and LiI–Li_2S–B_2S_3,[125] were already in the order of 1 mS cm^{-1} in the early 1980s.

In the xLi_2S-$(1-x)P_2S_5$ system, glasses with more than 70 mol% Li_2S exhibit lithium-ion conductivities of over 0.1 mS cm^{-1}.[126,127] The glasses are commonly prepared by rapid-quenching or mechanical milling techniques. The combination of several anion species, also known as mixed-anion effect, is effective in increasing the conductivity of glasses.[128] The addition of lithium salts such as lithium halides,[125] lithium borohydride ($LiBH_4$)[129] and lithium *ortho*-phosphate (Li_3PO_4)[130] is useful for enhancing the ionic conductivity of glasses from the order of 0.1 to 1 mS cm^{-1} at RT. Besides the high ionic conductivity, an advantage of sulphide electrolytes over oxide based SEs is the easy reduction of grain-boundary resistance by conventional cold-pressing of electrolyte powders.[131] This mechanical property is convenient for construction of SSBs. The mechanical softness of sulphide electrolytes is also favourable to compensate volume changes of active materials during cycling and allows to form dense cathode composites.[15] In addition, sulphides require in general significantly lower crystallisation and sintering temperatures, which reduces the production costs. However, sulphide based SEs suffer from instability and release toxic H_2S in contact with aqueous electrolytes or under ambient air.[132]

2.2.3 Electrochemical Stability

The difference between the electrochemical potentials of the anode μ_A and cathode μ_C defines the open circuit voltage (V_{OC}) of the battery, as previously shown in equation 2-1. If the anode or cathode is a metal electrode such as Li the electrochemical potential is given by the Fermi energy of the metal.[133]

The intrinsic electrochemical stability window E_g of the SE is the energy gap between the top of its valence band and the bottom of its conduction band.[23]

The formation of a thermodynamic stable interface between the SE and the electrode materials requires that the electrochemical potential μ_A of the anode is below the conduction band of the SE, whereas the electrochemical potential of the cathode μ_C has to be above the valence band of the SE, as illustrated in Figure 2-9.[23]
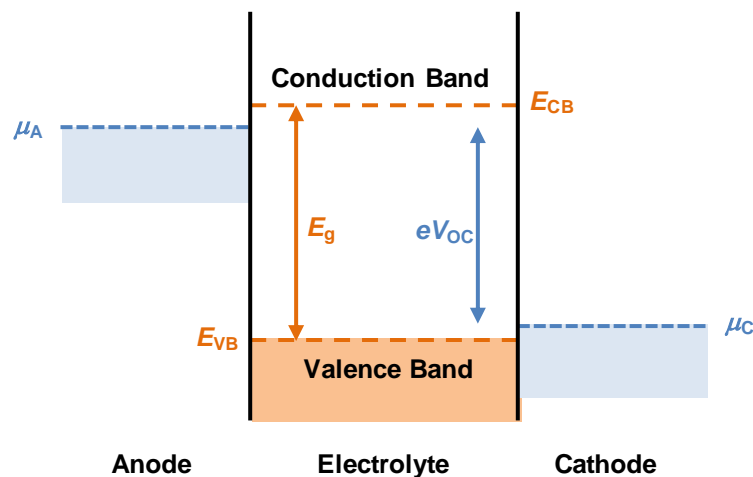
Figure 2-9: Relative energies of the electrochemical stability window E_g of the electrolyte and the electrode electrochemical potentials μ_A and μ_C. Drawn after Goodenough *et al.*[23]

When E_g is lower than V_{OC}, an interface forms between the electrodes and the SE. An electrochemical anode potential above the conduction band leads to an reduction of the SE, while an oxidation occurs when the electrochemical cathode potential is lower than the valence band of the SE.[23]

To prevent undesired interphase formation in SSBs, a wide electrochemical stability window of the SE is required, especially when Li metal anodes (very low μ_A) or high voltage cathode materials (high μ_C.) are used. However, most SEs have limited electrochemical windows and form interphases at the anode and/or cathode side.

Anodic Interface/ Interphases

Theoretical first-principle investigations showed that the reduction of lithium thiophosphates like *e.g.* LGPS, Li_6PS_5Cl and Li_3PS_4 starts around 1.6 – 1.7 V *vs.* Li+/Li, while lithium oxides and phosphates such as LLTO, LATP, LAGP and LISICON start to decompose between 1.4 and 2.2 V *vs.* Li+/Li,[58] which is consistent with experimental studies.[134,135,136,137,138] A lower reduction potential of 0.7 V *vs.* Li+/Li is obtained for LiPON. The reduction of LiPON in contact with Li was also revealed by *in situ* XPS studies.[139] At lower potentials Li binary compounds such as LiX (X = Halogen), Li_2O, Li_2S, Li_3P, $Li_{15}Ge_4$, La_2O_3 or Li_3N are formed in the anode interphase as thermodynamic stable decomposition products.[58] The garnet LLZO has the lowest reduction potential of 0.05 V against Li with the smallest reaction enthalpy. Therefore, the reduction of LLZO by Li might be kinetically hindered, which explains the reported wide electrochemical window of 0 – 5 V *vs.* Li+/Li of garnets.[140,141] Up to date, garnets seem to be the only lithium-ion conducting SEs that form a thermodynamically stable interface.

The nature of the decomposition product determines the type of interphase that is formed. For Li metal anodes in contact with SEs Wenzel *et al.* describe three different types of interphases or interfaces as visualised in Figure 2-10: (a) a thermodynamically stable interface, (b) a mixed conducting interphase (MCI), or (c) a solid electrolyte interphase (SEI).[142]
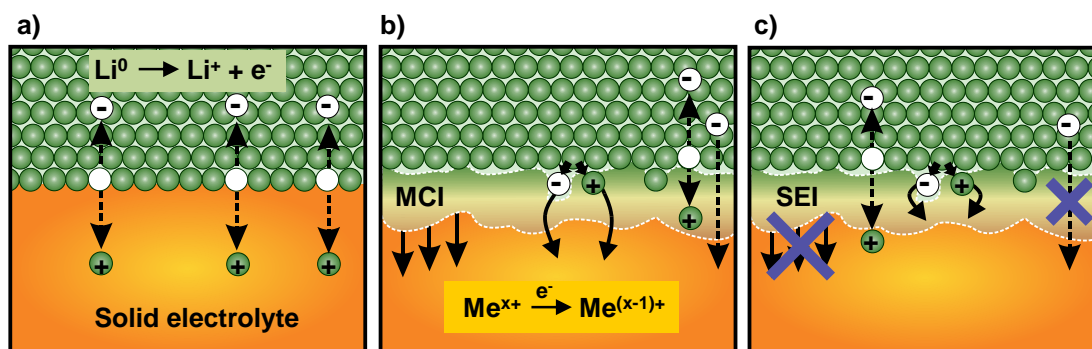
Figure 2-10: Upon contact between SEs and lithium metal three different interphase/interface types can form: (a) thermodynamically stable interface; (b) reactive and mixed-conducting interphase (MCI) or (c) metastable, kinetically stabilised solid electrolyte interphase (SEI). Drawn after Wenzel *et al.*[142]

A MCI describes a growing reactive interphase and is formed, when the SE decomposes into ionic and electronic conductive products. If both ionic and electronic conductivity are in the same order of magnitude, the interphase grows throughout the SE leading to a short circuit and the SSB discharges. MCIs are often formed, when reducible transition metal ions are incorporated in the SE structure. Consequently, titanium containing LLTO or LATP are MCI forming materials that cannot be used in SSBs with lithium metal anode.

A SEI describes a reactive but kinetically stabilised interphase with very small growth rates due to electron and/or ion blocking properties of the decomposition products. Therefore, the SEI passivates the SE and inhibits the continuous bulk decomposition. LiPON,[66] Li_3PS_4[123,143] or $Li_7P_2S_8I$[144] are reported to be compatible with Li anodes, which hints a stabilisation of the SE by its interphase. However, the conductivities of the decomposition products in the SEI highly influence the interfacial resistance of the cell. High interfacial resistances might lead to mechanical failure of the SSB.[52,145] The resistance in symmetrical cells with Li metal electrodes increases of around 30% and 300% with $Li_7P_3S_{11}$ and LGPS as electrolytes, respectively, which is related to the SEI formation.[146,147]

Cathodic Interface/ Interphases

First principle investigations on the cathode side revealed that lithium thiophosphates were oxidised to S and P_2S_5 between 2.1 and 2.3 V *vs.* Li^+/Li with highly favourable reaction energies, whereas lithium oxides and phosphates such as LiPON, LLZO, LISICON, LLTO, LATP and LAGP were oxidised between 2.6 and 4.3 V *vs.* Li^+/Li.[58] Therefore, oxide SEs exhibit a significantly wider electrochemical window than thiophosphate SEs and have lower decomposition energies, but lithium oxides have the disadvantage that they can form gaseous O_2 or N_2 upon oxidation. An overpotential is expected for the oxidation of the SEs as a result of kinetic limitations such as slow diffusion of non-Li elements and slow nucleation and release of gas molecules.

Artificial Interphases

The narrow electrochemical window of lithium thiophosphates results in the formation of high interfacial resistances at the cathode/ SE interphase. The application of coating layers such as $Li_4Ti_5O_{12}$,[61,62] $LiTaO_3$,[148] $LiNbO_3$,[63,64] Li_2SiO_3,[149] Li_3PO_4,[150] on cathode particles has been reported to lead to reduced interfacial resistances and the suppression of mutual diffusion of Co, P and S. First

principle investigations showed that these coating layers exhibit reduction and oxidation potentials between 0.7-1.7 V and 3.7-4.2 V *vs.* Li$^+$/Li, respectively.[58] Overpotentials might even further increase the oxidation limit. Therefore, oxide coatings prevent the thiophosphates from oxidation at the cathode side and act as artificial SEI. This concept could also be applied at the anode side to prevent the reduction of the SEs in contact with Li metal. However, the protection of the lithium anode needs further investigation. PolyPlus Battery Company has developed a protective lithium electrode (PLE) for lithium air batteries that prevents the reduction of the LATP solid electrolyte.[151] By SEI formation or by artificial coatings between the SE and the electrodes, the intrinsic electrochemical window of the electrolyte can be extended, as shown in Figure 2-11.
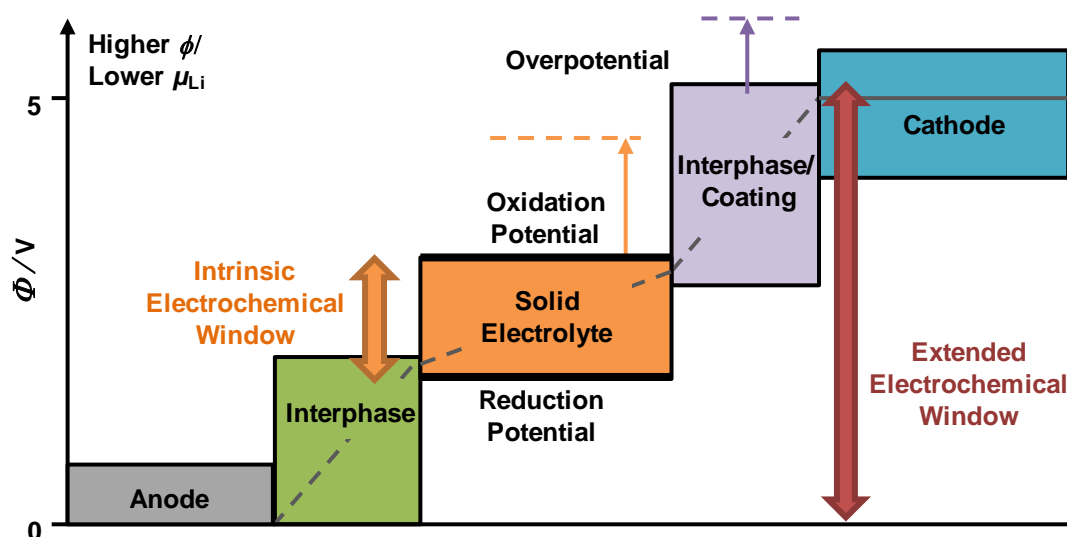
Figure 2-11: Schematic diagram of the electrochemical window (colour bars) and the Li chemical potential profile (grey line) in the SSBs. The (electro)chemical (Li) potentials are beyond the stability window of the SE. The intrinsic electrochemical window is extended by the overpotential and by the interphases. Drawn after Zhu *et al.*[58]

For optimal performance of the SSB, it is required that the interphases or coatings on both anode and cathode side exhibit low electronic conductivity and high ionic conductivity. While coating of electrode materials is widely described in literature for thiophosphates at the cathode side, protection of highly conductive thiophosphates such as Li$_7$P$_3$S$_{11}$ and LGPS from the reduction at the lithium anode has not been investigated in detail. Lithium-ion conducting thin-films might also be used as such protective layers for lithium anodes.

Recently, Xu *et al.* reported a SSB with lithium metal anode and SE bilayers of LGPS and $70Li_2S–29P_2S_5–1P_2O_5$, where $70Li_2S–29P_2S_5–1P_2O_5$ forms a protecting interface layer against lithium metal.[152,153]

Therefore, thin-films of thermodynamically or kinetically stable SEs may also be used as protective layers for lithium anodes to prevent dendrite formation and electrolyte decomposition.

2.2.4 Lithium-Ion Conducting Thin-Films

Similar to bulk type SEs various lithium-ion conducting thin-films have been described in literature: (i) garnets such as $Li_6BaLa_2Ta_2O_{12}$ or (aluminium doped) LLZO, (ii) perovskite type LLTO, (iii) lithium thiophosphates such as $80Li_2S-20P_2S_5$ and LGPS and (iv) several lithium silicates and phosphates.[154,155] The most prominent lithium-ion conducting thin-film is lithium phosphorus oxynitride (LiPON), which is known for its excellent stability against Li metal and was successfully integrated and cycled in microbatteries with Li metal anode.[66] While oxide thin-film electrolytes have been under intense investigation, only a few publications cover lithium thiophosphate thin-films. Table 2-2 gives an overview about the reported SE thin-films and summarises their deposition method, lithium-ion conductivity and activation energy.

In general, SE thin-films exhibit slightly lower lithium-ion conductivities compared to bulk type electrolytes with the same composition ranging from $1·10^{-5} - 1·10^{-7}\,S\,cm^{-1}$. Up to date, $Li_4GeS_4-Li_3PS_4$ thin-films prepared by pulsed laser deposition (PLD) exhibit the highest ionic conductivity with $1.8 · 10^{-3}$.[156]

Additionally to high lithium-ion conductive crystalline thin-films, several materials such as LLZO or LLTO also exhibit high ionic conductivities in the amorphous state.[157,158] In general, crystalline thin-films require higher temperatures during film preparation or annealing, which might limit their application and highlights the advantage of amorphous films. For both crystalline and amorphous thin-films the substrate properties might affect the final layer: *e.g* the lattice parameter influences epitaxial film growth or preferred crystal orientation, while mismatching thermal expansion coefficients of substrate and film could result in cracking. In addition, the atmosphere during deposition and annealing is a critical parameter and could have a negative impact on the substrate properties.

The major drawback of most SE thin-films including LiPON is their fabrication by expensive vacuum deposition techniques such as PLD, radio frequency magnetron sputtering (rf-MS), electron beam evaporation (e-BE) or chemical vapour deposition (CVD), which limits their applications to SEs in microbatteries. A different approach would be their integration as coating layer on the cathode or anode side in bulk type SSBs to prevent to reduction or oxidation of the SE. Chemical solution deposition (CSD) provides an alternative strategy for the deposition of lithium-ion conductive thin-films as it does not require expensive vacuum equipment and allows a cost-effective upscale production. Therefore, it will be discussed in more detail in chapter 2.3.4.

Table 2-2: Solid electrolyte thin-films and their deposition method, lithium-ion conductivity at room temperature and activation energy.

Material	Deposition method	σ_{RT} / S cm^{-1}	E_a / eV	Ref.
LiPON	rf-MS	$2.2 \cdot 10^{-6}$	0.56	[78]
Li$_{0.29}$S$_{0.28}$O$_{0.35}$N$_{0.09}$	rf-MS	$2 \cdot 10^{-5}$	0.47	[159]
Li-La-Zr-O	rf-MS	$4 \cdot 10^{-7}$	0.70	[157]
Al/Ta-Li$_7$La$_3$Zr$_2$O$_{12}$	rf-MS	$4 \cdot 10^{-7}$ (In plane)	0.47	[160]
Li-Al-Ti-P-O	rf-MS	$2.5 \cdot 10^{-5}$	0.31	[161]
Li$_{0.31}$La$_{0.41}$TiO$_3$	rf-MS	$5.3 \cdot 10^{-5}$	0.35	[162]
6LlI-4Li$_3$PO$_4$-P$_2$S$_s$	rf-MS	$2 \cdot 10^{-5}$	n.a.	[87]
Li$_{3.6}$Si$_{0.6}$P$_{0.4}$O$_4$	rf-S	$5 \cdot 10^{-6}$	0.50	[90]
Li$_{6.10}$V$_{0.61}$Si$_{0.39}$O$_{5.36}$	rf-S	$1.0 \cdot 10^{-4}$	0.50	[94]
Li$_3$PO$_4$	PLD	$5.1 \cdot 10^{-7}$	0.59	[163]
Li$_4$SiO$_4$	PLD	$1.2 \cdot 10^{-8}$	0.64	[163]
50Li$_4$SiO$_4$-50Li$_3$PO$_4$	PLD	$1.6 \cdot 10^{-6}$	0.53	[163]
80Li$_2$S-20P$_2$S$_5$	PLD	$2.8 \cdot 10^{-4}$	0.39	[164]
Li$_3$PS$_4$	PLD	$5.3 \cdot 10^{-4}$	0.47	[165]
Li$_{3.25}$Ge$_{0.25}$P$_{0.75}$S$_4$	PLD	$1.7 \cdot 10^{-4}$	0.38	[166]
Li$_4$GeS$_4$-Li$_3$PS$_4$	PLD	$1.8 \cdot 10^{-3}$	0.29	[156]
Al-Li$_7$La$_3$Zr$_2$O$_{12}$ (100)	PLD	$2.5 \cdot 10^{-6}$	0.52	[167]
Al-Li$_7$La$_3$Zr$_2$O$_{12}$ (111)	PLD	$1.0 \cdot 10^{-5}$	0.55	[167]
Al-Li$_7$La$_3$Zr$_2$O$_{12}$	PLD	$1.6 \cdot 10^{-5}$ (In plane)	0.35	[168]
Li$_7$La$_3$Zr$_2$O$_{12}$	PLD	$7.4 \cdot 10^{-6}$	0.32	[169]
Li$_6$BaLa$_2$Ta$_2$O$_{12}$	PLD	$2 \cdot 10^{-6}$	0.42	[154]
Li$_{0.34}$La$_{0.54}$TiO$_3$	PLD	$1.9 \cdot 10^{-5}$	0.30-0.35	[170]
Li$_{0.5}$La$_{0.5}$TiO$_3$	PLD	$1.1 \cdot 10^{-5}$	n.a.	[171]
Li$_{0.29}$La$_{0.57}$TiO$_3$	PLD	$8.2 \cdot 10^{-4}$	0.34	[172]
Li$_{0.33}$La$_{0.56}$TiO$_3$	PLD	$3.5 \cdot 10^{-5}$	0.35	[173]
Li$_{0.5}$La$_{0.5}$TiO$_3$	PLD	$1.2 \cdot 10^{-3}$	0.35	[155]
Li-La-Ti-O	PLD	$3.0 \cdot 10^{-4}$	0.28	[158]
Li$_{0.5}$La$_{0.4}$TiO$_3$	e-BE	$1.8 \cdot 10^{-7}$	0.32	[174]
Li$_7$La$_3$Zr$_2$O$_{12}$	CVD	$4.2 \cdot 10^{-6}$	0.50	[175]
Li$_7$La$_3$Zr$_2$O$_{12}$	CVD	n.a.	n.a.	[176]
Li$_7$La$_3$Zr$_2$O$_{12}$	CSD	$1.67 \cdot 10^{-6}$	0.18	[177]
Li$_7$La$_3$Zr$_2$O$_{12}$	CSD	$2 \cdot 10^{-5}$	0.58	[178]
Al-Li$_7$La$_3$Zr$_2$O$_{12}$	CSD	$2.4 \cdot 10^{-6}$	0.52	[179]
Li$_{0.5}$La$_{0.5}$TiO$_3$	CSD	$4.5 \cdot 10^{-6}$	0.36	[180]
Li$_{0.5}$La$_{0.5}$TiO$_3$	CSD	$3.5 \cdot 10^{-5}$	n.a.	[181]
Li$_{0.32}$La$_{0.51}$TiO$_{2.93}$	CSD	$8.0 \cdot 10^{-6}$	0.38	[182]
Li$_{0.35}$La$_{0.50}$TiO$_3$	CSD	$3.8 \cdot 10^{-8}$	n.a.	[183]
LiTi$_2$(PO$_4$)	CSD	$6.7 \cdot 10^{-7}$	0.48	[184]
Li$_{0.18}$La$_{0.27}$TaO$_3$	CSD	$7 \cdot 10^{-3}$ (bulk)	n.a.	[185]
Li$_{0.155}$La$_{0.281}$TaO$_3$	CSD	$1.5 \cdot 10^{-5}$	0.39	[186]
Li$_{3.25}$Ge$_{0.25}$P$_{0.75}$S$_4$	CSD	$1.8 \cdot 10^{-4}$ (bulk)	n.a.	[187]

2.3 CHEMICAL SOLUTION DEPOSITION (CSD)

The preparation of inorganic thin-films can be classified into physical and chemical methods. Chemical deposition methods use precursor molecules, which decompose by chemical and/or thermal treatment into a solid film and removable byproducts. Figure 2-12 gives an overview of the typical thin-film deposition techniques.

	Physical Methods	Chemical Methods
Vapour Phase	**Physical Vapour Deposition (PVD)** Thermal Evaporation (TE) Electron Beam Evaporation (EBE) (Magneton) Suttering (MS) Ion Beam Sputtering (IBS) Ion Beam Assisted Deposition (IBAD) Pulsed Laser Deposition (PLD) Molecular Beam Epitaxie (MBE) Plasma Spraying	**Chemical Vapour Deposition (CVD)** Metalloganic CVD (MOCVD) Plasma Enhanced CVD (PECVD) Metallorganic Molecular Beam Epitaxy (MOMBE)
Liquid Phase	**Liquid Phase Depositon (LPD)** Liquid Phase Epitaxy (LPE) Melting	**Chemical Solution Deposition (CSD)** Solution-Gelation (Sol-Gel) Metallorganic Decomposition (MOD) Electrochemical Formation Hydrothermal Formation

Figure 2-12: Deposition techniques for inorganic thin-films.

Deposition of thin-films from the gas phase with both physical and chemical vapour deposition (PVD and CVD) techniques is well established and shows several advantages such as the possibility of the fabrication of ultrathin films, conformal coverage, epitaxial film growth, and the formation of highly pure layers. However, these techniques rely on gas phase processes, which require low pressures achieved with powerful vacuum pumps.

Thin-film deposition from the liquid phase can be achieved via liquid phase deposition (LPD) or chemical solution deposition (CSD). Physical deposition from the liquid phase is a less commonly applied technique, while CSD is successfully

applied in different fields of functional inorganic thin-films. However, the deposition of ultrathin layers with thicknesses below 20-30 nm or the conformal coating of extremely small lateral dimensions and 3-D devices remain challenging. In addition, the retention of carbon in the layers might be problematic. Compared to vacuum techniques, CSD offers the advantage to fabricate functional thin-films at moderate precursor and investment costs as the use of expensive vacuum systems is avoided.

2.3.1 History of Chemical Solution Deposition

The CSD technique first appeared in 1868, when different colourful sulphide layers – most likely correlated to interference patterns – were fabricated. These copper, lead and antimony sulphide layers were obtained from aqueous solutions of sodium thiosulfate and the corresponding copper, lead or antimony salts ($CuSO_4$, $Pb(CH_3COO)_2 \cdot 3 H_2O$, $K_2Sb_2(C_4H_2O_6)_2 \cdot 3 H_2O$).[188]

An early driving force for CSD was the reported photoconductivity of PbS layers deposited by CSD in 1906.[189] Later PbS and PbSE thin-films were applied as IR detectors.[190] In 1989 photovoltaic cells based on CdS films deposited by CSD onto CdTe (and later on $CuInSe_2$) were reported. Up to date, several thin-film solar cells applying absorber materials such as $Cu_2ZnSn(Se_{1-y}S_y)_4$ or $Cu(In_{1-x}Ga_x)(Se_{1-y}S_y)_2$ fabricated by CSD have been developed.[191,192] Parallel to the development of sulphide and selenide thin-films, functional oxide films have been reported.

Most oxide layers are obtained from sol-gel based CSD processes, which date back to the mid of the 19th century, when Ebelmen observed that liquid silicon alkoxides transform slowly to a gel state (hydrated silica) upon exposure to humidity.[193,194,195] At the beginning the research focused on modification of optical glasses by coatings of SiO_2, TiO_2, ZrO_2 or Al_2O_3.[196,197,198] The first solution deposited electrically conducting oxide thin-films were prepared in the 1980s.[199] Since the initial studies, a wide variety of functional oxides such as perovskite lead zirconate titanate (PZT) thin-films have been prepared with CSD techniques.[200,201,202] These PZT ferroelectric thin-films are applied in storage media and considered one of the main drivers for the research progress of CSD. Meanwhile, the CSD method was also successfully applied in other fields of functional inorganic thin-films, such as electronic-, ionic or superconducting layers, for applications in displays, solid oxide fuels cells, coated conductors, solid-state batteries or photovoltaics.[203]

2.3.2 Chemical Solution Deposition Process

Figure 2-13 shows a generalised flow chart of the CSD procedure including the relevant processing steps. Several parameters influence the properties of the final layer such as involved precursor chemistry, solvent, temperatures, heating processes, etc.
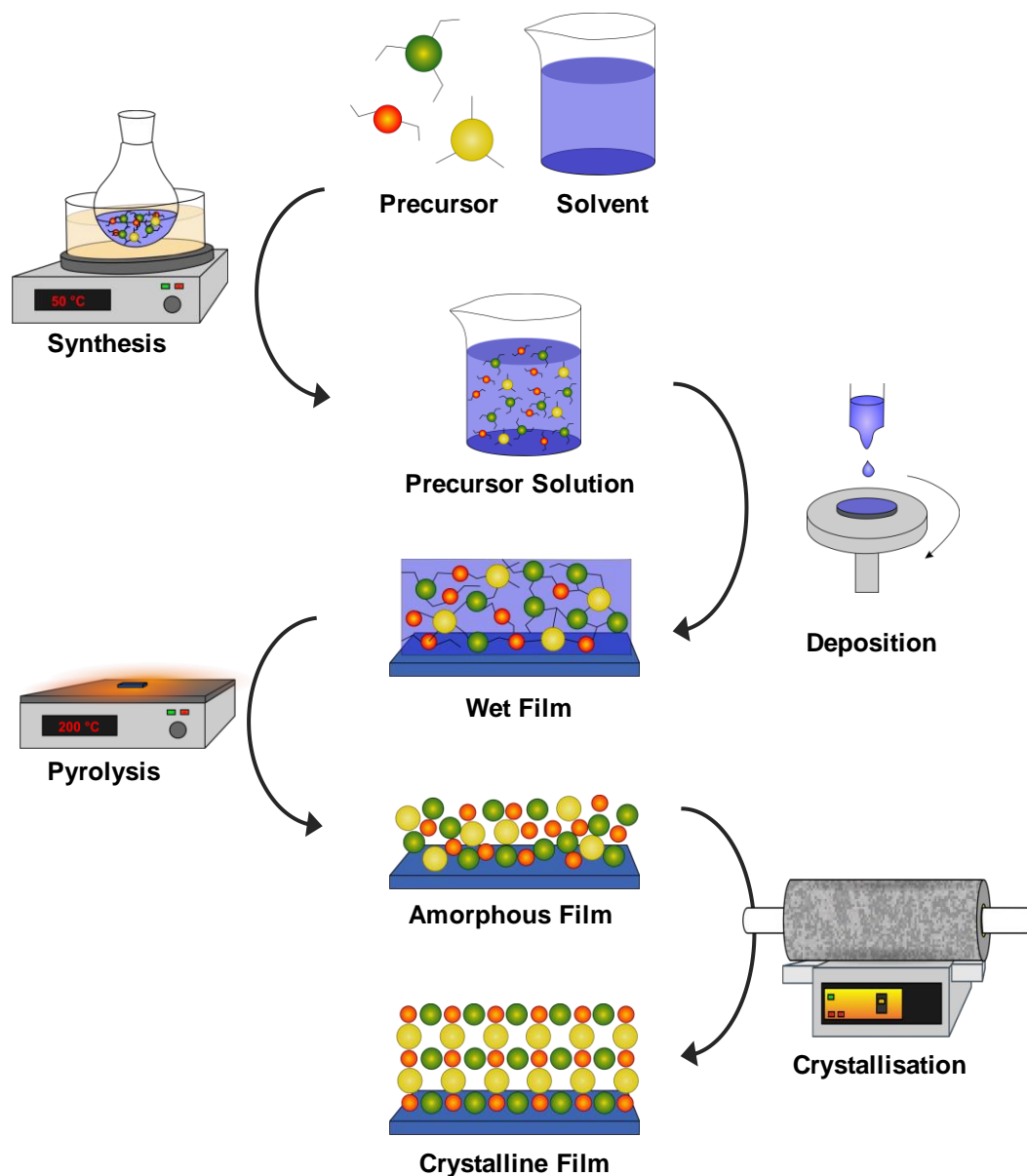
Figure 2-13: Flow chart of a typical CSD process. The different processing steps are visualised schematically starting with solution synthesis, followed by deposition, pyrolysis and crystallisation and ending with functional inorganic thin-films. Included are also drawings of the different process steps on a microscopic scale.

The first step of CSD includes the preparation of the coating solution. This solution consists of molecular precursors that are dissolved in an organic solvent, and is deposited by various techniques on a substrate. The wet, as deposited film is then dried and pyrolysed for the removal or decomposition of the organic matrix and an amorphous layer is obtained. An additional thermal treatment at higher temperatures might be involved for crystallisation of the amorphous thin-film. During the whole CSD process homogeneity and compositional uniformity should be retained, *e.g.* the macroscopic phase separation of precursor components in the solution, during drying or pyrolysis should be prevented. In the following, the most important steps are described in more detail.

Solution Chemistry

A suitable precursor solution is a key factor in the CSD technique. The synthesis of the coating solution typically starts by s dissolving or refluxing the molecular precursors in appropriate solvents. Intermediate distillation steps or elevated temperatures are sometimes required for the formation of a stable precursor solution, where the metal cations are homogeneously distributed in a liquid.[204] The desired stoichiometry is usually obtained by mixing of the educts in the correct stoichiometric ratio, although compositional corrections with respect to the exact stoichiometry are required if: (i) losses occur due to the volatility of a component; (ii) losses due to component diffusion into the substrate take place; or (iii) deliberate off-stoichiometry is desired for the generation of secondary phases or native point defects. Additives such as chemical stabilisers are often required to adjust properties such as rheology of the coating solution. Depending on the desired film composition, different precursors have to be used:

- Sulphur precursors for the preparation of metal sulphide films include *e.g.* thiourea, thioacetamide or thiosulfate. Thiourea can only be used to form sulphides in relatively alkaline environments, while both thioacetamide and thiosulfate can also be used in acidic solutions.
  The formation of the sulphide layers can occur through different mechanisms. Thiourea as an example can (i) form a complex with the metal (ion or hydroxide) followed by decomposition or (ii) hydrolyse to sulphide, followed by either ionic reaction between metal and sulphide ions or the formation of metal hydroxides.

The presence or absence of hydroxides in the precursor solution can be controlled by complexation and pH.[205]

- The chemical routes to fabricate metal oxide films can be classified in three main categories: (i) sol-gel processes, (ii) metal organic decomposition (MOD) and (iii) hybrid routes. The classical sol-gel processes use metal alkoxide precursors which undergo hydrolysis and polycondensation during solution preparation or film deposition. MOD requires metal carboxylates or β-diketonates as educts that do not undergo significant condensation reactions. Hybrid routes utilise a mixture of sol-gel and MOD precursors, which exhibit condensation reactions at several process stages.[204]

Deposition Techniques

In general, the deposition process of the precursor solution is one of the most important steps in CSD and determines properties of the final film such as homogeneity and film thickness. The CSD process involves the coating onto a substrate by different deposition techniques. The choice of the substrate can be limited by (i) the purpose of the film that might require a transparent or electrically conducting substrate, (ii) by the chemistry of the precursor solution or (iii) the subsequent heat treatment process. In addition, pre-treatment of the substrate might be important to achieve the desired film properties (*e.g.* adequate wetting behaviour of the substrate for conformal coating). Furthermore, interdiffusion of film and substrate constituents might occur changing the properties of both substrate and deposited layer. Contamination of the film with dust particles should be avoided and often cleanroom facilities are preferred.[206]

Pasquarelli *et al.* provide an excellent overview of the different coating technologies belonging to the CSD process:[207]

- Spin coating and dip coating are most commonly used deposition methods in research laboratories. While the precursor solution is deposited onto a rotating substrate in spin coating, it is the substrate that is dipped into the precursor solution in the dip coating process. However, both techniques can only be applied on relative small scale.
- Aerosol deposition (often denoted as spray coating) and ink-jet printing are more advanced methods, that allow a more conformal and structured coating

with reduced material consumption. These techniques allow an easy scale-up for industrial applications.

- Slot die casting is another scalable coating technique, which allows continuous solution deposition on long length substrates.

Figure 2-14 shows various chemical solution deposition methods.
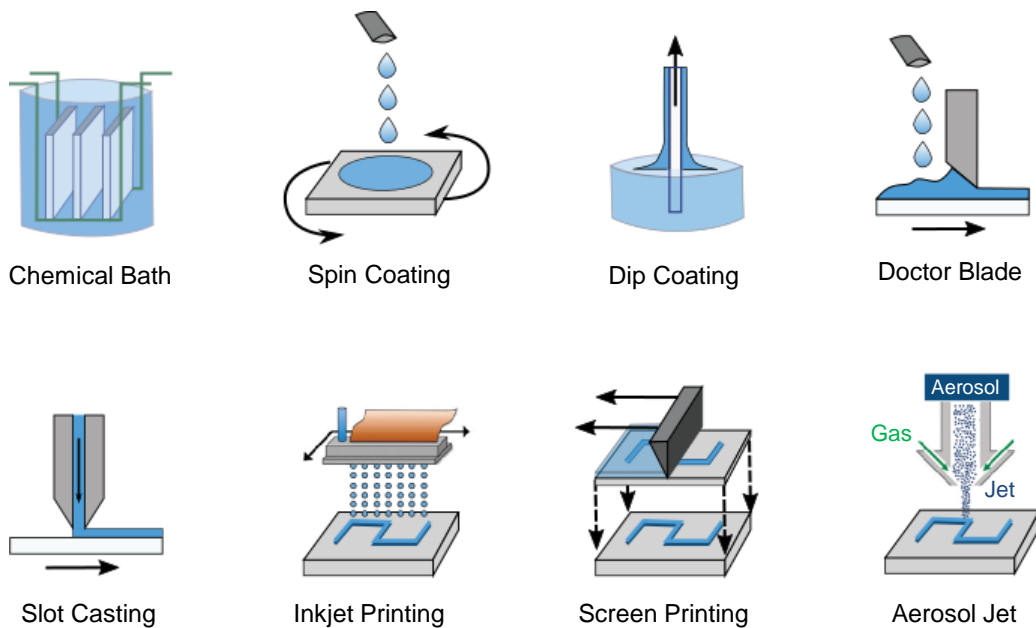
Figure 2-14: Depiction of various chemical solution deposition methods. Drawn after Pasquarelli *et. al.*[207]

Depending on the applied coating technique properties of the coating solution such as surface tension or viscosity have to be adjusted, which might involve additives or a solvent change.[204]

Thermal processing

Often, the drying process starts directly after the deposition without addition thermal treatment by partial solvent evaporation turning the wet, as-deposited film into a semi-rigid form. The conversion of this layer into the final film is induced through controlled thermal processes involving different steps such as drying, pyrolysis, crystallisation and post-annealing for further densification or microstructure manipulation.[204] Not all involved reactions can be separated in individual processes (*e.g.* gel formation and organic removal).

The thermal processes have to be adjusted according to the desired properties of the thin film (*e.g.* crystalline or amorphous), the crystallisation behaviour of the material and/ or the properties of the precursor solution. Process parameters of the individual processes include temperature, time, heating and cooling ramps and atmosphere. In general, a well-adjusted temperature treatment allows precise control of the film microstructure such as grain size or film orientation in crystalline layers.[208] In addition, crack formation or delamination of the dried film resulting from internal stresses have to be avoided during thermal processing. Instrinsic stress can be caused *i.a.* by phase transformations, grain growth or solvent evaporation, while thermic stress is a result of different thermal expansion coefficients of substrate and final film.[209] Another important factor is the stability of the substrate during the thermal processing. For example metal substrates could be oxidised in oxygen atmosphere under high temperatures, while glass substrates might melt during the heat treatment.

Hot plates, muffle ovens, tubular furnaces, or rapid thermal annealing (RTA) ovens are typically employed for the thermal treatment. Lasers can also be used for the annealing process, especially when temperature sensitive substrates are used.[210,211]

Sometimes, deposition and heat treatment have to be repeated several times to obtain the desired film thickness and properties. At the end of the subsequent deposition and thermal processing steps a final heat treatment at a higher temperature might be applied to initiate crystallisation, to improve microstructure, or to increase film density.[204]

2.3.3 Thin-Film Solid Electrolytes

In order to serve the expected increase of the electrical energy demand in the future, applications in the energy sector require the ability for large scale production of materials. Thus, CSD offers a promising path towards economic processing of coated materials for energy storage, conversion and transmission. In case of SSBs, thin films of thermodynamically or kinetically stable solid electrolytes may also be used as protective layers for lithium anodes to prevent the reduction of the unstable bulk solid electrolyte.

Only few lithium-ion conducting SE thin-films have been fabricated by CSD: (i) garnet and perovskite lithium oxides such as (aluminum doped) $Li_7La_2Zr_3O_{12}$ and $Li_{3x}La_{1/3-x}TaO_3$, respectively; (ii) lithium phosphates such as NASICON $LiTi_2(PO_4)_3$ and $Li_{1.5}Al_{0.5}Ti_{1.5}(PO_4)_3$; and (iii) lithium thiophosphate LGPS.[177-187] Table 2-3 provides an overview of the precursor solutions and deposition parameters that were used for the fabrication of these lithium-ion conducting layers. The precursor solutions were deposited on various substrates by spin or dip coating.

Thin films of lithium oxides and phosphates can be easily synthesised via sol-gel routes using metal alkoxides, nitrates or carboxylates as precursors and alcohols, water or acids as solvents. Thin-films of lithium oxides and phosphates suffer from rigidity, low ionic conductivities and high crystallisation temperatures. Furthermore, SEs that contain easily reducible elements like titanium (Ti) are unstable against Li metal. Good stability against Li metal is predicted for garnet-type solid electrolytes thin-films, although stability investigations or cycling studies with Li anode have not been reported so far.[177-179]

Lithium thiophosphates decompose in air and in aqueous solutions, therefore, a different approach for solution deposition has to be considered.[132] Additionally to the reactivity and instability of lithium thiophosphate, the poor solubility of the individual components, *e.g.* Li_2S, P_2S_5 or GeS_2, is problematic. LGPS thin-films have been prepared by dissolution of LGPS powder obtained by solid-phase synthesis, which appears to be more soluble than the individual components.[187] However, highly toxic hydrazine is required as solvent and no lithium-ion conductivity of the thin-film have been reported.

Even though no thin-films were fabricated, various sulphur containing SEs have been prepared by wet chemistry approach including Li_2S-P_2S_5 (*N*-methylformamide

(NMF)),[212] β-Li$_3$PS$_4$ (tetrahydrofuran (THF)),[123] Li$_7$P$_2$S$_8$I (acetonitrile (ACN)),[144] Li$_7$P$_3$S$_{11}$ (1,2-dimethoxyethane (DME) or ACN),[213,214] agyrodite Li$_6$PS$_5$Cl (ethanol) and 0.4LiI-0.6Li$_4$SnS$_4$ (methanol).[215,216] Additionally to the bulk synthesis of these electrolytes, the reported solutions and dispersions were used for the coating of LCO cathode particles and infiltration of conventional LIB electrodes to improve the ionic contacts.[215,216,217,218] These solutions might be considered as precursor solutions for the chemical solution deposition of LPS thin-films.

Table 2-3: Overview of lithium-ion conducting thin-films prepared by CSD. Precursors, solvents, synthesis routes, substrates, deposition technique (DT) and maximum temperature during thermal processing T_{max} are compared.

Material	Precursors	Solvent	Route	Substrate	DT	T_{max} / °C	Ref
Li$_7$La$_3$Zr$_2$O$_{12}$	Li(O-t-C$_4$H$_9$), La(NO$_3$)$_3$ · 6 H$_2$O, Zr(O-n-C$_3$H$_7$)$_4$	2-methoxy-ethanol	Sol-Gel	Si/SiO$_2$/ Ti/Pt	Spin Coating	600	[177]
Li$_7$La$_3$Zr$_2$O$_{12}$	Li-, La-, Zr-, Al-alkoxides	2-methoxy-ethanol	Sol-Gel	Si/Ti/Pt (111)	Spin Coating	600	[178]
Al-Li$_7$La$_3$Zr$_2$O$_{12}$	LiNO$_3$, La(NO$_3$)$_3$ ·6 H$_2$O, Zr(O-n-C$_3$H$_7$)$_4$, Al(O-sec-C$_4$H$_9$)$_3$	1-propanol, ethylaceto-acetate	Sol-Gel	MgO	Dip Coating	900	[179]
Li$_{0.5}$La$_{0.5}$TiO$_3$	Li(O-i-C$_3$H$_7$) La(OCH$_2$OCH$_3$)$_3$, Ti(O-i-C$_3$H$_7$)$_4$,	2-methoxy-ethanol	Sol-Gel	Al$_2$O$_3$ (1$\bar{1}$02)	Spin Coating	600	[180]
Li$_{0.5}$La$_{0.5}$TiO$_3$	LiNO$_3$, La(NO$_3$)$_3$ ·6 H$_2$O, Ti(OC$_4$H$_9$)$_4$	acetyl acetone, ethylene glycol monomethyl ether	Sol-Gel	SiO$_2$	Spin Coating	550	[181]
Li$_{0.32}$La$_{0.51}$TiO$_{2.93}$	Li^{i}OC$_3$H$_7$, La(OC$_2$H$_4$OCH$_3$)$_3$, Ti(O-i-C$_3$H$_7$)$_4$	2-methoxy-ethanol, water	Sol-Gel	Al$_2$O$_3$ (1$\bar{1}$02)	Spin Coating	700	[182]
Li-La-Ti-O	LiNO$_3$, La(NO$_3$)$_3$ ·6 H$_2$O, Ti(O-i-C$_3$H$_7$)$_4$,	water, citric acid, ammonia, hydrogen peroxide	Sol-Gel	TiO$_2$/Pt	Spin Coating	500	[183]
LiTi$_2$(PO$_4$)	LiOC$_2$H$_5$, Ti(O-i-C$_3$H$_7$)$_4$, PO(OC$_2$H$_5$)$_{3-x}$(OH)$_x$	ethanol	Sol-Gel	SiO$_2$/Pt	Spin Coating	800	[184]
Li$_{0.18}$La$_{0.27}$TaO$_3$	La(O-i-C$_3$H$_7$)$_3$, LiOC$_2$H$_5$, Ta(OC$_2$H$_5$)$_5$	2-methoxy-ethanol	Sol-Gel	SiO$_2$, SrTiO$_3$ (100)	Dip Coating	1000	[185]
Li$_{0.155}$La$_{0.281}$TaO$_3$	Li(OOCCH$_3$) ·2 H$_2$O, La(OOCCH$_3$)$_3$ ·H$_2$O, Ta(OC$_2$H$_5$)$_5$	acidic acid, propionic acid, methanol	Sol-Gel	Cu	Spin Coating	900	[186]
Li$_{3.25}$Ge$_{0.25}$P$_{0.75}$S$_4$	Li$_{3.25}$Ge$_{0.25}$P$_{0.75}$S$_4$	hydrazine	Solution	SiO$_2$/Mo	Spin Coating	240	[187]

3 EXPERIMENTAL

This work focuses on the synthesis of lithium thiophosphate (LPS) solid electrolyte thin-films by chemical solution deposition on various substrates. For electrochemical characterisation gold (Au) or lithium (Li) electrodes were evaporated on top of LPS solid electrolyte layers. The synthesis of lithium titanate thin-film electrodes (LTO) by CSD approach is also reported, as LTO electrodes were necessary to develop thin-film microbatteries and test the performance of LPS thin-films solid electrolytes in a functional system.

3.1 CHEMICALS AND MATERIALS

The substrates for LTO and LPS thin-film deposition were ultra-sonificated in ambient air for 15 min in acetone (Sigma Aldrich, 99.9%), then for 15 min in isopropanol (Sigma Aldrich, 99.5%), and dried under flowing oxygen (O_2) prior to the CSD process, if not mentioned otherwise. All substrates were activated by plasma etching (Pico System, Diener Electronics) just before coating to improve the wetting behaviour. The plasma chamber was flushed with argon (Ar) gas at 17 L h^{-1} flow rate before a voltage of 1 V was applied for 2 min.

3.1.1 CSD of Lithium Thiophosphate (LPS) Thin-Films

All synthesis steps for preparing the LPS solid electrolyte thin-films were carried out in an Ar filled glove box (MBraun). The procedure started with the synthesis of the precursor material by mechanochemical ball-milling, followed by preparation and deposition of the coating solution on various substrates and heat treatment of the LPS thin-films.

Mechanochemical synthesis of LPS precursors

Three different stoichiometries of amorphous lithium thiophosphates were chosen as precursors: $70Li_2S - 30P_2S_5$ [70-30] (provided by Dr. Dominik Weber, JLU Gießen), $75Li_2S - 25P_2S_5$ [75-25] (provided by Christian Dietrich, JLU Gießen) and $80Li_2S - 20P_2S_5$ [80-20] (provided by Dr. Wenbo Zhang, JLU Gießen). The precursors were prepared by combining stoichiometric amounts of lithium sulphide (Li_2S, Sigma Aldrich, 99.98%) and phosphorous pentasulphide (P_2S_5, Sigma Aldrich, 99%). The mixture was ball-milled under Ar atmosphere (Pulverisette 7 Premium Line, Fritsch) using a ZrO_2 grinding bowl of 45 mL volume and ca. 110 g ZrO_2 balls with a diameter of 3 mm. Up to 300 milling cycles, each consisting of 5 min milling at 510 rpm followed by a cooling rest of 15 min, were performed until powder X-ray diffraction (XRD) showed no reflections anymore, indicating complete amorphisation and final LPS precursor formation.

LPS coating solutions

All LPS solutions were prepared by dissolving the amorphous LPS precursors in *N*-methylformamide (Sigma Aldrich, 99%). The solutions were stirred at RT for 1 h before they were passed through a nylon filter with 0.45 µm pore diameter. Solutions with a concentration *c* of 4 wt% were used for NMR measurements and for LPS thin-film preparation within 1 h after filtration, unless indicated otherwise in the text.

Substrates for LPS thin-films

LPS thin-films were coated on: (i) Silicon (Si) (<100> orientation, p-type, B-doped) with a resistivity of less than 0.005 Ω cm, (ii) glass, (iii) ITO coated glass with a sheet resistance of $8 - 12\,\Omega$, (iv) LTO coated ITO substrates, (v) slurry based LFP composite cathodes (including carbon (C) and polyvinylidene fluoride (PVDF) as

additives) on aluminium (Al) foil and (vi) Ohara glass. Solid electrolyte Ohara glass and LFP cathodes were used as substrates without solvent cleaning. Table 3-1 summarises supplier and substrate dimensions of the various substrates used for LPS thin-film deposition in this thesis.

Table 3-1: Supplier and substrate dimensions of the substrates used for CSD of LPS thin-films.

Substrate	Supplier	Size / mm²	Thickness / mm
Quartz glass/ ITO	Präzisions Glas & Optik GmbH	25 x 25 (± 0.5)	1 (± 0.1)
Silicon	Siegert Wafer	10 x 10 (± 0.1)	0.525 (± 0.02)
Glass	Carl Roth	26 x 26	1
Glass/ITO	Sigma Aldrich	25 x 25	1.1
LFP (C + PVDF)/ Al	BASF SE (GCN/BB)	25 x 25	0.12
Ohara glass	Ohara	12 x 12	0.17

To enable direct ITO contact for subsequent electrochemical tests an adhesive Kapton® tape with a diameter of 5 mm was fixed on one side of the ITO and LTO substrates just before LPS deposition.

The LFP composite cathodes were attached with adhesive Kapton® tape or ceramic glue on glass substrates to improve the handling and LPS deposition.

LPS thin-film Preparation

A defined volume V of the LPS coating solution ($2-8$ µl cm^{-2}) was drop casted onto pre-treated substrates maintained at elevated temperatures (T_1: $60-120$ °C). LPS films were dried stepwise: first for $15-60$ min (t_1) at the deposition temperature T_1 followed by a heating ramp r_H ($2-20$ °C min^{-1}) up to the maximum drying temperature T_2 ($200-300$ °C), which was held for $30-120$ min (t_2) before the LPS films were quenched to room temperature (RT). The exact deposition and drying parameters for all LPS layers are given in Table 3-2.

Table 3-2: LPS thin-film deposition and drying parameters. Aged coating solutions (1 week) are marked with an asterisk (*).

Number	Substrate	Precursor	c / wt%	V / µL cm^{-2}	T_1 / °C	T_1 / min	r_H / °C min^{-1}	T_2 / °C	T_2 / min
AB01	Si	[70-30]	4	6	80	30	10	250	60
AB02	Si	[75-25]	4	6	80	30	10	250	60
AB03	Si	[80-20]	4	6	80	30	10	250	60
AB04	Si	[70-30]*	4	6	80	30	10	250	60
AB05	Si	[75-25]*	4	6	80	30	10	250	60
AB06	Si	[80-20]*	4	6	80	30	10	250	60
AB07	Si	[70-30]	4	6	60	30	10	225	60
AB08	Si	[70-30]	4	6	70	30	10	225	60
AB09	Si	[70-30]	4	6	80	30	10	225	60
AB10	Si	[70-30]	4	6	90	30	10	225	60
AB11	Si	[70-30]	4	6	100	30	10	225	60
AB12	Si	[70-30]	4	6	110	30	10	225	60
AB13	Si	[70-30]	4	6	120	30	10	225	60
AB14	Si	[70-30]	4	6	80	15	10	225	60
AB15	Si	[70-30]	4	6	80	60	10	225	60
AB16	Si	[70-30]	4	6	80	30	10	200	60
AB17	Si	[70-30]	4	6	80	30	10	225	60
AB18	Si	[70-30]	4	6	80	30	10	250	60
AB19	Si	[70-30]	4	6	80	30	10	275	60
AB20	Si	[70-30]	4	6	80	30	10	300	60
AB21	Si	[70-30]	4	6	80	30	10	275	30
AB22	Si	[70-30]	4	6	80	30	10	275	90
AB23	Si	[70-30]	4	6	80	30	10	275	120
AB24	Si	[70-30]	4	6	80	30	20	275	90
AB25	Si	[70-30]	4	6	80	30	5	275	90
AB26	Si	[70-30]	4	6	80	30	2	275	90
AB27	Si	[70-30]	4	2	80	30	5	275	90
AB28	Si	[70-30]	4	4	80	30	5	275	90
AB29	Si	[70-30]	4	6	80	30	5	275	90
AB30	Si	[70-30]	4	8	80	30	5	275	90
AB31	Si	[70-30]	2	4	80	30	5	275	90
AB32	Si	[70-30]	6	4	80	30	5	275	90
AB33	Si	[70-30]	8	4	80	30	5	275	90
AB34	Si	[70-30]	4	7.5	80	30	10	250	60
AB35	Si	[70-30]	4	7.5	80	30	10	250	60
AB36	Si	[70-30]	4	7.5	80	30	10	250	60
AB37	LTO/ITO	[70-30]	4	7.5	80	30	10	250	60
AB38	ITO	[70-30]	4	7.5	80	30	10	250	60
AB39	Glass	[70-30]	4	7.5	80	30	10	250	60
AB40	ITO	[70-30]	4	7.5	80	30	10	250	60
AB41	ITO	[70-30]	4	7.5	80	30	10	250	60
AB42	ITO	[70-30]	4	7.5	80	30	10	250	60
AB43	LTO/ITO	[70-30]	4	7.5	80	30	10	250	60
AB44	LTO/Al	[70-30]	4	7.5	80	30	10	250	60
AB45	LTO/Al	[70-30]	4	15	80	30	10	250	60
AB46	LTO/Al	[70-30]	4	30	80	30	10	250	60
AB47	LTO/Al	[70-30]	4	15	80	30	10	250	60
AB48	Ohara	[70-30]	4	7.5	80	30	10	250	60
AB49	Ohara	[70-30]	4	7.5	80	30	10	250	60
AB50	Ohara	[70-30]	4	7.5	80	30	10	250	60
AB51	Ohara	[70-30]	4	7.5	80	30	10	250	60

Figure 3-1 visualises the used substrates coated with LPS thin-films.
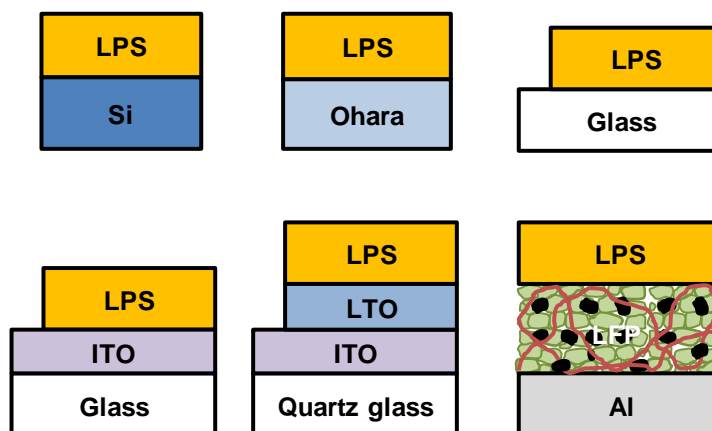
Figure 3-1: Investigated LPS setups. Different substrates were used for LTO and LPS film deposition. The slurry based LFP cathode includes C particles (black) and the binder PVDF (red).

3.1.2 Thermal Evaporation of Gold (Au) and Lithium (Li) Thin-Films

Thermal evaporation (TE) of gold (Au) or lithium (Li) electrodes for electrochemical characterisation was carried out in an Ar filled glove box (MBraun). The TE chamber was evacuated down to $8 \cdot 10^{-6}$ mbar prior to the evaporation process.

Au was evaporated at $0.1 - 0.3$ nm s^{-1} up to film thicknesses of ~150 nm. Au electrodes were deposited (i) on top of several LPS thin-films (4 contacts, each 1.6×1.6 mm²) and (ii) on the back side of all Si and Ohara substrates (full coverage).

Li electrodes were evaporated at $0.5 - 1.5$ nm s^{-1} up to film thicknesses of ~1 µm. Li was deposited on top of LPS thin-films on (i) selected Si or Ohara substrates (4 contacts) and (ii) ITO or LTO/ITO substrates (9 contacts). The active area of an individual Li contact was estimated to be (i) 1.4×1.4 mm² and (ii) 1.5×1.5 mm², which was confirmed from the blue colouring of $Li_7Ti_5O_{12}$ after discharge.

3.1.4 CSD of Li$_4$Ti$_5$O$_{12}$ (LTO) Thin-Films

The LTO coating solution and thin-films were prepared in a nitrogen (N$_2$) filled glove box (Sylatech). The procedure started with the preparation of the LTO coating solution, followed by deposition of the solution by inkjet printing and heat treatment of the LTO thin-films.

LTO coating solution

For the LTO coating solution anhydrous lithium acetate (Sigma Aldrich, 99.95%) – which was dried 24 h at 100 °C under vacuum and stored in the N$_2$ glovebox afterwards – was dissolved in 2-methoxyethanol (Sigma Aldrich 99.8%). Subsequently, glacial acetic acid (Sigma Aldrich, 99.95%) as surfactant and titanium isopropoxide (Sigma Aldrich, 99.999%) were added to the solution. The final molar ratios of Li: Ti: 2-methoxyethanol: acetic acid were 4.4: 5: 130: 13. The solution was stirred at room temperature (RT) for 1 h and filtered using a PTFE-filter with a pore diameter of 0.45 µm.

Substrates for LTO thin-films

ITO (indium tin oxide, indium oxide In$_2$O$_3$ doped with tin oxide SnO$_2$) coated quartz glass (Präzisions Glas & Optik GmbH) with a dimension of 25 x 25 x 1 mm³ and a sheet resistance of 20 ± 5 Ω was used as substrate for Li$_4$Ti$_5$O$_{12}$ (LTO) thin-film deposition. To enable direct ITO contact for subsequent electrochemical tests an adhesive Kapton® tape with a diameter of 5 mm was fixed on one side of the ITO substrates after substrate pre-treatment just before LTO deposition.

LTO Thin-Film Preparation

LTO thin-films were deposited on ITO coated quartz glass substrates by inkjet printing. A XY-positioning system and an electromagnetic drop on demand inkjet printing head (Domino Macrojet nozzle), with 7 nozzles and a distance between the nozzles of 0.2 cm, were used. The printing head was placed 3 mm above the substrate. Two slightly overlapping lanes were printed with an offset of 10 cm before substrate coating. The lanes were printed with 6 out of 7 nozzles in a square pattern by adjustment of the printing head in a 45° angle resulting in a drop distance of 1.414 mm. An opening time of 425 ms and a pressure of 380 mbar were used for printing.

The printing pattern is visualised in Figure 3-2.
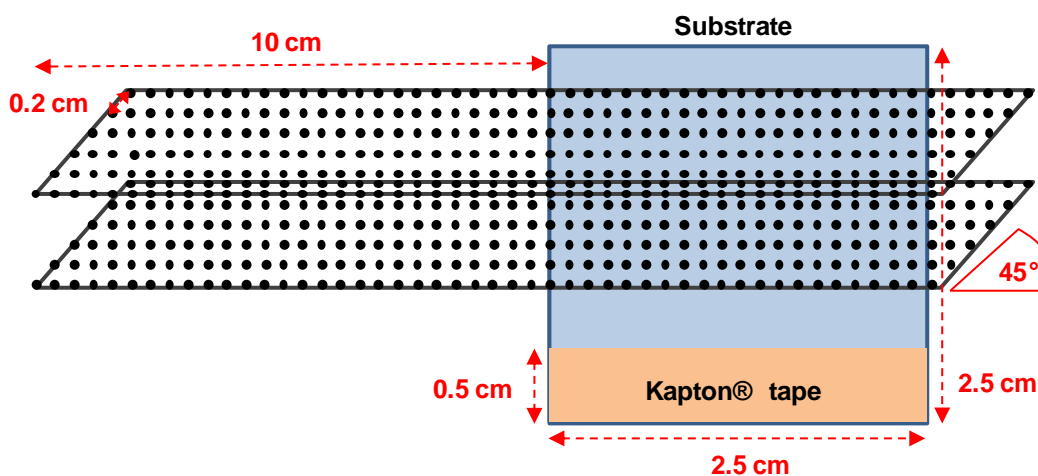
Figure 3-2: Square pattern used for LTO deposition on ITO substrates: Two slightly overlapping lanes were printed with an offset of 10 cm before substrate coating. 6 nozzles with a distance of 0.2 cm were used for the whole printing process. An adhesive Kapton® tape with a diameter of 0.5 cm was fixed on one side of the ITO substrate.

15 min after coating the wet LTO thin-films were transferred into a furnace (Carbolite) for pyrolysis and crystallisation. The furnace was flushed with a gas mixture of N_2 (160 L h^{-1}) and O_2 (40 L h^{-1}). After an aging period of 1 h the LTO thin-films were dried stepwise: 10 °C min^{-1} heating ramp up to 650 °C, interrupted by 1 h dwell at 300 °C, followed by 1 h dwell at 650 °C and quenching to RT.

3.2 CHARACTERISATION METHODS

In the following the equipment and setups used for the structural and electrochemical characterisation of LPS thin-films are described. An overview of the investigated systems and their corresponding characterisation techniques can be found in Table 0-1 in the appendix.

3.2.1 Structural Characterisation

The structural properties of LPS thin-films were investigated by scanning electron microscopy (SEM), energy dispersive X-ray spectroscopy (EDX), X-ray diffraction (XRD) and X-ray photoelectron spectroscopy (XPS) analysis. Time-dependant nuclear magnetic resonance spectroscopy (NMR) was used for characterisation of LPS coating solutions.

Scanning Electron Microscopy (SEM)

Cross-section and top-view images of LPS thin-films were obtained with a Supra™ 25 scanning electron microscope (Carl Zeiss AG). The samples were transferred from the glove box into the SEM under Ar atmosphere.
SEM analysis of the ITO/LTO/LPS/Li system (AB43) after cycling was performed in a Stata 400 (FEI). The cross section of the system was prepared by focused ion beam (FIB).

Energy Dispersive X-Ray Spectroscopy (EDX)

EDX of LPS thin-films (AB01-AB06) was carried out with an acceleration voltage of 10 kV in a Supra™ 25 scanning electron microscope (Carl Zeiss AG) equipped with an INCAEnergy detection unit (Oxford instruments).

X-Ray Diffraction (XRD)

The XRD patterns of LPS thin-films (AB01-AB06) were collected in a 2θ angular range between 15 and 38° using a D4 Endeavor powder diffractometer in Bragg-Bretano focusing geometry (Bruker) with a Cu K_α source. The patterns were evaluated with the Eva software (Bruker). A dome holder, filled with Ar gas, was used for measurements to protect LPS thin-films from ambient air.

X-Ray Photoelectron Spectroscopy (XPS)

XPS characterisation was carried out using a PHI Versaprobe II Scanning ESCA Microprobe (Physical Electronics) with a monochromatised Al K_α X-ray source (200 µm beam diameter, 50 W X-ray power). Depth profiling and Li deposition (*in situ* XPS) were carried out using the built in Ar ion gun.

The *in situ* XPS method was previously described by Wenzel *et al.*[142] The procedure involves sequential XPS analysis and Li sputter deposition onto the surface of the sample as shown schematically in Figure 3-3. The performed *in situ* XPS analysis of a LPS thin-film (AB35) included 3 min Li deposition steps followed by data acquisition.
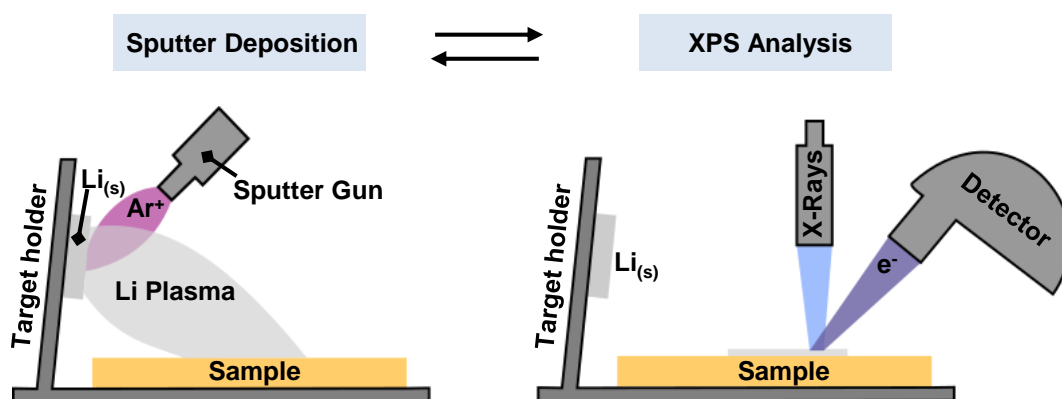
Figure 3-3: Procedure of the *in situ* XPS technique which involves sequential XPS analysis and sputter deposition of metals such as Li. Drawn after Wenzel *et al.*[219]

The samples were transferred from the glove box into the XPS machine under Ar atmosphere. The pass energy of the analyser was set to 49.5 eV for detail spectra, and the chamber pressure was in the range of 10^{-7} Pa. The LPS thin-films (AB01-AB06, AB35) were studied at temperatures between −80 and −90 °C to prevent sulphur sublimation under ultra-high vacuum (UHV) conditions.

Data evaluation was performed using CasaXPS V2.3.17 software. Charge correction was carried out relative to the C 1s signal of adventitious carbon at 284.8 eV. The S 2p and P 2p signals both comprised a peak doublet because of spin−orbit splitting with an intensity ratio of 1:2 and defined peak separations of 1.22 eV and 0.91 eV for the S 2P for the P 2P lines, respectively.

Nuclear Magnetic Resonance Spectroscopy (NMR)

NMR spectra were recorded using a Bruker Advance III HD 400 MHz spectrometer (^{1}H at 400.25 Hz, ^{13}C at 100.64 Hz and ^{31}P at 162.02 Hz). An external standard d_8-dioxane in a closed capillary was used to avoid direct contact and reactions of the dissolved LPS compounds with the standard. The setup is visualised in Figure 3-4.

Capillary with d_8-dioxane (standard)

NMR tube with $xLi_2S-(1-x)P_2S_5$ dissolved in *N*-Methylformamide
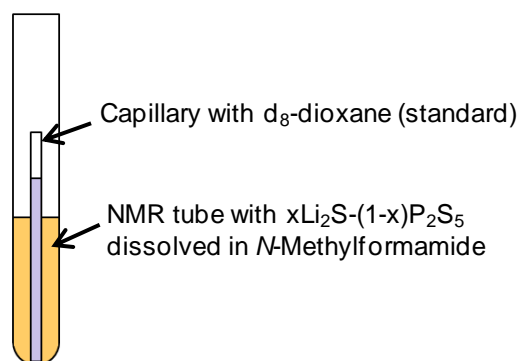
Figure 3-4: Setup of time-dependant NMR measurements.

Chemical shifts are given relative to the residual protons/ resonance signal of deuterated d_8-dioxane in ppm. Couplings are denoted in Hz. The multiplicity of signals are given with following abbreviations: singulet (s), doublet (d) and multiplet (m).

3.2.2 Electrochemical Characterisation

Electrochemical characterisation was performed in an Ar filled Glovebox (MBraun) using an Interface 1000 potentiostat/ galvanostat/ ZRA (zero resistance ammeter) from Gamry Instruments. Various systems were analysed and are visualised schematically in Figure 3-5. The back side of the substrate and the front side Li or Au contact acted as electrodes for vertical measurements through the different layers. Conductive copper (Cu) tape was used to connect the isolating glass back side with the electronically conductive ITO. To enable a better contact for electrochemical characterisation the back sides of Si and Ohara substrates were coated with Au.
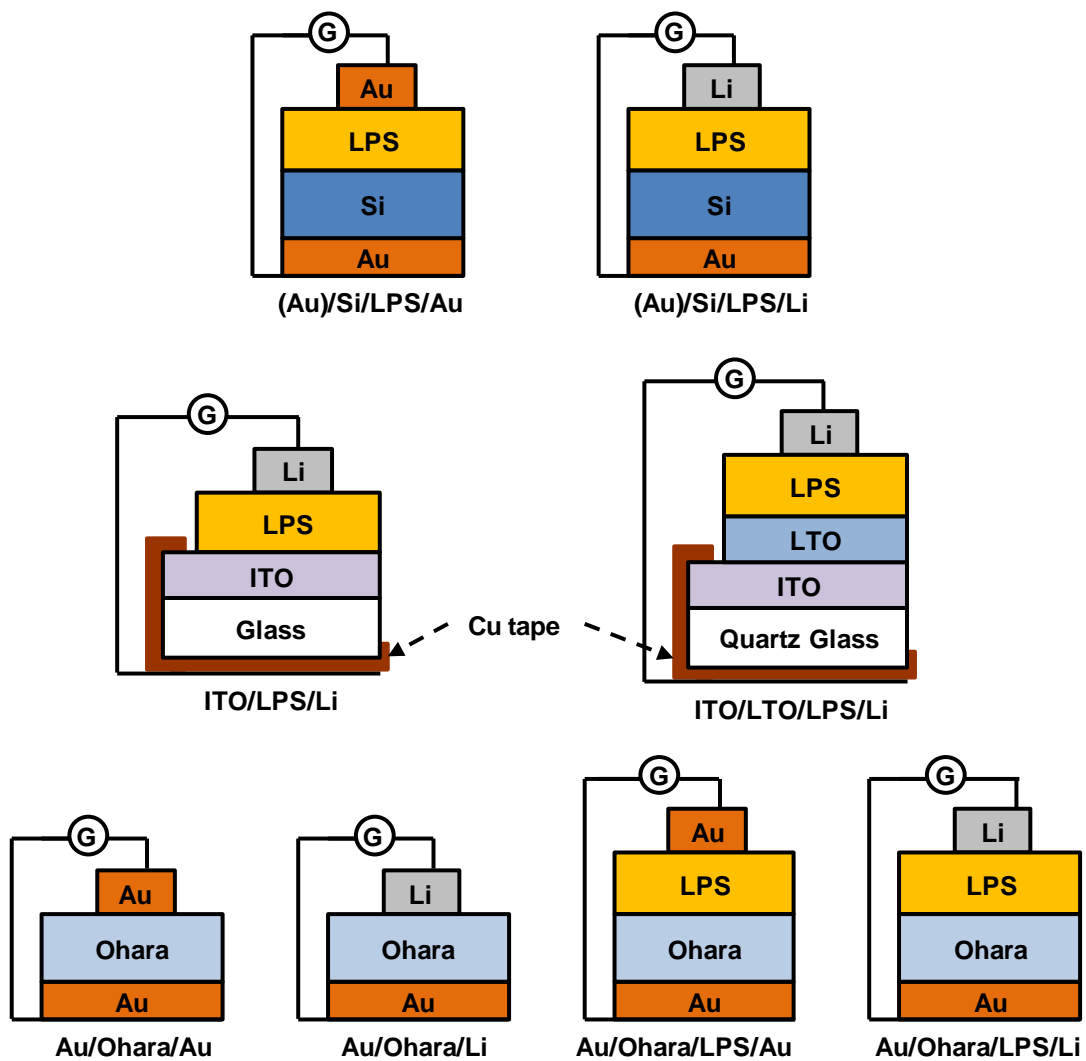
Figure 3-5: Measurement setup of the various systems for electrochemical characterisation. G marks the Interface 1000 potentiostat/ galvanostat/ ZRA from Gamry Instruments.

Electrochemical Impedance Spectroscopy (EIS)

Electrical conductivities were determined by EIS. The measurement parameters are summarised in Table 3-3.

Table 3-3: EIS parameters of the various setups investigated. The spectra were fitted either with Echem analyst software (Gamry) or with software from RelaxIS (rhd instruments).

Number	Measurement	System	Voltage	Frequency	points per decade	Amplitude
AB01-AB06	EIS	Au/Si/LPS/Au	V_{OC}	1 MHz - 100 Hz	10	10 mV
AB06	EIS (*T*)	Au/Si/LPS/Au	V_{OC}	1 MHz - 1 kHz	10	10 mV
AB34	EIS (*t*)	Au/Si/LPS/Li	2.2 V *vs.* Li	1 MHz - 1 Hz	10	10 mV
AB50	EIS (*t*)	Au/Ohara/Li	V_{OC}	1 MHz - 1 Hz	10	10 mV
AB48	EIS (*t*)	Au/Ohara/LPS/Li	V_{OC}	1 MHz - 1 Hz	10	10 mV
AB51	EIS (*t*)	Au/Ohara/Au	0 V *vs.* Au	1 MHz - 1 Hz	10	10 mV
AB49	EIS (*t*)	Au/Ohara/LPS/Au	0 V *vs.* Au	1 MHz - 1 Hz	10	10 mV
AB36	EIS + CCD	Au/Si/LPS/Li	4.0 V *vs.* Li	1 MHz - 1 kHz	10	10 mV
AB43	EIS + CCD	ITO/LTO/LPS/Li	2.0 V *vs.* Li 1.4 V *vs.* Li	1 MHz - 1 Hz	10	10 mV

Temperature dependant EIS (*T*) of the Au/Si/LPS/Au system (AB01) was performed from -10 to 30 °C in 5 °C steps. Time-dependant EIS (*t*) of the Au/Si/LPS/Li system (AB34) and the different Ohara setups (AB48-AB51) was measured from 0 to 60 h (1 h increments) and from 0 to 72 h (24 h increments), respectively. Galvanostatic charge discharge (CCD) was coupled with EIS measurements, which were performed after each charge in the Au/Si/LPS/Li half-cell (AB36) and after each charge and discharge in the ITO/LTO/LPS/Li system (AB43).

EIS data are usually analysed by fitting with reasonable electrical circuit models. Most of the circuit elements in the model are common electrical elements such as resistors, capacitors, and inductors. In this thesis data fitting was performed either with Echem analyst software (Gamry) or with software from RelaxIS (rhd instruments, only AB43). The used equivalent circuits included resistors and constant phase elements (CPEs), which describe non-ideal capacitors.

Resistors are used to account for the resistances R of an electrolyte. Resistances can be converted into (i) area resistances by multiplication with the contact area A or (ii) into conductivities σ according to equation 3-1:

$$\sigma = \frac{1}{R} \cdot \frac{l}{A}, \tag{3-1}$$

where l the electrolyte thickness. The ratio of layer thickness to contact area ${l}/{A}$ is also known as cell constant.

The electric conductivity σ obtained from EIS measurements is the sum of electronic conductivity σ_{el} and ionic conductivity σ_{ion} according to to equation 3-2:

$$\sigma = \sigma_{ion} + \sigma_{el}\,.\tag{3-2}$$

If the electronic conductivity is several orders of magnitude lower than the electric conductivity the conductivity obtained from EIS measurements represents the ionic conductivity.

A capacitor is formed when two conducting plates are separated by a non-conducting media, called the dielectric. The value of the capacitance C depends on the contact area A, the distance between the contacts l and the properties of the dielectric:

$$C = \frac{\varepsilon_0 \varepsilon_r A}{l}\,.\tag{3-3}$$

The permittivity of free space ε_0 is a physical constant ($\varepsilon_0 = 8.854 \cdot 10^{-12}\,\mathrm{F\,m^{-1}}$), whereas the dielectric constant ε_r depends on the analysed material. The impedance of an ideal capacitor is defined as:

$$Z_C = \frac{1}{j\omega C}\,,\tag{3-4}$$

where j is imaginary unit $\left(\sqrt{-1}\right)$ and ω is radial frequency. Capacitors in EIS experiments often do not behave ideally and act like a CPE. The impedance of a CPE can be expressed as:

$$Z_{CPE} = \frac{1}{(j\omega)^{\alpha} Y_0}\,.\tag{3-5}$$

The exponent α account for the non-ideal behaviour of the CPE and should be treated as an empirical constant with no real physical basis. For an ideal capacitor the exponent α equals 1; and for a non-ideal CPE α is less than one.

If an equivalent circuit is used for fitting with a CPE is parallel to a resistor, Y_0 can be used to calculate the capacitance C according to equation 3-6:

$$C = \frac{(R Y_0)^{\frac{1}{\alpha}}}{R}\,.\tag{3-6}$$

Direct current (DC) polarisation

DC polarisation measurements in Au/Si/LPS/Au setups enables estimating the electronic resistance of LPS thin-films deposited from various precursor solutions (AB01-AB06). A potential of 1 V was applied against the reference electrode (top Au contact) over 1 min and the current I was measured as a function of time.

The partial electronic conductivity of the LPS thin-films in an Au/Si/LPS/Li system (AB34) was obtained from DC polarisation measurements. The Au/Si bottom contact was polarised positively for 15 min against the Li contact and the current response at a constant potential was measured as a function of time. The applied potential U was subsequently increased in 0.1 V steps from 1.9 V to 4.0 V $vs.$ Li$^+$/Li. The average of the last 10 measurement points was used to determine the steady state current I_{SS}.

The electronic resistance R_{el} can be calculated according to equation 3-7:

$$R_{el} = \frac{U}{I}.$$

(3-7)

For intact contacts the electronic resistance of the thin-films is calculated using the steady state current I_{SS}. Electronic area resistances are obtained by multiplication of the electronic resistances with the contact area A. Resistances can be converted into electronic conductivities according to equation 3-1.

Cyclic Voltammetry (CV)

CV measurements of the Au/Si/LPS/Li (AB36) and ITO/LTO/LPS/Li (AB37) systems were conducted in the range from 0 to 4 V (5 cycles) and 1.2 to 2.0 V (10 cycles) $vs.$ Li$^+$/Li, respectively, using a scan rate of 1 mV s^{-1}.

The potential window of the ITO/LPS/Li system (AB38) was determined by CV from V_{OC} to different lower limit potentials using a scan rate of 1 mV s^{-1}. This lower limit was decreased stepwise from 1.4 V to 0.5 V $vs.$ Li$^+$/Li. After each cycle the system was disconnected for optical observations.

Galvanostatic Charge Discharge (CCD)

Galvanostatic cycling of the Au/Si/LPS/Li half-cell (AB36) was conducted from 0.1 to 4.0 V $vs.$ Li$^+$/Li and consisted of 10 cycles. A constant current density of 100 µAh cm^{-2} was applied to the cell assuming an effective contact area of

1.96 mm². Each half cycle was limited to 20 min for ensuring that not all Li is inserted into the Si wafer leading to the disappearance of the Li electrode.

CCD of the ITO/LTO/LPS/Li system (AB43) was carried out applying current densities of 13 µA cm⁻², 25 µA cm⁻², 50 µA cm⁻² and 100 µA cm⁻² (considering an active LTO area under the Li contact area of 2.25 mm²) in the range from 1.4 to 2.0 V *vs.* Li⁺/Li. In the first 40 cycles the current density was subsequently increased after 10 performed cycles. This procedure was repeated up to the 200th cycle. From cycle 200 to cycle 500 a current density of 100 µA cm⁻² was applied for charge and discharge of the cell. The cycling was paused after cycle 40 and 200 for 30.5 h and 7.5 h, respectively. C-Rates (Applied current/ theoretical capacity of LTO) were calculated based on a theoretical LTO capacity C_{th} of 175 mAh g⁻¹, a LTO film thickness d_{LTO} of 95 nm (as revealed from the SEM images), a theoretical LTO density ρ_{LTO} of 3.5 g cm⁻³[220] and an active LTO area A_{LTO} of 2.25 mm². Similarly, the measured capacity of the cell C was transformed into the specific capacity of the cell C_{sp}.

4 RESULTS AND DISCUSSION

The results and discussion chapter is divided in four main parts. In the first section suitable coating solutions for the synthesis of lithium thiophosphate (LPS) thin-films by chemical solution deposition (CSD) are formulated and analysed. The second part covers LPS thin-film preparation by CSD from various coating solutions and includes systematic investigation of the process parameters and their influence on the thin-film properties to optimise the deposition process. The third section of this chapter deals with the electrochemical characterisation of the LPS thin-films as solid electrolytes, including stability against lithium metal and behaviour upon lithium cycling. Finally, the LPS thin-films are applied as solid electrolyte separators by integrating them into a microbattery system, on composite cathodes and as protective coating on bulk type electrolytes.

4.1 LPS PRECURSOR SOLUTIONS

LGPS thin-films are reported to be the only solid electrolyte layers based on lithium-ion conducting sulphides prepared by CSD, however, no lithium-ion conductivity of the thin film has been reported and their synthesis required the use of hydrazine, which is a highly toxic compound. The LGPS thin-films were prepared from LGPS powder prepared by solid phase synthesis, which appeared to be better soluble than the individual compounds.[187]

Additionally, at the beginning of the PhD project in 2014, some sulphur containing bulk SEs have been prepared by wet chemistry approach including Li_2S-P_2S_5 (*N*-methylformamide (NMF)),[212] β-Li_3PS_4 (tetrahydrofuran (THF))[123] and $Li_7P_3S_{11}$ (1,2-

dimethoxyethane (DME)).[213] However, LPS systems only dissolve homogeneously in NMF, while dispersions are obtained with THF or DME.

In this thesis, additionally to NMF, di-methylformamide (DMF), acetonitrile (ACN), pyridine and dioxane were tested as solvents for amorphous $70Li_2S - 30P_2S_5$ [70-30], $75Li_2S - 25P_2S_5$ [75-25] and $80Li_2S - 20P_2S_5$ [80-20] precursors, which were prepared by ball milling. Homogeneous solutions were only obtained with NMF as solvent and used for the deposition of LPS thin-films (chapter 4.2).

NMF based coating solutions changed their appearance over time suggesting ongoing reactions inside of the solutions. Figure 4-1 shows pictures of freshly prepared (top) and aged (bottom, 20 days old) precursor solutions.
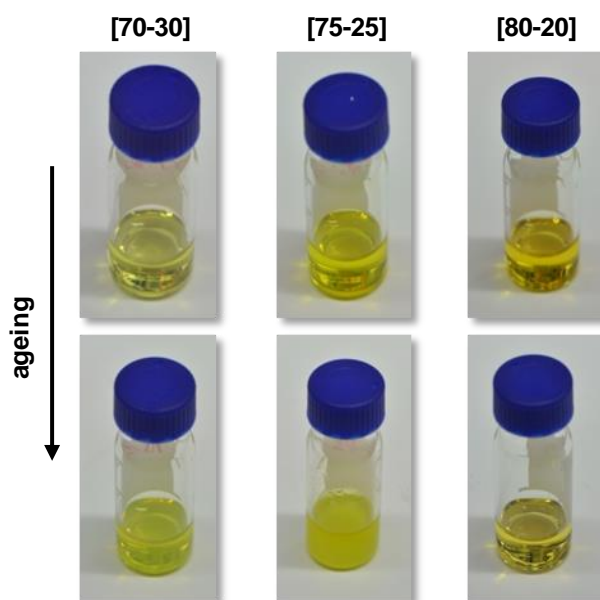
Figure 4-1: Ageing of NMF based coating solutions.

Although the yellow solutions looked clear after filtering, a white precipitate appeared after a few days for [70-30] and [75-25] coating solutions. The ageing of the coating solutions might be ascribed to the reaction of the different amorphous lithium thiophosphates with the solvent NMF.

In general, [70-30], [75-25] and [80-20] contain various thiophosphate anions as determined by solid-state NMR and Raman studies by Dietrich *et. al*.[221] Figure 4-2 shows the corresponding polyhedral motifs. Because of the resonance bonding P-S-Li and P=S bonds cannot be distinguished in all thiophosphate anions.

- In the *ortho*-thiophosphate anion (PS_4^{3-}) P is bound tetrahedrally to 4 S atoms.[222]

- *Pyro*-thiophosphate anions ($P_2S_7^{4-}$) contain two corner sharing tetrahedra with one bridging S atom.[223]

- In *meta*-thiophosphate more than two tetrahedra are connected by bridging S atoms to form long PS_3^- chains.

- *Hypo*-thiodiphosphate ($P_2S_6^{4-}$) consists of ethane like polyhedra with a P-P bond.

Amorphous [75-25] and [80-20] consist mainly of *ortho*-thiophosphate.[221] The latter contains also some remaining amounts of Li_2S. In contrast [70-30] contains *ortho*-thiophosphate and *pyro*-thiophosphate in a ratio of 1:1.[223] *Hypo*-thiophosphate units can be found as impurities in all glasses, whereas *meta*-thiophosphate impurities are only observed for lower amounts of Li_2S during synthesis.[221,224]
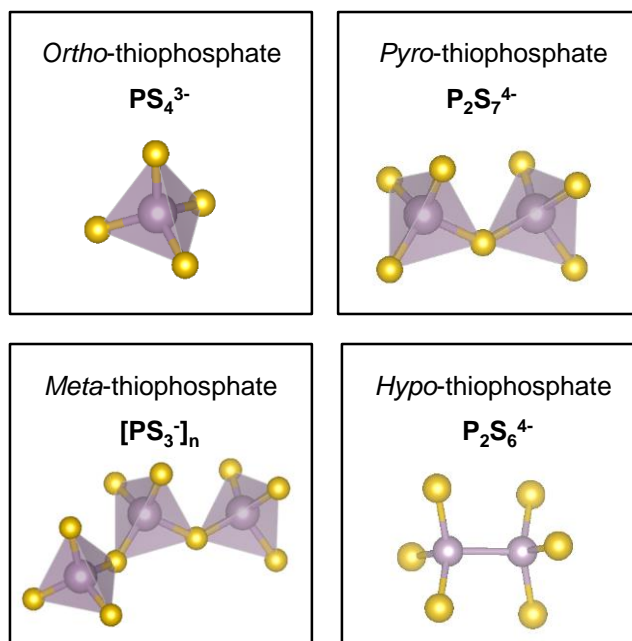
Figure 4-2: Different thiophosphate anions found in lithium thiophosphate glasses. Polyhedral motifs are based on reported structures by Dietrich *et. al.*[221,225]

4.1.1   Reaction monitoring by *in situ* NMR measurements

Time-dependent ^{1}H-, ^{13}C- and ^{31}P-NMR studies were performed to investigate whether the lithium thiophosphates react with the solvent NMF. Three different NMF based solutions were prepared using various amorphous LPS glasses ([70-30], [75-25], [80-20]). NMR analysis was carried out to determine the species present in these coating solutions.

^{1}H and ^{13}C NMR studies

^{1}H- and ^{13}C-NMR studies reveal the development of signals, which are shifted downfield compared to the ones ascribed to NMF and increase upon ageing of the solutions as shown in Figure 4-3. A similar shift is observed when the ^{1}H- and ^{13}C-NMR spectra of dimethylformamide (DMF)[226] are compared with the spectra of thio-DMF.[227] Therefore, the recorded signals are ascribed to NMF and thio-NMF. Note that NMF and thio-NMF are mixtures of *cis* and *trans* forms with *trans*-(thio)-NMF being the major diastereomere (92%).[228]

Scheme 1 displays the suggested reaction of *trans*-NMF with lithium thiophosphates to *trans*-thio-NMF.
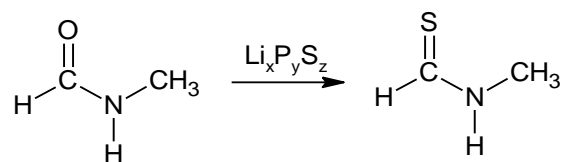
Scheme 1: Reaction of NMF with LPS to thio-NMF.

The thionation of amides (*N*-phenylmethanamide and *N*-phenylethanamide) by phosphorus pentasulphide P_2S_5 was already reported in 1872 by Hoffmann.[229] LPS might react in a similar way with the amide NMF.
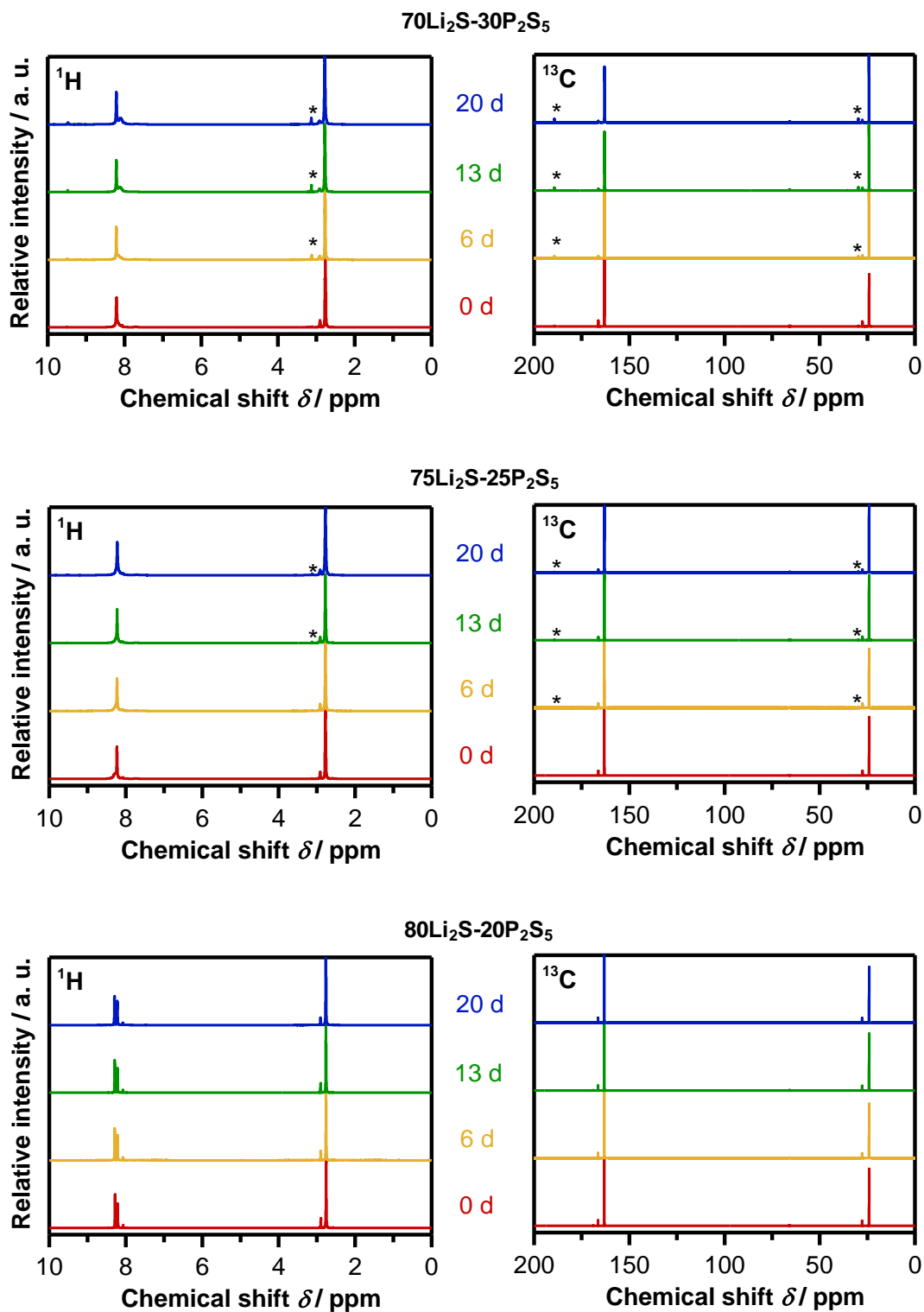
Figure 4-3: ^1H and ^{13}C NMR spectra of xLi_2S-$(1-x)P_2S_5$ (x=70, 75, 80) dissolved in NMF and aged for several days. The asterisk (*) marks the signals ascribed to thio-NMF.

The relative amounts of NMF and thio-NMF in the LPS solutions are obtained from integration of the ^{1}H-NMR signals from the corresponding methyl groups (Figure 4-4).
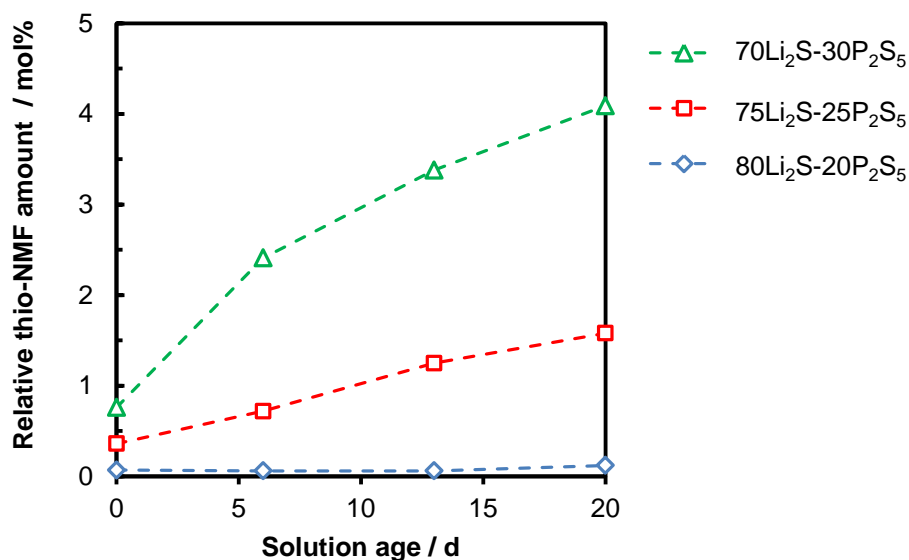
Figure 4-4: Relative amount of thio-NMF to amount of NMF. Results were obtained from the ratios of the integrated ^{1}H NMR signals from the CH$_3$-groups of thio-NMF and NMF.

The diagram reveals that the formation of thio-NMF strongly depends on the precursor stoichiometry with the highest reactivity for [70-30], whereas nearly no thio-NMF signal could be detected for [80-20]. These results are in accordance with the optical observations, as the [80-20] solution remained unchanged in contrast to [70-30] and [75-25] solutions.

^{31}P NMR studies

Time-dependent ^{31}P NMR of the different LPS solutions allows monitoring the reaction at the thiophosphate side. Table 4-1 summarises the recorded signals, while the spectra are displayed in Figure 0-1 to Figure 0-3 in the appendix. The amount of signals increases from the [80-20] to the [70-30] solution, which suggests that the amount of thiophosphate species depends on the precursor stoichiometry.

The intensity and shape of these signal change with ageing of the solutions, which corresponds to a changing ratio of the different thiophosphate species.

According to the signal intensities and the chemical shifts the signals at 92.0 ± 0.3 ppm, 105.9 ± 0.1 ppm and 115.6 ± 0.4 ppm are ascribed to PS_4^{3-}, $P_2S_7^{4-}$ and $P_2S_6^{4-}$, respectively. These values vary from the reported LPS signals in solid-state NMR, where Li_3PS_4 appears between 82.8 – 88.4 ppm, $Li_4P_2S_7$ between 89.8 – 91 ppm and $Li_4P_2S_6$ between 103 – 109.1 ppm. The large signal difference between solid and liquid state NMR can be ascribed to solvation of the thiophosphates. As a signal shift up to 4 ppm is reported for the same compound in different solvents,[230] an even larger signal shift can be expected when moving from solid to liquid state NMR.

Phosphite species such as tributyl thiophosphite $(C_4H_9S)_3P$ and thriethyl thiophosphite $(C_2H_5S)_3P$) are reported to show a signal in liquid state NMR at 116 pmm,[230,231,232] which is close to the signal ascribed to $Li_4P_2S_6$. This could be related to (i) the same chemical shift of $Li_4P_2S_6$ and lithium thiophosphite Li_3PS_3 in solution or (ii) to a reaction of $Li_4P_2S_6$ to Li_3PS_3 in the NMF solution. A possible reaction is shown in equation 4-1, where $Li_4P_2S_6$ reacts with an excess of Li_2S to Li_3PS_4 and Li_3PS_3:

$$Li_4P_2S_6 + Li_2S \rightarrow Li_3PS_4 + Li_3PS_3. \qquad (4\text{-}1)$$
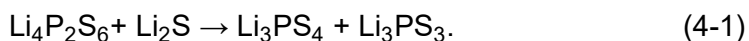
Table 4-1: Chemical shifts received from ^{31}P NMR measurements from NMF solutions of (a) [80-20], (b) [75-25] and (c) [80-20] relative to 85% H_3PO_4. Signals with integrated peak areas higher than 1% are shown in bold.

a)

Chemical Shift/ ppm			
0 days	**6 days**	**13 days**	**20 days**
115.81 (s)	**115.80 (s)**	**115.83 (s)**	**115.83 (s)**
105.94 (s)	105.93 (s)	105.96 (s)	105.96 (s)
102.52 (s)	102.47	102.45 (s)	102.45 (s)
92.24 (s)	**92.23**	**92.25 (s)**	**92.25 (s)**
88.85 (s)	**88.84**	**88.87 (s)**	**88.86 (s)**
81.01 (s)	81.01	81.02 (s)	81.02 (s)
64.27 (s)	**64.26**	**64.28 (s)**	**64.28 (s)**

b)

Chemical Shift/ ppm			
0 days	**6 days**	**13 days**	**20 days**
	119.81 (s)	119.82 (s)	119.81 (s)
115.77 (s)	**115.81 (s)**	**115.79 (s)**	**115.78 (s)**
110.03 (s)	110.04 (s)	110.04 (s)	110.04 (s)
109.57 (s)	109.59 (s)	109.58 (s)	109.58 (s)
	106.96 (s)	106.96 (s)	106.96 (s)
106.50 (s)	106.49 (s)	106.49 (s)	106.49 (s)
105.89 (s)	**105.91 (s)**	**105.89 (s)**	**105.88 (s)**
92.21 (s)	**92.23 (s)**	**92.21 (s)**	**92.20 (s)**
80.89 (s)	80.87 (s)	80.86 (s)	80.85 (s)
80.57 (s)			
80.36 (d, J_{PP}=41.8 Hz)	**80.34 (d, J_{PP}=41.7 Hz)**	**80.30 d (J_{PP}=41.7 Hz)**	**80.26 (d, J_{PP}=42.0 Hz)**
	39.55 (s)	39.54 (s)	39.54 (s)
38.60 (d, J_{PP}=40.5 Hz)	**38.52 (d, J_{PP}=42.3 Hz)**	**38.40 (d, J_{PP}=42.0 Hz)**	**38.29 (d, J_{PP}=41.9 Hz)**

c)

Chemical Shift/ ppm			
0 days	**6 days**	**13 days**	**20 days**
119.80 (s)	**119.78 (s)**	**119.76 (s)**	**119.80 (s)**
115.15 (s)	**115.47 (s)**	**115.39 (s)**	**115.30 (s)**
111.64 (s)	111.64 (s)	111.63 (s)	111.66 (s)
			111.32 (s)
110.02 (s)	**110.01 (s)**	**110.00 (s)**	**110.01 (s)**
	109.54 (s)	109.54 (s)	109.54 (s)
	106.95 (s)		
105.87 (s)	**105.80 (s)**	**105.75 (s)**	**105.75 (s)**
102.83 (s)	102.78 (s)		
	101.78 (s)		101.40 (d, J_{PP}=61.9 Hz)
			100.58 (d, J_{PP}=23 Hz)
			97.63
91.50 (s)	**91.84 (s)**	**91.73 (s)**	**91.61 (s)**
			87.65
82.75 (d, J_{PP}=32.1 Hz)			**82.60 (d, J_{PP}=32.0 Hz)**
80.94 (s)	**80.80 (s)**	**80.78 (s)**	**80.76 (s)**
80.77 d (J_{PP}=42.1 Hz)	**80.47 (d, J_{PP}=42.1 Hz)**	**80.45 (d, J_{PP}=42.2 Hz)**	**80.46 (m)**
42.89 (s)	42.87 (s)		
41.29 (m)	**41.02 (m)**	**41.03 (m)**	**40.95 (m)**
39.57 (s)	**39.57 (s)**	**39.58 (s)**	**39.60 (s)**
39.34 (d, J_{PP}=42.1 Hz)	**38.51 (d, J_{PP}=41.7 Hz)**	**38.22 (m)**	**38.35 (m)**
-6.34 (d, J_{PP}=30.5 Hz)			**-6.73 (m)**

Table 4-2 compares the signals for the different lithium thiophosphates from crystalline and amorphous phases measured by solid-state NMR and in NMF solution.

Table 4-2: Reported chemical shifts obtained by solid-state ^{31}P NMR measurements of crystalline and amorphous phases in the system xLi_2S-$(1-x)P_2S_5$. In addition the assignment of the related chemical shifts measured in NMF solution to the different phases is shown.

	Crystalline	**Amorphous**	**NMF solution**
Li_3PS_4	88.4 ppm,[224] 86 ppm[233]	82.8 ppm[233]	92.0 ppm
$Li_4P_2S_7$	90.8 ppm[233], 91 ppm[234]	89.8 ppm,[224] 90.1 ppm[233]	105.9 ppm
$Li_4P_2S_6$	109.1 + 108.5 ppm[224,234]	103-105 ppm,[224] 106.3 ppm[233]	115.6 ppm
Li_7PS_6	86.6 ppm,[224] 88.5 ppm[234]	-	-
$Li_2P_2S_6$/ LPS_3	54.9[221]	121.7 ppm[221]	-

Table 4-1 and Table 4-2 reveal more signals and, consequently, more species for lithium thiophosphate dissolved in NMF than for lithium thiophosphate measured by solid-state NMR. This could be ascribed to the higher resolution of liquid state NMR, which enables the detection of smaller fractions (because of very narrow signals) in comparison with the broad and overlapping signals of solid-state NMR. Therefore, some species might not be detected in the solid state. A different explanation includes the formation of new species in solution due to the reaction of lithium thiophosphates with NMF or internal redox processes (as suggested in equation 4-1).

Several recorded signals are comparable to values measured in *ortho*-thiophosphate ester/ P_2S_5 systems [$(C_4H_9S)_3PS \rightarrow P_2S_5$] by Maier *et al.* at 119, 111, 103 and 63 ppm.[231] They ascribe the signal at 63 ppm to a thiophosphate branching group and the two signals at 111 and 103 ppm to triply connected phosphorus. It can be expected that similar thiophosphates are present in the NMF solutions.

Interestingly, two areas with changing intensity upon ageing in the range from 79 – 83 ppm and 37 – 42 ppm were recorded for [75-25] and [70-30] solutions and are shown in Figure 4-5. These regions might be related to oxygenated thiophosphates as O is more electronegative than S and hence the chemical shift for P → O should be more positive than for P → S compounds.[235] However, there is no convenient quantitative correlation between the chemical shifts and the nature of the atoms (S or O) bound to P.[230] Regarding $80Li_2S-18P_2S_5-2P_2O_5$ glass, which was analysed by solid-state NMR, values of 83 ppm (PS_4^{3-}), 83 ppm (POS_3^{3-}), 65 ppm ($PO_2S_2^{3-}$) and 35 ppm (PO_3S^{3-}) have been reported for the successive replacement of S by O in thio-*ortho*-phosphates.[236]
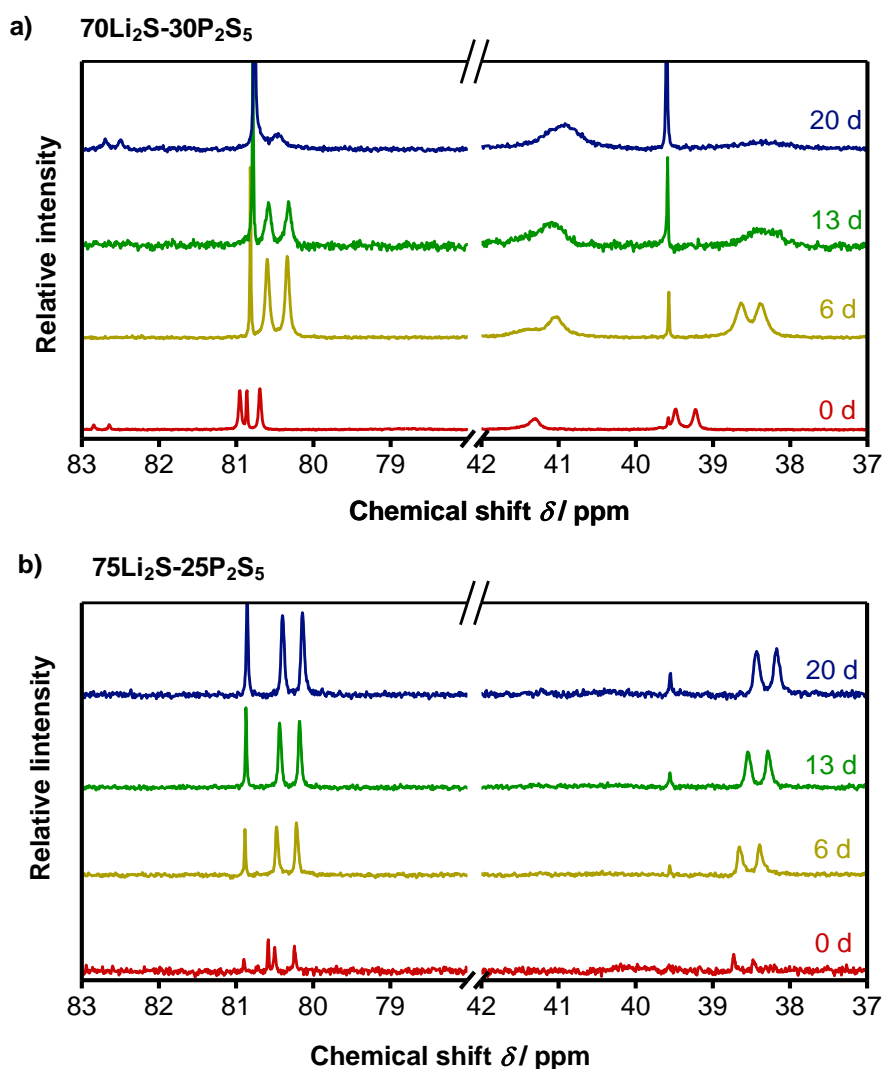
Figure 4-5: a) Selected regions from ^{31}P NMR spectra of a) [70-30] and b) [75-25] dissolved in NMF and aged for several days.

Table 4-3 summarises the assignment of the different signals to certain species, whereas Figure 4-6a) shows the respective structures.

Table 4-3: Signal assignment of chemical shifts obtained from ^{31}P NMR analysis of $x\text{Li}_2\text{S}$-$(1-x)\text{P}_2\text{S}_5$ glasses dissolved in NMF solution.

δ / ppm	Assumed (thio)phosphate structures
115.6 ± 0.4	PS_3^{3-} / $P_2S_6^{4-}$
105.9 ± 0.1	$P_2S_7^{4-}$
92.0 ± 0.3	PS_4^{3-}, POS_3^{3-}
80.8 ± 0.1	$PO_2S_2^{3-}$
39.6 ± 0.1	PO_3S^{3-}
80.4.0 ± 0.4 + 38.6 ± 0.7	PO_2S-S-PO_3^{4-}
80.7± 0.1 + -6.5 ± 0.2	POS_2-O-PO_3^{4-},
41.1 ± 0.1	PO_3-S-PO_3^{4-}, PSO_2-O-PSO_2^{4-}

The sharp singulets at 80.8 ± 0.1 and 39.6 ± 0.1 are assigned to $PO_2S_2^{3-}$ and PO_3S^{3-}, respectively. The signal of POS_3^{3-} might overlap with the signal of PS_4^{3-} at 92 ppm as their signals are reported to have similar values.

[70-30] solutions exhibit a multiplet (or two broad singulets) at 41.1 ± 0.1 ppm, which indicates the overlapping of several signals. The chemical shift is similar to PO_3S^{3-}, therefore, the signal is ascribed to the symmetric *pyro*-thiophosphates PO_3-S-PO_3^{4-} and PSO_2-O-PSO_2^{4-}, where each P is bound to one S.

Both [70-30] and [75-25] coating solutions show two doublets at 80.4 ± 0.4 and 38.6 ± 0.7 ppm with ^{31}P-^{31}P coupling constants of 42 Hz and similar areas. An additional ^{31}P-2D-NMR experiment (Figure 0-4 in the appendix) verified that the signals belong to the same molecule. The signals are ascribed to the asymmetric *pyro*-thiophosphate PO_2S-S-PO_3^{4-} with bridging S, as the observed coupling constant of 42 Hz is higher when compared to reported coupling constants of 31 Hz for bridging O (in thionated adenosindiphosphate (ADP) analogues).[237] Comparing spin coupling between ^{31}P and ^{1}H a bridging S results in a 5-10 Hz higher coupling constants compared to bridging O.[235]

In some coating solutions two doublets were detected at 80.7 ± 0.1 and -6.5 ± 0.2 ppm with coupling constants of 32 Hz and similar areas. The smaller coupling constant and the signal at -6.5 ppm suggests the formation of the

asymmetric *pyro*-thiophosphate $POS_2\text{-}O\text{-}PO_3^{4-}$ with bridging O and one completely oxygenated phosphate at one side.

The fractions of the species were calculated for the different coating solutions using the relative signal areas from integration. These results are only approximations, which should show a general trend as some signals overlap (especially in the case of [70-30]). Figure 4-6b) displays the results, which reveal that the amount of oxygenated thiophosphates strongly depends on the precursor stoichiometry. [70-30] shows the highest reactivity, whereas nearly no reaction could be detected for [80-20], which is in accordance with the quantitative results from ^{1}H NMR studies.

In addition, the results hint that also a condensation is involved, which is clearly visible for [75-25] as the amount of *ortho*-(thio)phosphates (green) decreases, whereas the amount of *pyro*-(thio)phosphates (red) increases. Lithium *ortho*-(thio)phosphates might condensate to lithium *pyro*-(thio)phosphates. An exemplary reaction is shown in equation 4-2 for the condensation of lithium *ortho*-thiophosphate to lithium *pyro*-thiophosphate, which includes the formation of lithium sulphide:

$$2\ Li_3PS_4 \rightarrow Li_4P_2S_7 + Li_2S. \qquad (4\text{-}2)$$
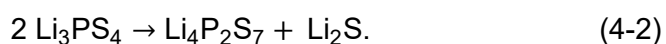
Mixed *ortho*-oxy-thiophosphates are also present in the solutions and might condensate with each other in a similar way creating mixed *pyro*-oxy-thiophosphates and lithium sulphide or lithium oxide.

a)

1 $P_2S_6^{4-}$

2 $P_2S_7^{4-}$

3 PS_4^{3-}

3a POS_3^{3-}

4 $PO_2S_2^{3-}$

5 PO_3S^{3-}

6 $P_2O_5S_2^{4-}$

7 $P_2O_5S_2^{4-}$

8a $P_2O_6S^{4-}$

8b $P_2O_5S_2^{4-}$

b)
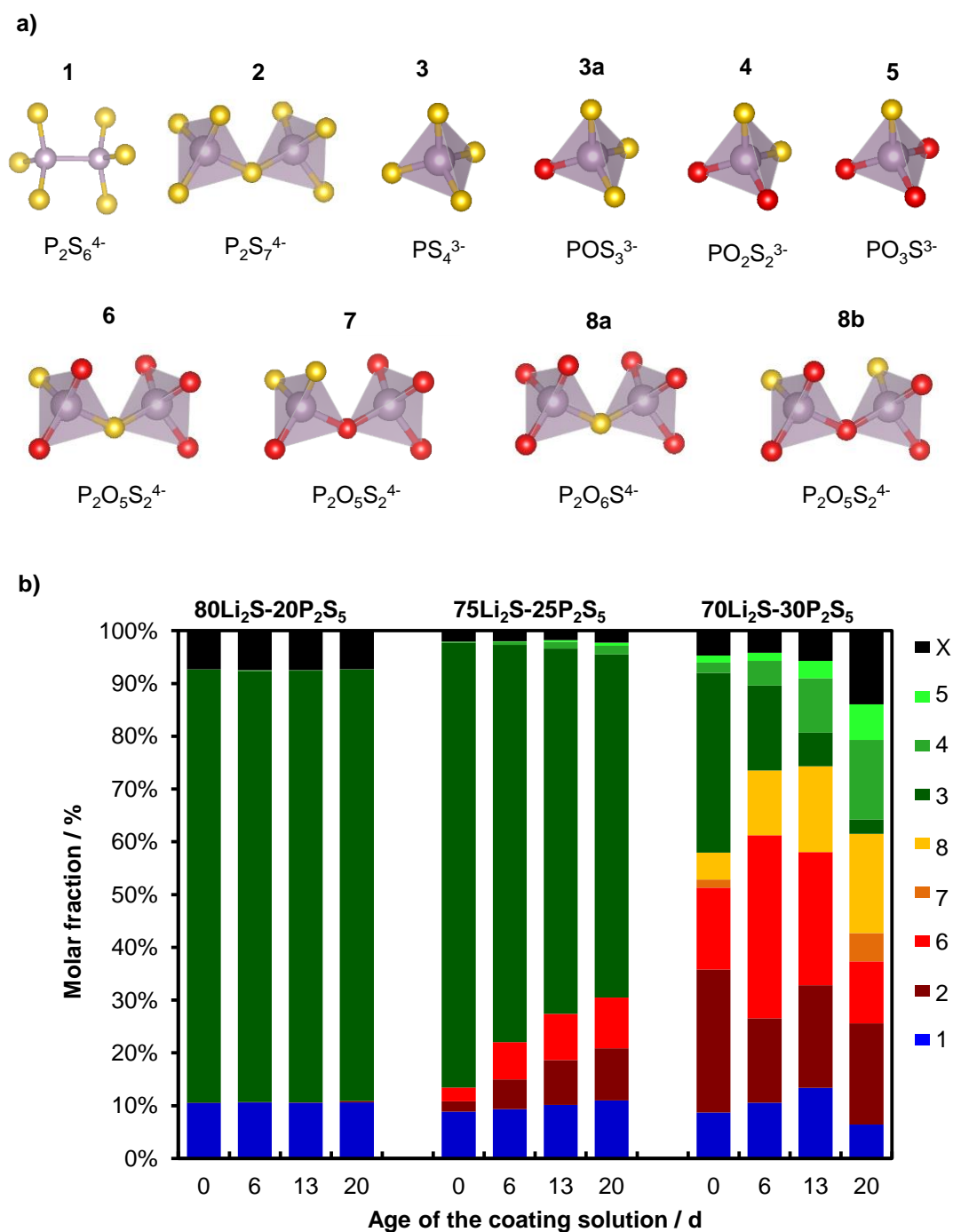
Figure 4-6: a) Assumed structures of different thio-oxy-phosphates found in differently aged solutions of xLi_2S-$(1-x)P_2S_5$ (x=70, 75, 80) in NMF. b) Quantitative results of different (thio)phosphate species derived from integrated peak areas of ^{31}P NMR spectra. The numbers (1-8) are related to the structures given in a). X describes the sum of all unknown species.

4.1.2 Reaction mechanism

A reaction mechanism for the S-O exchange for *ortho*-thiophosphate with NMF is suggested and shown in Scheme 2 on basis of the results obtained from ^{1}H, ^{13}C and ^{31}P NMR studies. This mechanism is similar to a published mechanism for the reaction of O,O-dialkyldithiophosphoric acids with ketones and aldehydes.[238]
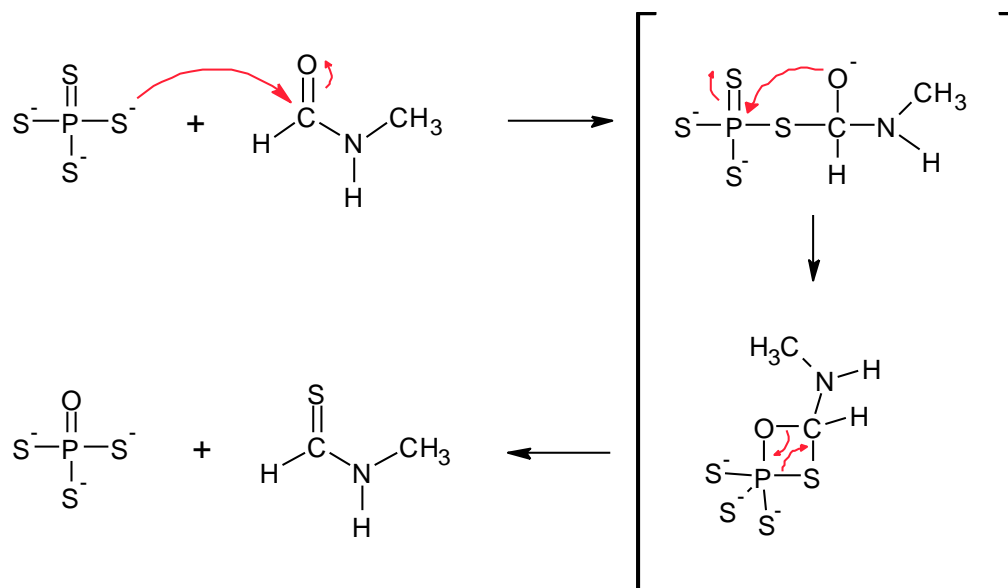
Scheme 2: Reaction mechanism of the reaction of tetrathio-*ortho*-phosphate with *N*-methylformamide to *N*-methylthioformamide and trithio-*ortho*-phosphate.

The first step in the reaction involves the nucleophilic attack of the mercapto function to the carbonyl carbon of the amide group. Afterwards, or simultaneously, the oxygen attacks the phosphorous generating a four-membered ring intermediate with a pentacoordinated P, which is similar to the oxaphosphetane observed in the *Wittig Reaction*. This intermediate undergoes elimination to give thio-NMF and trithio-*ortho*-phosphate, which could continue to react subsequently to sulphur free phosphate. A similar mechanism is expected for the reaction of *pyro*-thiophosphate with NMF.

4.1.3 Summary

Suitable coating solutions were formulated based on NMF as solvent and the amorphous LPS glasses [70-30], [75-25] and [80-20] as precursors. However, ageing of the precursor solutions was observed.

In situ NMR measurements revealed a S-O substitution between the amorphous LPS precursors and NMF. The S-O exchange led to the formation of (i) thio-NMF as revealed by time-dependant ^{1}H and ^{13}C NMR and (ii) different thio-oxy-phosphates within the precursor solutions as shown by time-dependant ^{31}P NMR. Quantitative evaluation of the results from ^{1}H NMR and ^{31}P NMR revealed that the reaction rate depends on the LPS precursor stoichiometry. [70-30] showed the highest reactivity, whereas nearly no reaction was detected for [80-20]. Therefore, the various lithium thiophosphate species seem to exhibit different reactivities with NMF. [80-20] and [75-25] consist mainly of *ortho*-thiophosphate, while [70-30] contains stoichiometric amounts of *pyro*- and *ortho*-thiophosphate. Therefore, *pyro*-thiophosphate appears to be more reactive than *ortho*-thiophosphate towards S substitution by NMF.

The NMR measurements were performed at RT, while the formation of LPS thin-films from NMF based solutions requires higher temperatures, which might accelerate the S-O exchange. Therefore, LPS thin-films might contain higher oxygenated (thio)phosphates compared to the species that were found in the coating solutions. The NMR studies of the NMF solutions might help to understand the reaction processes involved during LPS film synthesis.

It is expected that LPS film composition and, consequently, the properties of LPS thin-films depend on the precursor stoichiometry and the age of the coating solution. LPS thin-films consisting of mixed oxy-thiophosphates are considered also as interesting SE for applications in SSBs.

4.2 CHEMICAL SOLUTION DEPOSITION OF LPS THIN-FILMS

Even though partial S-O substitution was revealed by time-dependant NMR studies, LPS thin-films were prepared from NMF based solutions. This chapter deals with the influence of the precursor solution and several deposition parameters on LPS thin-film properties such as morphology, crystallinity, film stoichiometry or/and conductivity. Preliminary experiments revealed the formation of NiS, FeS and CuS on nickel (Ni), stainless steel (SS) and copper (Cu) substrates, respectively. Si substrates showed no reaction, so conductive Si was chosen as substrate for first deposition experiments. NMF tend to dry very slowly due to its high boiling point of 200 °C so drop casting on a hotplate at elevated temperatures (60-120 °C) was chosen as coating technique. Other suitable techniques to consider in the future include inkjet-printing or slot die coating. After the coating process the deposition temperature was maintained for $15-60$ min before heating the predried films ($2-20$ °C min^{-1}) up to the final drying temperature ($200-300$ °C), where the films were dried for $30-120$ min. A schematic overview of the film formation steps is shown in Figure 4-7.

Figure 4-7: Schematic overview of the film formation process.

4.2.1 Influence of the precursor solution

Three different amorphous LPS glasses with various stochiometries ([70-30], [75-25], [80-20]) were dissolved in NMF for CSD of LPS thin-films. The influence of LPS precursor stoichiometry and age of the coating solution on LPS thin-film properties such as morphology, crystallinity, elemental distribution and electrochemical behaviour was investigated by SEM, XRD, EDX, XPS, DC and EIS analysis.

Time-dependent NMR studies showed a continuous S-O exchange of [70-30] and [75-25] with NMF at room temperature (RT). As the temperatures during thin-film preparation exceeded 200 °C the reaction could be enhanced leading to even higher oxygenated (thio)phosphates in the thin-films compared to the coating solutions. So it is expected that LPS film composition and thus the properties of LPS thin-films depend on the precursor stoichiometry and the age of the coating solution.

Morphology

Figure 4-8 and Figure 4-9 show SEM images of LPS thin-films with various precursor stochiometries deposited from fresh (0 days) and aged (7 days) coating solutions, respectively. The SEM images reveal a clear dependence of the precursor solution with the obtained film morphology.

- Cross section SEM images from both [80-20] thin-films reveal a porous granular structure with a thickness of 2-4 µm. The top view image for the layer obtained from a fresh solution shows a granular or columnar morphology, whereas the film prepared from an aged solution exhibits a denser structure with small cracks throughout the layer. The granular mircrostructure could result from crystallisation of the thin films.

- SEM images from the two [75-25] thin-films display similar morphologies indicating negligible influence of the solution aging behaviour. The images reveal two different areas: thin and dense areas with a thickness of less than 1 µm (shown in Figure 0-5 in the appendix) correlated to an amorphous structure, and thick areas of several µm with a porous granular or columnar structure correlated to crystalline material.

- The morphology of [70-30] thin-films changes drastically upon ageing of the coating solution. The layer from a fresh coating solution shows a dense, homogeneous and continuous structure with a thickness of around 1 µm, whereas a whitish film was obtained from an aged solution that exhibits a

similar morphology but cracks throughout the layer. The dense structure could indicate amorphous materials.

Only fresh coating solutions of [70-30] result in homogeneous, continuous and dense LPS thin-films.

80Li$_2$S-20P$_2$S$_5$

75Li$_2$S-25P$_2$S$_5$

70Li$_2$S-30P$_2$S$_5$
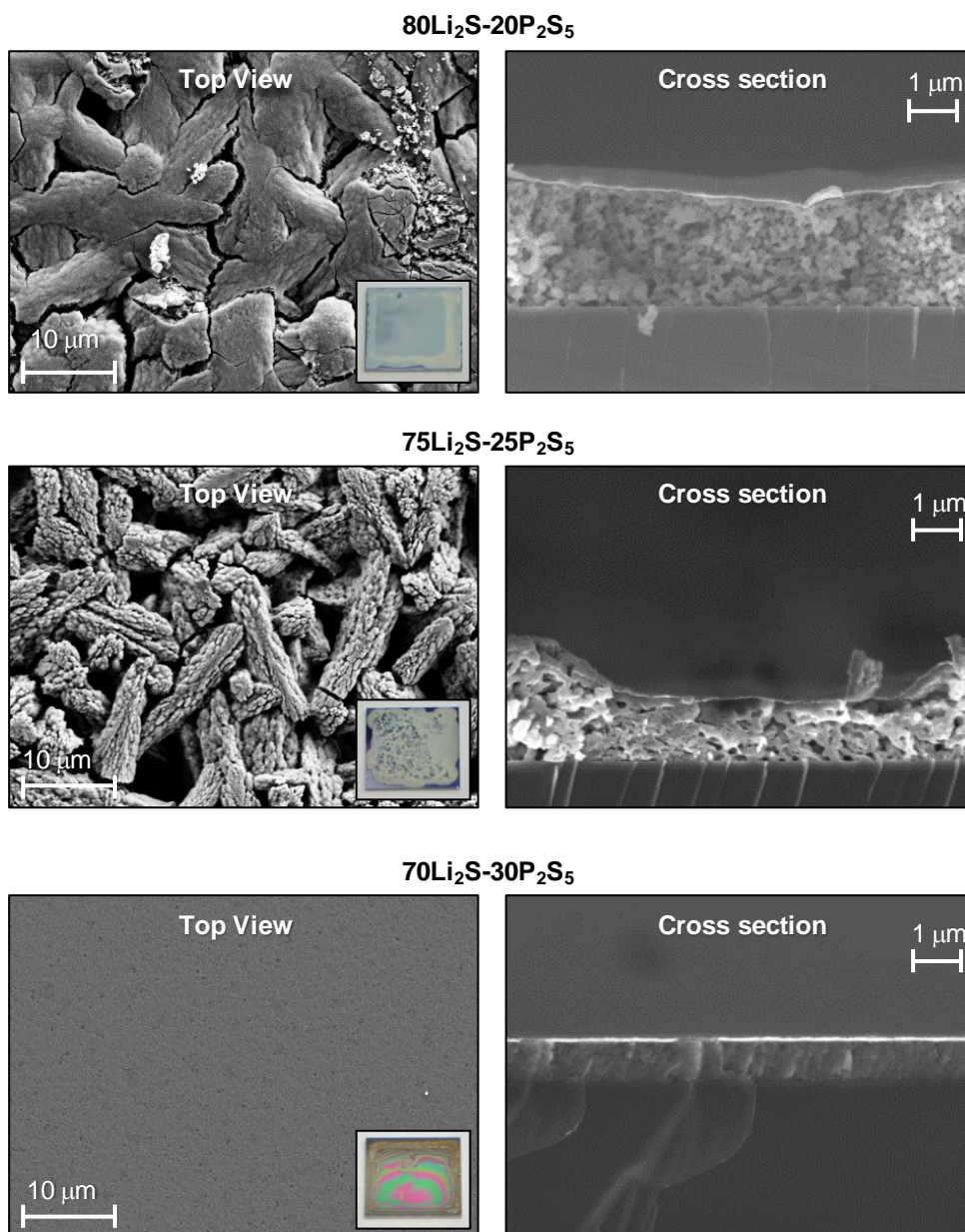
Figure 4-8: SEM cross section and top view images from LPS thin-films (AB01-AB03) prepared on Si substrates from freshly prepared coating solutions. A picture of each thin-film is shown as insert.

80Li$_2$S-20P$_2$S$_5$

75Li$_2$S-25P$_2$S$_5$

70Li$_2$S-30P$_2$S$_5$
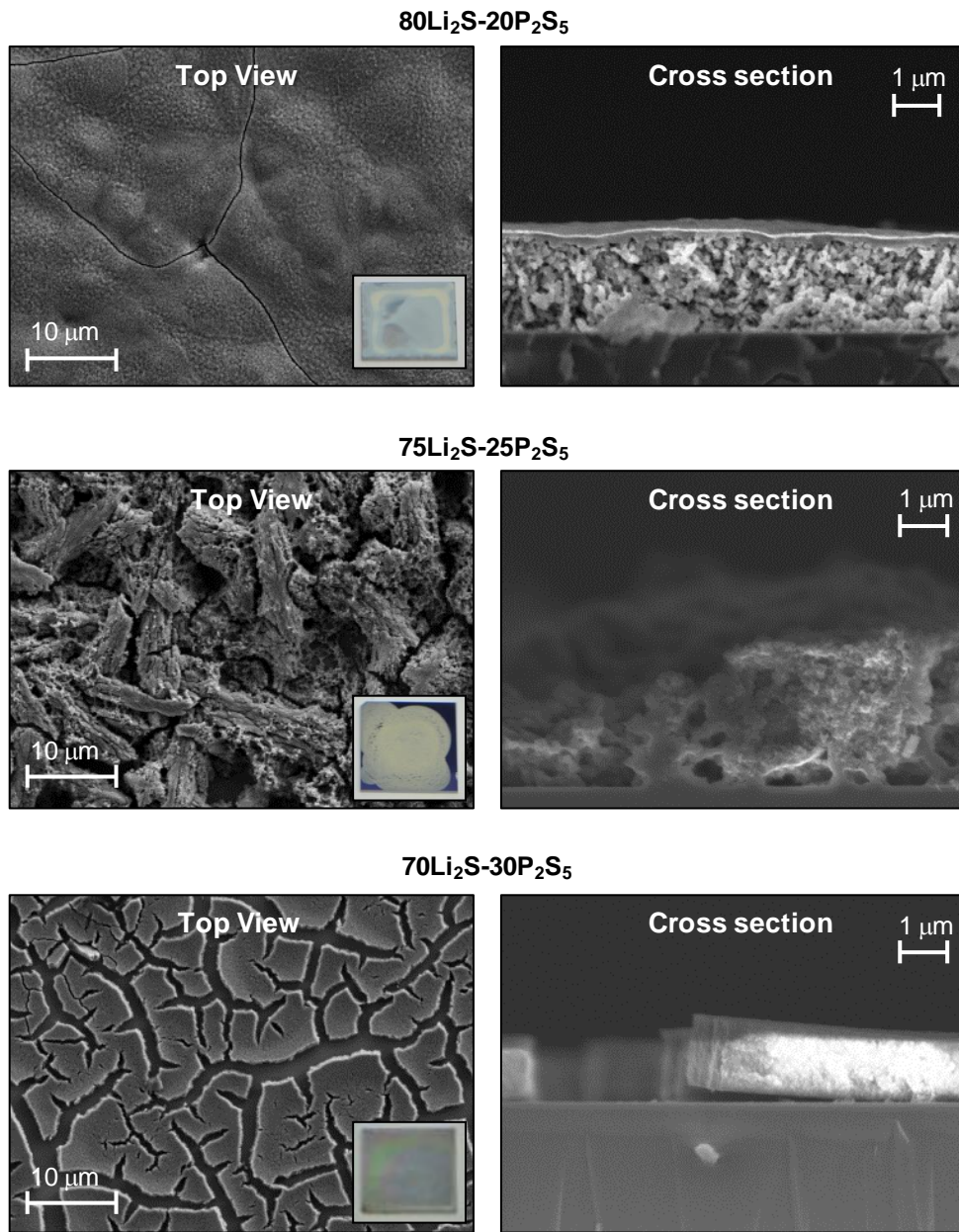
Figure 4-9: SEM cross section and top view images from LPS thin-films (AB04-AB06) prepared on Si substrates from 7 d old coating solutions. A picture of each thin-film is shown as insert.

Crystallinity

Crystalline structures of LPS thin-films deposited from coating solutions with different stoichiometries and ages were analysed by X-ray diffraction (XRD). Figure 4-10 shows the recorded diffractograms.
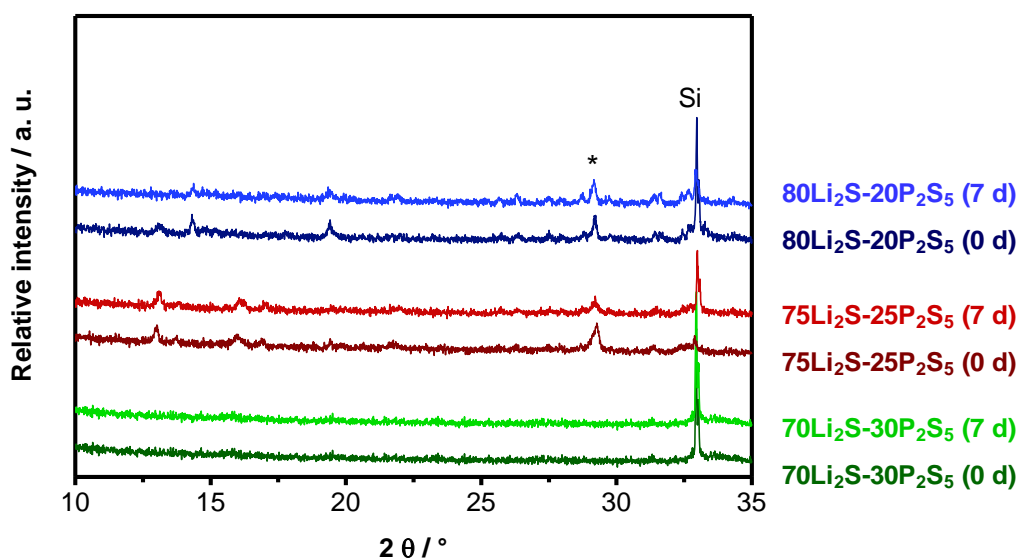
Figure 4-10: Diffractograms of lithium thiophosphate thin-films made from different aged coating solutions using different starting stoichiometries. The reflection marked with an asterisk is related to the adhesive material for sample fixation. The age of the used coating solution is shown in brackets.

XRD measurements reveal a strong correlation between the precursor stoichiometry and the LPS thin-film crystallinity, while aging of the coating solution does not show any effect.

The recorded diffractograms show the crystalline nature of LPS thin-films obtained from [80-20] and [75-25] coating solutions although the observed reflections do not resemble previously reported structures such as Li_3PS_4, $Li_7P_3S_{11}$, $Li_4P_2S_6$ or Li_7PS_6.[239]

The lack of reflections in both diffractograms of [70-30] thin-films indicates that the layers are amorphous. The XRD results correlate with the morphology observed in the SEM images, as [80-20] and [75-25] thin-films exhibit granular or columnar structures, whereas [70-30] thin-films are dense and homogeneous.

Elemental distribution

The composition of the LPS systems was further investigated by XPS and EDX analysis, shown in Figure 4-11a) and b), respectively. The elemental ratios of LPS thin-films produced from fresh and aged coating solutions are compared to the composition of the precursor for the three different stoichiometries chosen. Note that EDX cannot detect Li and Li signals are weak in the XPS, which might lead to significant fitting errors. Therefore, Li contents will not be discussed in detail.

As XPS is a surface sensitive technique depth profiling of the samples was performed. The XPS spectra of the pristine LPS thin-films were recorded followed by subsequent ion gun etch cycles (ion sputtering) and XPS analysis. Figure 0-6 in the appendix displays the atomic ratios of the different recorded species as a function of sputtering time.

The surface composition differs from the elemental distribution in the depth of the films caused by C contamination. C species on the surface of LPS samples are commonly found by XPS analysis and can be ascribed to impurities in the inert gas atmosphere in the glovebox leading, for example, to the formation of carbonates. Once the surface is removed by ion sputtering, the elemental distribution along the depth profile remains relatively constant. Therefore, Figure 4-11a) shows the average LPS thin-film compositions derived from XPS depth profile analysis $(2-8$ min sputter time).

The recorded values do not agree well with the nominal composition of the precursors. XPS analysis reveals small C contents $(1.3-8.5\%)$ in the depth of the samples which increases upon aging of the coating solution. Interestingly, also traces of N are found in the [70-30] thin-films by XPS analysis. However, N contents should be handled with caution as they are very low and hence N signals are too weak for reliable analysis. C and N contents were not included in evaluation of EDX spectra because the N contents were too low for reliable analysis and C contents were difficult to quantify due to sample fixation with C tape. Both C and N contents in LPS thin-films could result from the decomposition of the organic solvent NMF.

The P content of the thin-films is comparable to the stoichiometric values of the precursor. As expected from NMR studies, elemental analyses of LPS films compared to the precursors reveal a S deficiency and a O excess. The sum of O and S content (S+O) correlates to the initial S composition in the coating solution, which is consistent with the suggested S-O substitution of LPS systems and NMF.
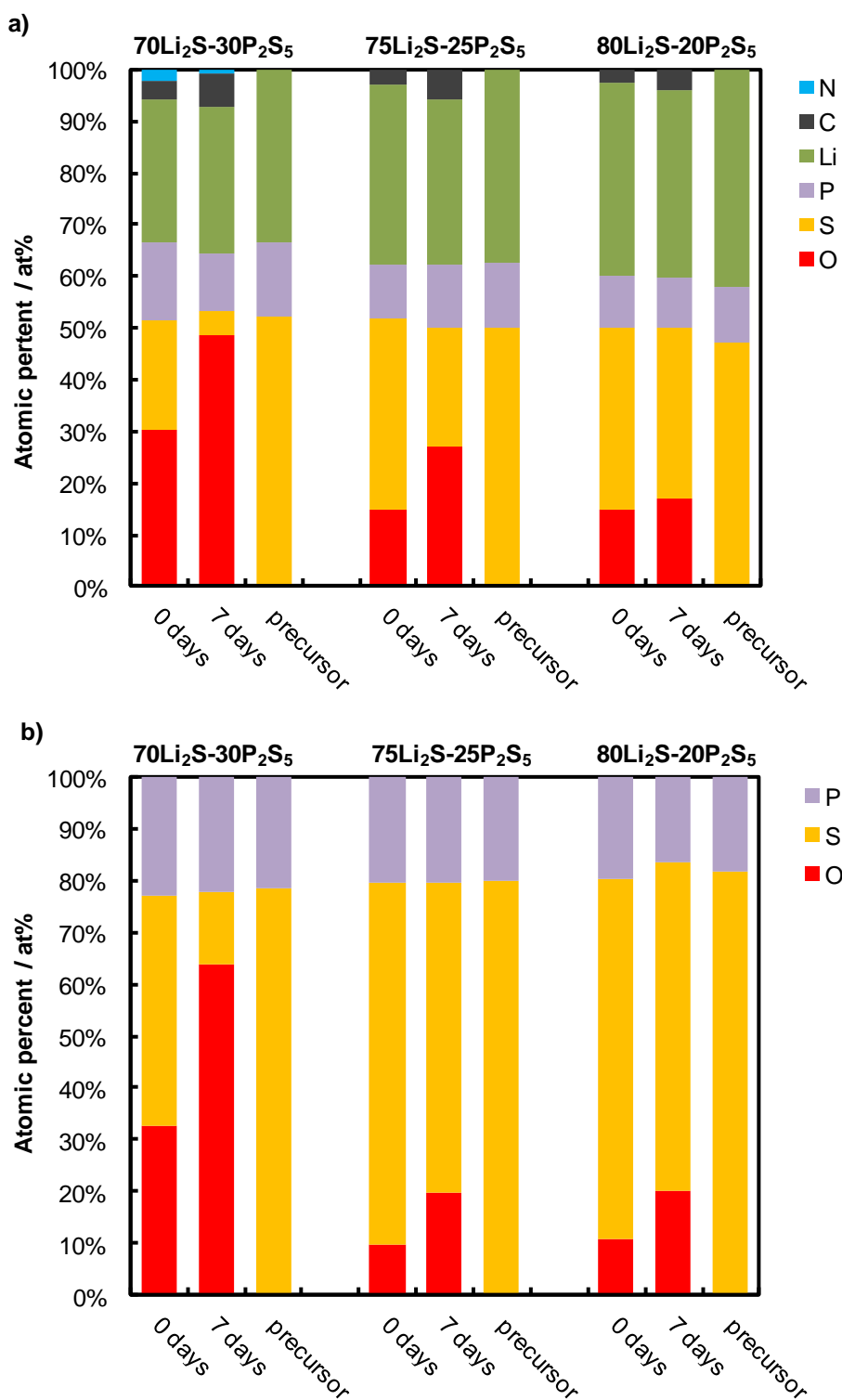
Figure 4-11: Elemental composition of LPS systems (AB01-AB06) with different precursor stoichiometries by XPS (a) and EDX (b). Note that Li cannot be detected in EDX measurements. XPS results display averaged atomic ratios derived from XPS depth profile analysis (2 – 8 min sputter time).

The fractions of P and (S+O) are similar for thin-films produced from fresh and aged coating solutions, although the O content depends strongly on the stoichiometry and age of the precursor solution with a higher amount of O for LPS layers deposited from aged solutions.

While EDX shows a similar atomic ratio between O and S for [75-25] and [80-20] thin-films, XPS reveals a higher O content for [75-25] layers obtained from aged coating solutions compared to [80-20]. Still, both elemental analyses show the highest O amount for [70-30] thin-films.

Both XPS and EDX results support the suggested substitution of S by O during film formation, where lithium thiophosphates react with the solvent NMF. The reaction rate depends on the precursor stoichiometry with [70-30] being the most reactive precursor similar to the results obtained from NMR studies.

Bonding behavior of O and S species

The oxidation state and bonding behaviour of the different elements can be extracted by fitting the XPS data. S and O are from special interest as different S and O species can be found in LPS coating solutions: non-bridging sulphur S_{nb} (present in *ortho*-, *pyro*- and *meta*-thiophosphate), bridging sulphur S_b (present in *pyro*- and *meta*-thiophosphate), non-bridging oxygen O_{nb} (present in *ortho*- and *pyro*-phosphate) and bridging oxygen O_b (present in *pyro*-phosphate).

Figure 4-12a) and b) show the detail spectra and the fitting results of the S 2p and O 1s signals, from the different samples after a sputtering time of 8 min respectively. The S 2p peak shape resembles the data reported for amorphous LPS glasses.[240] Wang *et al* found two different species assigned to bridging sulfur S_b and non-bridging sulfur S_{nb}. However, 4 different species have been considered when fitting LPS thin-films: (i) S_{nb} at 161.5 eV, (ii) S_b at 162.2 eV, (iii) an unknown species S_u at 163.1 eV and (iv) Li_2S at 160.0 eV.[241] The given values correspond to the respective S $2p_{3/2}$ component. Koerver *et al.* ascribed a signal at 163.7 eV to oxidised S species, which were assigned to the formation of –S-S- polysulfide bonds.[242] The signal of the unknown S species found in LPS thin-films appears at slightly lower energies but as the fitting of the signal was difficult and only possible with a high error (due the weak signal which overlaps with other S signals) it could also originate from oxidised S species.
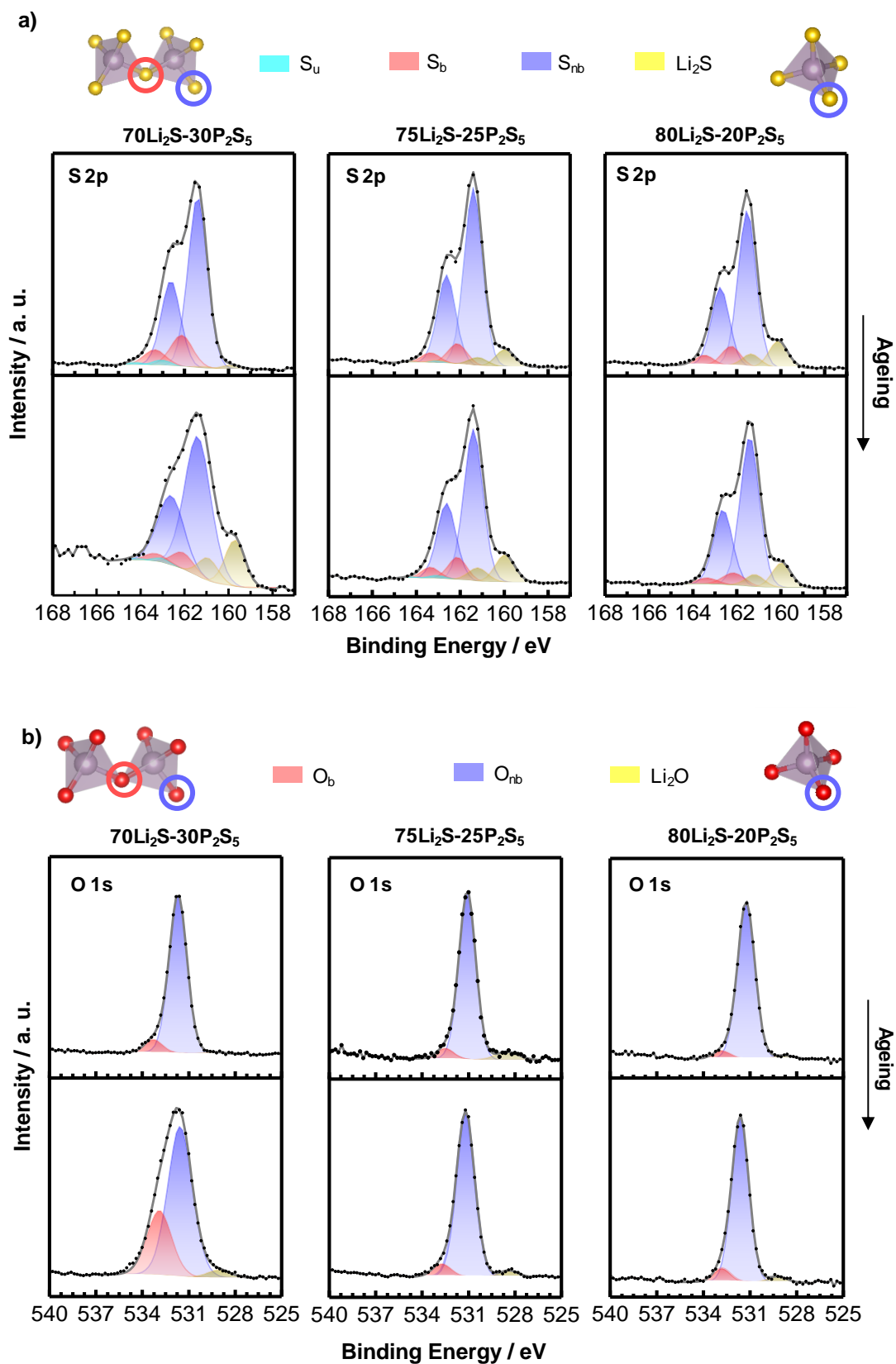
Figure 4-12: Detail spectra and fitting results of the S 2p (a) and 0 1s (b) signals of the different samples (AB01-AB06) after a sputtering time of 8 min.

The O 1s emission line resembles the data observed for LiPON thin-films.[139] Three signals at 528.9 eV, 531.4 eV and at 532.9 eV were measured, characteristic for Li_2O, non-bridging oxygen O_{nb} and bridging oxygen O_b, respectively.[139]

The amount of the different S and O species in the different films was calculated and is shown in Figure 0-7 in the appendix. The results suggest that S_b and S_{nb} are replaced by O_b and O_{nb} in the LPS thin-films. Upon aging both O_b and O_{nb} signals increase, whereas S_b and S_{nb} signal decreases.

In contrast to the NMR studies, a S-O exchange was also revealed for LPS films derived from [80-20] coating solutions. This might be correlated to the higher temperatures during film deposition enhancing the S-substitution. Therefore, all LPS thin-films probably consist of mixed thio-oxy-phosphates with various combinations of S_{nb}, S_b, O_{nb} and O_b. Especially thin-films prepared from aged [70-30] coating solutions exhibit a high amount of O_{nb} and O_b.

Electrochemical properties

Both electrochemical impedance spectroscopy (EIS) and direct current (DC) polarisation measurements were carried out to determine ionic and electronic conductivity of the various LPS thin-films. To do so, four square Au blocking electrodes were evaporated on a single sample with a contact area of 2.56 mm². Electrochemical measurements were performed vertically through the different films, where the evaporated Au contact and the Si substrate act as electrodes.

The electronic resistance was estimated from DC polarisation measurements by applying a potential of 1 V against the reference electrode (top Au contact) over 1 min. In some DC polarisation curves the measured current shows an exponential decay. As a steady state current I_{SS} was not completely reached after 1 min the last measured data point was used to determine an estimation of the electronic resistance R_{el} of the thin-films according to equation 3-7. Other samples exhibit a nearly linear current response in the DC polarisation curves, where the order of magnitude of the current is in general at least 2 orders of magnitude higher compared to the steady state current. It is assumed that a steady state current is reached on intact contacts, while the linear current responses correlate with short circuits through the films, which are probably related to porosity or cracks in the layers. Table 4-4 shows the amount of short circuits per sample and the averaged electronic area resistance. No short circuits were observed for freshly prepared [70-

30] and both [80-20] films, while all contacts of aged [70-30] and both [75-25] films are short circuited.

Table 4-4: Calculated conductivity values obtained by EIS measurement and fitting of the measured data. Resistance, thickness and conductivity values from different films made from NMF solutions. LPS thin-film deposited from aged coating solutions (1 week) are marked with an asterisk (*).

Number	Salt	Short circuits/ sample / %	Electronic Area Resistance R_{el}/ Ω cm²	Electric Area Resistance R_1 / Ω cm²	Thickness/ µm	Conductivity σ_{Li^+}/ S cm^{-1}
AB03	80-20	0	$5.25 \cdot 10^6$	36.6	3.0	$1.03 \cdot 10^{-5}$
AB06	80-20*	0	$5.50 \cdot 10^6$	22.1	2.0	$1.11 \cdot 10^{-5}$
AB02	75-25	100	$6.53 \cdot 10^4$			
AB05	75-25*	100	$5.40 \cdot 10^4$			
AB01	70-30	0	$2.01 \cdot 10^7$	2.84	0.91	$3.20 \cdot 10^{-5}$
AB04	70-30*	100	$1.13 \cdot 10^2$			

EIS measurements were only performed on intact contacts. Representative Nyquist plots and the measurement setup are shown in Figure 4-13a) and b), respectively. The Nyquist plots show the onset of a semicircle at lower frequencies and a straight line at higher frequencies. The measured data were fitted with a resistance parallel to a constant phase element (CPE) in series with a second CPE $(R_1 Q_1) Q_2$. Table 0-2 in the appendix summarises the fitting results, while Figure 4-13c) displays the equivalent circuit. In this equivalent circuit $R_1 Q_1$ describes the semicircle and Q_2 the straight line. The semicircle is ascribed to the transport of lithium ions through the LPS layer, while the straight line refers to the blocking (capacitive) behaviour of the Au/Si electrodes.

The area resistances R_1 listed in Table 4-4 are the average values obtained from four different contacts on one film. The LPS thin-films showed area resistances between 36.6 Ω cm² ([80-20]) and 2.84 Ω cm² ([70-30]). Conductivities of these layers are calculated using equation 3-1 and are shown in Table 4-4. The conductivities obtained from EIS measurements are some orders of magnitude higher than the electronic conductivity determined by DC polarisation. According to equation 3-2 the lithium-ion conductivity is therefore given by the conductivity obtained from EIS. Lithium-ion conductivities range from $1.03 \cdot 10^{-5}$ S cm^{-1} for [80-20] films to $3.00 \cdot 10^{-5}$ S cm^{-1} for films made from [70-30]. All LPS thin-films showed higher lithium-ion conductivities compared to LiPON films with a conductivity of $2.3 \cdot 10^{-6}$ S cm^{-1}.[79] Therefore, these partially oxygen substituted LPS materials are

interesting as thin-film solid electrolytes and NMF in particular seems to be a good solvent for the synthesis of LPS thin-films.
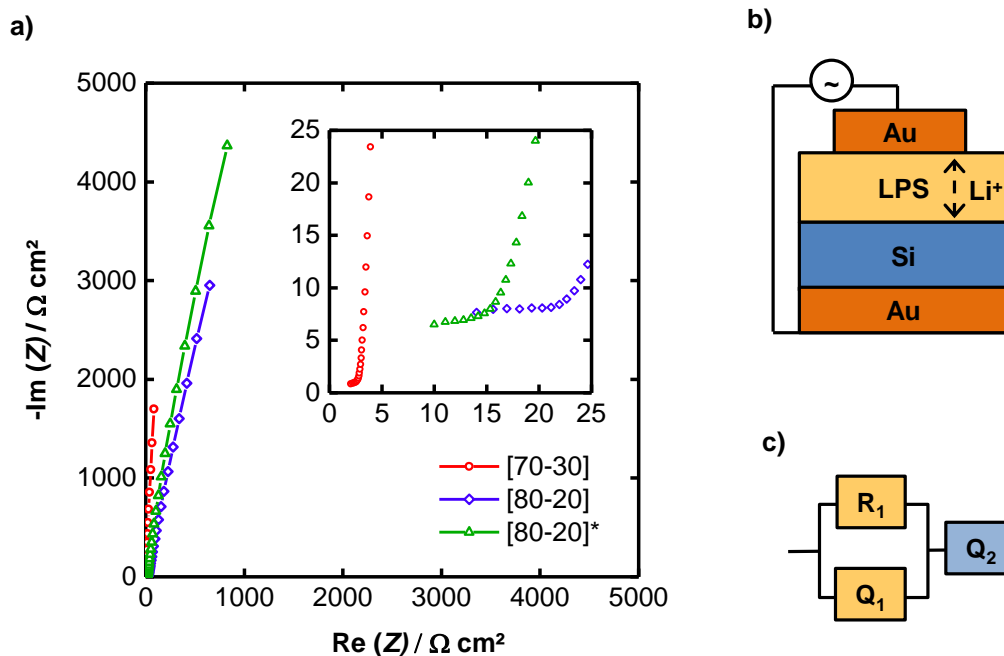
Figure 4-13: a) Representative Nyquist plots of various LPS thin-films (AB01, AB03, AB06). The asterisk (*) marks an LPS thin-film deposited from an aged coating solution (1 week).b) Setup used for EIS measurement. c) Equivalent circuit used for fitting the measured EIS data.

From all analysed layers, films made from ball milled [70-30] dissolved in NMF seems to be the most suitable films for applications in SSBs, despite the high amount of oxygen, as these films exhibit a high ionic conductivity, a low electronic conductivity as well as a crack free and homogeneous layer. However, only freshly prepared [70-30] coating solutions should be used for chemical solution deposition of LPS thin-films as ageing leads to morphology and conductivity changes. Therefore, further studies were only performed for LPS thin-films derived from freshly prepared [70-30] precursor solution.

4.2.2 Deposition process

The influence of the deposition parameters on the layer morphology and lithium-ion conductivity was investigated for LPS thin-films derived from [70-30] coating solutions. The deposition temperature was varied between 60 and 120 °C with 10 °C increments. Temperatures lower than 60 °C are not favourable as the film would still be extremely wet after the deposition and the movement of the film would be challenging. Figure 4-14 shows photographs taken of the different films, while Figure 0-8 in the appendix show top view and cross-section SEM images of the obtained layers.

60 °C   *T*   **120 °C**
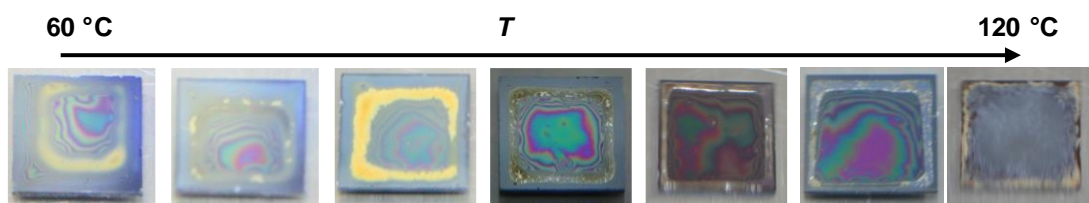
Figure 4-14: Photographs taken of LPS films (AB07-AB13) deposited at different temperatures. The drying process included predrying at the deposition temperature for 30 min and subsequent heating with 10 °C min⁻¹ to the drying temperature of 225 °C, where the films were dried for 60 min.

Temperatures above 110 °C lead to the formation of whitish layers. At temperatures lower than 110 °C shiny layers with a homogeneous coating in the middle of the sample as well as edge effects at the sides are obtained. Higher temperatures led to smaller edge effects and according to SEM images to slightly thinner films with less variation in layer thickness (see Figure 4-14).

Au contacts were evaporated on top of LPS films for EIS. The measurement and data fitting was performed as previously described. SEM images were recorded from half of the prepared LPS films and are shown in Figure 0-8 in the appendix. Conductivities were calculated for LPS films assuming LPS layer thicknesses of 920 nm (60 °C), 950 nm (80 °C), 885 nm (100 °C) and 835 nm (120 °C) as determined from the SEM images. Figure 4-15 shows the area resistances and conductivities of LPS thin-films deposited at different temperatures. The lowest resistance and the highest conductivity are obtained for LPS films deposited at 80 °C. Lower deposition temperatures lead to a slight increase in resistance, while higher deposition temperatures significantly increase the layer resistance and lead to higher errors. The resistance increase at elevated deposition temperatures might

be explained by an enhanced O-S substitution at higher temperatures resulting in films with a higher oxygen content and lower conductivity. Further LPS depositions were therefore carried out at 80 °C as these films exhibit both a good morphology and a high conductivity.

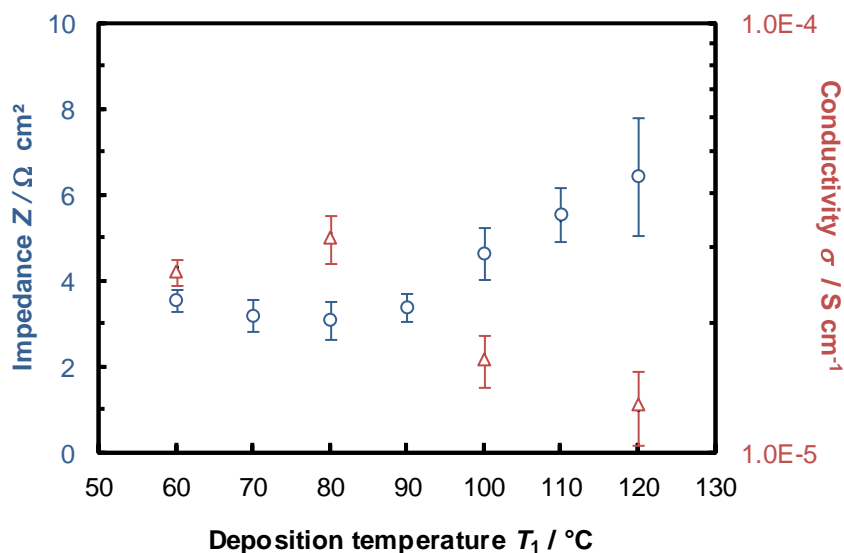**Figure 4-15**: Area resistances (blue) and conductivities (red) of LPS thin-films (AB07-AB13) deposited at different temperatures. The drying process included predrying at the deposition temperature for 30 min and subsequent heating with 10 °C min^{-1} to the drying temperature of 225 °C, where the films were dried for 60 min.

In addition, the deposition time was varied between 15 and 60 min, but neither a significant change in conductivity nor in the film morphology was recorded. LPS films predried for only 15 min exhibit slightly higher variations in conductivity and layer thickness. Therefore, LPS thin-films were predried for 30 min.

4.2.1 Heating process

Next the influence of the heating process including drying temperature T_2, drying time t_2 and heating rate r_H for the layer morphology and ionic conductivity was analysed by SEM and EIS, respectively. EIS measurements and data fitting was performed as previously described. Conductivities were calculated assuming the layer thicknesses from SEM analyses given in Table 0-3 in the appendix.

The heating temperature was varied between 200 and 300 °C with 25 °C increments. Figure 0-9 in the appendix shows top view and cross-section SEM images of the obtained films dried at the different temperatures, while Figure 4-16a) shows the area resistances. The morphology and conductivity change in the investigated area: drying temperatures higher than 250 °C lead to more porous layers, which can be seen in the top view images; LPS thin-films dried at 200 °C exhibit a significantly lower conductivity.

Next, the drying time was varied between 30 and 120 min. Figure 0-10 in the appendix and Figure 4-16b) show SEM images and area resistances/ conductivities of these LPS films, respectively. The morphology is independent on the drying time and also the measured conductivities are all in the same range.

The last investigated parameter was the heating rate, which was changed between 2 and 20 °C min^{-1}. SEM images of these films can be found in Figure 0-11 in the appendix, while Figure 4-16c) displays the resistances and conductivities of the different layers. Again all LPS films exhibit similar morphologies, while the measured conductivity is in the same range. Higher heating rates seem to lead to a minor decrease in conductivity.

LPS films characterised as solid electrolyte and prepared for applications in microbatteries or protective coatings as described in chapter 4.3 and 4.4 were heated to 250 °C with a heating rate of 10 °C min^{-1} and dried for 60 min. These parameters were considered as ideal regarding conductivity and morphology of LPS films and industrial requirements such as fast processability at low costs.
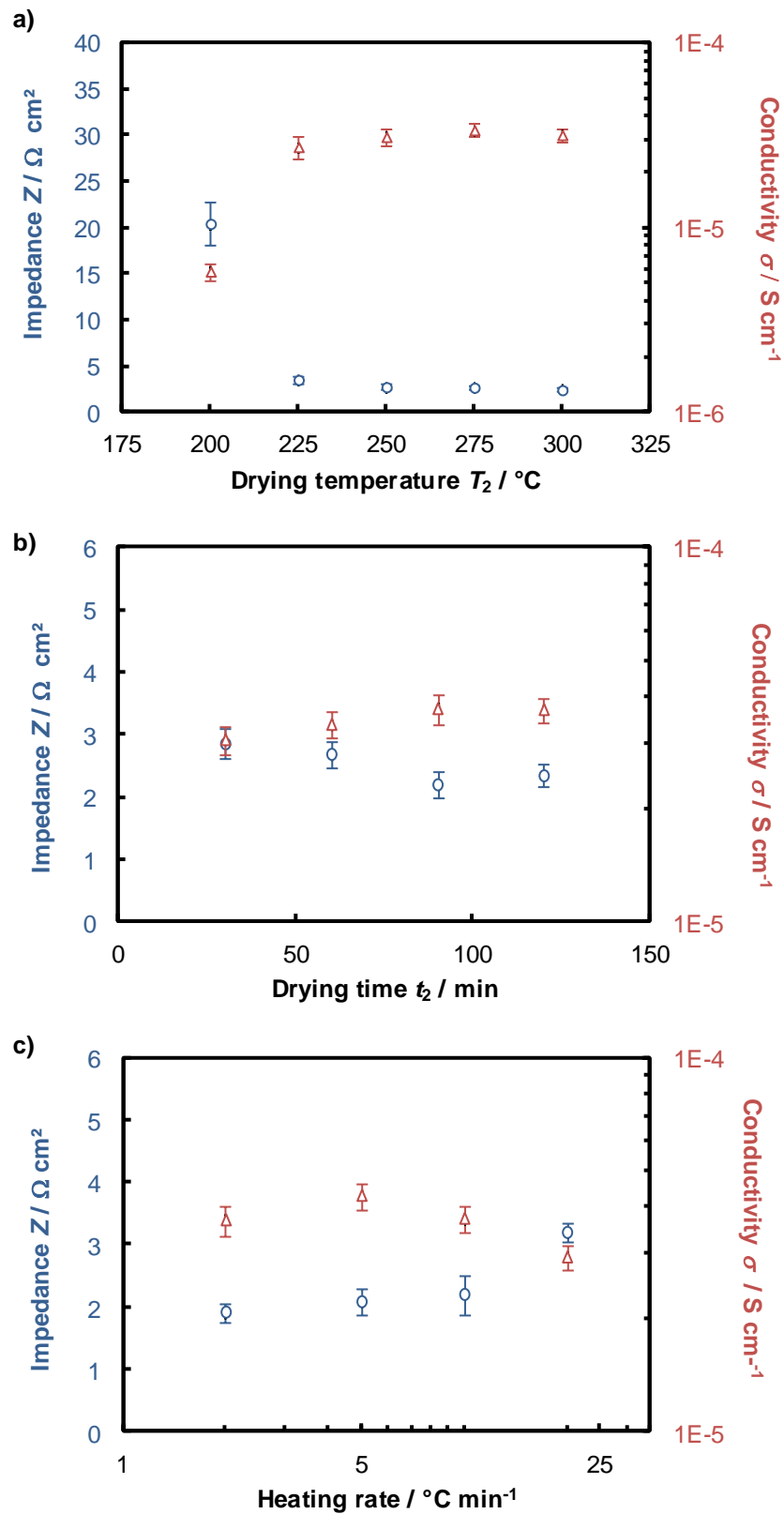
Figure 4-16: Area resistances (blue) and conductivities (red) of LPS thin-films (a) dried at different temperatures (AB16-AB20), (b) for different times (AB15, AB21-AB23) and (c) heated with different rates (AB22, AB24-AB26).

4.2.2 Variation of the layer thickness

The layer thickness can be adjusted by changing the deposition volume or by changing the concentration of the coating solution. Figure 4-18 shows LPS thin-films obtained with solution concentration and deposition volumes ranging from 2 to 8wt% and 2 to 8 µL, respectively. A picture of each thin-film is shown as insert. The photographs and SEM images of the LPS films show that thinner layers have a larger homogeneous middle area with less edge effects and smaller thickness variations. The layer thickness determined from these images ranges from 300 nm to 1.4 µm as shown in Figure 4-17.
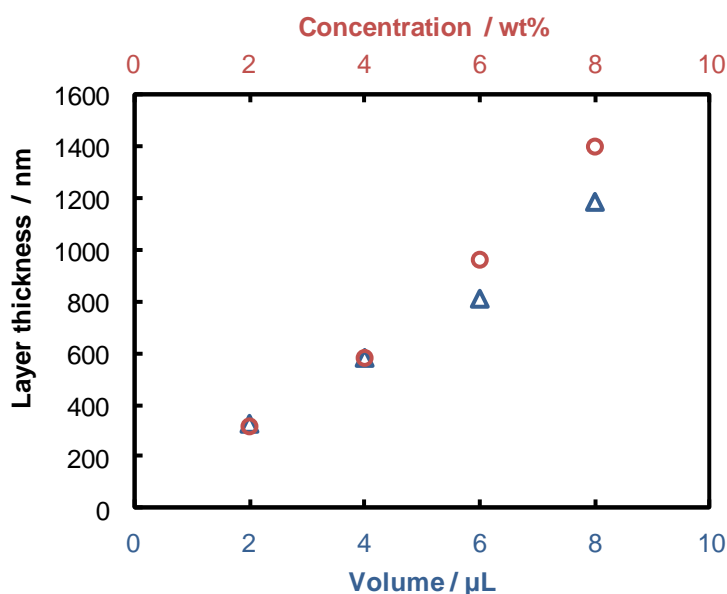
Figure 4-17: LPS layer thickness derived from SEM cross section images deposited by drop casting with various concentrations (AB27-AB30, purple) and volumes (AB28, AB31-AB33, green).

The diagram reveals that the thickness can be tuned precisely in the area of interest by varying the deposition volume and/or the concentration of the coating solution. However, thicker films might require the coating of larger areas to improve the ratio of edge effects to homogeneous middle area.
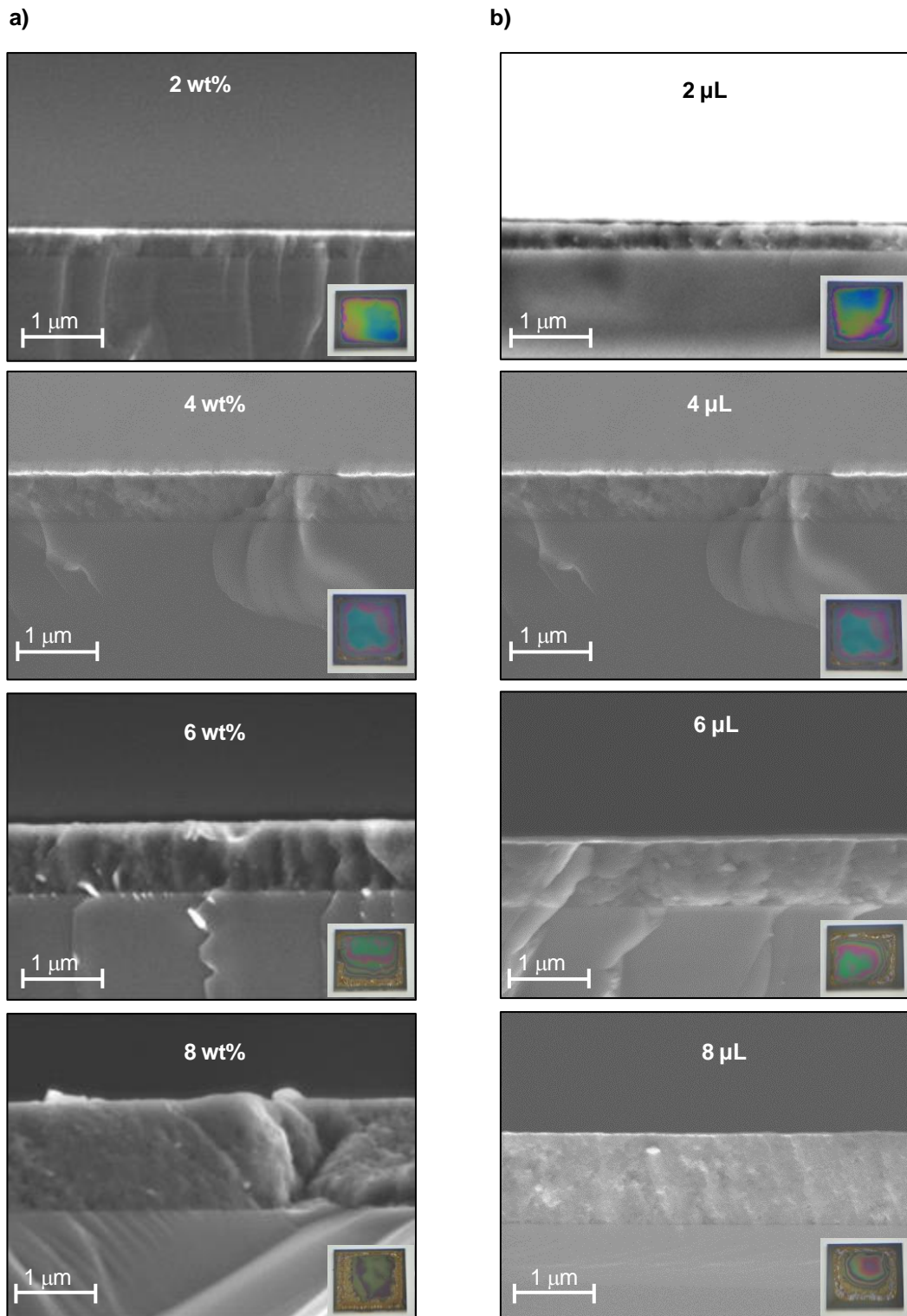
Figure 4-18: a) Cross-section SEM images from LPS thin-films on Si substrate coated with different concentrated coating solution (AB27-AB30). The deposition volume was kept constant (4 µl). b) Cross-section SEM images from LPS thin-films on Si substrate coated with different coating volumes (AB28, AB31-AB33). The concentration was kept constant (4wt%).

4.2.3 Summary

LPS thin-films were prepared by drop casting of [70-30], [75-25] and [80-20] coating solutions on Si substrates. XPS and EDX studies confirmed a high oxygen content in all LPS thin-films and bridging and non-bridging sulphur and oxygen species. The reaction rate for the S-O substitution depends on the precursor stoichiometry with [70-30] being the most reactive among the investigated precursors.

Structural and electrochemical properties of the LPS films also depend on the precursor stoichiometry and age of the coating solution. XRD showed that LPS thin-films prepared from [70-30] solution are amorphous, while LPS thin-films obtained from [80-20] and [75-25] precursors exhibit crystalline structures. The XRD results correlate with the morphology observed in the SEM images as [80-20] and [75-25] thin-films have granular or columnar structures, whereas [70-30] thin-films are dense and homogeneous. Electrochemical analysis showed that crystalline and porous LPS films derived from [75-25] coating solution are short circuited and, therefore, not suitable as solid electrolytes. In contrast, LPS thin-films prepared from [70-30] and [80-20] solution exhibit lithium-ion conductivities in the order of 10^{-5} S cm^{-1}. Among these films, amorphous LPS layers derived from [70-30] dissolved in NMF seems to be the promising candidates for applications as solid electrolyte in SSBs, as these films are homogeneous and crack free and exhibit high ionic and low electronic conductivity values despite their high amount of oxygen. However, ageing of the coating solution leads to morphology and conductivity changes of the LPS thin-films. The influence of several deposition parameters on morphology and lithium-ion conductivity was investigated for LPS thin-films derived from freshly prepared [70-30] precursor solutions. The most promising layers were obtained applying a two stage heating process including deposition at elevated temperatures (80 °C) and predrying at this temperature for 30 min, followed by drying at 250 °C for 60 min. Precise tuning of the film thickness from 0.3 to 2.3 μm was achieved by changing the deposition volume or the concentration of the coating solution.

4.3 LPS THIN-FILM CHARACTERISATION AS SOLID ELECTROLYTE

LPS thin-films should exhibit high lithium-ion conductivities and low electronic conductivities when applied as solid electrolyte in lithium based batteries in order to suppress self-discharge of the battery, while being stable in contact with the electrode materials. Especially, Li anodes are highly reactive with SEs, which leads to the formation of interphases between them. This chapter starts with the detailed electrochemical characterisation of the LPS thin-films. Then, stability of the LPS thin-films against Li metal and cycling behaviour of the LPS thin-films with Li anode will be investigated.

4.3.1 Electrochemical characterisation

The electrochemical properties of the LPS thin-films were further analysed by temperature impedance spectroscopy and DC polarisation. EIS measurements were performed vertically through the LPS thin-film, where the evaporated top Au layer and the Si substrate act as top and bottom electrodes, respectively. Figure 4-19 shows (a) corresponding Nyquist plots obtained at various temperatures with (b) the measurement setup. The Nyquist plots show the onset of a semicircle, which disappears at higher temperatures and transforms into a dominant capacitive straight line. The data were fitted using an equivalent circuit $(R_1 Q_1) Q_2$, that comprises a resistance R_1 parallel to a CPE Q_1 in series with a second CPE Q_2. Table 0-4 in the appendix summarises the fitting results. In this equivalent circuit, $R_1 Q_1$ describes the semicircle and Q_2 the straight line. The semicircle is ascribed to ionic transport across the LPS layer, while the straight line refers to the blocking (capacitive) behaviour of the electrodes. A layer thickness of 0.91 µm (as assumed from SEM cross-section) results in a room temperature (RT) conductivity σ = $3.2 \cdot 10^{-5}$ S cm^{-1} of the thin LPS film. RT conductivity values for the 70Li$_2$S-30P$_2$S$_5$ precursor material were slightly higher with $4 \cdot 10^{-5}$ S cm^{-1} as determined by Dietrich *et al.*[225] The capacitance and dielectric constant of the LPS layer were calculated according to equation 3-6 and 3-6, respectively. At RT the LPS thin-films exhibit a capacitance of 787 pF corresponding to a dielectric constant of 32. Koerver *et. al.*

reported a bulk capacitance of 40 pF for β-Li$_3$PS$_4$ solid electrolyte.[242] Considering the cell constant this capacitance corresponds to a dielectric constant of 64, which is slightly higher but still in the same order of magnitude compared to the value obtained for LPS thin-films. Le Van-Jodin *et. al.* reported a dielectric constant of 20 - 30 for LiPON thin-films, which is even closer the obtained dielectric constant of LPS thin-films.[243]
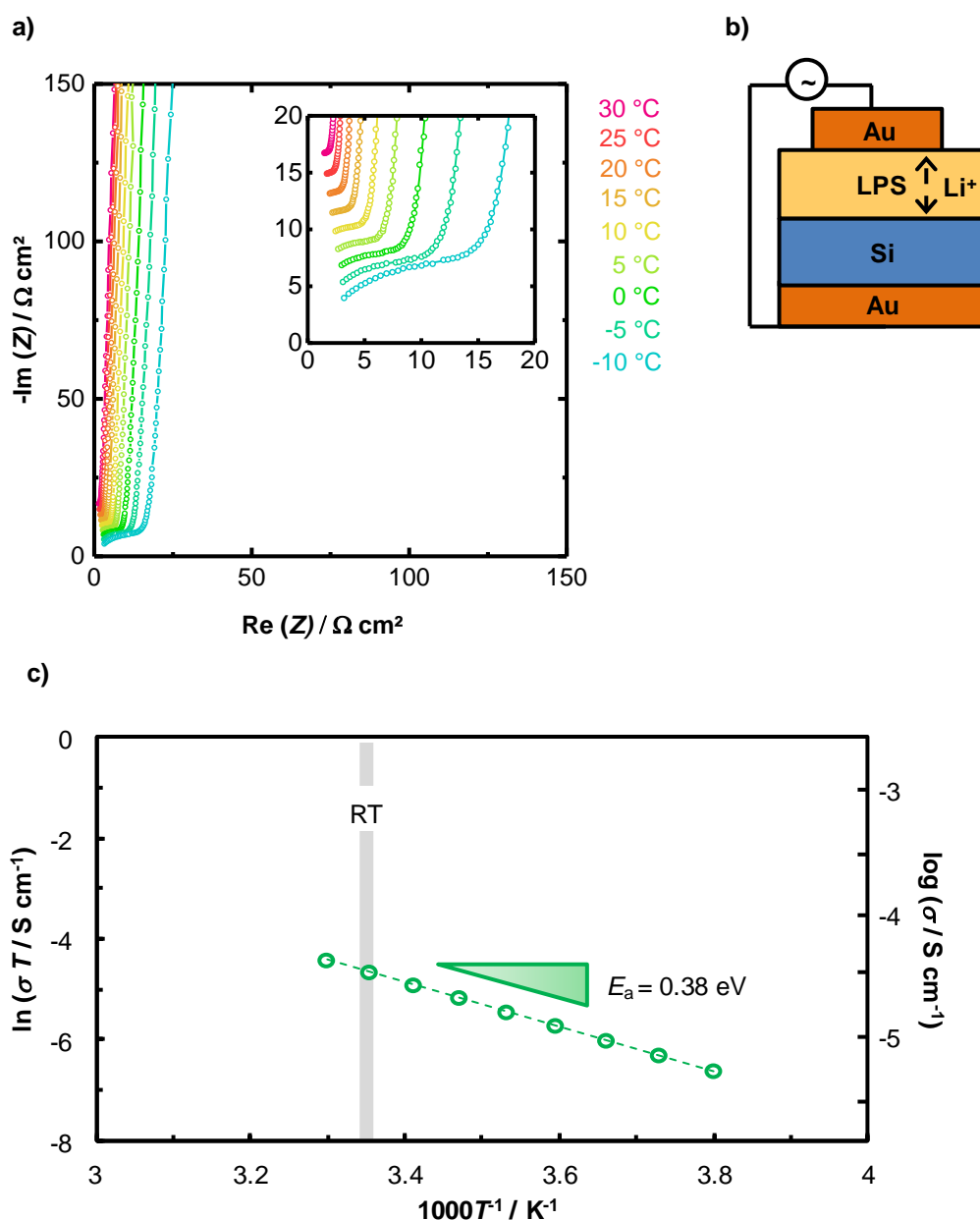
Figure 4-19: a) Nyquist plots of LPS thin-film (AB01 - 0.91 µm) measured vertically at various temperatures; curves offset for clarity by 2 Ω·cm² in y-direction. b) Setup used for this measurement. c) Arrhenius plot of LPS thin-film with the activation energy of the charge transfer calculated from the slope of the linear fit; the dots represent the measured data and the dashed line represents the fit.

Figure 4-19c) depicts the Arrhenius plot of the LPS thin-film. The activation energy of the ionic conductivity was determined from the slope of the linear fit and equals 0.38 eV. The obtained value is slightly lower when compared to the activation energy of 0.43 eV determined for the $70Li_2S-30P_2S_5$ precursor material.[225]

Both the lower activation energy and lithium-ion conductivity might be explained by the S-O exchange in the coating solution leading to a modified layer composition with different electrochemical properties.

The partial electronic conductivity of the LPS thin-films is extracted from DC polarisation measurement using an Au/Si/LPS/Li cell arrangement. A constant potential ranging from 1.9 V to 4.0 V *vs.* Li^+/Li was applied for 15 min leading to the positive polarisation of Si against the Li electrode and the current is measured as a function of time. Figure 4-20a) shows the current response for a potential difference of 2 V, 3 V and 4 V, while Figure 4-20b) the measurement setup scheme and Figure 4-20c) the steady state current, which was reached after 15 min, of each polarisation potential as a function of the applied voltage.

The electronic conductivity σ_{el} ranges from $4.0 \cdot 10^{-12}$ (1.9 V) to $3.3 \cdot 10^{-11}$ S cm^{-1} (4 V) assuming the LPS layer thickness of 1.3 µm, as confirmed by cross-section SEM (Figure 4-25d), and an area of 1.96 mm². With increasing potential difference, LPS thin-films show an increase in the current response and an increase in the electronic conductivity. This current increase could be ascribed to the anodic polarisation of the LPS films leading to an oxidation of the LPS thin-films by the formation of electron holes and lithium vacancies within the LPS volume. The electronic conductivity is the sum of electron conductivity σ_{e^-} and hole conductivity σ_h as shown in equation 4-2:

$$\sigma_{el} = \sigma_{e^-} + \sigma_h. \tag{4-2}$$

Consequently, the formation of holes results in an increased electronic conductivity. Similar results were previously reported for garnet type materials.[105,154]

In the case of LPS thin-films, the partial lithium-ion conductivity can be approximated by the total conductivity obtained from EIS measurements according to equation 3-2, as the electronic conductivity is several orders of magnitude lower than the total conductivity.
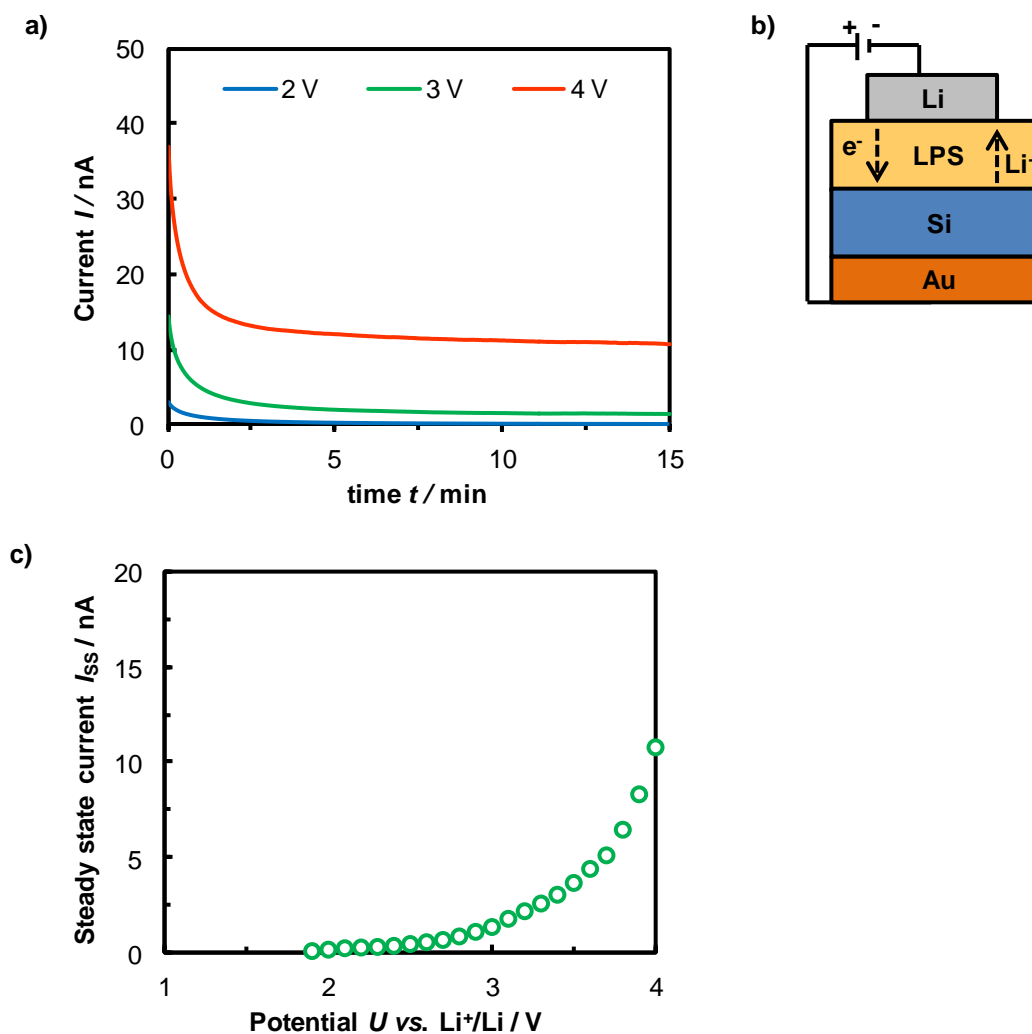
Figure 4-20: DC polarisation measurement using a Si/LPS/Li cell (AB34). a) Current as a function of time for 2 V, 3 V and 4 V *vs.* Li+/Li. b) . Setup used for this measurement. c) Steady state current plotted as a function of applied potential difference.

The measured conductivities correspond to an electronic transference number in the order of 10^{-6} and an lithium-ion transference number of approximately unity, which is favorable for a solid electrolyte.

Finally, the LPS thin-films prepared by CSD exhibit higher lithium-ion conductivities ($\sigma_{Li^+} = 3.2 \cdot 10^{-5}$ S cm^{-1}) than oxide solid electrolyte thin-films, *e.g.* as LiPON ($\sigma_{Li^+} = 2.3 \cdot 10^{-6}$ S cm^{-1}).[79]

4.3.2 Stability against Lithium metal

The stability of LPS thin-films against Li metal is crucial for the application as solid electrolyte in SSBs with Li anode. The different interphases that form upon contact between the SE and Li metal were previously described by Wenzel *et al.*[142] The nature of the interphases can be examined by combination of *in situ* XPS with time resolved EIS. *In situ XPS* provides insight into the chemical identity of the reaction products during interphase formation, while time resolved EIS provides kinetic information about the interphase.

The XPS spectrum of the as-deposited LPS thin-film was recorded first, followed by repeating cycles of Li deposition onto the film surface and XPS analysis. Li was deposited in 3 min sputtering steps up to 60 min of total sputtering time Figure 4-21 shows the recorded spectra of S 2P, P 2P, O 1s and Li 1s signals for the as deposited LPS thin-film and after lithiation. The atomic concentrations of the different recorded elements as a function of Li deposition time are shown in Figure 0-12 in the appendix.
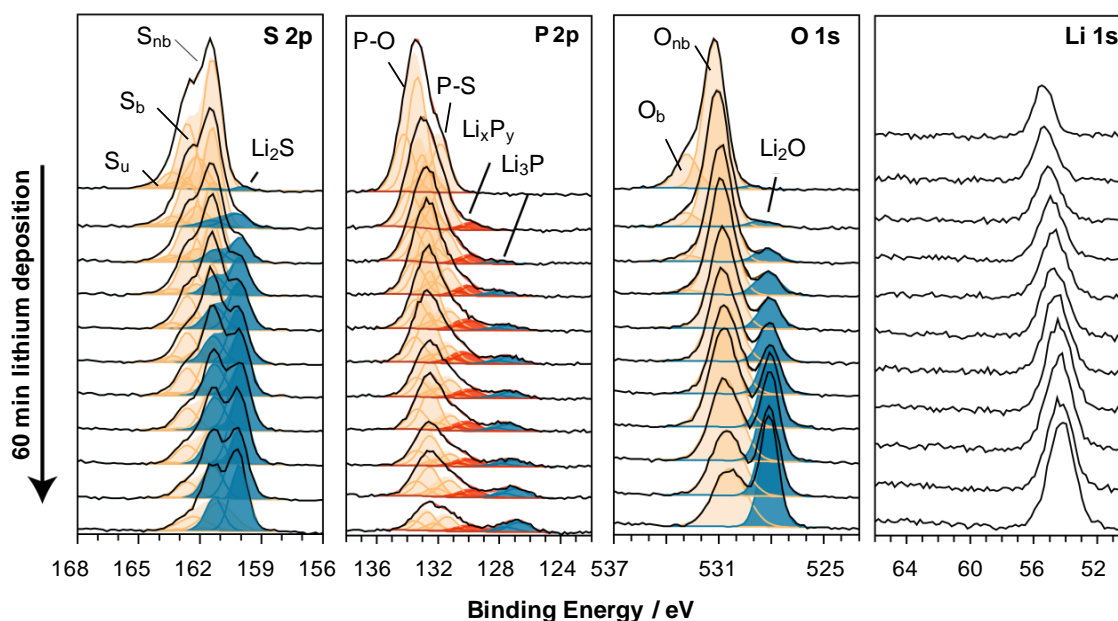
Figure 4-21: Evolution of XPS detail spectra for sulphur (S 2p), phosphorous (P 2p), oxygen (O 1s) and lithium (Li 1s) in the course of subsequent Li deposition. The topmost spectra were obtained from the as-deposited sample.

The S 2p and O 1s peaks were fitted as previously described. Four different species are assumed for the peak fit of the S 2p emission line: S_{nb} at 161.4 eV, S_b at 162.1 eV, S_u at 163.0 eV and Li_2S at 160.1 eV. The given values correspond to the respective S $2p_{3/2}$ component. The O 1s peak consists of signals from O_{nb} at 531.2 eV, O_b at 532.8 eV and Li_2O at 528.2 eV. Figure 4-22a) and b) show the atomic concentrations of the different recorded oxygen and sulphur species, respectively, as a function of Li deposition time.
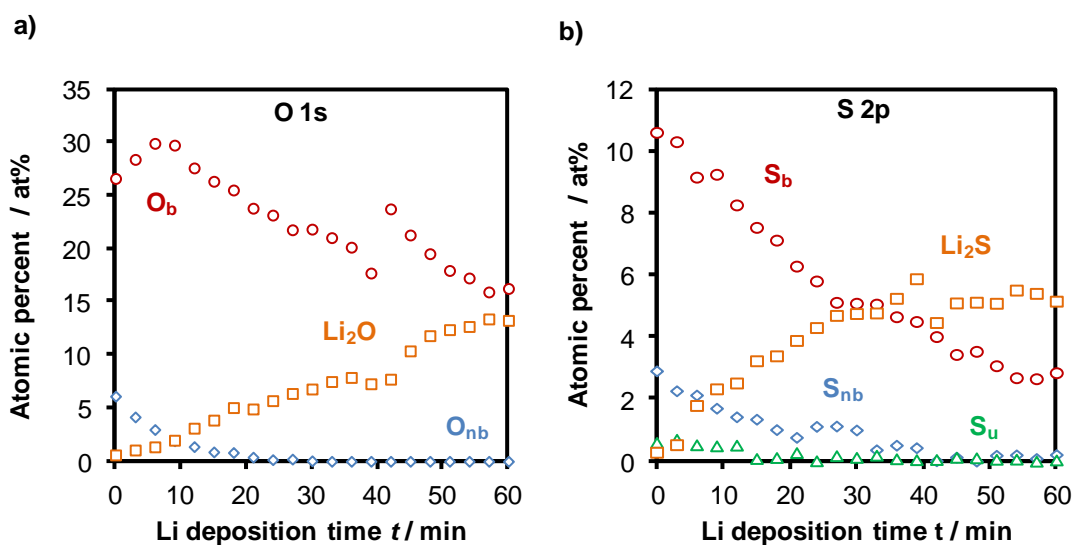
Figure 4-22: Atomic concentration of the different recorded a) oxygen and b) sulphur species in the LPS thin-film (AB35) determined by XPS analysis in the course of Li deposition.

The O_b/O_{nb} ratio decreases upon lithiation; after 60 min of Li deposition no O_b can be detected. Similar behaviour was observed for LiPON thin-films during Li deposition.[139] The signal of Li_2O constantly increases in the course of Li deposition. A fraction of Li_2O is most likely related to the reaction of freshly deposited Li with unavoidable traces of oxygen in the UHV analysis chamber (frequently observed in this type of experiment).[142] Consequently, a thin Li_2O film is always present on lithium metal, which may also obscure the end of interphase formation. Nonetheless, most Li_2O will be formed in an interphase between LPS and Li due to the reaction of O_b and Li. In the case of LiPON thin-films an exemplary reaction is described by the reaction of *pyro*-phosphate $Li_4P_2O_7$ with Li to *ortho*-phosphate Li_3PO_4, Li_3P and Li_2O.[139]

The concentration of Li_2S also grows in the course of Li deposition but saturates after about 30 min. The increase of the Li_2S signal is ascribed to the reaction of S_{nb}, S_b and S_u with Li and the formation of an interphase between LPS and Li. In the case of crystalline $Li_7P_3S_{11}$ the complete reaction with Li leads to the formation of Li_3P and Li_2S.[146]

So both LiPON and $Li_7P_3S_{11}$ react with Li metal and form interphases between the SE and Li. Similar degradation reactions are expected in LPS thin-films. However, LPS thin-films consist of mixed thio-oxy-phosphates with various combinations of O_b, O_{nb}, S_b and S_{nb}, as previously revealed by *in situ* NMR measurements. Species containing S as well as O like *ortho*-dithiophosphate $Li_3PS_2O_2$ were found in the coating solution and are probably present in the LPS thin-film as well.

The P 2p signal of the pristine sample could be fitted by two species at 133.3 eV and at 131.8 eV. As the relative intensities of these lines ((P-S)/(P-O) ≈ 0.44) match with S/O elemental ratio (S/O ≈ 0.43), they are assigned to P-O and P-S bonds, respectively. Upon lithiation a shoulder on the low binding energy side of the signal evolves. This new line at approximately 129.9 eV might be attributed to Li_xP_y polyphosphide species.[146] Moreover, a signal at 127.2 eV with increasing intensity upon lithiation is ascribed to the formation of Li_3P.[244]

The Li 1s signal grows in the course of Li deposition, as anticipated. No detailed fit analysis was performed due to the weak nature of the Li 1s signal. The signal comprises Li signals from the LPS layer, the interphase compounds and probably a Li metal layer on top of LPS and the interphase layer. However, no clear evidence for Li metal such as plasmon loss features, which should occur at about 63 eV, was found. The missing plasmon loss features could possibly be related to the thin Li_2O layer on top of the deposited Li metal, which delays their appearance.

The depth profiling of the pristine sample shows small amounts of N incorporated in the bulk and on the surface of the thin-film. The N signal shifts towards low binding energies during the first Li deposition steps and then quickly disappears upon further lithiation. Although reliable peak fit analysis was not possible due to too weak N signals (low nitrogen content), the collected data hints the formation of Li_3N traces.

XPS analysis reveals, in sum, the interphase formation between Li metal and LPS solid electrolyte thin-films. Upon contact with Li metal, P-S, P-S-P and P-O-P bonds in the LPS layer are not stable and the thio-oxyphosphates are reduced. The resulting interphase consists of Li_2S, Li_2O, Li_3P, Li_xP_y, and traces of Li_3N and

Li_3PO_4 could possibly also be present in the interphase as the reaction of Li_3PO_4 with Li to Li_2O and Li_3P is kinetically hindered.[245] Figure 4-23 visualises the results of the *in situ* XPS analysis including Li_3PO_4 even though its formation cannot be confirmed unequivocally.
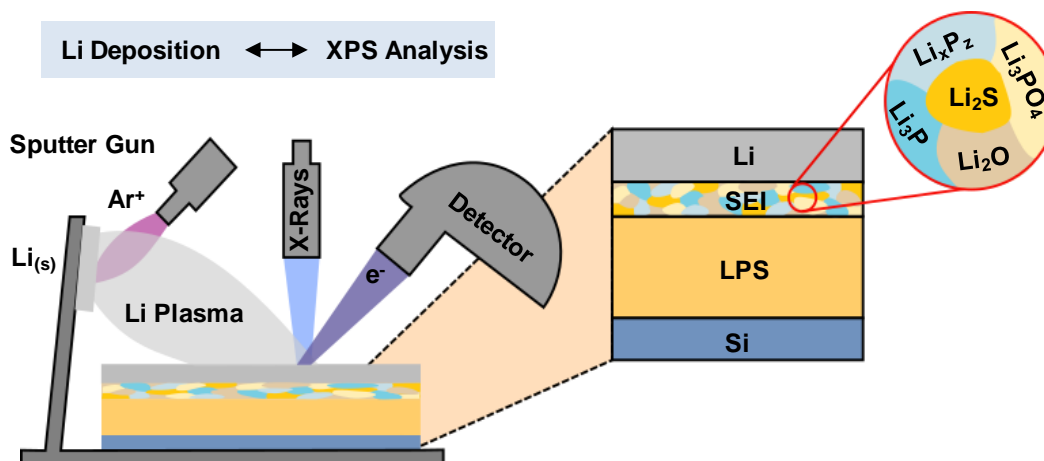
Figure 4-23: Interphase formation between Li and LPS thin-film as revealed by in situ XPS measurements.

Regarding the type of interphase/ interface which is formed between Li and LPS thin-films a thermodynamically stable interface without any reaction can be excluded. Therefore either a MCI or SEI is formed between Li and LPS thin-films. Depth profiling was performed by ion sputtering and XPS analysis after the *in situ* XPS measurement was completed. Figure 4-24 displays the atomic ratios of the recorded elements as a function of sputtering time. In the first few minutes of ion sputtering the Li 1s peak intensity decreases, whereas the S 2p, P 2p and O 1s signals increase until they reach a constant level. The Li and N fractions should be handled with caution, as the signals were too small for reliable fit analysis. The depth profiling results suggests that the surface layer consisting of sputtered Li and the interphase is successfully removed by ion sputtering.

Afterwards the XPS depth profile shows the homogeneous composition of the solid electrolyte as the signal shape as well as the S/P, S/O and O/P ratios are comparable with the depth profiling values of a LPS film without exposure to Li metal as shown in Table 0-6 in the appendix.
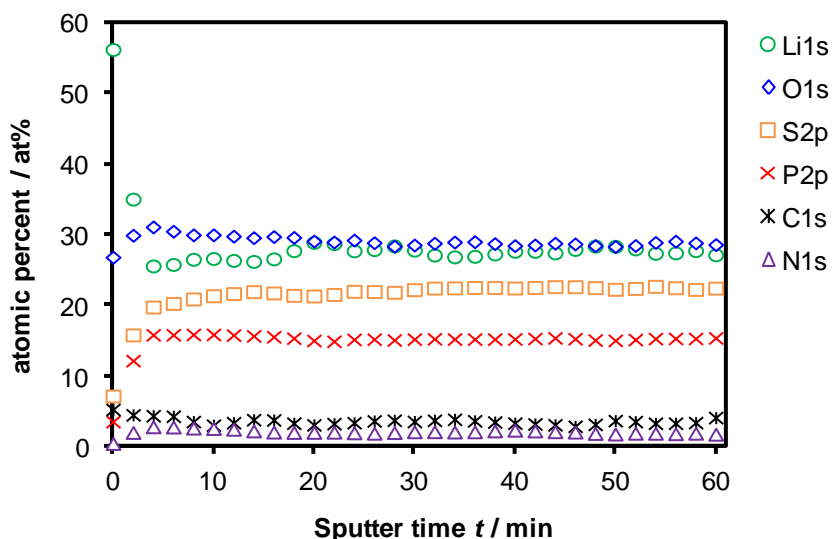
Figure 4-24: Depth profile of LPS thin-film (AB35) with interlayer formed upon contact with Li metal (after *in situ* XPS analysis).

Time-dependant EIS measurements were performed to gain more information about the kinetic behaviour of the LPS/Li interphase, which depends on the conductivity of degradation products formed upon LPS contact with Li. In the case of a MCI the impedance will gradually decrease related to the reduction of the SE by Li and the formation of species with high electronic conductivity. A MCI could grow through the whole solid electrolyte leading short circuiting of the cell. On the contrary, the impedance of a SEI saturates after a certain time due to a very low ionic or electronic conductivity of the degradation products in the SEI. Depending on the conductivity of the formed degradation products the impedance can either increase or decrease slightly before reaching saturation level.

EIS was measured in 1 h increments up to a total time of 60 h using Li contacts evaporated on top of LPS thin-films on Si substrates. Figure 4-25a) and b) display characteristic Nyquist plots and the measurement setup, respectively, which show the onset of a semicircle at high frequencies and a subsequent straight line.
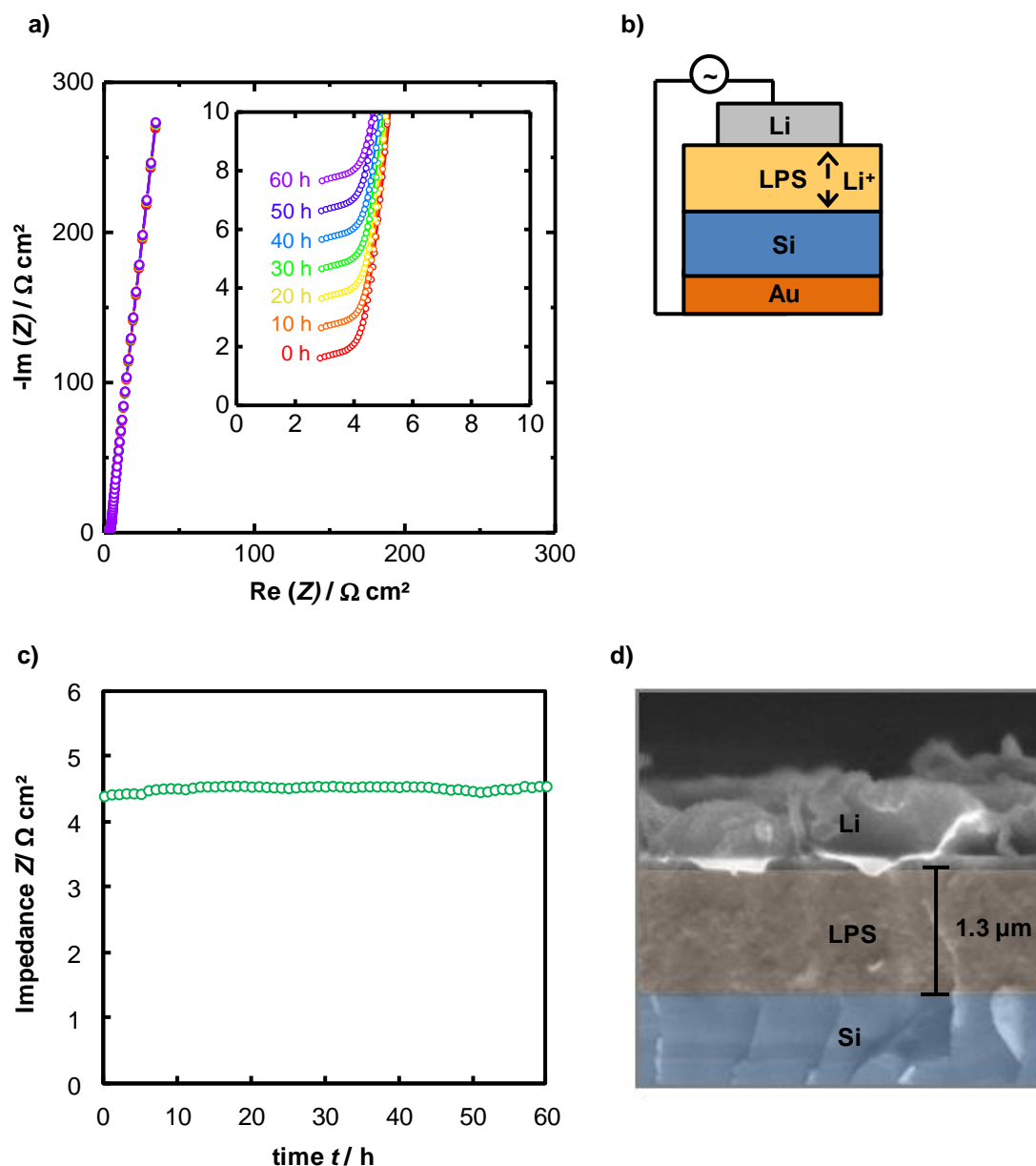
Figure 4-25: Time-dependent EIS: a) Nyquist plots of 1.3 µm thick LPS film (AB34) with evaporated Li contacts recorded for 60 h with 1 h increments. Curves in the inlet diagram are offset by 1 $\Omega \cdot cm^2$ in y-direction for clarity. b) Schematic representation of the measurement setup. c) Impedance values as a function of time of the studied LPS thin-film (AB34). d) Cross-section SEM image after time-dependant EIS measurements.

Generally, two semicircles are expected in the Nyquist plot, one representing the interphase and the other the LPS layer. The acquired data points in the high frequency region were, however, insufficient for a clear distinction of interphase and LPS resistances due to the limitations of the measurement device. The data were fitted using the same equivalent circuit model $((R_1Q_1)Q_2)$ that was described above for the Si/LPS/Au system. In this case, the semicircle is ascribed to the sum of resistances from the interphase and LPS layer and the straight line to the blocking behaviour of the electrodes. Even though Li should ideally behave as a non-blocking electrode, this behaviour would only be visible at lower frequencies. The fitting results are summarised in Table 0-5 in the appendix.

Figure 4-25c) shows the area resistance of a LPS film assuming a contact area of 1.96 mm² as a function of time and the measurement setup. The area resistance ranges from 4.4 Ω cm^2 directly after Li evaporation to 4.5 Ω cm^2 after 13 h. This minor impedance variation is ascribed to the slight temperature variation of around 1 °C, which is revealed during overnight measurements. The averaged area resistance measured with Li contacts (4.5 Ω cm^2 at 26 °C) is 60% higher than the area resistance measured with Au blocking electrodes (2.8 Ω cm^2 at 25 °C). However, an increase in the LPS film thickness of 43% was determined for the setup with lithium contacts (1.3 µm and 0.91 µm). The area resistance measured with Li contacts still remains roughly 10% higher than the area resistance measured with Au blocking electrodes considering same layer thicknesses. This higher area resistance could be related to the formation of an interphase during the Li evaporation process between Li and LPS thin-films with lower conductivity, which is in good agreement with the outcome of the previously discussed XPS study.

Capacitances and dielectric constants of the LPS layer were calculated according to equation 3-6 and 3-6, respectively. LPS thin-films in contact with Li metal exhibit an averaged capacitance of 360 pF corresponding to a dielectric constant of 27, which is comparable to the previous results with Au electrodes with 32.

Figure 4-25d) displays a SEM cross-section image of the LPS film after completed EIS measurement. The analysis did not visualise the interphase between LPS film and Li contact, but reveal similarities in the morphology of the LPS thin-films in the Si/LPS/Li and in the Si/LPS/Au cells.

The XPS and EIS results strongly support the formation of a thin, virtually non-growing solid electrolyte interphase (SEI) between Li and LPS thin-films. Despite presence of the SEI, the LPS thin-film exhibits a mean conductivity σ of

$2.9 \cdot 10^{-5}$ S cm^{-1} assuming a layer thickness of 1.3 µm, which is still one order of magnitude higher than $2.3 \cdot 10^{-6}$ S cm^{-1} measured for LiPON thin-films.[79] SEI formation in contact with Li was also reported for LiPON thin-films by XPS analysis and impedance measurements.[139,246] SEI formation in contact with Li was already reported for crystalline Li$_7$P$_3$S$_{11}$ bulk material.[146] However, a stronger influence of the SEI on the total resistance was observed. The different behaviour of amorphous LPS thin-films and Li$_7$P$_3$S$_{11}$ bulk material may originate from composition differences. LPS thin-films derived from [70-30] dissolved in NMF contain a large fraction of O, which leads to a different composition of the SEI and might increase the stability of the LPS thin-film against Li. The improved electrochemical stability of lithium thiophosphate glasses by substitution of some amounts of S by O was previously reported in the literature.[247,248] LiCoO$_2$/Li cells using Li$_2$S-Li$_2$O-P$_2$S$_5$ solid electrolytes showed a higher reversible capacity and better cycle stability with increasing Li$_2$O content even though the conductivity of the electrolytes decreases with increasing Li$_2$O content.[248] The high O fraction in the LPS thin-films explains the excellent stability against Li metal and the slightly reduced lithium-ion conductivity of the LPS thin-films compared to the precursor. The observed electrochemical properties of LPS thin-films appear ideal for their application as a lithium-ion conducting separator or membrane for Li anodes.

4.3.3 Analysis of cycling behaviour of a Si/LPS/Li half cell

The behaviour of LPS thin-films upon cycling is investigated using a Si/LPS/Li half-cell (the same setup was analysed in the previous studies by EIS, SEM and XPS). The potential window of LPS thin-films against Li was determined by cyclic voltammetry (CV) between 0 and 4 V *vs*. Li$^+$/Li. The CV shown Figure 4-26 exhibits no significant current peaks in the range from 1 to 4 V *vs*. Li$^+$/Li. The peaks observed in the 0 to 1 V range *vs*. Li$^+$/Li can be ascribed to the formation and dissolution of different intermetallic phases α-Li$_x$Si. Zamfir *et al.* discussed in detail various alloys in lithiated Si.[249] The observed peak positions are summarised in Table 0-7 in the appendix.
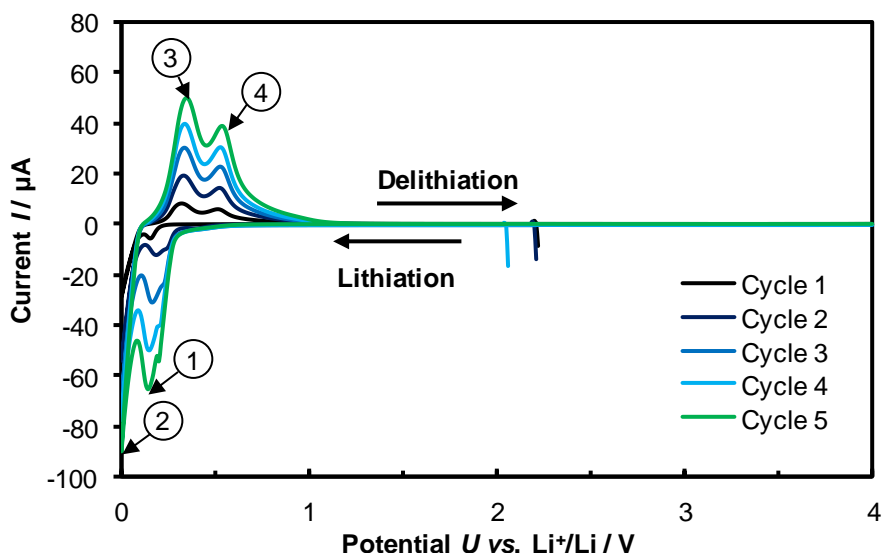
Figure 4-26: Cyclic voltammetry (CV) curves of a Si/LPS/Li (AB36) system recorded between 0 and 4 V *vs*. Li$^+$/Li with a scan rate of 1 mV s^{-1}.

The shape of the CV resembles curves recorded for crystalline Si (*c*-Si) nanowires mounted in half-cell geometry with liquid electrolyte and Li counter electrode, whereas the peak positions in the Si/LPS/Li system slightly differ from the positions observed for *c*-Si nanowires.[34,249] This difference could be ascribed to the doping of the Si substrate (100, p-doped) used in this study, as it is known that p-doping shifts the start of the lithiation to higher voltages.[250]

Cycling experiments also reveal a small peak shift, which was previously observed for the Si nanowires.[34] During first lithiation, Peak 1 does not follow this trend, which

indicates that different processes, *e.g.* SEI formation between Si and LPS, might be involved upon initial lithiation. Sang *et al.* previously reported the interphase formation consisting of $Li_4P_2S_6$ and Li_2S from β-Li_3PS_4 at an Au/ β-Li_3PS_4 interface during discharge, which is not completely reversible upon charge.[251] It is possible that a similar process is involved during cycling of LPS thin-films creating a SEI between Si and LPS.

Figure 4-27 shows the suggested steps involved during lithiation and delithiation of the Si/LPS/Si cell.
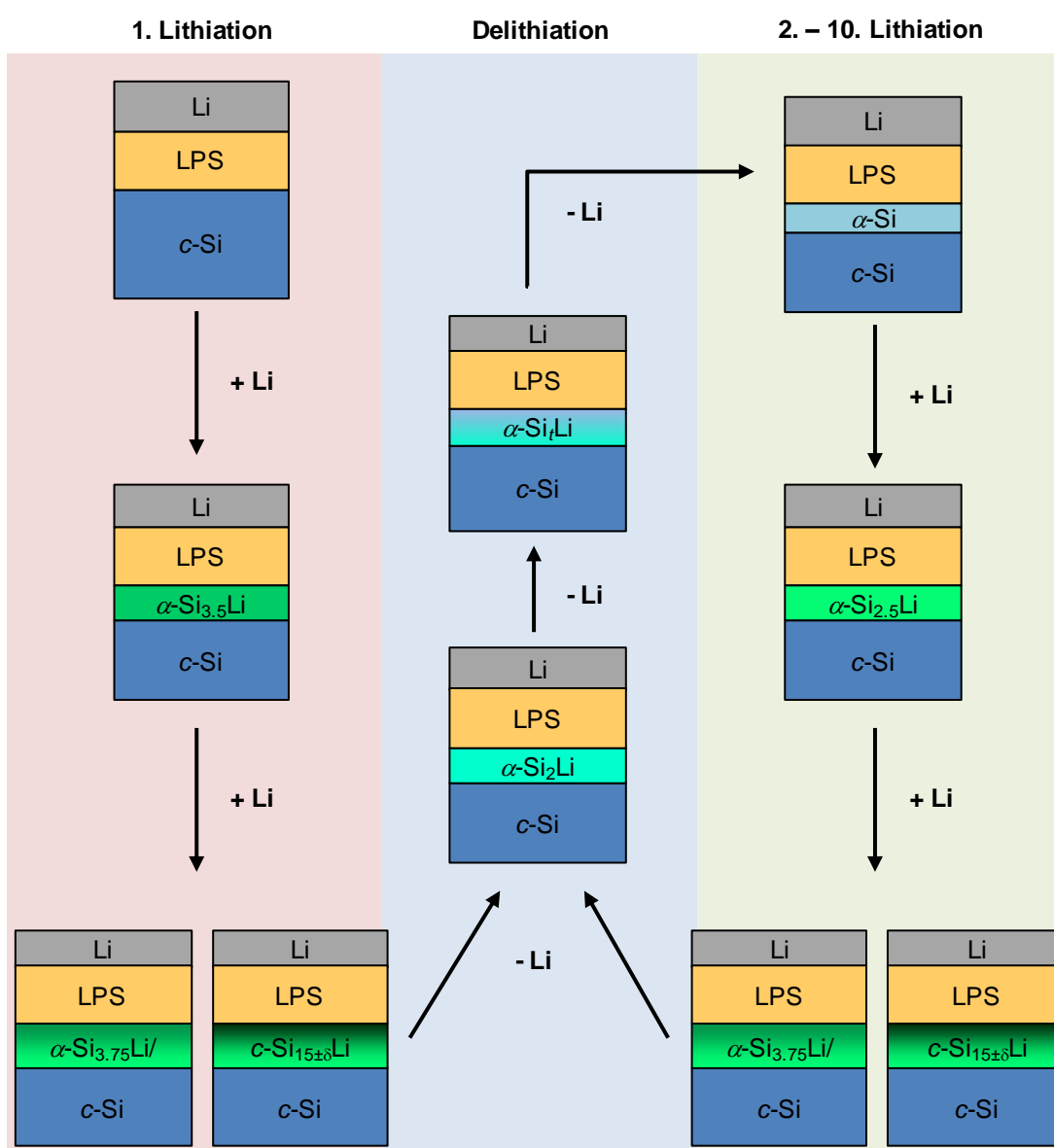
Figure 4-27: Li-Si alloys involved during lithiation (+Li) and delithiation (-Li) of Si in the Li/LPS/Si cell.

With further potential reduction the lithiation of c-Si starts with the partial lithiation of c-Si to α-Li$_{3.5}$Si (Peak 2).[252] This transformation occurs by a two phase mechanism with a sharp interface between the two amorphous phases.[253] α-Li$_{3.5}$Si can be further lithiated to α-Li$_{3.75}$Si,[252] which can crystallise suddenly at voltages of around 50 mV into the metastable phase c-Li$_{15\pm\delta}$Si$_4$.[249]

Upon delithiation α-Li$_{3.75}$Si or Li$_{15\pm\delta}$Si$_4$ reacts to α-Li$_2$Si (Peak 3), which is gradually delithiated (α-Li$_t$Si with 2>t>0) to α-Si (Peak 4).[252]

In the second and subsequent lithiations α-Si instead of c-Si is lithiated, which involves the formation of different Li-Si alloys. This explains the changed shape of the cyclic voltammogram between the first and subsequent lithiation (Peak 1 and 2). The lithiation of α-Si starts with the formation of α-Li$_{2.5}$Si by a two phase mechanism with a very sharp interface between the two different amorphous phases. After all α-Si is consumed, α-Li$_{2.5}$Si is further lithiated to α-Li$_{3.75}$Si without a visible interface.[254] Crystallisation of Li$_{15\pm\delta}$Si$_4$ might suddenly occur at lower voltages. During CV measurements the capacity increases with each cycle suggesting only partial conversion of c-Si to α-Si and resulting in lithiation of more c-Si during each cycle.[42] Similar behaviour was previously observed for c-Si nanowires, c-Si powder and microstructured c-Si anodes.[34,255,256] Clearly, the CV measurements demonstrate the stability of a Si/LPS/Li half-cell from 0 to 4 V $vs.$ Li$^+$/Li up to 5 cycles.

In addition to the CV measurements, galvanostatic cycling (cycling charge-discharge, CCD) with 10 cycles was carried out between 0 and 4 V $vs.$ Li$^+$/Li. A constant current density of 100 µA cm^{-2} was applied to the cell (assuming an effective contact area of 1.96 mm²). Each half cycle was limited to 20 min, which corresponds to 160 nm cycled Li, to ensure that not all Li is inserted into the Si wafer leading to the complete consumption of the Li electrode. Similar to CV measurements, CCD tests relate mainly to the electrode performance. Therefore, EIS measurements were performed after each charge at 4 V to investigate the LPS layer during cycling. Figure 4-28a), b), c) and d) show the recorded CCD curves, the measurement setup, the corresponding Nyquist plots and the area resistance of the LPS film assuming a contact area of 1.96 mm², respectively.

The recorded voltage profile is consistent with previous Si studies. The initial discharge exhibits a long plateau, which corresponds to the reaction of c-Si with Li forming amorphous α-Li$_{3.5}$Si.[253] The crystallisation of c-Li$_{15\pm\delta}$Si$_4$ from α-Li$_{3.5}$Si is not expected during CCD as the voltage never drops below 100 mV. After the first

discharge no more lithiation of c-Si takes place. Therefore, the subsequent discharge curves exhibit a slope instead of a plateau in the voltage profile, which is characteristic for the lithiation of α-Si to α-Li$_{2.5}$Si which it is further lithiated to α-Li$_{3.75}$Si.[254]
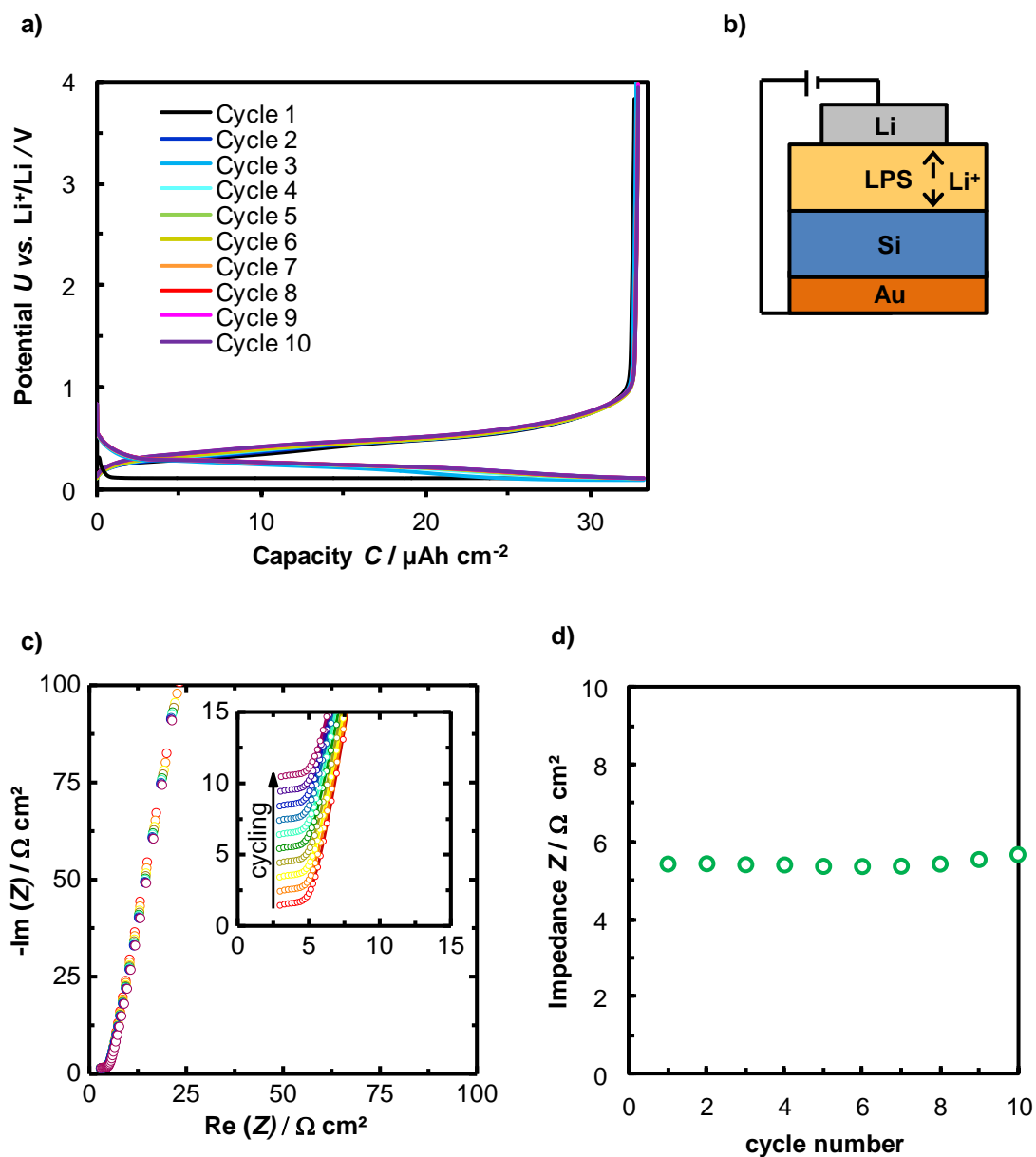
Figure 4-28: a) Galvanostatic cycling (cycling charge-discharge, CCD) of a Si/LPS/Li half cell (AB36) with a current density of 100 µA cm^{-2} and a duration of 20 min. A schematic representation of measurement setup used for the measurement is shown as inlet. b) Nyquist plots of LPS film (1.3 µm) with evaporated Li contacts recorded after each charge (of galvanostatic cycling) at 4 V $vs.$ Li$^+$/Li; curves offset for clarity 1 Ω cm^2 in y direction. c) Impedance values obtained from EIS measurements.

Figure 4-29 shows the SEM analysis of (a) the LPS film deposited on a Si substrate and (b) the Si/LPS/Li half-cell after 20 min long galvanostatic discharge with a current density of 100 µA cm⁻². The SEM pictures reveal the formation of a 200 nm thick interphase between c-Si and LPS, which probably consisted of α-Li$_x$Si with x = 2.5 – 3.75 after lithiation of the Si substrate.
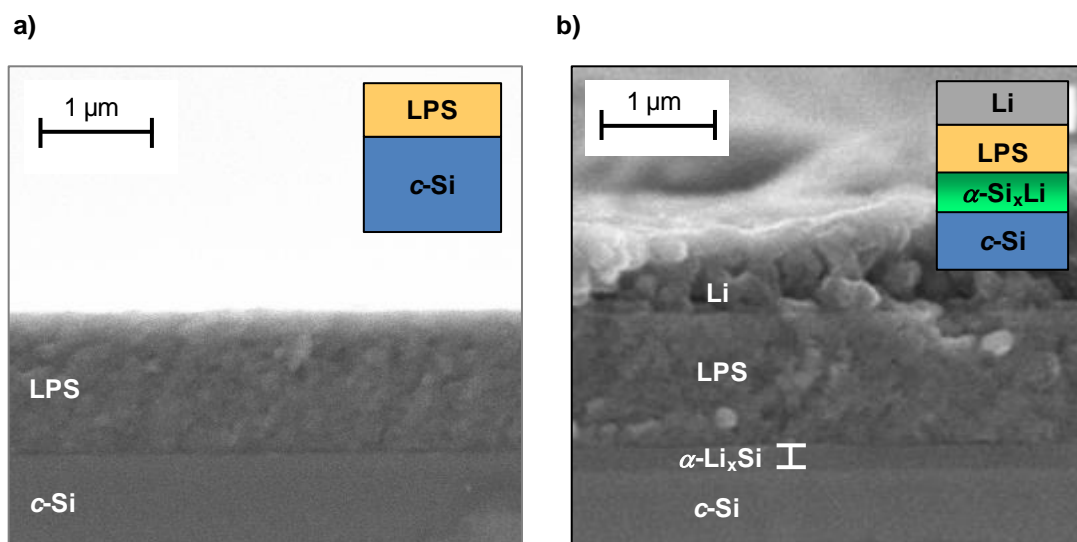
Figure 4-29: Cross-section SEM image of a Li/LPS/Si cell (AB36) before (a) and after (b) galvanostatic cycling (10 cycles) for 20 min with a current density of 100 µA cm⁻². It should be noted that Li contacts already darkened upon storage possibly related to Li reaction with traces of N left in the glovebox to Li$_3$N.

The shape of the charge curve does not change during galvanostatic cycling: a slope is observed up to 1 V followed by a sudden potential increase up to 4 V indicating the completed discharge of the lithiated Si. As previously described α-Li$_{3.75}$Si is gradually delithiated to α-Si during discharge.[252] Galvanostatic cycling with a current density of 100 µA cm⁻² reveals no capacity fading up to 10 cycles, which is unexpectedly stable for cycling of a c-Si wafer. However, it is known that the cycle life can be improved by avoiding the crystallisation of Li$_{15\pm\delta}$Si$_4$.[255] Therefore, the stable behaviour could be correlated to the limitation of the cycling above 100 mV so that no phase transformation to crystalline Li$_{15\pm\delta}$Si$_4$ occurs.

The EIS measurements resemble the data obtained for time-dependant EIS of the Si/LPS/Li system without cycling. Acquired data were fitted using the same $(R_1Q_1)Q_2$ equivalent circuit where R_1Q_1 describes the behaviour of the LPS layer and Q_2 the blocking behaviour of the electrodes. The non-blocking behaviour of Li and Si

electrodes would only be visible at lower frequencies. Table 0-8 shown in the appendix summarises the obtained fitting results. Capacitances and dielectric constants of the LPS layer were calculated according to equation 3-6 and 3-6, respectively. LPS thin-films in contact with Li metal exhibit an averaged capacitance of 364 pF corresponding to a dielectric constant of 27 F m^{-1}, which is the same value that was obtained previously without cycling.

The area resistance ranges from 5.3 Ω cm^2 after 6 cycles to 5.6 Ω cm^2 after 10 cycles. Although still in the range of the fitting error, the variations of 5.4% can also be well explained by small temperature changes during the more than 6 h long measurement, as previously discussed. The averaged area resistance obtained during cycling is roughly 20% higher (5.4 Ω cm^2 at 29 °C) compared to uncycled LPS thin-films (4.5 Ω cm^2 at 26 °C). This strongly supports the hypothesis of additional SEI formation between Si and LPS thin-films during cycling characterised by a lower lithium-ion conductivity. The SEI formation is consistent with theoretical studies from Zhu *et al.* who determined a very narrow thermodynamic stability window of 1.71-2.31 V for Li$_3$PS$_4$.[58]

The lithium-ion conductivity of the LPS thin-film appears, however, to be stable during cycling. This demonstrates the excellent cyclability of the amorphous LPS solid electrolyte and the flexibility of the thin-film, which apparently deals well with the volume changes of the silicon substrate of around 280% upon its (de)lithiation.[254]

4.3.4 Summary

LPS thin-films prepared by drop casting from [70-30] solution exhibit a lithium-ion conductivity of $3.2 \cdot 10^{-5}$ S cm^{-1}, an activation energy of 0.38 eV and an electronic conductivity of $4.0 \cdot 10^{-12} - 3.3 \cdot 10^{-11}$ S cm^{-1}.

For applications in SSBs with Li anode, the stability against Li metal is crucial and was therefore analysed in depth. *In situ* XPS analysis revealed the formation of a stable SEI between lithium metal and LPS solid electrolyte layers (within the time of the experiment). Time-dependent impedance spectroscopy showed long-term stability of LPS films in contact with lithium metal and only a slight increase in the area resistance, indicating the protecting function of the SEI.

The excellent electrochemical properties of amorphous LPS layers were demonstrated by successful lithium cycling (cyclic voltammetry and galvanostatic charge and discharge) in a Si/LPS/Li half-cell.

4.4 APPLICATIONS OF LPS
SOLID ELECTROLYTE THIN-FILMS

In this chapter possible applications of LPS thin-films are discussed. In the first part the integration of the LPS thin-film electrolyte in a microbattery is shown.

The application of LPS thin-films in bulk type SSBs with Li anode might be achieved in different ways: (i) by direct coating of composite cathodes or (ii) by coating of bulk tye SEs, which show high lithium-ion conductivity but are unstable against Li metal. Direct coating of the Li anode is not possible as the temperatures during LPS film formation exceed the melting temperature of Li metal.

In (i) the LPS thin-films would act as separator and no additional bulk SE has to be integrated in the SSB. The high surface roughness and porosity of the composite cathodes might be challenging and could require thicker LPS layers than in a microbattery.

In (ii) the LPS layers act as protective coating to prevent the decomposition of bulk type SEs in contact with Li metal or to suppress dendrite formation and to improve the cycling stability of the SSB.

The setups of the different applications of LPS thin-films, which were analysed in this thesis, are shown in Figure 4-30.

a) SE in a Microbattery   **b) SE in a SSBs**   **c) Protective Coating**
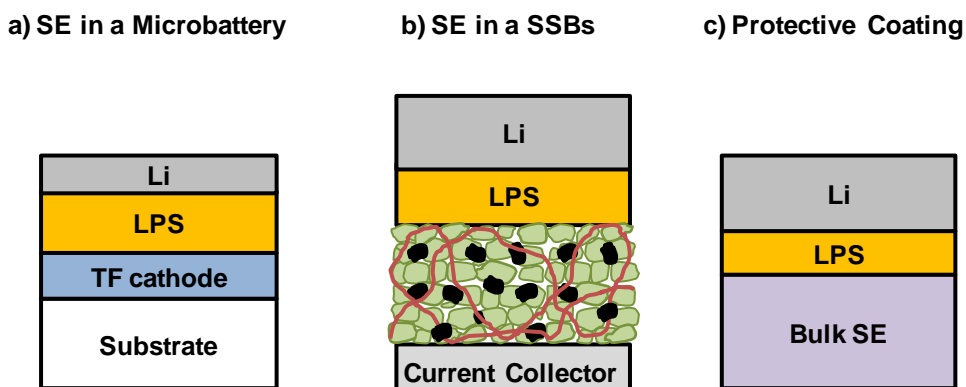
Figure 4-30: Setups for different applications of LPS thin-films: Integration of LPS layers (a) as solid electrolyte in a microbattery, (b) as solid electrolyte in a bulk type SSB with composite cathode and (c) as protective coating on bulk solid electrolytes.

4.4.1 Integration of LPS solid electrolyte in a microbattery

A solid-state microbattery that uses Li metal as anode material, LPS as solid electrolyte, and lithium titanate (LTO) as cathode was developed. Even though LTO is normally considered as anode due to its low redox potential of 1.55 V *vs.* Li+/Li [257] it is employed as cathode in this thesis as LTO undergoes negligible volume changes during lithiation and delithiation and is therefore referred to as a zero-strain material,[258] which shows excellent cycling stability.[35] In addition, a chemical solution deposition process for preparation of LTO thin-films by a sol-gel route was already developed.[259] The steps involved in the formation of the microbattery are shown in Figure 4-31.
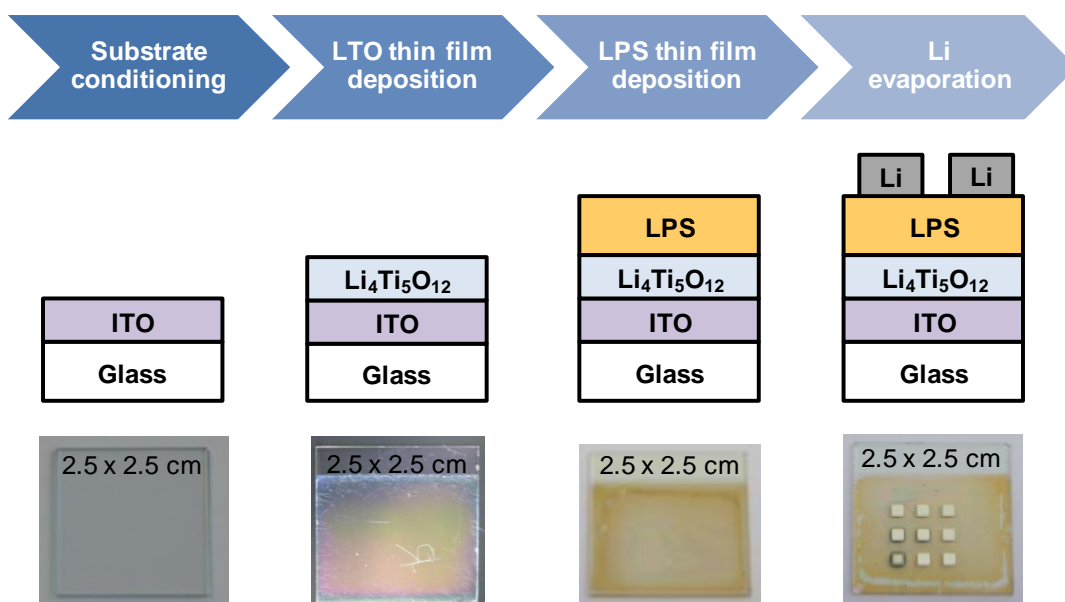
Figure 4-31: Steps involved in TF-SSB preparation starting with substrate conditioning, LTO deposition via CSD followed by LPS deposition via CSD and evaporation of Li contacts.

A quartz glass covered with a transparent conducting ITO (In_2O_3 doped with Sn) thin-film was chosen as substrate. The electronically conductive ITO should act as current collector, while quartz glass was required for LTO crystallisation due to its excellent thermal stability at higher temperatures. The assembly of the LTO/LPS/Li cell started with the deposition of the LTO electrode on the ITO substrate by inkjet printing, followed by CSD of a LPS thin-film, and evaporation of Li top contacts.

Figure 4-32 shows a schematic picture of this microbattery and the processes therein. Upon discharge lithium ions move through the LPS solid electrolyte thin-film from the Li electrode towards the LTO electrode leaving behind a Li vacancy and an electron. At the LTO electrode lithium ions are reversibly intercalated at a potential of approximately 1.55 V *vs.* Li+/Li. During (dis)charge the lithium content in the LTO can be varied between 4<x<7 resulting in a maximum theoretical gravimetric capacity of 175 mAh g^{-1}. This reaction leads to a topotactic transformation of spinel type $Li_4Ti_5O_{12}$ to rock-salt type $Li_7Ti_5O_{12}$.[260] Upon charge the direction of all processes is reversed. A scheme of this phase transformation was published by Haetge *et al.*[260]

Thin Film Solid State Battery
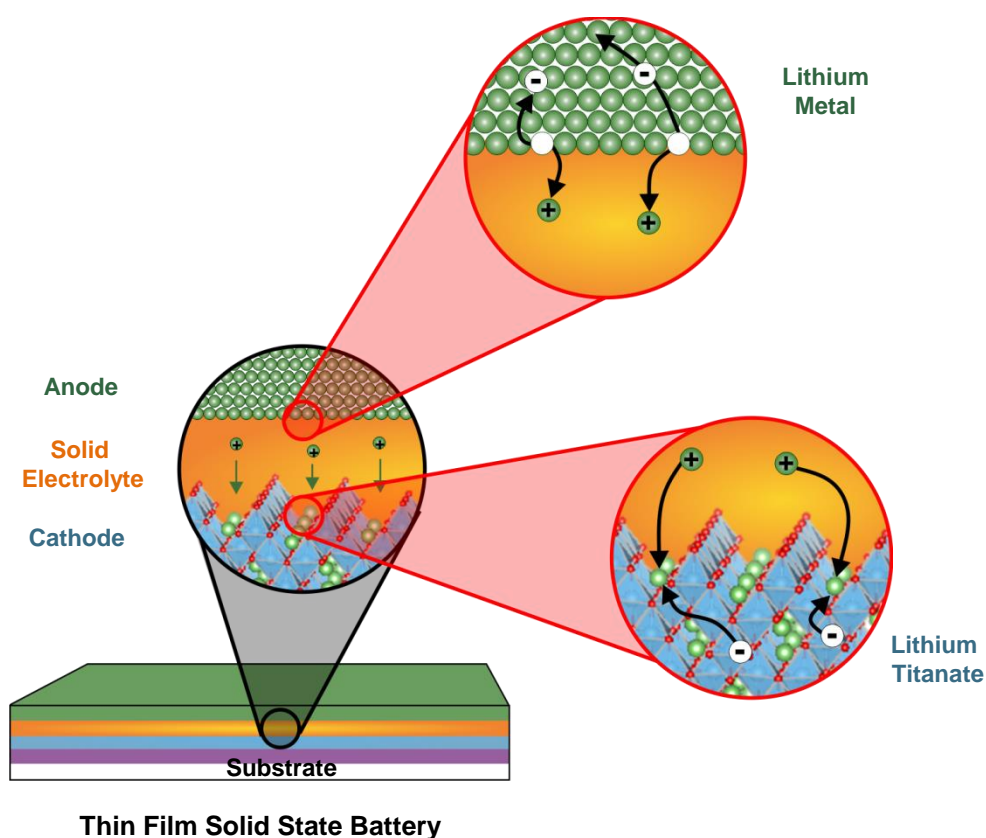
Figure 4-32: Schematic setup of a thin-film SSB using Li metal as anode, LTO as cathode and LPS as solid electrolyte.

Interestingly, the formation of black spots around some of the evaporated Li contacts was observed. A Li contact surrounded by a black circle always showed a short circuit as determined by electrochemical tests. Different configurations such as glass/ITOLTO//LPS/Li (a), glass/ITO/LPS/Li (b) and glass/LPS/Li (c) were studied to

investigate the nature of these circles and are shown in Figure 4-33. Black circles were also observed on ITO substrates without LTO coating but not on glass substrates. Therefore, it can be assumed that the formation of black circles around Li contacts is most likely related to the ITO substrate.
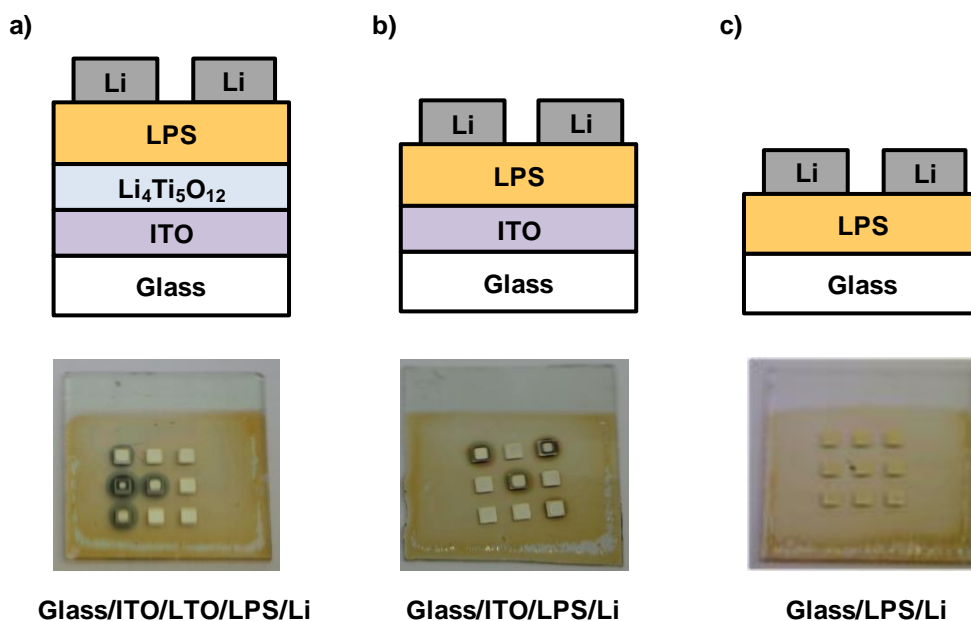
Figure 4-33: Different analysed configurations to investigate the nature of black circles around Li contacts: a) glass/ITOLTO//LPS/Li (AB37), b) glass/ITO/LPS/Li (AB38) and c) and glass/LPS/Li (AB39). Schematic pictures of analysed configurations are shown at the top. Images from different samples after Li evaporation are shown at the bottom.

As these black circles were easily visible, they were initially used for quality control of the LPS thin-films and to quantify the short circuited contacts in the thin-film cells. $6-18\%$ of evaporated Li contacts were short circuited for the ITO/LPS/Li system as shown in Figure 0-14 in the appendix.

Defects were often related to dust or dirt particles as clean room conditions could not be applied during deposition. On the contrast, the amount of short circuits for ITO/LTO/LPS/Li cells varies from $0-100\%$ and strongly depends on the quality of the LTO layer. LTO thin-films showed a huge amount of defects probably related to LTO crystals of the size of a few µm as shown in optical microscopy and SEM images of LTO films in Figure 0-15 in the appendix. These defects could lead to a crack or porosity in the LPS layer resulting in the observed short circuits. Optimisation of the LTO thin-film cathode and LPS solid electrolyte deposition is further required to reduce the amount of short circuits but is beyond the scope of this

work. By direct contact between Li and ITO, In^{3+} in the In_2O_3 might be reduced to In according to eq. 4-2:

$$In_2O_3 + 6\,Li^+ + 6\,e^- \rightarrow 2\,In + 3\,Li_2O. \tag{4-2}$$
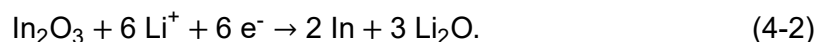
This reaction explains the dark colour of the contacts due to the formation of In metal. The reduction of In_2O_3 to In metal would lead to a volume expansion of 97% considering the densities and molar masses of In_2O_3, In and Li_2O. SEM images of black and transparent ITO contacts of an ITO/LTO/LPS/Li cell shown in Figure 0-16 in the appendix support this assumption as the thickness of the ITO changes from around 140 nm to 320 nm if the LTO thickness remains unaffected by the phase transformation. This corresponds to an ITO volume change of nearly 130%.

During initial cycling experiments of the ITO/LTO/LPS/Li cells several intact contacts turned black after discharge depending on the depth of discharge (DoD). As the black contacts look similar to the previous observations, the reduction of the ITO substrate might occur upon discharge. Bressers *et al.* discovered a colour change of transparent ITO to metallic black below voltages of 1 V *vs.* Li^+/Li.[261] This colour change is coupled with an irreversible decrease of crystalline ITO signal intensities in XRD. At potentials lower than 0.8 V *vs.* Li^+/Li signal intensities in XRD even further decrease accompanied by the appearance of an In(101) peak. This indicates the formation of a crystalline In phase. At potentials lower than 0.6 V *vs.* Li^+/Li a second peak corresponding to In(110) developed. Complete disappearance of the ITO (222) reflection was observed after extended reduction at 0.5 V *vs.* Li^+/Li. Even though these experiments were conducted with liquid electrolytes, similar redox processes in the ITO substrate might be involved for SEs such as LPS thin-films. Therefore, the potential window for cycling experiments of ITO/LPS/Li cells was determined by CV. The cutoff voltages were set to different lower limit potentials after each cycle and optical examinations were carried out after each step. The pictures taken from the back of the contact and the recorded CV curves are shown in Figure 4-34. The lower limit was decreased stepwise from 1.4 V to 0.5 V *vs.* Li^+/Li.
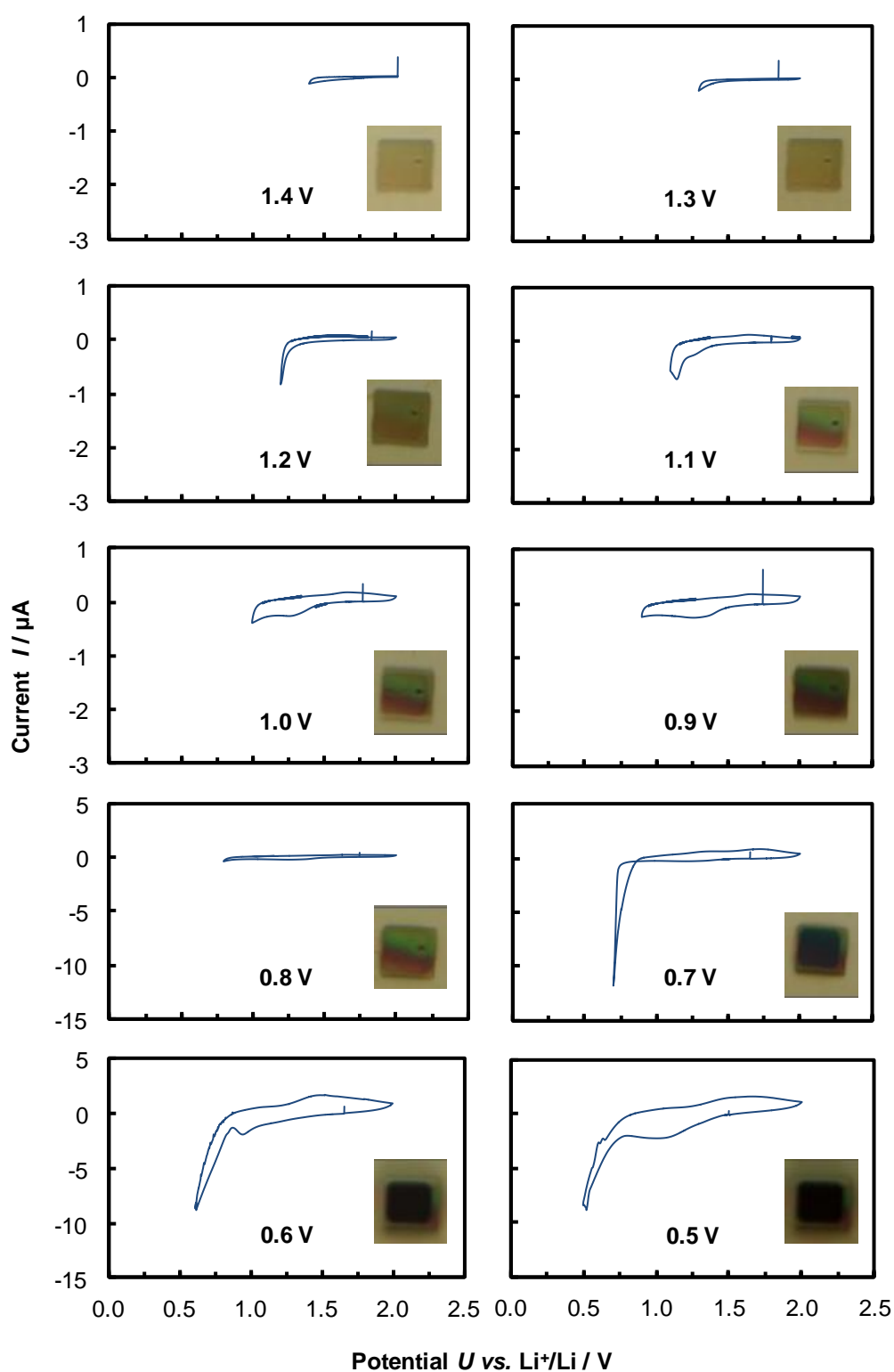
Figure 4-34: Cyclic voltammetry at a rate of 1 mV s^{-1} collected on an ITO/LPS/Li cell (AB38). The cutoff voltages were decreased stepwise from 1.4 V to 0.5 V *vs.* Li$^+$/Li after each cycle. Pictures taken from the back of the contact after each cycling step are shown as inlet.

Already in the first cycle with a cut-off voltage of 1.4 V *vs.* Li$^+$/Li the start of a cathodic peak can be observed. This peak starts to increase reaching its maximum signal intensity at a cut-off voltage of 1.2 V *vs.* Li$^+$/Li. The reaction seems to be irreversible up to 2.0 V *vs.* Li$^+$/Li as no anodic peak was detected, which correlates with a slight irreversible colouring of the ITO as can be seen in the pictures taken from the back of the sample. The intensity of the colouring increases up to a cut-off voltage of 0.8 V *vs.* Li$^+$/Li. The start of a second cathodic peak with significantly higher intensity was observed starting from 0.7 V *vs.* Li$^+$/Li. The redox reaction related to this peak seems to be partly reversible as a broad anodic peak at higher potentials was detected. In addition, darkening of ITO was observed for lower cut-off voltages than 0.7 V *vs.* Li$^+$/Li possibly related to the observed cathodic peak in the CV curves. The results support the previously discussed results from Bressers *et al.* and the reduction of In$_2$O$_3$ to In metal for potentials <0.7 V *vs.* Li$^+$/Li.

The chosen voltage window for subsequent electrochemical tests should restrict the intercalation of lithium ions to the LTO thin-film, while the ITO substrate remains passive. Therefore, the assembled battery or cell will referred to as LTO/LPS/Li, while the complete setup includes the ITO substrate (ITO/LTO/LPS/Li). Initial structural characterisation of the assembled ITO/LTO/LPS system was carried out by SEM analysis (see Figure 4-35). Figure 4-35 reveals that both LPS and LTO thin-films are dense and homogeneous with a thickness of 105 nm for the LTO layer and 1 µm for the LPS thin-film.
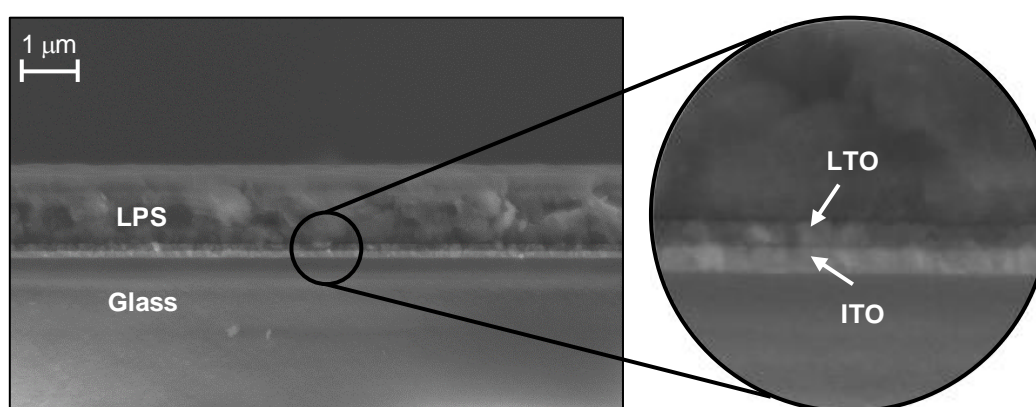
Figure 4-35: SEM images recorded with a magnification of 25 000 (left) and 50 000 (right) from the ITO/LTO/LPS system (AB37).

Lithium metal was evaporated on top of the previously described system leading to the architecture of a lithium based thin-film battery (LTO/LPS/Li), which was further characterised by cyclic voltammetry (CV) measurements from 1.2 to 2.0 V *vs.* Li^{+}/Li at a scan rate of 1 mV s^{-1}. Figure 4-36 (b) shows the 10 CV cycles that were performed, and (c) the setup of the complete system, respectively.

The cathodic peak at 1.52 V *vs.* Li^{+}/Li correlates with the reversible intercalation of lithium ions (Li^{+}) into the spinel lattice of $Li_4Ti_5O_{12}$, which transforms into cubic rock-salt $Li_7Ti_5O_{12}$ by the reduction of Ti^{4+} to Ti^{3+}. The anodic peak at 1.59 V *vs.* Li^{+}/Li can be attributed to the deintercalation of Li^{+} from $Li_7Ti_5O_{12}$, which is converted back into cubic spinel type $Li_4Ti_5O_{12}$ by oxidation of Ti^{3+} to Ti^{4+}.[260] No side peaks were recorded from 1.2 to 2.0 V *vs.* Li^{+}/Li. Therefore, the main phase in the LTO thin-films prepared by CSD is $Li_4Ti_5O_{12}$.

The CV curves show a small deviation from the 1st (grey) to the 2nd cycle (black), especially for the cathodic peak, which correlates to a 5% decrease of the discharge capacity. This capacity loss can be ascribed to irreversible degradation of the LTO thin-film which might be caused by small amounts of impurities or by the formation of an interphase, which partly consumes active LTO. However, the nearly perfect overlap of the CV curves starting from the 2nd cycle confirms the stability of the LTO/LPS/Li cell.
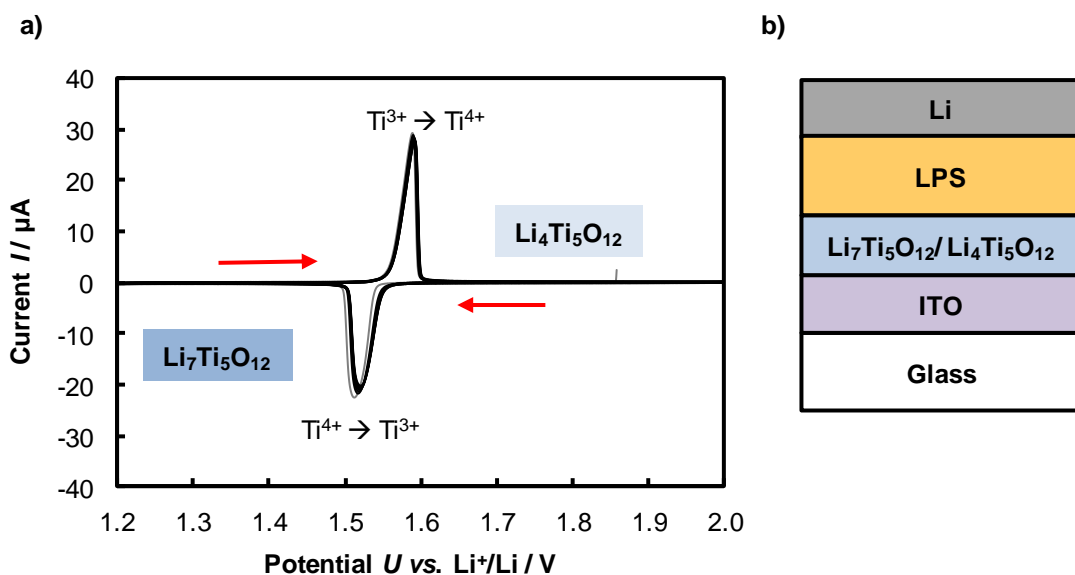
Figure 4-36: a) Cyclic voltammetry (CV) curves of the LTO/LPS/Li cell (AB37) recorded between 1.2 and 2.0 V *vs.* Li^{+}/Li with a scan rate of 1 mV s^{-1}. The 10 CV cycles are superimposed (1st cycle in grey). b) Schematic picture of the complete ITO/LTO/LPS/Li setup.

The cycling behaviour and stability of the system was further investigated by galvanostatic cyclic charging and discharging (CCD). The performed measurements consist of 200 cycles with varying current densities (13 µA cm^{-2} (2.2C), 25 µA cm^{-2} (4.3C), 50 µA cm^{-2} (8.6C) to 100 µA cm^{-2} (17.2C)) followed by 300 cycles at 100 µA cm^{-2} (17.2C). Cutoff voltages were set to 1.4 V and 2.0 V *vs.* Li$^+$/Li (Figure 4a). Figure 4-37 displays the SEM images of the complete cell (LTO/LPS/Li) after 500 cycles, where the LTO layer has a thickness of 95 nm. The pictures neither reveal interphases on the LTO/LPS side nor on the LPS/Li side. There is no degradation of the ITO, LTO or LPS layers. Li exhibits a highly porous structure, which is most likely not related to a reaction of Li contacts with the LPS layer but to a reaction of Li with traces of N$_2$ to Li$_3$N in the glovebox during storage until SEM measurement (ca. 7 weeks). XPS analyses previously revealed the formation of a SEI between Li and LPS. Even if no interphases are visible in SEM images, they will also be present in the ITO/LTO/LPS/Li system.
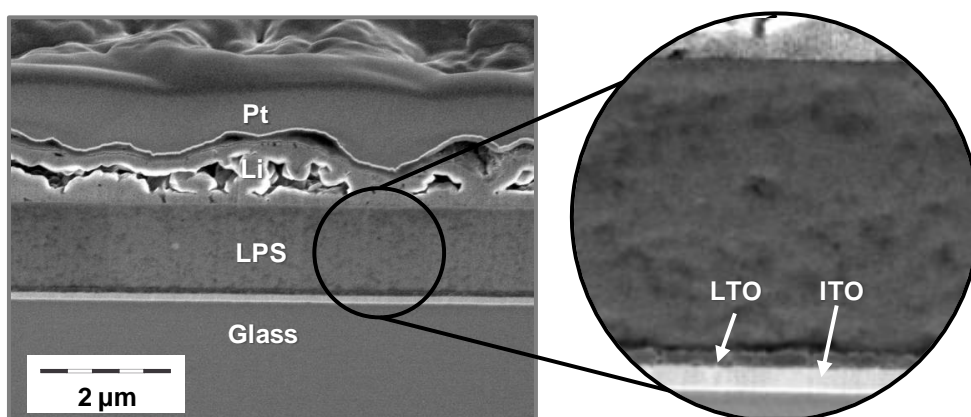
Figure 4-37: SEM images of the ITO/LTO/LPS/Li system (AB43) after 500 cycles. Pt on top of Li was deposited for the FIB-cut after cycling of the ITO/LTO/LPS/Li system. SEM images were taken with a magnification of 15 000 (left) and 50 000 (right).

Figure 4-38a) shows representative galvanostatic charge and discharge curves for different current densities, whereas Figure 4-38b) displays the specific capacity of the cell and the coulombic efficiency as a function of cycle number.

The thin-film battery exhibits stable galvanostatic cycling performance at current densities up to 100 µA cm^{-2} with a specific capacity of initially 149 mAh g^{-1} (13 µA cm^{-2}), which is slightly lower than the theoretical specific capacity of 175 mAh g^{-1}. The lower capacity can be ascribed to impurity phases in the LTO or interphase formation, which leads to the consumption of active LTO. This interphase

can occur at the LPS or ITO side and might already be formed either during the different deposition and annealing steps or upon cycling of the system.

The discharge curves show a constant voltage plateau at approx. 1.55 V *vs.* Li⁺/Li, whereas the charge curve reaches a voltage plateau at 1.57 V *vs.* Li⁺/Li, which could be related to polarisation effects.

The specific capacity depends on the applied current density; averaged capacities at the various current densities are: 137 mAh g^{-1} (13 µA cm^{-2}), 132 mAh g^{-1} (25 µA cm^{-2}), 129 mAh g^{-1} (50 µA cm^{-2}), and 124 mAh g^{-1} (100 µA cm^{-2}). The dependency on the current density of LTO electrodes is known from literature and might be related to kinetic limitations.[260]
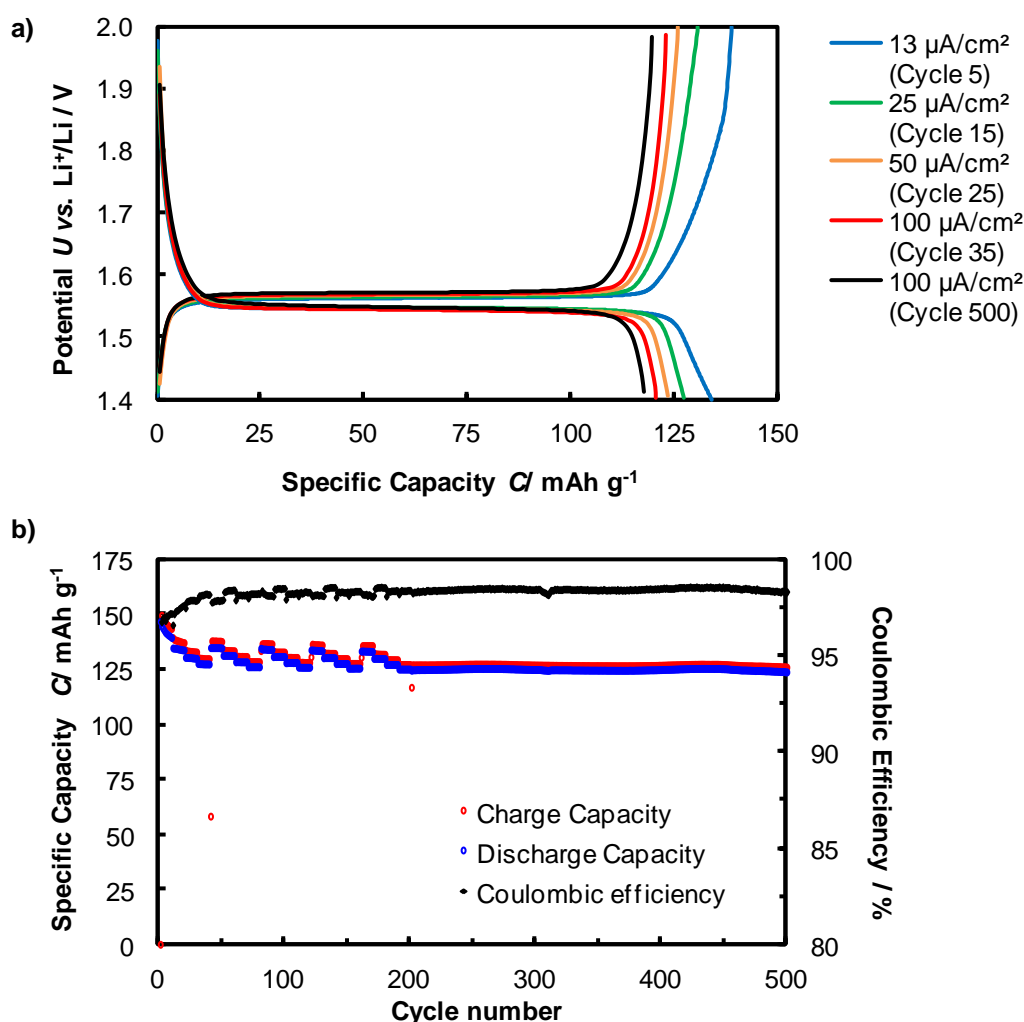
Figure 4-38: a) Galvanostatic cycling charge/discharge (CCD) curves obtained of an ITO/LTO/LPS/Li cell (AB43) at various current densities. Cutoff voltages were set at 2.0 and 1.40 V *vs.* Li⁺/Li. The 5th (13 µA cm^{-2}), 15th (25 µA cm^{-2}), 25th (50 µA cm^{-2}), 35th (100 µA cm^{-2}) and 500th (100 µA cm^{-2}) cycles are superimposed. b) Specific capacity and coulombic efficiency as a function of cycle number.

The capacity retention of the cell is 94.9% after 10 cycles (13 µA cm⁻²) and 84.3% after 500 cycles (100 µA cm⁻²). The high capacity loss of 5.1% in the first cycles is close to the capacity decrease recorded by CV in the first cycle correlated to LTO degradation.

In addition, a slightly higher charge than discharge capacity was recorded. The coulombic efficiency increases from 96.7% up to 98%, with minimal changes depending on the applied current density. The higher charge capacity can be attributed to the existence of lithium-rich phases in the LTO thin-film, or to the partial lithiation of the ITO substrate during the deposition or annealing of the LTO thin-film. The additional Li could be expelled upon charge and not reinserted upon discharge.

CCD only provides information about the electrodes. Therefore, galvanostatic cycling was coupled with EIS measurements performed after each charge (2.0 V) and discharge (1.4 V) to obtain information about the solid electrolyte conductivity and stability upon cycling. Figure 4-39 displays representative Nyquist plots at 2.0 V (blue) and 1.4 V (red) of an ITO/LTO/LPS/Li system.
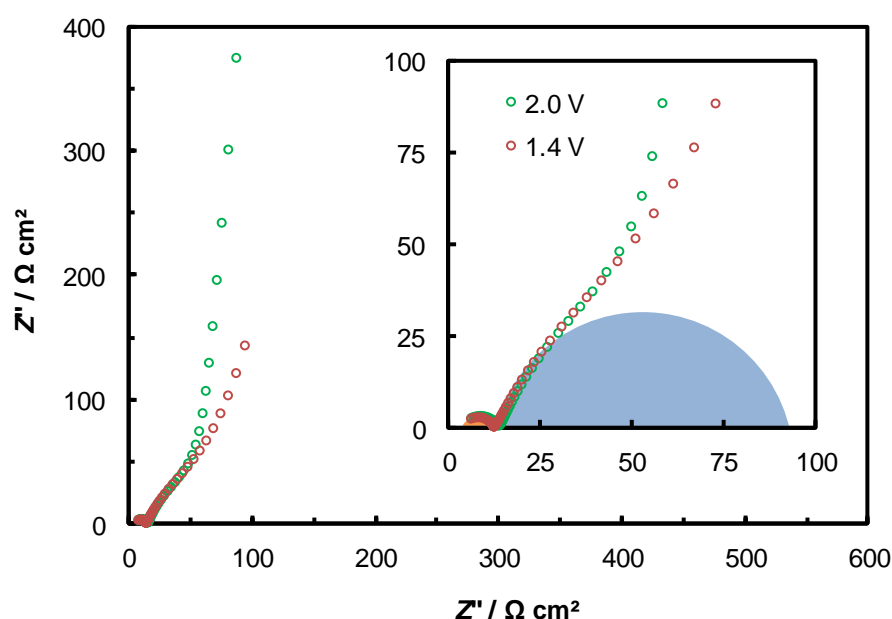
Figure 4-39: Characteristic Nyquist plot of an LTO/LPS/Li cell (AB43). Two different processes are identified: one in the high frequency (HF) and one in the mid frequency (MF) region. The respective elements in the equivalent circuit can be attributed to the LPS thin-film and Li/LPS interphase resistance (HF) and the ionic transport through the LTO thin-film (MF).

The Nyquist plots show two semicircles in the high frequency (HF) region and in the mid frequency (MF) region, respectively. Each semicircle can be fitted by a resistor parallel to a CPE. The equivalent circuit model for fitting also includes a resistor for the offset of the first semicircle and a CPE for the straight line in the low frequency (LF) region. Therefore, the impedance data were fitted using a $R_1(R_2Q_2)(R_3Q_3)Q_4$ equivalent circuit. The offset resistance is ascribed to the ohmic behaviour of the current collector ITO plus the cables ($R_1=R_{ITO}$) and the straight line at low frequencies to the blocking behaviour of the Li electrode (Q_4). Even though Li would ideally behave as a non-blocking electrode, this behaviour would only be visible at lower frequencies. Previously, the formation of a SEI between Li and LPS was revealed, although two processes in the impedance data cannot be resolved, which was ascribed to limitations of the measurement device. Therefore, the two semicircles at (i) low and (ii) mid frequencies were correlate to (i) the ionic transport through the LPS electrolyte and the SEI between Li and LPS ($R_2=R_{LPS} + R_{SEI}$) and (ii) the ionic transport through the LTO thin-film ($R_3=R_{LTO}$). No contributions in the spectra could be ascribed to ionic charge transfer resistances between LTO and LPS or the current collector ITO. These results are similar to previous studies with LiPON solid electrolyte in (Ti/Pt)/LTO/LiPON/Li thin-film cells where the charge transfer resistance between LTO and LiPON was not visible and the resistance between LTO and the current collector Ti/Pt is low enough to avoid rate-limitation in the impedance spectra.[246] Figure 4-40a) shows the measurement setup and the equivalent circuit for fitting, whereas Figure 4-40b) displays the obtained impedance values of the different elements over cycle number.

The conductivity of the LTO layer was calculated assuming a film thickness of 95 nm, which derives from SEM cross section analysis of the cell after cycling (Figure 4-38a). The averaged conductivity of $Li_4Ti_5O_{12}$ at 2.0 V is $\sigma = 1.5 \cdot 10^{-7}$ S cm^{-1} with an irreversible conductivity increase in the first 40 cycles of 46% and overall variations up to 76%. This irreversible change cannot be explained by temperature variation (25.0 – 32.5 °C – black line) and might be associated with changes in the LTO layer, which also correlates with the capacity loss at the beginning of the cycling. $Li_7Ti_5O_{12}$ exhibits an average conductivity of $\sigma = 1.1 \cdot 10^{-7}$ S cm^{-1} at 1.4 V with overall variations of 35%, which is in accordance to the temperature change. Therefore, the conductivity of the LTO electrode is related to the state of charge (SoC) with a higher conductivity for a lower SoC. The SoC

dependent conductivity variations were expected and are caused by changes of the LTO structure upon cycling.[246] Interestingly, the conductivities found for LTO in the LTO/LPS/Li cell are two orders of magnitude higher than the conductivities recorded in the LTO/LiPON/Li systems.[246] The impedance spectra of the LTO/LPS/Li cell reveal only the onset of the second semicircle ascribed to the LTO resistance of the LTO electrode (see Figure 4-39), which could result in large fitting errors and over- or underestimated LTO conductivity. However, the different conductivity values of the LTO layers could also be attributed to the different deposition processes: CSD instead of pulsed laser deposition (PLD).
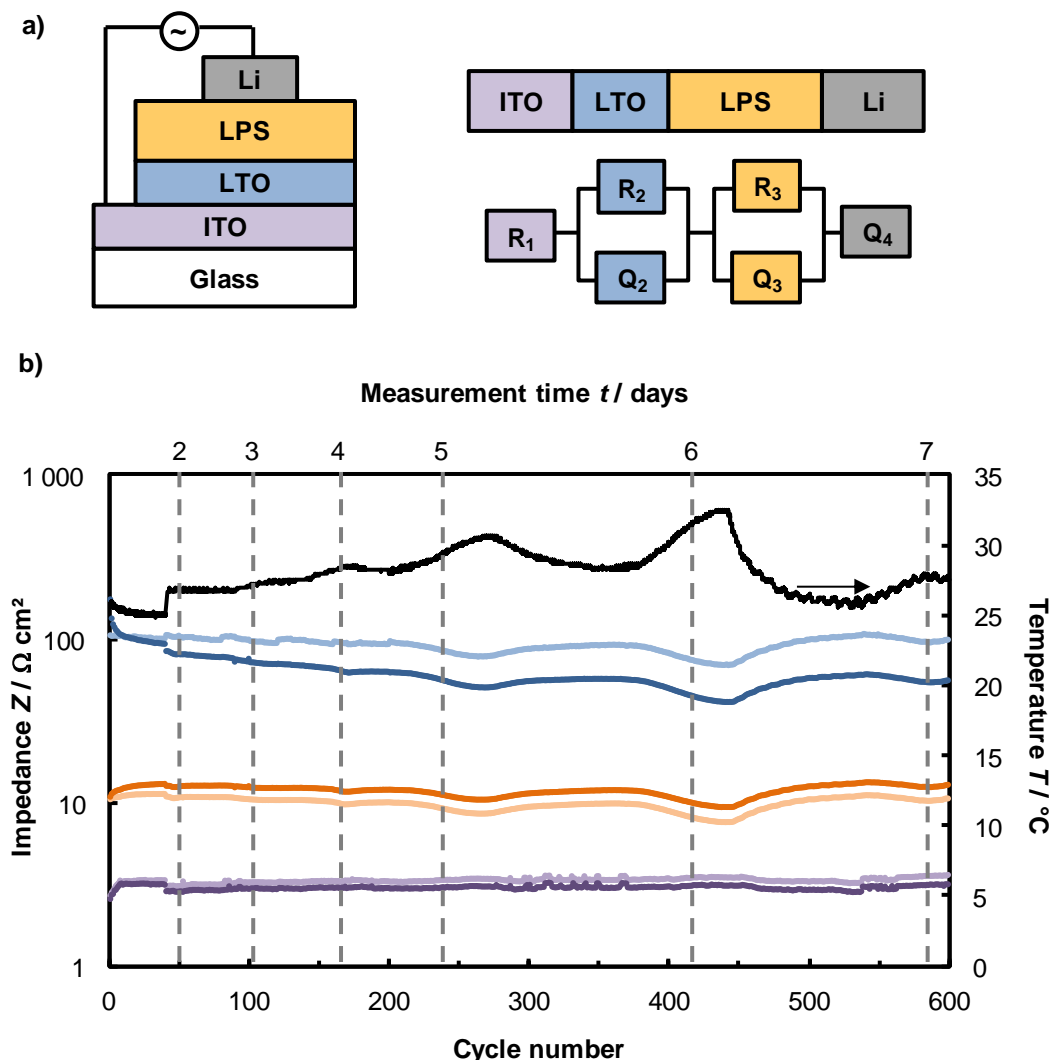
Figure 4-40: a) Schematic picture of measurement setup (AB43) and equivalent circuit used for this measurement. b) Impedance values over cycle number for ITO, LTO and LPS (dark: 2.0 V, bright: 1.4 V).

Capacitances and dielectric constants of the LTO layer were calculated according to equation 3-6 and 3-6, respectively. $Li_4Ti_5O_{12}$ after charge at 2.0 V and $Li_7Ti_5O_{12}$ after discharge at 1.4 V $Li_4Ti_5O_{12}$ exhibit averaged capacitances of 11 µF and 12 µF, respectively, corresponding to dielectric constant of $5.4 \cdot 10^4$ ($Li_4Ti_5O_{12}$) and $5.6 \cdot 10^4$ ($Li_7Ti_5O_{12}$). Although a higher SoC dependency of the dielectric constant was expected, the obtained values are in the same order of magnitude than the reported dielectric constant of $Li_{4+x}Ti_5O_{12}$ by Schichtel *et. al.*[246]

The resistance of the LPS layer varies about 33%, which correlates well with the recorded temperature variations. With an activation energy of 0.38 eV as previously determined for LPS thin-films the theoretical impedance decrease is 29% for a temperature increase from 25.0 °C to 32.5 °C, which is close to the measured impedance change. Despite the temperature related variations the resistance of the LPS layer remains stable upon cycling, which underscores the excellent behaviour as solid electrolyte. The averaged area resistance of the LPS layer - calculated assuming a contact area of 2.25 mm² – is $9.4 \, \Omega \, cm^2$ at 1.4 V and $11.3 \, \Omega \, cm^2$ at 2.0 V (average temperature 28.2 °C). Thus, a lower SoC correlates with a lower resistance, which could be originated from a reversible interphase formation or even changes in the LPS film composition depending on the SoC. Further experiments such as Raman or X-ray photoelectron spectroscopy during cycling of the cell are necessary to reveal structural changes of the LPS layer and to verify our assumptions. The obtained values are slightly higher when compared to the area resistance of LPS thin-films in Si/LPS/Li half cells with $5.4 \, \Omega \, cm^2$ (29.0 °C), which can result from variations in film thickness and active electrode areas or from the formation of a low conductive interphase between LTO and LPS. Still, the mean conductivity of the LPS solid electrolyte, calculated assuming a film thickness of 1.7 µm, which derives from SEM cross section analysis of the cell after cycling (Figure 4-38a), is around one order of magnitude higher with $1.7 \cdot 10^{-5} \, S \, cm^{-1}$ than the reported conductivity of LiPON thin-films ($\sigma = 2.3 \cdot 10^{-6}$ S/cm).[79]

Capacitances and dielectric constants of the LPS layer were calculated according to equation 3-6 and 3-6, respectively. LPS thin-films in a LTO/LPS/Li cell exhibit averaged capacitances of 786 pF (at 1.4 V) and 753 pF (at 2.0 V) over 500 cycles, corresponding to dielectric constants of 67 and 64, respectively. These values are comparable to the previous results of LPS films in a Si/LPS/Au setup but slightly

higher when compared to LPS layers in Si/LPS/Li setups, which might also be explained by the formation of an interphase between LTO and LPS.

The successful integration and cycling stability of a LPS thin-film electrolyte in a solid-state microbattery using Li as anode and LTO as cathode was demonstrated. Both LTO and LPS thin-films are prepared by solution routes, which enable fast and inexpensive deposition. By cyclic voltammetry the stability of the system from 1.2 to 2 V *vs.* Li$^+$/Li was shown. Moreover, the microbattery exhibits stable galvanostatic cycling performance up to 500 cycles in the voltage range from 1.4 to 2 V *vs.* Li$^+$/Li. During cycling variations in the LPS and LTO conductivity were recorded by EIS. However, this is mainly attributed to temperature changes upon measurement. This highlights the excellent stability of the LPS thin-films – which might also be combined with other cathode materials – during cycling. Therefore, LPS thin-films provide an alternative to LiPON layers currently applied as electrolyte in thin-film SSBs with the possibility to develop a printed microbattery.

4.4.2 Coating of conventional slurry based cathodes

The application of LPS thin-films in bulk type SSBs with high energy densities might be achieved by direct coating of composite cathodes. The LPS thin-films would act as separator and no additional bulk SE has to be integrated in the SSB, which enables the possibility to reduce the SE thickness to a few µm. Therefore, deposition of LPS coating solution on top of LFP composite cathodes on aluminium foils was investigated.

Despite the flatness of the substrates ensured by either Kapton tape or ceramic glue, the LPS coating was unsuccessful. Pictures of the LPS coated LFP cathodes are shown in Figure 4-41, while Figure 0-17 in the appendix displays SEM images from uncoated LFP cathodes. Changes in the wetting behaviour were revealed most likely due to the porous structure of the composite cathode (see Figure 0-17). Interestingly, the formation of "bubbles" was noticed exactly in the points, where the coating solution was dropped, which might have been due to the reaction of the coating solution with the composite cathode components such as PVDF binder. In addition, the drying temperature (250 °C) exceeds the decomposition temperature of PVDF. By the decomposition of the binder, carbon from the electrode may be dissolved in the LPS solution and incorporated in the solid electrolyte layer. The dissolved carbon can also explain the darkening of the ceramic glue when more coating solution is deposited on the LFP cathode as can be seen in Figure 4-41a).
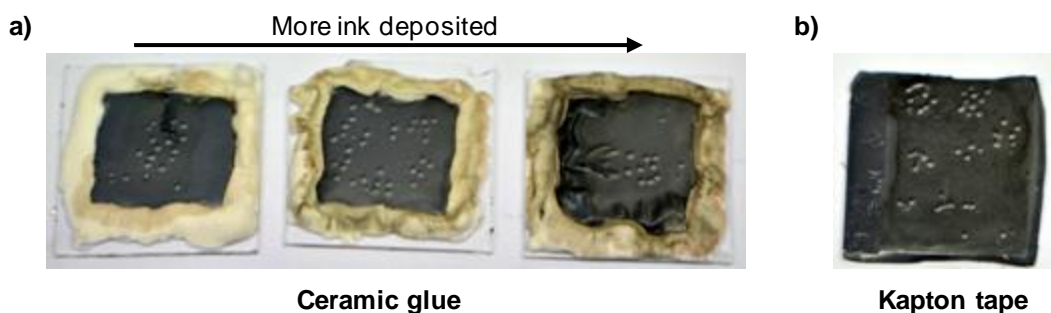
Figure 4-41: LPS deposited on composite cathodes fixed with (a) ceramic glue (AB44-AB46) and (b) Kapton tape (AB47).

Evaporation of Au contacts and electrochemical measurements revealed that all contacts are short circuited, which might result from dissolved carbon in the LPS layer or the porous structure of the composite cathode soaking up the whole LPS coating solution. Further experiments would require densification of the electrodes and the evaluation of different binders with higher decomposition temperatures.

4.4.3 Protective coating

A different approach to integrate LPS thin-films in bulk type SSBs with Li anodes is the coating of bulk solid electrolytes characterised by high ionic conductivity, which are unstable against the Li metal anode. LPS thin-films show ideal electrochemical and mechanical properties for protective coating applications, where such a bulk solid electrolyte could benefit from the stability of the LPS layer against Li metal.

The concept of solution-processed LPS as protective coating was investigated by coating Ohara glass substrates, a commercially available NASICON type ceramic solid electrolyte, with LPS thin-films. Figure 4-42 demonstrates the lack of stability against Li metal for Ohara solid electrolyte and most importantly the protective behaviour of LPS films for the tested Ohara electrolyte/Li metal electrode. While the pristine Ohara electrolyte turned from white (Figure 4-42a) to black when pressed against Li metal for 20 h (Figure 4-42c), the Ohara substrate coated with LPS film (Figure 4-42b) remained unaffected after contact with Li (Figure 4-42d).
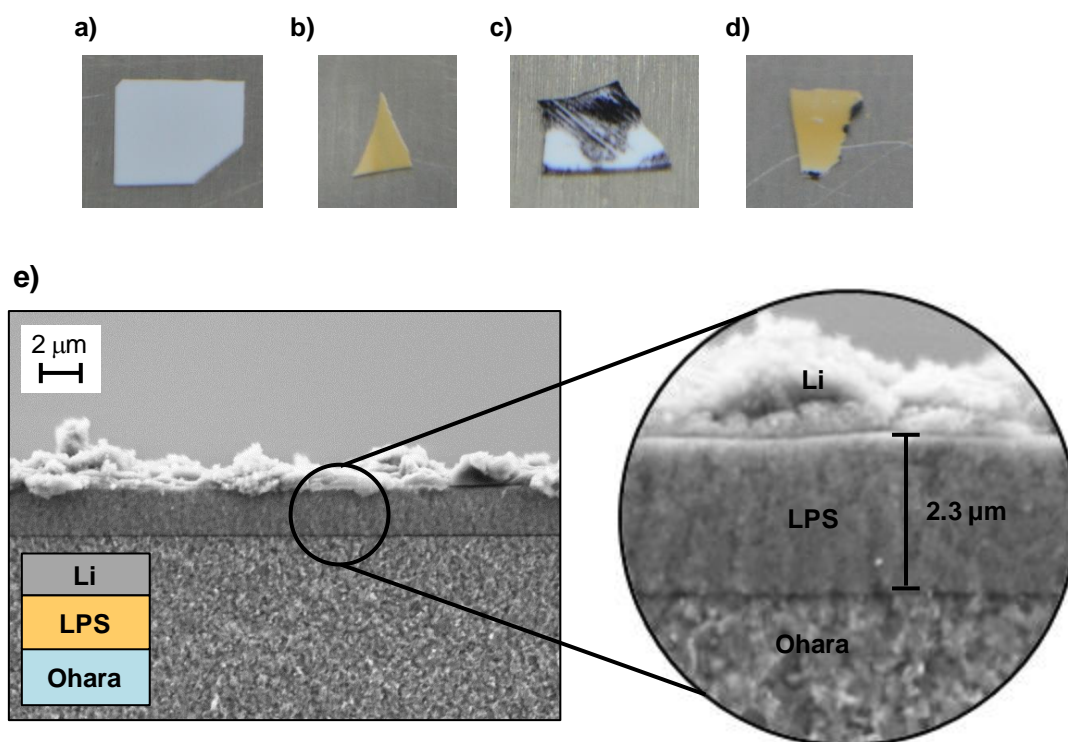
Figure 4-42: Optical images of (a) pristine Ohara electrolyte, (b) Ohara electrolyte after LPS deposition, (c) pristine Ohara electrolyte after 20 h long contact with Li metal and (d) LPS-protected Ohara electrolyte after 20 h long contact with Li metal. e) Cross-section SEM images of Ohara/LPS/Li system (AB48) recorded at 25 000x (right) and 10 000x (left) magnification using a secondary electron (SE) detector with the scheme of investigated setup.

Figure 4-42e) shows a cross-section SEM image of coated Ohara electrolyte with a LPS layer and evaporated Li contacts. The LPS thin-film exhibits a thickness of about 2.3 µm with a smooth surface and dense structure on top of the Ohara electrolyte.

Time-dependent EIS was performed on the LPS-coated samples, using evaporated Au and Li contacts as electrodes and including reference samples of Ohara electrolyte coated only with Au and Li electrodes. Figure 4-43a) and b) shows the recorded Nyquist plots and schematic representations of the measurement setups, respectively.

The Nyquist plots of the reference sample of the Ohara electrolyte coated with Au electrodes show (i) a semicircle with an offset resistance in the high frequency part, (ii) the onset of a second semicircle in the mid frequency range, which dismisses in (iii) the onset of a third semicircle at low frequencies. The data was fitted using a $R_0(R_1Q_1)(R_2Q_2)(R_3Q_3)$ equivalent circuit.

Both LPS-coated Ohara setups exhibit similar Nyquist plots in the high and mid frequency range, while they show a capacitive straight line at low frequencies. These setups were fitted with a $R_0(R_1Q_1)(R_2Q_2)Q_3$ equivalent circuit. Table 4-5 sumarises the equivalent circuits used for EIS data fitting, while Table 0-10 in the appendix summarises the fitting results of the various Ohara systems.

Table 4-5: Equivalent circuits used for fitting of the various Ohara systems.

System	Number	Equivalent circuit
Au/Ohara/Au	AB51	$R_0(R_1Q_1)(R_2Q_2)(R_3Q_3)$
Au/Ohara/LPS/Au	AB50	$R_0(R_1Q_1)(R_2Q_2)Q_3$
Au/Ohara/LPS/Li	AB48	$R_0(R_1Q_1)(R_2Q_2)Q_3$
Au/Ohara/Li	AB49	(R_1Q_1)

The Nyquist plots in the high frequency part resemble previous reported plots from Ohara electrolytes.[262] The resistances R_2 and R_3 of the semicircles at mid and lower frequencies are therefore ascribed to interfacial or charge-transfer resistances and will not be discussed in detail. Fu ascribed the offset of the first semicircle R_0 to the bulk resistance R_b and the resistance of the first semicircle R_1 to the grain boundary resistance R_{gb} of the Ohara electrolyte.[262] The sum of (R_0+R_1) describes

the electrolyte resistance. Figure 4-43c) shows the obtained area resistances for the electrolyte (R_0+R_1) as a function of time after contact formation by evaporation.
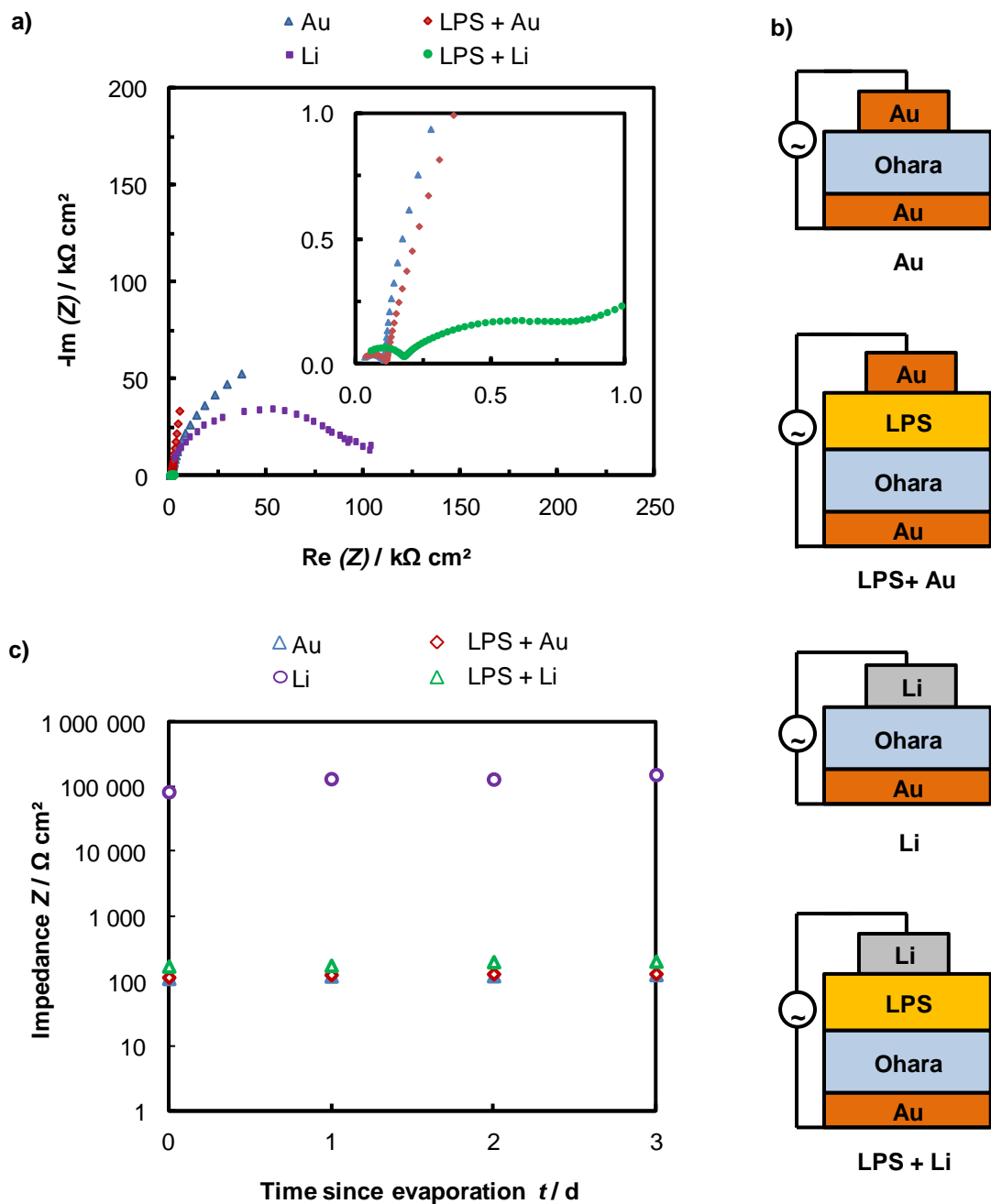
Figure 4-43: a) Nyquist plots obtained directly after contact evaporation (AB48-AB51). b) Time-dependent impedance values for the different setups. c) Schematic representation of the investigated setups (AB48-AB51).

Coating of the Ohara electrolyte with LPS layer increases the area resistance by roughly 5% when Au electrodes are used. Area resistance increases around 50% when Li contacts where used on top of LPS-coated Ohara electrolyte. The increase of the area resistances in the Ohara/LPS/Au and Ohara/LPS/Li systems is attributed to the LPS layer and the SEI formation between Li and LPS, respectively. Thickness differences of LPS layers in the two investigated systems with Au and Li electrodes can also lead to different fitting results. Nevertheless, the area resistances for the pure Ohara electrolyte with Au electrodes and the two systems with LPS layer protection remain in the same range.

In contrast, very high impedance values were recorded for the reference sample of the Ohara electrolyte in direct contact with Li metal, which lead to highly scattered data in the low and high frequency part. Still one semicircle can be observed in the range from 100 Hz to 100 kHz, which was fitted using a $(R_1 Q_1)$ equivalent circuit. The resistance is nearly four orders of magnitude higher for unprotected Ohara in direct contact with Li metal when compared to LPS-coated Ohara setups.

These results strongly support the idea of LPS thin-film application as a protective coating for Li anodes to prevent the decomposition of bulk solid electrolytes.

4.4.4 Summary

LPS thin-film electrolytes were successfully integrated as solid electrolyte separator in a microbattery using Li as anode and printed LTO as cathode. The microbattery exhibited stable cycling performance up to 500 cycles, which highlights the excellent stability of the LPS thin-films during cycling. LPS thin-films might also be combined with other thin-film cathodes to increase the energy density of the microbattery. Solution-prepared LPS thin-films provide an alternative to LiPON layers prepared by vacuum deposition and currently applied as electrolyte in thin-film SSBs with the possibility to develop a printed microbattery.

The direct coating of LPS thin-films on composite cathodes was also investigated. However, the results hint a decomposition of the organic binder and dissolution of carbon additives in the LPS film leading to short circuits through the LPS layers.

In addition, the successful application of LPS as protective films to prevent reduction of bulk solid electrolyte by Li metal anodes is shown. In a next step these coated bulk SEs would have to be integrated in SSBs with Li metal anodes and the cycling behaviour of these SSBs would have to be analysed.

5 CONCLUSION AND OUTLOOK

This thesis reports the synthesis by chemical solution deposition, the characterisation and the application of lithium thiophosphate (LPS) solid electrolyte thin-films as separators for SSB.

First suitable coating solutions for the synthesis of lithium thiophosphate (LPS) thin-films by chemical solution deposition (CSD) are formulated and analysed followed by preparation of LPS thin-films by CSD. For optimisation of the deposition process systematic investigation of the process parameters and their influence on the thin-film properties were carried out. Next, LPS thin-films were electrochemically characterised as solid electrolytes, including investigation of the stability against lithium metal and behaviour upon lithium cycling. Finally, the LPS thin-films are applied as solid electrolyte separators by integrating them into a microbattery system, on composite cathodes and as protective coating on bulk type solid electrolytes.

Suitable coating solutions were formulated based on the solvent N-methylformamide (NMF) and the amorphous LPS glasses $70Li_2S-30P_2S_5$ [70-30], $75Li_2S-25P_2S_5$ [75-25] and $80Li_2S-20P_2S_5$ [80-20], which were prepared by ball-milling. *In situ* NMR measurements of the solutions revealed S-O substitution between the amorphous LPS precursors and NMF. The S-O exchange leads to the ageing of the coating solution and the formation of mixed thio-oxy-phosphates within the solutions. Exact structures for these thio-oxy-phosphates were proposed based on the NMR studies for the coating solution. Simulation of ^{31}P NMR spectra or 2D ^{31}P-^{31}P NMR measurements could help to verify the assumptions.

X-ray photoelectron spectroscopy (XPS) and energy dispersive X-ray spectroscopy (EDX) confirmed high oxygen contents in the LPS films and bridging and non-bridging sulphur and oxygen species. Solid-state NMR measurements on LPS layers could help to identify the exact structures of the thio-oxy-phosphates within

the thin-films. The reaction rate for the S-O substitution depends on the precursor stoichiometry with [70-30] being the most reactive among the investigated glasses. As the various amorphous glasses contain different ratios of the thiophosphate anions, it was concluded that *pyro*-phosphate shows a higher reactivity towards S substitution by NMF than *ortho*-phosphate. Structural and electrochemical properties of the LPS films prepared from different coating solutions depend on precursor stoichiometry and age of the coating solution. X-ray diffraction (XRD) and scanning electron microscopy (SEM) showed that LPS thin-films prepared from [70-30] solution are dense, homogeneous and amorphous, while LPS thin-films obtained from [80-20] and [75-25] precursors are crystalline and have granular or columnar structures. Electrochemical analysis showed that LPS films derived from [75-25] coating solution are short circuited, while LPS thin-films prepared from [70-30] and [80-20] solution exhibit lithium-ion conductivities in the order of $10^{-5}\,S\,cm^{-1}$. Amorphous LPS layers derived from [70-30] seems to be the most suitable films for applications as solid electrolyte in SSBs, despite their high fraction of oxygen and the ageing of the coating solution, as these films exhibit a high ionic conductivity, a low electronic conductivity as well as a crack free and homogeneous layer.

The influence of several deposition parameters on morphology and lithium-ion conductivity of LPS thin-films derived from freshly prepared [70-30] coating solutions was investigated. The most promising layers were obtained by a drop casting process and by applying a two stage heating process including deposition at elevated temperatures (80 °C) and predrying at this temperature for 30 min followed by drying at 250 °C for 60 min. Precise tuning of the film thickness from 0.3 to 2.3 µm was achieved by changing the deposition volume or the concentration of the coating solution. Preliminary printing experiments with [70-30] coating solution were carried successfully, although further process optimisation is necessary.

LPS thin-films prepared by drop casting from [70-30] solution exhibit a lithium-ion conductivity of $3.2 \cdot 10^{-5}\,S\,cm^{-1}$ and an activation energy of 0.38 eV. The stability against Li metal was further investigated by *In situ* XPS analysis, which revealed the formation of a stable solid electrolyte interphase (SEI) between lithium metal and LPS solid electrolyte layers. Stable conductivities and cycling performance of Si/LPS/Li half-cells indicate the protecting function of the SEI and demonstrate the excellent electrochemical properties of amorphous LPS thin-films.

LPS thin-film electrolytes were successfully integrated as solid electrolyte separator in a microbattery using lithium (Li) as anode and printed lithium titanate $Li_4Ti_5O_{12}$

(LTO) as cathode. The microbattery exhibited stable cycling performance up to 500 cycles, which highlights the excellent stability of the LPS thin-films during cycling. In principle, LPS solid electrolyte layers might also be combined with other thin-film cathode materials. Therefore, solution-prepared LPS thin-films provide an alternative to LiPON layers prepared by vacuum deposition and currently applied as electrolyte in thin-film SSBs with the possibility to develop a printed microbattery.

The application of LPS thin-films as separator in bulk type SSBs with high energy densities might be achieved by direct coating of composite cathodes, which enables the possibility to reduce the SE thickness to a few µm. Therefore, deposition of LPS coating solution on top of LFP composite cathodes sheets was investigated. However, the results suggest a decomposition of the organic binder and dissolution of carbon additives in the LPS film leading to short circuits through the LPS layer. Further experiments require densification of the composite cathodes and the evaluation of different binders with higher decomposition temperatures.

In addition, the successful application of LPS as protective films to prevent reduction of bulk solid electrolytes by Li metal anodes is shown. In a next step these coated bulk SEs would have to be integrated in SSBs with Li metal anodes and the cycling behaviour of these SSBs would have to be analysed.

The excellent electrochemical properties and stability of LPS thin-films might be a result of the high oxygen content (around 50 % of S in LPS films is exchanged by O) in the thin-films. Further studies might include the variation of the oxygen content in LPS layers and the analysis of the influence of the oxygen content on electrochemical properties, stability or cycling behaviour. However, an exact adjustment of the oxygen content might be difficult to achieve with the current coating solution. A change of the concentration might offer a possibility to tune the elemental distribution of the resulting thin-film. An alternative approach would be the direct use of Li_2S-P_2S_5 glasses, where a certain amount of Li_2S or P_2S_5 is substituted by Li_2O or P_2O_5, respectively. For suppression of the S-O exchange in the coating solution thio-NMF could directly be used as solvent. Further additives might also enhance the stability of the coating solution or the resulting LPS thin-films. Thio-NMF also provides the possibility of lower drying temperatures due to the lower boiling point of thio-NMF compared to NMF. This might also enable the preparation of amorphous LPS layers from [75-25] or [80-20] solutions. However, it might be possible that thio-NMF will not dissolve the oxygen substituted LPS precursors.

SSBs offer the potential to replace LIBs especially when fast charging is required such as in EVs. However, the application of Li metal electrodes, which would be necessary to significantly increase the energy density of SSBs still remains challenging. Interfacial protection layers such as LPS solid electrolyte thin-films, which form stable interphases in contact with Li metal might prevent dendrite formation and enable the use of Li metal in SSBs.

APPENDIX
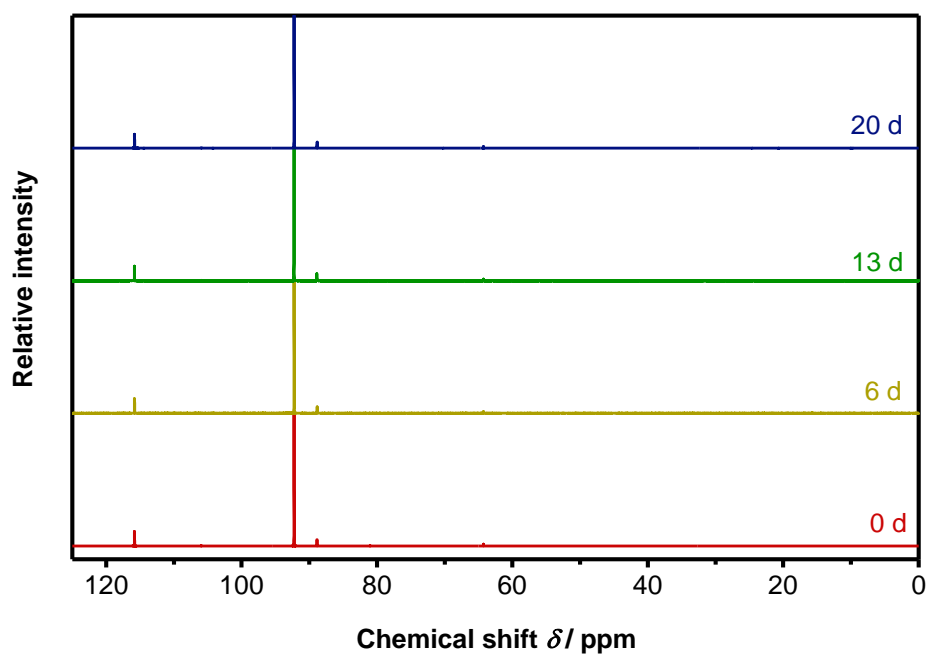
Figure 0-1: ^{31}P NMR spectra of $80Li_2S-20P_2S_5$ dissolved in NMF and aged for several days.
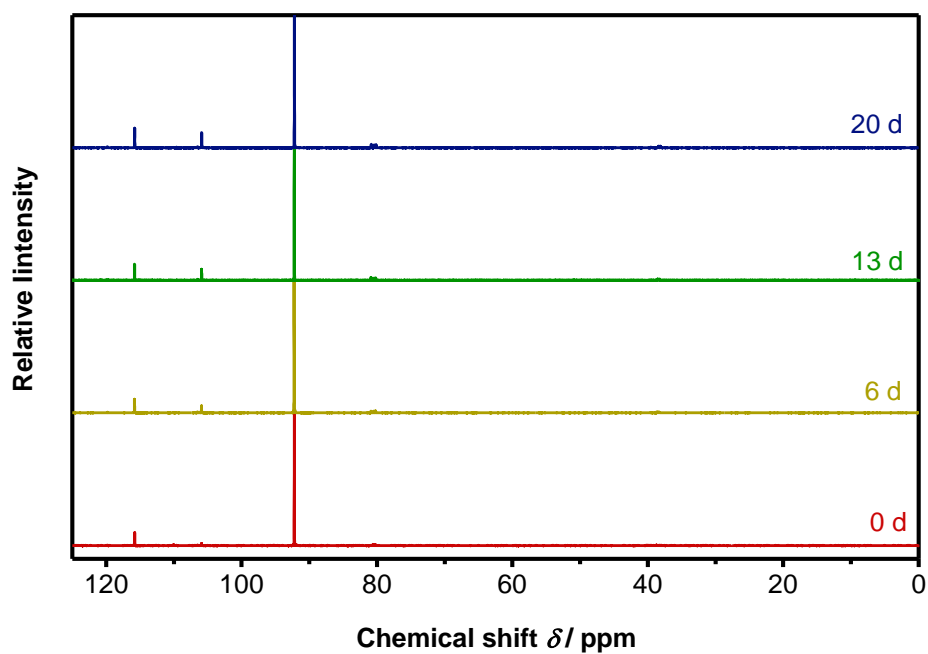
Figure 0-2: ^{31}P NMR spectra of $75Li_2S-25P_2S_5$ dissolved in NMF and aged for several days.
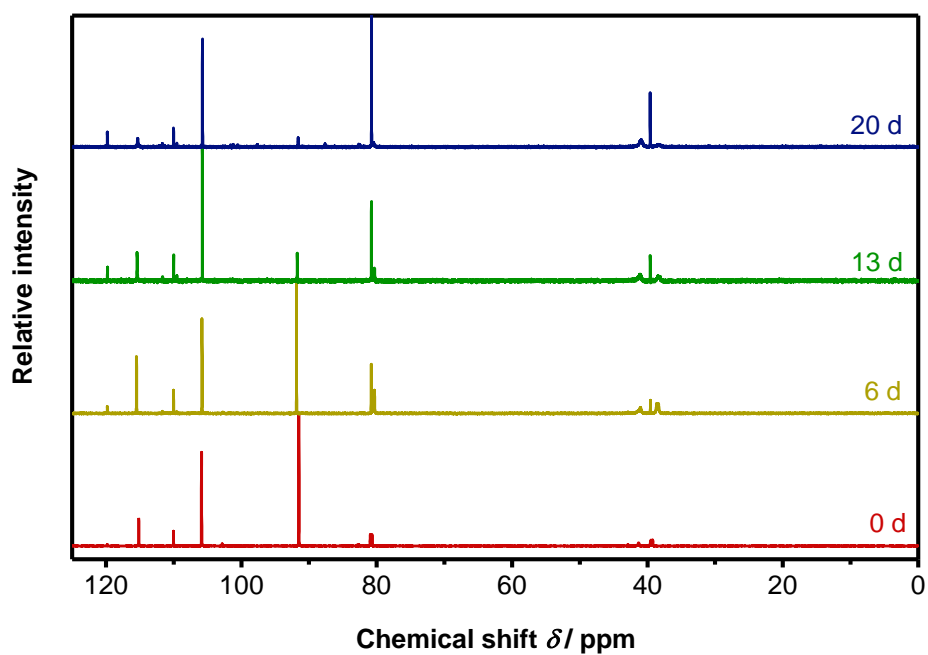
Figure 0-3: ^{31}P NMR spectra of $70Li_2S$-$30P_2S_5$ dissolved in NMF and aged for several days.
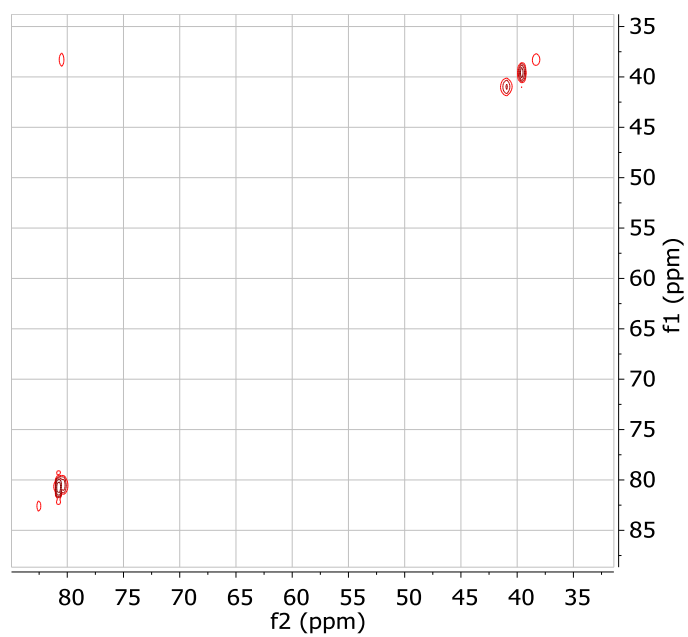
Figure 0-4: ^{31}P-^{31}P NMR spectra of $70Li_2S$-$30P_2S_5$ dissolved in NMF aged for 20 days.

75Li$_2$S-25P$_2$S$_5$
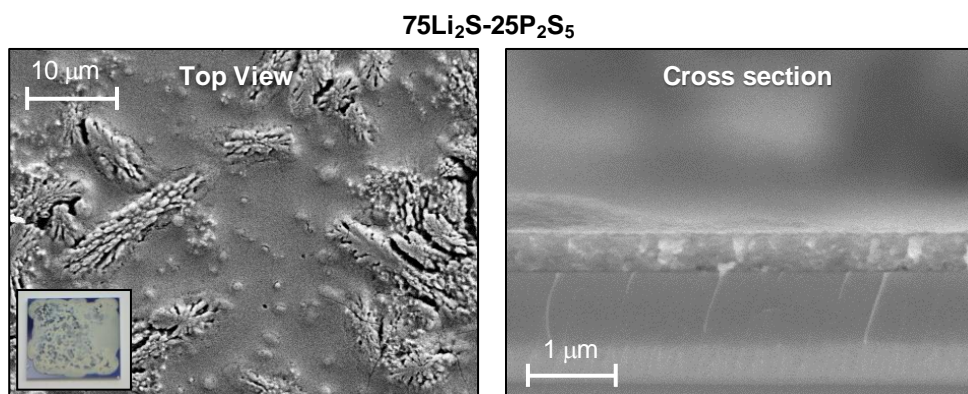
Figure 0-5: SEM cross section and top view image of a LPS thin-film (AB02) prepared on a Si substrate from a freshly prepared [75-25] coating solution. A picture of the thin- film is shown as insert.
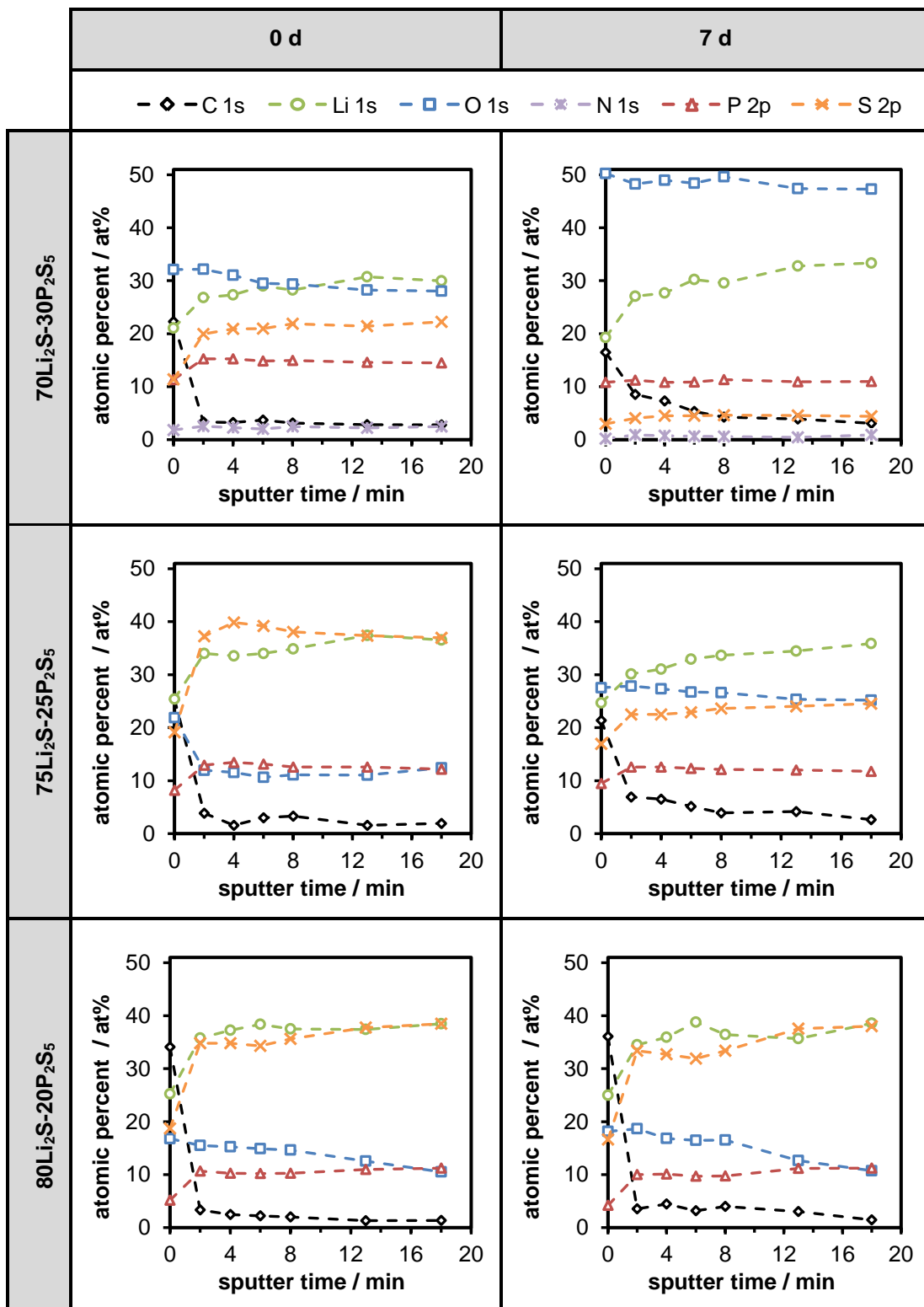
Figure 0-6: Depth profile determined by XPS analysis of LPS thin-films (AB01-AB06) derived from fresh (0 d) and aged (7 d) coating solutions using different starting materials. Shown are the atomic ratios of the different elements as a function sputter time.
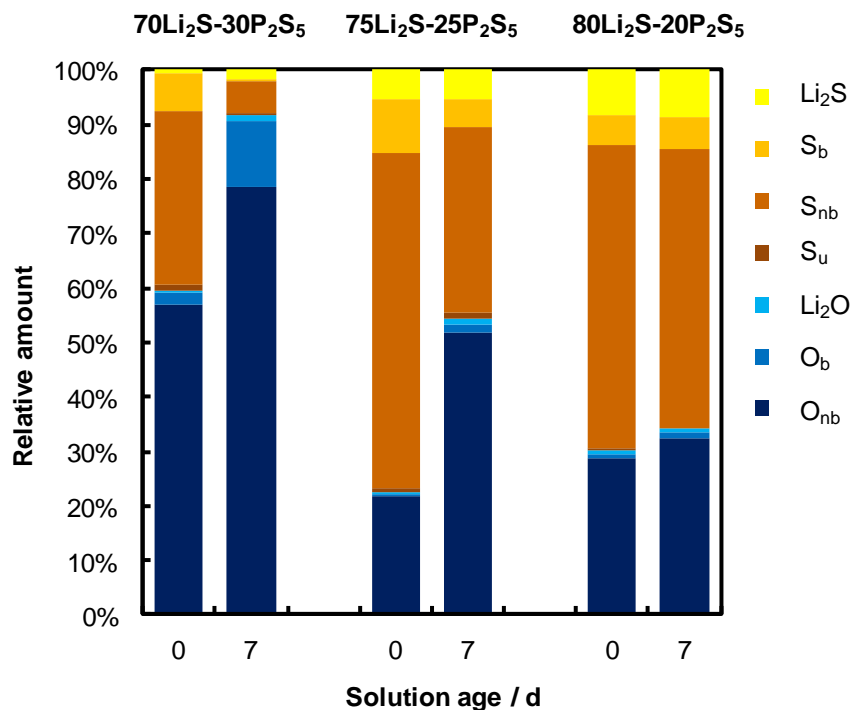
Figure 0-7: Amount of the different O and S compounds in different LPS films (AB01-AB06) relative to the stoichiometric amount of S in the precursor. The average of the fitting results from the XPS detail spectra of 2 min sputtering time to 8 min sputtering time was calculated.
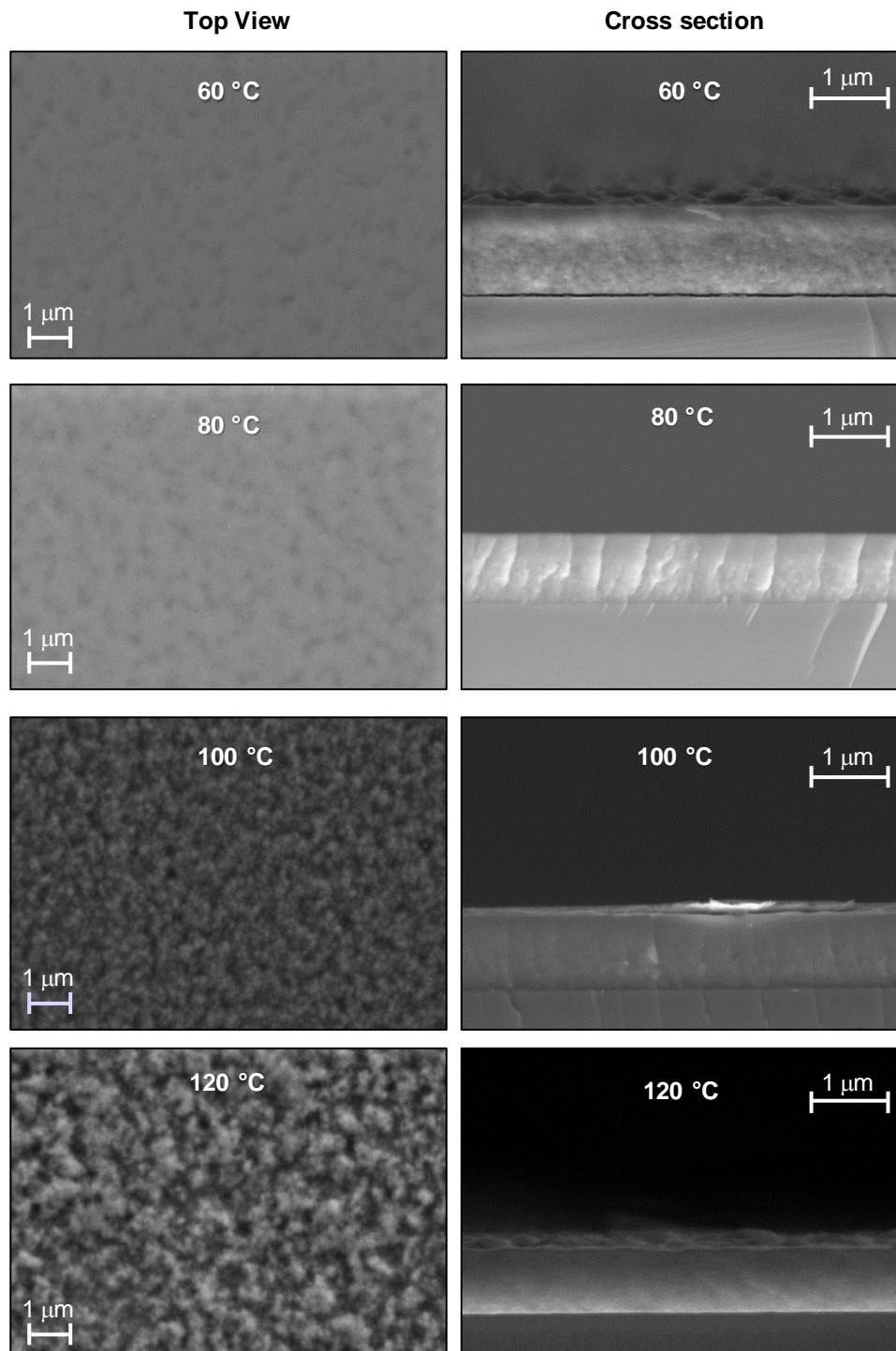
Figure 0-8: SEM cross section and top view images of LPS thin-films on conductive Si substrate deposited at different temperatures (AB07-AB13). The drying process included predrying at the deposition temperature for 30 min and subsequent heating with $10 \, °C \, min^{-1}$ to the drying temperature of 225 °C, where the films were dried for 60 min.

Top View | Cross section
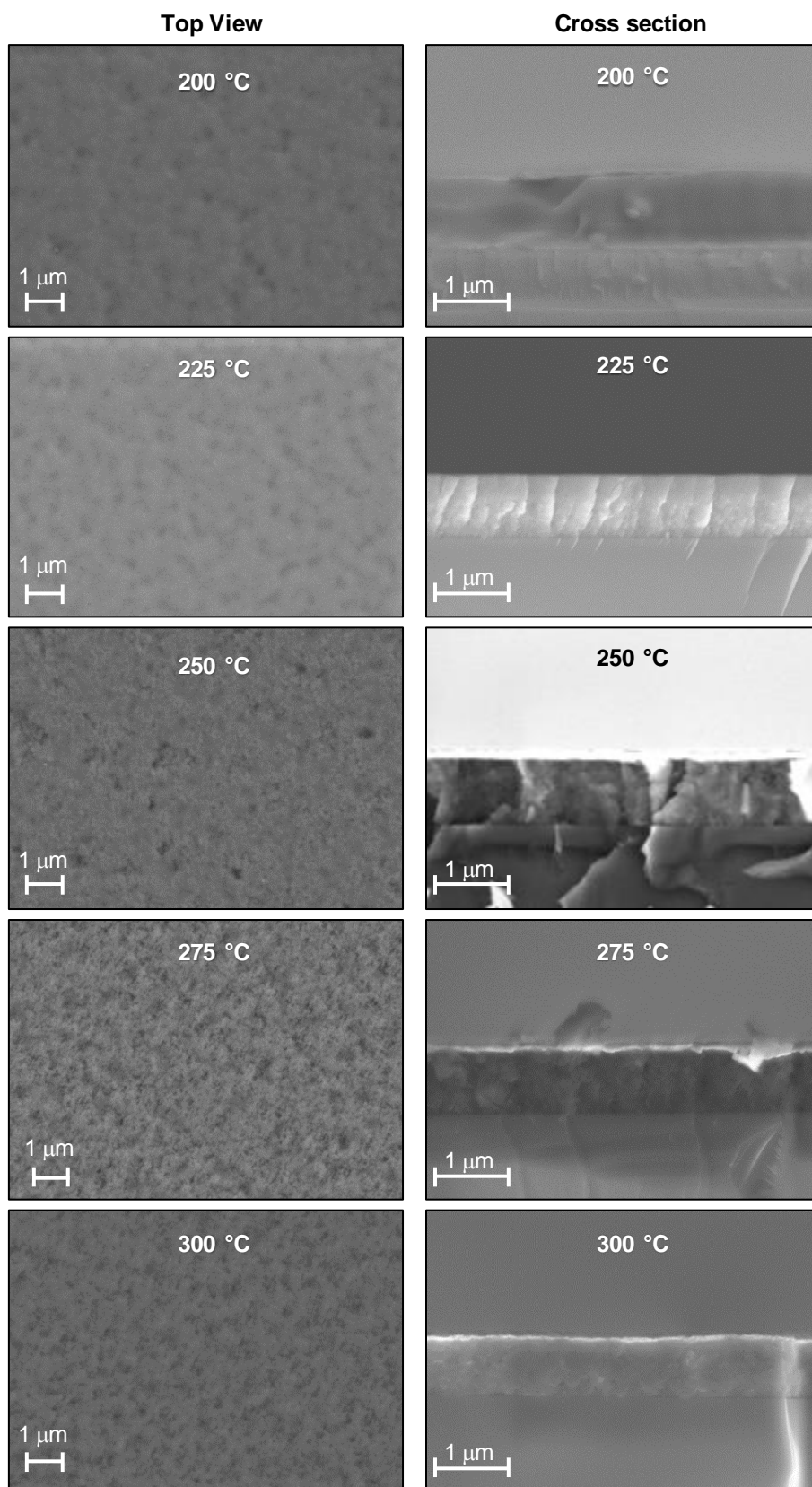
Figure 0-9: SEM cross section and top view images of LPS thin-films on Si substrates dried at different temperatures for 60 min and heated with 10 °C min^{-1} (AB16-AB20).

Top View
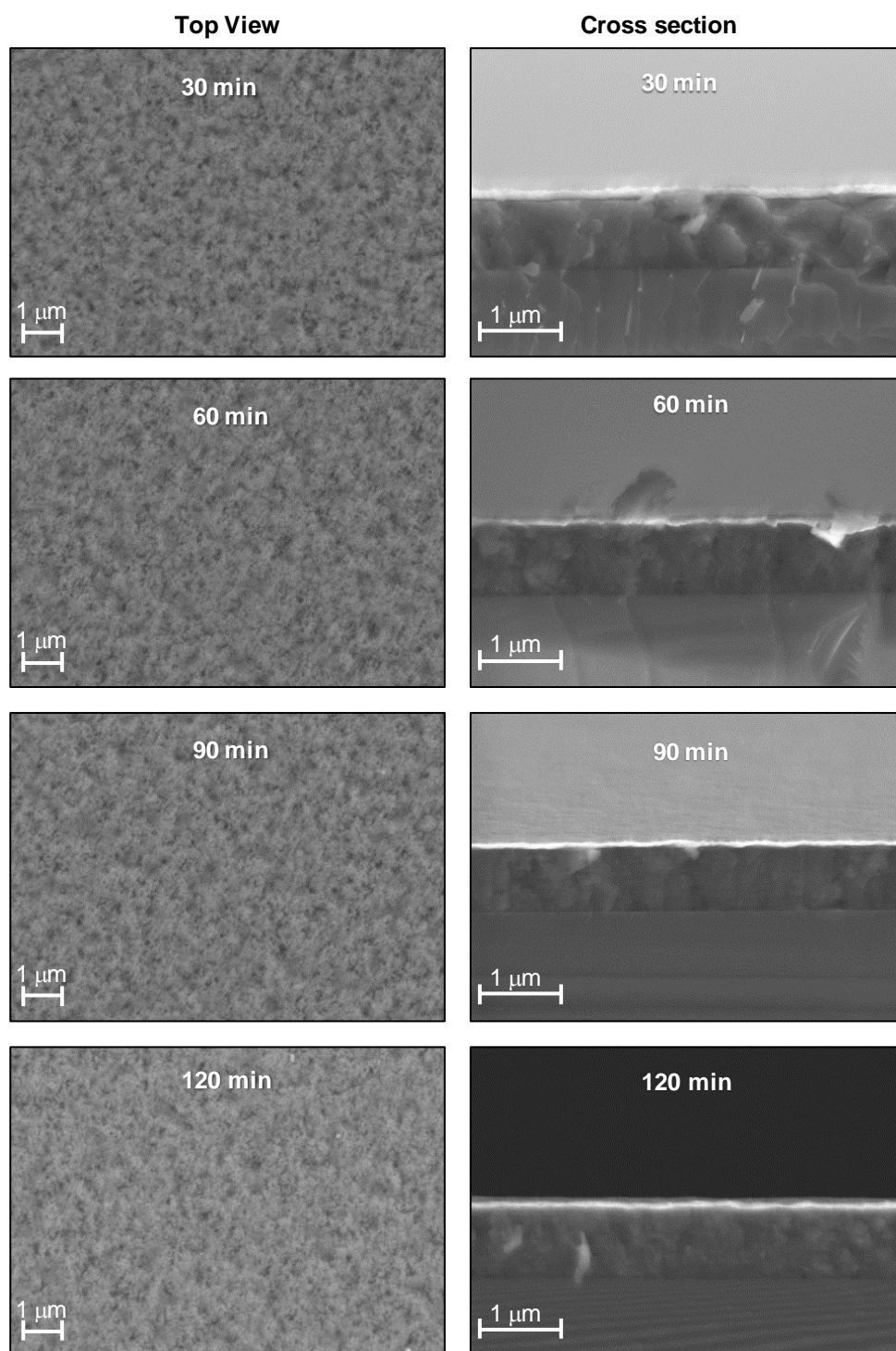
Cross section

Figure 0-10: SEM cross section and top view images of LPS thin-films on Si substrates heated with 10 °C min⁻¹ to the drying temperature of 275 °C, at which the films were dried for different times (AB15, AB21-AB23).
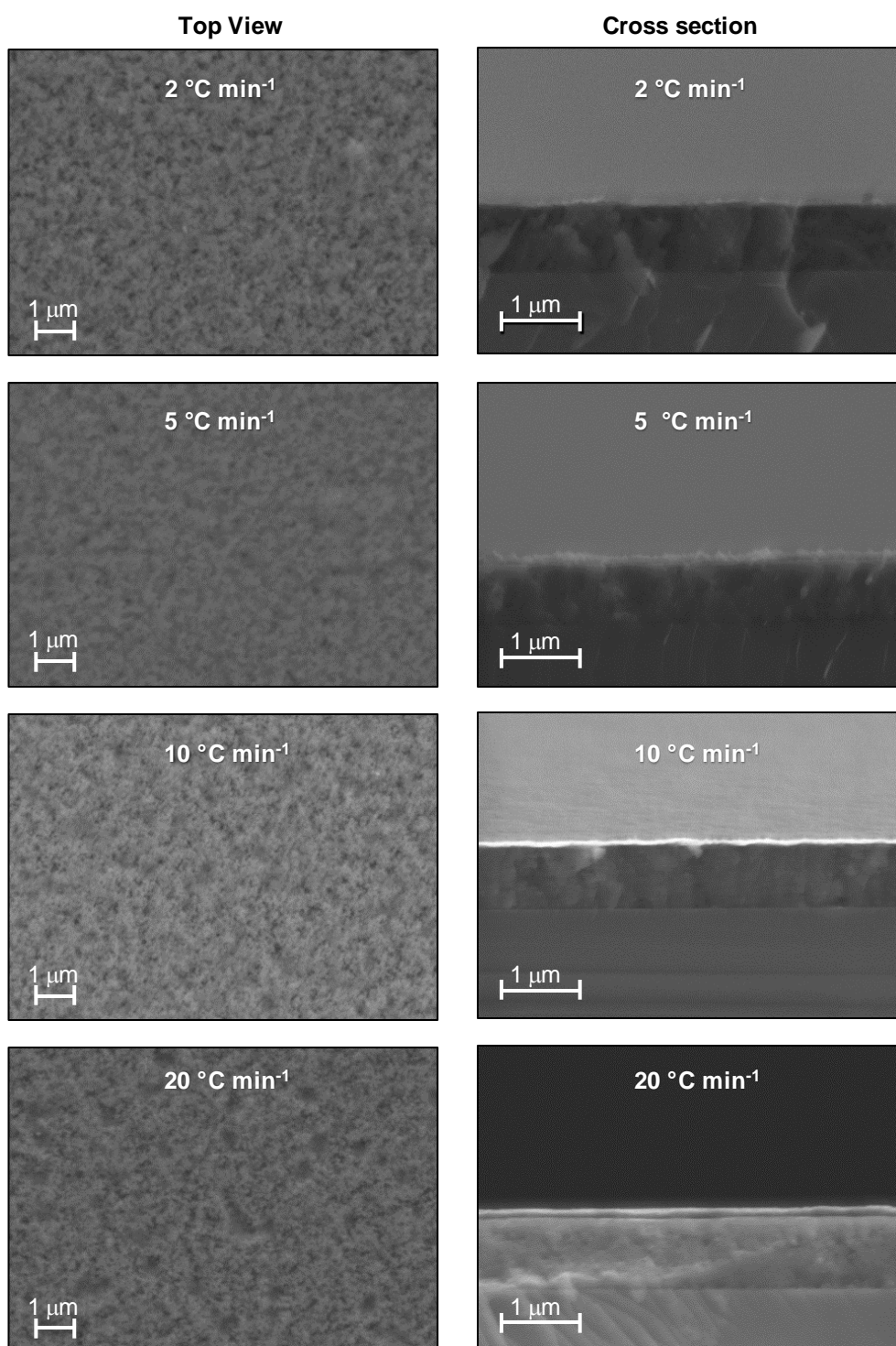
Figure 0-11: SEM cross section and top view images of LPS thin-films on Si substrates heated with different rates to the drying temperature of 275 °C, at which the films were dried for 60 min (AB22, AB24-AB26).
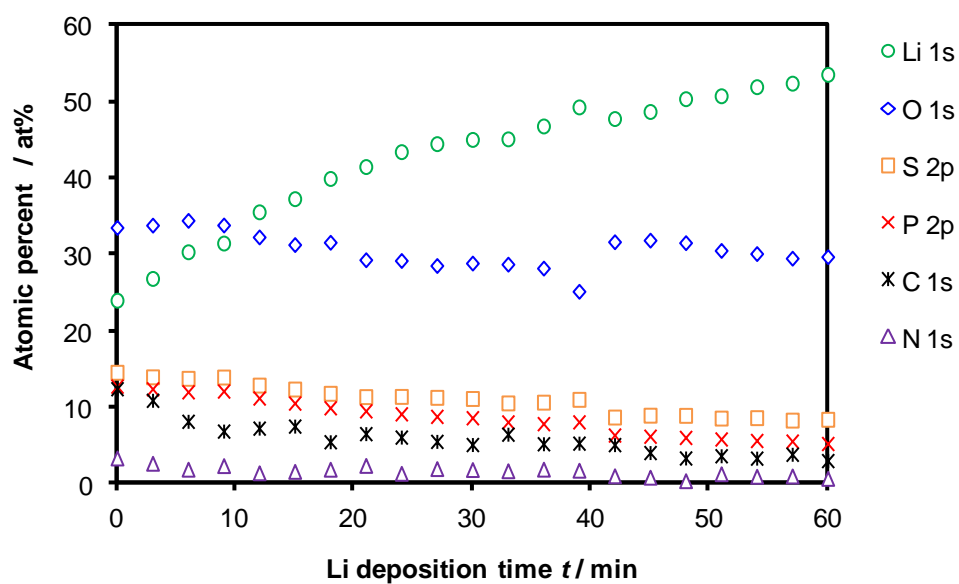
Figure 0-12: Atomic concentration of different elements in the LPS thin-film (AB35) as determined by XPS analysis in the course of Li deposition.
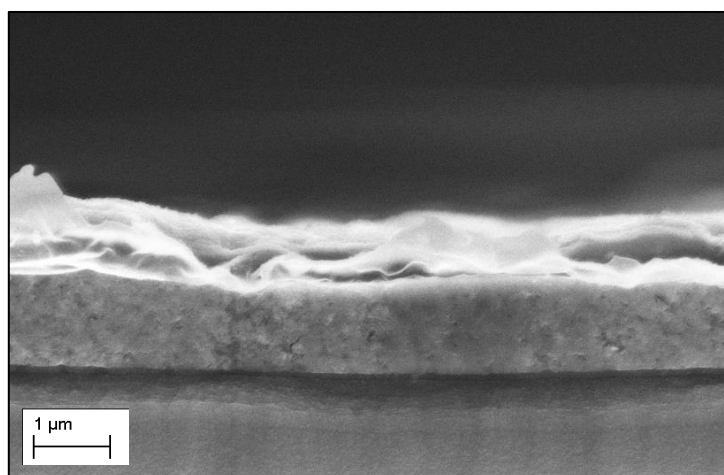
Figure 0-13: SEM picture of a Li/LPS/Si cell (AB36) after cyclic voltammetry (5 cycles) from 0 to 4 V *vs.* Li⁺/Li.
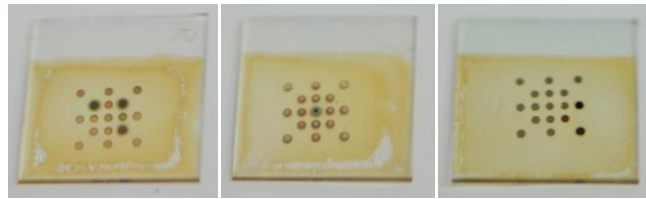
Figure 0-14: Quality control of LPS thin-films (AB40-AB42). Black circles were ascribed to short circuited contacts and defects (dust particles) in the LPS thin-film.
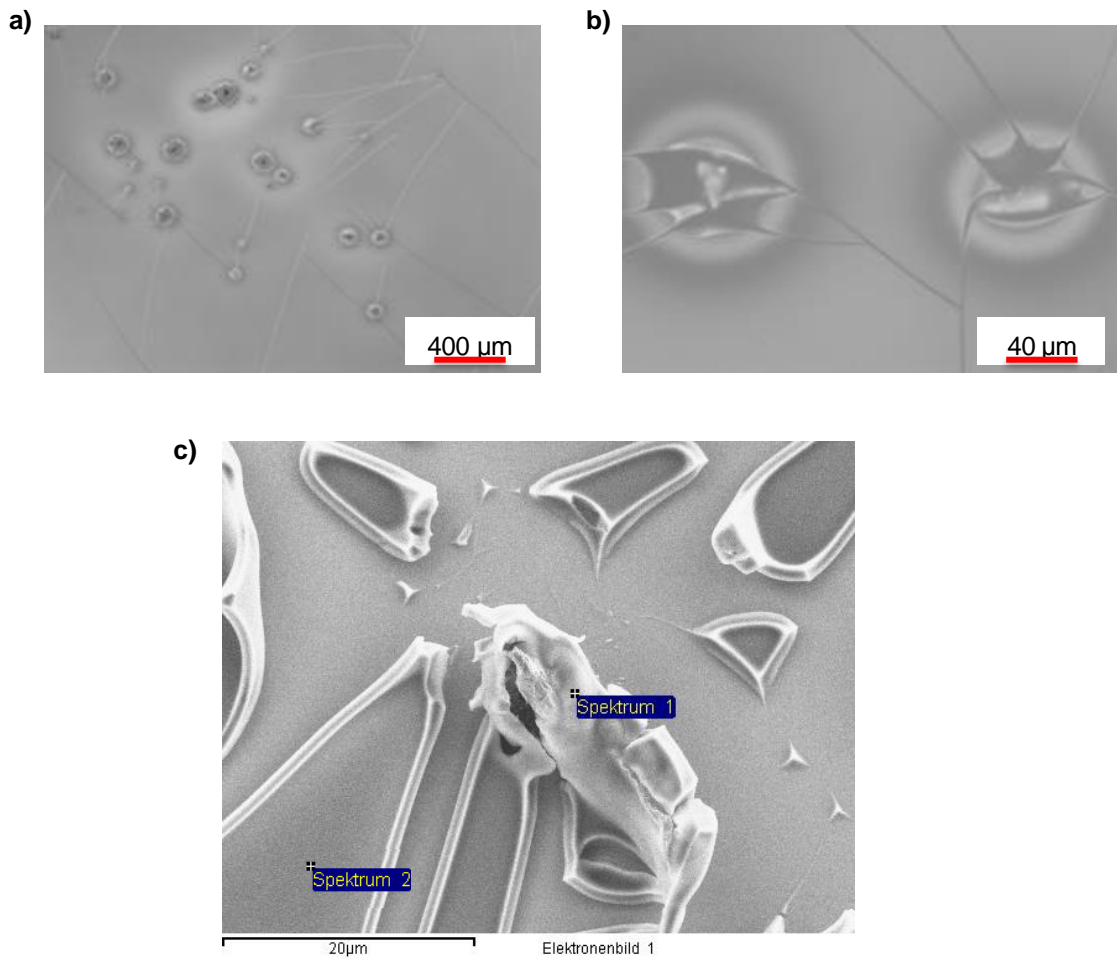
Figure 0-15: Optical microscope (a and b) and SEM images (c) of LTO thin-films prepared by inkjet-printing.

a)

b)
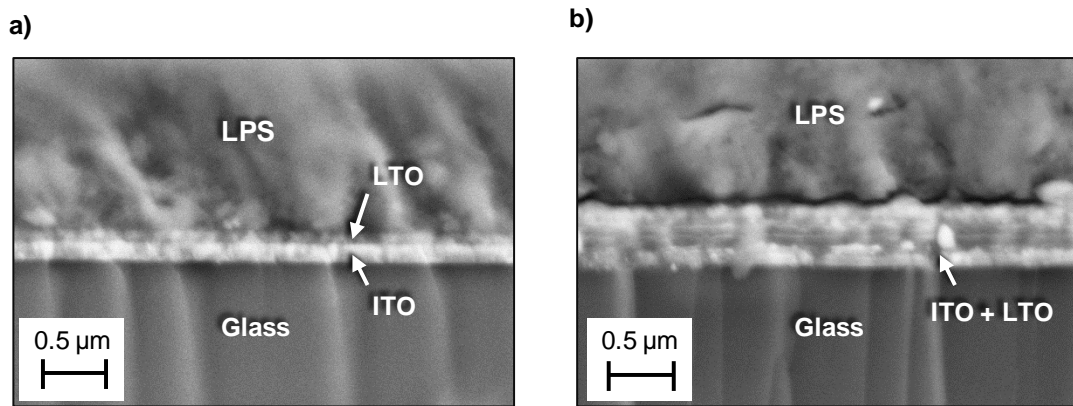
Figure 0-16: SEM image taken from a) transparent ITO in the ITO/LTO/LPS system (AB38) and b) a black ITO contact in an ITO/LTO/LPS/Li cell (AB37).
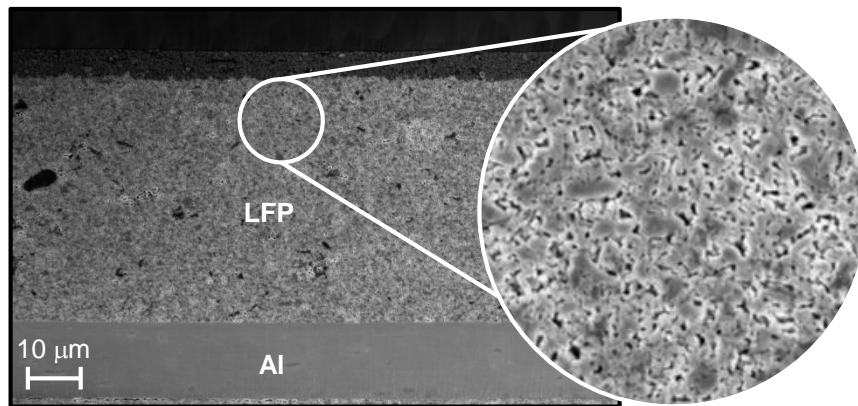
Figure 0-17: SEM cross section of LFP cathode on Al substrate.

Table 0-1: Overview of the investigated LPS systems and their corresponding structural and electrochemical characterisation techniques.

Number	Setup	Characterisation techniques
AB01	Au/Si/LPS/(Au)	SEM, XRD, EDX, XPS, EIS (T), DC
AB02	Au/Si/LPS/(Au)	SEM, XRD, EDX, XPS, DC
AB03	Au/Si/LPS/(Au)	SEM, XRD, EDX, XPS, EIS, DC
AB04	Au/Si/LPS/(Au)	SEM, XRD, EDX, XPS, DC
AB05	Au/Si/LPS/(Au)	SEM, XRD, EDX, XPS, DC
AB06	Au/Si/LPS/(Au)	SEM, XRD, EDX, XPS, EIS, DC
AB07	Au/Si/LPS/Au	SEM, EIS, DC
AB08	Au/Si/LPS/Au	EIS, DC
AB09	Au/Si/LPS/Au	SEM, EIS, DC
AB10	Au/Si/LPS/Au	EIS, DC
AB11	Au/Si/LPS/Au	SEM, EIS, DC
AB12	Au/Si/LPS/Au	EIS, DC
AB13	Au/Si/LPS/Au	SEM, EIS, DC
AB14	Au/Si/LPS/Au	EIS, DC
AB15	Au/Si/LPS/Au	EIS, DC
AB16	Au/Si/LPS/Au	SEM, EIS, DC
AB17	Au/Si/LPS/Au	SEM, EIS, DC
AB18	Au/Si/LPS/Au	SEM, EIS, DC
AB19	Au/Si/LPS/Au	SEM, EIS, DC
AB20	Au/Si/LPS/Au	SEM, EIS, DC
AB21	Au/Si/LPS/Au	SEM, EIS, DC
AB22	Au/Si/LPS/Au	SEM, EIS, DC
AB23	Au/Si/LPS/Au	SEM, EIS, DC
AB24	Au/Si/LPS/Au	SEM, EIS, DC
AB25	Au/Si/LPS/Au	SEM, EIS, DC
AB26	Au/Si/LPS/Au	SEM, EIS, DC
AB27	Au/Si/LPS/Au	SEM, EIS, DC
AB28	Au/Si/LPS/Au	SEM
AB29	Au/Si/LPS/Au	SEM
AB30	Au/Si/LPS/Au	SEM
AB31	Au/Si/LPS/Au	SEM
AB32	Au/Si/LPS/Au	SEM
AB33	Au/Si/LPS/Au	SEM
AB34	Au/Si/LPS/Li	SEM, EIS (t), DC
AB35	Si/LPS/Li	*In situ* XPS
AB36	Au/Si/LPS/Li	CV, CCD + EIS
AB37	ITO/LTO/LPS/Li	CV
AB38	ITO/LPS/Li	CV
AB43	ITO/LTO/LPS/Li	SEM, CV, CCD + EIS
AB48	Au/Ohara/LPS/Li	SEM, EIS (t)
AB49	Au/Ohara/Li	EIS (t)
AB50	Au/Ohara/LPS/Au	EIS (t)
AB51	Au/Ohara/Au	EIS (t)

Table 0-2: Fitting results of EIS from various LPS films (AB01, AB03, AB06) in Si/LPS/Au setups. The data were fitted using an equivalent circuit $(R_1Q_1)Q_2$, that comprises a resistance R_1 parallel to a constant phase element (CPE) Q_1 in series with a second constant phase element Q_2.

Number	R_1 / Ω	$Y_{0,1}$ / S s^a	a_1	$Y_{0,2}$ / S s^a	a_2
AB01	130 ± 16	$1.61{\cdot}10^{-7} \pm 3.24{\cdot}10^{-8}$	0.648 ± 0.009	$2.93{\cdot}10^{-8} \pm 1.48{\cdot}10^{-9}$	0.969 ± 0.001
AB03	1008 ± 456	$2.73{\cdot}10^{-7} \pm 4.32{\cdot}10^{-9}$	0.658 ± 0.018	$2.40{\cdot}10^{-8} \pm 1.38{\cdot}10^{-9}$	0.895 ± 0.011
AB06	862 ± 393	$9.25{\cdot}10^{-6} \pm 1.85{\cdot}10^{-5}$	0.572 ± 0.202	$2.63{\cdot}10^{-8} \pm 1.02{\cdot}10^{-8}$	0.902 ± 0.012

Table 0-3: Impedance, thickness and conductivity values of LPS thin-films with variation in the drying process. Impedance values are obtained from EIS data fitting, layer thicknesses from SEM images and conductivities are calculated according to equation 3-3. In addition, the temperatures during EIS measurements are given.

Number	Impedance / Ω	Impedance / Ω cm²	Thickness / µm	Conductivity / S cm^{-1}	Temperature / °C
AB07	138.5	4.00	0.92	$2.30{\cdot}10^{-5}$	26.0
AB08	124.1	3.59	-		26.0
AB09	120.5	3.48	0.95	$2.73{\cdot}10^{-5}$	26.0
AB10	131.8	3.81	-		26.1
AB11	180.9	5.23	0.89	$1.69{\cdot}10^{-5}$	26.3
AB12	216.5	6.26	-		26.3
AB13	251.3	7.26	0.84	$1.15{\cdot}10^{-5}$	26.0
AB16	797.7	23.05	1.17	$5.08{\cdot}10^{-6}$	25.5
AB17	137.5	3.97	0.95	$2.39{\cdot}10^{-5}$	24.9
AB18	107.1	3.10	0.84	$2.71{\cdot}10^{-5}$	24.5
AB19	104.7	3.03	0.90	$2.97{\cdot}10^{-5}$	25.1
AB20	94.5	2.73	0.76	$2.79{\cdot}10^{-5}$	25.1
AB21	111.5	3.22	0.87	$2.70{\cdot}10^{-5}$	25.7
AB22	85.9	2.48	0.81	$3.26{\cdot}10^{-5}$	25.3
AB23	91.5	2.64	0.86	$3.25{\cdot}10^{-5}$	25.3
AB24	124.7	3.60	0.93	$2.57{\cdot}10^{-5}$	25.3
AB25	81.3	2.35	0.89	$3.77{\cdot}10^{-5}$	25.3
AB26	74.8	2.16	0.69	$3.17{\cdot}10^{-5}$	25.5

Table 0-4: Fitting results from temperature dependent EIS measured in a Si/LPS/Au (AB01) setup. The data were fitted using an equivalent circuit $(R_1 Q_1) Q_2$, that comprises a resistance R_1 parallel to a constant phase element (CPE) Q_1 in series with a second constant phase element Q_2.

T / °C	R_1 / Ω	$Y_{0,1}$ / S s^a	a_1	$Y_{0,2}$ / S s^a	a_2
30	88.8	$5.91 \cdot 10^{-7}$	0.594	$2.62 \cdot 10^{-8}$	0.980
25	111	$4.01 \cdot 10^{-7}$	0.617	$2.53 \cdot 10^{-8}$	0.980
20	141	$2.57 \cdot 10^{-7}$	0.642	$2.55 \cdot 10^{-8}$	0.979
15	178	$1.79 \cdot 10^{-7}$	0.662	$2.56 \cdot 10^{-8}$	0.978
10	233	$1.37 \cdot 10^{-7}$	0.676	$2.58 \cdot 10^{-8}$	0.977
5	299	$1.04 \cdot 10^{-7}$	0.689	$2.62 \cdot 10^{-8}$	0.975
0	395	$8.46 \cdot 10^{-8}$	0.699	$2.66 \cdot 10^{-8}$	0.972
-5	515	$6.57 \cdot 10^{-8}$	0.712	$2.74 \cdot 10^{-8}$	0.969
-10	695	$5.62 \cdot 10^{-8}$	0.718	$2.78 \cdot 10^{-8}$	0.967

Table 0-5: Fitting results from time-dependent EIS measured in a Si/LPS/Li (AB34) setup. The data were fitted using an equivalent circuit $(R_1 Q_1) Q_2$, that comprises a resistance R_1 parallel to a constant phase element (CPE) Q_1 in series with a second constant phase element Q_2.

T / °C	R_1 / Ω	$Y_{0,1}$ / S s^a	a_1	$Y_{0,2}$ / S s^a	a_2
0	224	$3.45 \cdot 10^{-8}$	0.721	$1.94 \cdot 10^{-8}$	0.940
1	226	$3.45 \cdot 10^{-8}$	0.721	$1.93 \cdot 10^{-8}$	0.941
2	226	$3.46 \cdot 10^{-8}$	0.721	$1.92 \cdot 10^{-8}$	0.941
3	226	$3.40 \cdot 10^{-8}$	0.722	$1.92 \cdot 10^{-8}$	0.941
4	226	$3.39 \cdot 10^{-8}$	0.722	$1.93 \cdot 10^{-8}$	0.940
5	226	$3.39 \cdot 10^{-8}$	0.722	$1.92 \cdot 10^{-8}$	0.941
6	229	$3.39 \cdot 10^{-8}$	0.722	$1.92 \cdot 10^{-8}$	0.941
7	230	$3.44 \cdot 10^{-8}$	0.721	$1.92 \cdot 10^{-8}$	0.941
8	230	$3.43 \cdot 10^{-8}$	0.721	$1.92 \cdot 10^{-8}$	0.941
9	230	$3.44 \cdot 10^{-8}$	0.721	$1.91 \cdot 10^{-8}$	0.941
10	230	$3.44 \cdot 10^{-8}$	0.721	$1.91 \cdot 10^{-8}$	0.941
11	230	$3.33 \cdot 10^{-8}$	0.723	$1.93 \cdot 10^{-8}$	0.940
12	231	$3.39 \cdot 10^{-8}$	0.722	$1.91 \cdot 10^{-8}$	0.941
13	232	$3.46 \cdot 10^{-8}$	0.720	$1.91 \cdot 10^{-8}$	0.941
14	232	$3.39 \cdot 10^{-8}$	0.721	$1.91 \cdot 10^{-8}$	0.941
15	232	$3.42 \cdot 10^{-8}$	0.721	$1.91 \cdot 10^{-8}$	0.941
16	232	$3.41 \cdot 10^{-8}$	0.721	$1.91 \cdot 10^{-8}$	0.941
17	232	$3.47 \cdot 10^{-8}$	0.720	$1.90 \cdot 10^{-8}$	0.941
18	232	$3.41 \cdot 10^{-8}$	0.721	$1.90 \cdot 10^{-8}$	0.941
19	232	$3.40 \cdot 10^{-8}$	0.721	$1.90 \cdot 10^{-8}$	0.941
20	232	$3.46 \cdot 10^{-8}$	0.720	$1.90 \cdot 10^{-8}$	0.941
21	232	$3.42 \cdot 10^{-8}$	0.721	$1.90 \cdot 10^{-8}$	0.941
22	231	$3.39 \cdot 10^{-8}$	0.721	$1.90 \cdot 10^{-8}$	0.941
23	231	$3.42 \cdot 10^{-8}$	0.721	$1.90 \cdot 10^{-8}$	0.941
24	231	$3.37 \cdot 10^{-8}$	0.722	$1.90 \cdot 10^{-8}$	0.941
25	230	$3.38 \cdot 10^{-8}$	0.721	$1.90 \cdot 10^{-8}$	0.941
26	231	$3.37 \cdot 10^{-8}$	0.722	$1.90 \cdot 10^{-8}$	0.941
27	231	$3.38 \cdot 10^{-8}$	0.721	$1.90 \cdot 10^{-8}$	0.941
28	232	$3.39 \cdot 10^{-8}$	0.721	$1.90 \cdot 10^{-8}$	0.941
29	232	$3.41 \cdot 10^{-8}$	0.721	$1.90 \cdot 10^{-8}$	0.941
30	232	$3.40 \cdot 10^{-8}$	0.721	$1.90 \cdot 10^{-8}$	0.941
31	232	$3.40 \cdot 10^{-8}$	0.721	$1.90 \cdot 10^{-8}$	0.941
32	232	$3.39 \cdot 10^{-8}$	0.721	$1.90 \cdot 10^{-8}$	0.941
33	231	$3.40 \cdot 10^{-8}$	0.721	$1.90 \cdot 10^{-8}$	0.941
34	231	$3.41 \cdot 10^{-8}$	0.721	$1.90 \cdot 10^{-8}$	0.941
35	232	$3.39 \cdot 10^{-8}$	0.721	$1.90 \cdot 10^{-8}$	0.941
36	232	$3.37 \cdot 10^{-8}$	0.721	$1.90 \cdot 10^{-8}$	0.941
37	232	$3.39 \cdot 10^{-8}$	0.721	$1.90 \cdot 10^{-8}$	0.941
38	232	$3.37 \cdot 10^{-8}$	0.721	$1.90 \cdot 10^{-8}$	0.941
39	232	$3.37 \cdot 10^{-8}$	0.721	$1.90 \cdot 10^{-8}$	0.941
40	231	$3.36 \cdot 10^{-8}$	0.722	$1.90 \cdot 10^{-8}$	0.941
41	232	$3.37 \cdot 10^{-8}$	0.722	$1.90 \cdot 10^{-8}$	0.941
42	232	$3.33 \cdot 10^{-8}$	0.722	$1.90 \cdot 10^{-8}$	0.941

T / °C	R_1 / Ω	$Y_{0,1}$ / S s^a	a_1	$Y_{0,2}$ / S s^a	a_2
43	232	$3.34 \cdot 10^{-8}$	0.722	$1.90 \cdot 10^{-8}$	0.941
44	231	$3.39 \cdot 10^{-8}$	0.721	$1.90 \cdot 10^{-8}$	0.941
45	231	$3.37 \cdot 10^{-8}$	0.721	$1.90 \cdot 10^{-8}$	0.941
46	230	$3.37 \cdot 10^{-8}$	0.721	$1.90 \cdot 10^{-8}$	0.941
47	229	$3.34 \cdot 10^{-8}$	0.722	$1.90 \cdot 10^{-8}$	0.941
48	230	$3.36 \cdot 10^{-8}$	0.722	$1.90 \cdot 10^{-8}$	0.941
49	229	$3.38 \cdot 10^{-8}$	0.721	$1.90 \cdot 10^{-8}$	0.941
50	228	$3.33 \cdot 10^{-8}$	0.722	$1.91 \cdot 10^{-8}$	0.941
51	227	$3.35 \cdot 10^{-8}$	0.722	$1.91 \cdot 10^{-8}$	0.941
52	228	$3.38 \cdot 10^{-8}$	0.721	$1.90 \cdot 10^{-8}$	0.941
53	229	$3.37 \cdot 10^{-8}$	0.721	$1.90 \cdot 10^{-8}$	0.941
54	230	$3.35 \cdot 10^{-8}$	0.722	$1.90 \cdot 10^{-8}$	0.941
55	230	$3.36 \cdot 10^{-8}$	0.721	$1.90 \cdot 10^{-8}$	0.941
56	230	$3.37 \cdot 10^{-8}$	0.721	$1.90 \cdot 10^{-8}$	0.941
57	232	$3.38 \cdot 10^{-8}$	0.721	$1.90 \cdot 10^{-8}$	0.941
58	231	$3.35 \cdot 10^{-8}$	0.722	$1.90 \cdot 10^{-8}$	0.941
59	232	$3.38 \cdot 10^{-8}$	0.721	$1.90 \cdot 10^{-8}$	0.941
60	232	$3.36 \cdot 10^{-8}$	0.721	$1.90 \cdot 10^{-8}$	0.941

Table 0-6: Elemental quantification obtained from XPS analysis after depth profiling (AB35). One profile was recorded before lithium deposition the second after lithium deposition at a different position.

	O 1s	Li 1s	C 1s	P 2p	S 2p	N 1s	S/P	S/O	P/O
Before Li deposition	28%	31%	3.1%	15%	21%	2.6%	1.4	0.74	0.51
After Li deposition	29%	28%	3.5%	14%	22%	2.1%	1.4	0.77	0.53

Table 0-7: Peak positions from CV curves of a Si/LPS/Li system (AB36) recorded between 0 and 4 V *vs.* Li$^+$/Li for 1 to 5 cycles. Peak positions from CV measurements of Si nanowires are included as reference.[249]

Peak	Cycle 1	Cycle 2	Cycle 3	Cycle 4	Cycle 5	Ref [249]
1	147.3 mV*	181.7 mV	159.3 mV	153.1 mV	139.3 mV	211 mV
2	0 mV	0 mV	0 mV	0 mV	0 mV	0 mV
3	317.2 mV	326.6	339.2 mV	343.0	349.1 mV	345 mV
4	507.1 mV	516.5 mV	529.1 mV	532.9	539.0 mV	485 mV

Table 0-8: Fitting results of EIS coupled with galvanostatic cycling of a Si/LPS/Li half-cell (AB36). The data were fitted using an equivalent circuit $(R_1Q_1)Q_2$, that comprises a resistance R_1 parallel to a constant phase element (CPE) Q_1 in series with a second constant phase element Q_2.

Cycle number	R_1 / Ω	$Y_{0,1}$ / S s^a	a_1	$Y_{0,2}$ / S s^a	a_2
1	276	$2.91 \cdot 10^{-7}$	0.588	$7.76 \cdot 10^{-8}$	0.894
2	276	$3.07 \cdot 10^{-7}$	0.585	$8.18 \cdot 10^{-8}$	0.891
3	275	$3.27 \cdot 10^{-7}$	0.581	$8.52 \cdot 10^{-8}$	0.889
4	275	$3.42 \cdot 10^{-7}$	0.579	$8.75 \cdot 10^{-8}$	0.888
5	273	$3.53 \cdot 10^{-7}$	0.577	$8.95 \cdot 10^{-8}$	0.886
6	272	$3.81 \cdot 10^{-7}$	0.572	$9.05 \cdot 10^{-8}$	0.886
7	273	$3.99 \cdot 10^{-7}$	0.569	$9.21 \cdot 10^{-8}$	0.885
8	276	$4.21 \cdot 10^{-7}$	0.565	$9.31 \cdot 10^{-8}$	0.884
9	282	$4.26 \cdot 10^{-7}$	0.564	$9.45 \cdot 10^{-8}$	0.883
10	288	$4.29 \cdot 10^{-7}$	0.562	$9.56 \cdot 10^{-8}$	0.882

Table 0-9: EDX results of LTO thin-films prepared by inkjet-printing. The corresponding SEM image is shown in Figure 0-15.

	O/ At.-%	Si/ At.-%	Ti/ At.-%	In/ At.-%
$Li_4Ti_5O_{12}$	70.59		29.41	
Spektrum 1	71.46	0.59	27.95	-
Spektrum 2	69.4	0.76	27.44	2.41

Table 0-10: Fitting results of time-dependent EIS of the different Ohara setups (AB48-AB51). The data were fitted using the equivalent circuits given in Table 4-5.

Setup	Number	t / d	R_0 / kΩ	R_1 / kΩ	$Y_{0,1}$ / S s^a	a_1	R_2 / kΩ	$Y_{0,2}$ / S s^a	a_2	R_3 / kΩ	$Y_{0,3}$ / S s^a	a_3
Au/Ohara/Au	AB51	0	0.856	3.24	$1.86 \cdot 10^{-10}$	0.971	32.8	$5.73 \cdot 10^{-8}$	1.00	7 110	$3.65 \cdot 10^{-8}$	0.907
Au/Ohara/Au	AB51	1	0.726	3.85	$3.92 \cdot 10^{-10}$	0.913	36.6	$4.59 \cdot 10^{-8}$	0.998	24 500	$3.04 \cdot 10^{-8}$	0.934
Au/Ohara/Au	AB51	2	0.704	3.85	$3.95 \cdot 10^{-10}$	0.910	53.4	$5.75 \cdot 10^{-8}$	1.00	3 630	$3.89 \cdot 10^{-8}$	0.897
Au/Ohara/Au	AB51	3	0.772	4.04	$4.02 \cdot 10^{-10}$	0.910	59.7	$7.52 \cdot 10^{-8}$	0.931	16 300	$2.68 \cdot 10^{-8}$	0.947
Au/Ohara/LPS/Au	AB50	0	0.751	3.66	$4.30 \cdot 10^{-10}$	0.902	48.9	$3.50 \cdot 10^{-7}$	0.820	-	$8.49 \cdot 10^{-8}$	0.939
Au/Ohara/LPS/Au	AB50	1	0.767	4.08	$4.72 \cdot 10^{-10}$	0.893	35.4	$2.09 \cdot 10^{-7}$	0.912	-	$9.05 \cdot 10^{-8}$	0.909
Au/Ohara/LPS/Au	AB50	2	0.849	4.07	$4.54 \cdot 10^{-10}$	0.894	28.3	$1.32 \cdot 10^{-6}$	0.682	-	$9.18 \cdot 10^{-8}$	0.946
Au/Ohara/LPS/Au	AB50	3	0.789	4.22	$4.53 \cdot 10^{-10}$	0.895	41.0	$3.62 \cdot 10^{-7}$	0.823	-	$8.66 \cdot 10^{-8}$	0.927
Au/Ohara/LPS/Li	AB48	0	1.15	7.10	$1.88 \cdot 10^{-10}$	0.911	57.0	$2.20 \cdot 10^{-7}$	0.682	-	$1.32 \cdot 10^{-5}$	0.441
Au/Ohara/LPS/Li	AB48	1	0.991	7.62	$1.83 \cdot 10^{-10}$	0.912	64.5	$1.85 \cdot 10^{-7}$	0.697	-	$1.17 \cdot 10^{-5}$	0.459
Au/Ohara/LPS/Li	AB48	2	1.01	8.44	$2.87 \cdot 10^{-10}$	0.877	65.4	$1.39 \cdot 10^{-7}$	0.733	-	$1.08 \cdot 10^{-5}$	0.399
Au/Ohara/LPS/Li	AB48	3	1.01	8.88	$1.87 \cdot 10^{-10}$	0.902	83.1	$1.30 \cdot 10^{-7}$	0.716	-	$1.01 \cdot 10^{-5}$	0.447
Au/Ohara/Li	AB49	0	-	4 970	$3.64 \cdot 10^{-11}$	0.821	-	-	-	-	-	-
Au/Ohara/Li	AB49	1	-	11 700	$3.04 \cdot 10^{-11}$	0.830	-	-	-	-	-	-
Au/Ohara/Li	AB49	2	-	25 900	$8.35 \cdot 10^{-11}$	0.748	-	-	-	-	-	-
Au/Ohara/Li	AB49	3	-	13 600	$5.23 \cdot 10^{-11}$	0.778	-	-	-	-	-	-

BIBLIOGRAPHY

[1] M. Barghamadi, A. Kapoor, C. Wen, *J. Electrochem. Soc.* **2013**, *160*, 1256-1263.

[2] *Energie in Deutschland –Trends und Hintergründe zur Energieversorgung*, Herausgeber: Bundesministerium für Wirtschaft und Technologie (BMWi), August **2010.**

[3] J. Tellefson, *Nature* **2008***, 456*, 436-440.

[4] http://www.ford.com/cars/focus/2017/models/focus-electric/, **11.10.2017**.

[5] https://www.bmw.com/en/all-models/bmw-i/i3/2016/at-a-glance.html.html#tab-0, **10.11.2017**.

[6] https://www.nissan.co.uk/vehicles/new-vehicles/leaf.html, **10.11.2017.**

[7] https://www.tesla.com/de_DE/about/press/releases/strategic-partnership-daimleracquires-stake-tesla, **10.11.2017.**

[8] http://fueleconomy.gov, **13.12.2017**.

[9] https://www.epa.gov/greenvehicles/explaining-electric-plug-hybrid-electric-vehicles, **13.12.2017**.

[10] https://www.tesla.com/de_DE/model3, **13.12.2017**.

[11] https://www.renault.de/modellpalette/renault-modelluebersicht/zoe.html, **14.12.2017**.

[12] media.peugeot.de/file/41/8/katalog-ion-2013-07.37418.pdf, **14.12.2017**.

[13] http://www.citroen.de/modelle/citroen/citroen-c-zero.html, **14.12.2017**.

[14] G. G. Eshetu, S. Grugeon, S. Laruelle, S. Boyanov, A. Lecocq, J.-P. Bertrand, G. Marlair, *Phys. Chem. Chem. Phys.* **2013**, *15*, 9145−9155.

[15] J. Janek, W. G. Zeier, *Nat. Energy* **2016**, *1*, 16141-16144.

[16] J.-M. Tarascon, M. Armand, *Nature* **2001**, *414*, 359-367.

[17] P. G. Bruce1, S. A. Freunberger, J. Hardwick, J.-M. Tarascon, *Nat. Mat.* **2012**, *11*, 19-29.

[18] Y. Kato, S. Hori, T. Saito, K. Susuki, M. Hirayama, A. Mitsui, M. Yonemura, H. Iba, R. Kanno, *Nat. Energy* **2016**, *1*, 16030-16037.

[19] P. Adelhelm, P. Hartmann, C. L. Bender, M. Busche, C. Eufinger, J. Janek, *Beilstein J. Nanotechnol.* **2015,** *6,* 1016–1055.

[20] Z. Lin, C. Liang, *J. Mater. Chem. A* **2015**, *3*, 936-958.

[21] B. J. Bergner, A. Schümann, K. Peppler, A. Garsuch, J. Janek, *J. Am. Chem. Soc.* **2014**, *136*, 15054-15064.

[22] A. L. Robinson, J. Janek, *MRS Bull.* **2014**, *39*, 1046-1047.

[23] J. B. Goodenough, K.-S. Park*, J. Am. Chem. Soc.* **2013**, *135*, 1167-1176.

[24] W. Weppner, *Materials for Lithium-Ion Batteries* **2000**, 401-412.

[25] M. Winter, R. J. Brodd, *Chem. Rev.* **2004,** *104*, 4245-4269.

[26] B. D. McCloskey, *J. Phys. Chem. Lett.* **2015***, 6,* 4581−4588.

[27] R. A. Huggins, Advanced Batteries, Springer Science+Business Media, Stanford **2009**.

[28] http://www.elv.de/batterien-hoergeraete.html, **13.12.2017.**

[29] R. Spotnitz, Chemical Engineering Progress **2013**, *109*, 39-43.

[30] J. B. Goodenough, Y. Kim, *J. Power Sources* **2011**, *196*, 6688-6694.

[31] N.-S. Choi, Z. Chen, S. A. Freunberger, X. Ji, Y.-K. Sun, K. Amine, G. Yushi, L. F. Nazar, J.Cho, P. G. Bruce, *Angew. Chem*. **2012**, *214*, 10134-10166.

[32] M. Barghamadi, A. Kapoor, C. Wen, *J. Electrochem. Soc.* **2013**, *160*, 1256-1263.

[33] U. Kasavajjula, C. Wang, A. John Appleby, *J. Power Source*s **2007**, *163*, 1003-1039.

[34] C. K. Chan, H. Peng, G. Liu, K. McIlwrath, X. F. Zhang, R. A. Huggings, Y. Cui, *Nat. Techn.* **2008**, *3*, 31-35.

[35] A. S. Prakash, P. Manikandan, K. Ramesha, M. Sathiya, J. M. Terascon, A. K. Shukla, *Chem. Mater*. **2010**, *22*, 2857-2863.

[36] H. Yan, X. Huang, L. Zhonghua, H. Huang, R. Xue, L. Chen, *J. of Power Sources* **1997**, *68*, 530–532.

[37] Z. Shi-xi, Liu Han-xing, Ouyang Shi-xi, Li Qiang *J. Wuhan University Technology-Mater. Sci. Ed.* **2003**, *18*, 5-8.

[38] R. Gopalakrishnan, S. Goutam, L. M. Oliveira, J.-M. Timmermans, N. Omar, M. Messagie, P. Van den Bossche, J. van Mierlo , *J. Electrochem. En. Conv. Stor.* **2017**, *13*, 040801-25.

[39] A. Dinger, R. Martin, X. Mosquet, M. Rabl, D. Rizoulis, M Russo, G. Sticher, Batteries for Electric Cars: Challenges, Opportunities, and the Outlook to 2020, *The Boston Consulting Group* **2010**.

[40] K. Xu, *Chem. Rev.* **2004,** *104*, 4303-4417.

[41] Z: Li, J. Huang, B. Y. Liaw, V. Metzler, J. Zhang, *J. Power Sources* **2014**, *254*, 168-182.

[42] M. Petzel, M. Kasper, M. A. Danzer, *J. Power Sources* **2015**, *275*, 799-807.

[43] J. W. Jiang, H. Fortier, J. N. Reimers, J. R. Dahn, *J. Electrochem. Soc.* **2004**, *151*, A609-A613.

[44] P. Verma, P. Maire, P. Novák, *Electrochim. Acta* **2010**, *55*, 6332-6341.

[45] M. Falk, PhD Thesis: *Investigation of Surface Film Formation on Based Liquid Electrolytes Using the Secondary Ion Mass Spectrometry*, Justus-Liebig-Universität Gießen, **2014**.

[46] Z. Chen, Y. Qini, Y. Ren, W. Lu, C. Orendorff, E. P. Roth, K. Amine, *Energy Environ. Sci.* **2011**, *4*, 4023-4030.

[47] S. Zugmann, M. Fleischmann, M. Amerellera, R. M. Gschwind, H. D. Wiemhöfer, H. J. Gores, Electrochimica Acta **2011**, *56*, 3926–3933.

[48] K. Amine, J. Liu, S. Kang, I. Belharouak, Y. Hyung, D. Vissers, G. Henriksen, *J. Power Sources* **2004**, *129*, 14–19

[49] B. Michalak, H. Sommer, D. Mannes, A. Kaestner, T. Brezesinski, J. Janek, *Sci. Rep.* **2015**, *5*, 15627-1-15627-9.

[50] K. Naoaki, K. Shinichi, K. Yoichi, K. Makoto, *Chem. Lett.* **2000**, 1154–1155.

[51] M. C. Smart, B. V. Ratnakumar, *J. Electrochem. Soc.* **2011**, *158*, A379-A389.

[52] K. Takada, *Acta Mater.* **2013**, *61*, 759-770.

[53] A. M. Stephan, K. S. Nahm, *Polymer* **2006,** *47,* 5952–5964.

[54] Y. Seino, T. Ota, K. Takada, *Energy Environ. Sci.* **2014**, *7*, 627-631.

[55] N. Kamaya, K. Homma, Y. Yamakawa, M. Hirayama, R. Kanno, M. Yonemura, T. Kamiyama, Y. Kato, S. Hama, K. Kawamoto, A. Mitsui, *Nat. Mater.* **2011**, *10*, 682–686.

[56] K. Kerman, A. Luntz, V. Viswanathan, Y.-M. Chiang, Z. Chena, *J. Electrochem. Soc.* **2017**, *164*, A1731-A1744.

[57] A. L. Robinson, J. Janek, *MRS Bull.* **2014**, *39*, 1046-1047.

[58] Y. Zhu, X. He, Y. Mo, *ACS Appl. Mater. Interfaces* **2015**, *7*, 23685-23693.

[59] A. Sakuda, A.Hayashi, and M. Tatsumisago, *Chemistry of Materials* **2010**, 22, 949-956.

[60] J. Haruyama, K. Sodeyama, and Y. Tateyama, *ACS Appl. Mater. Interfaces* **2017**, *9*, 286-292.

[61] N. Ohta, K. Takada, I. Sakaguchi, L. Zhang, R. Ma, K. Fukuda, M. Osada, T. Sasaki, *Electrochem. Commun.* **2007**, *9*, 1486−1490.

[62] T. Kato, T. Hamanaka, K. Yamamoto, T. Hirayama, F.; Sagane, M. Motoyama, Y. Iriyama, *J. Power Sources* **2014**, *260*, 292−298.

[63] N. Ohta, K. Takada, L. Zhang, R. Ma, M. Osada, T. Sasaki,. *Adv. Mater.* **2006**, *18*, 2226−2229.

[64] H. Kitaura, A. Hayashi, K. Tadanaga, M. Tatsumisago,. *Solid State Ionics* **2011**, *192,* 304−307.

[65] T. Minami, A. Hayashi, M. Tatsumisago, *Solid State Ionics* **2006,** *177*, 2715–2720.

[66] B. Wang, J. B. Bates, F. X. Hart, B. C. Sales, R. A. Zuhr, J. D. Robertson, *J. Electrochem. Soc.* **1996***, 143,* 3203-3213.

[67] N. J. Dudney, B. J. Neudecker, *Current Opinion in Solid State and Materials Science* **1999**, *4*, 479-482.

[68] J. F. M. Oudenhoven, L. Baggetto, P. L. Notten, *Adv. Energy Mater.* **2011**, *1*, 10-33.

[69] C. Feldman, M. Hacskaylo, M. W. Charles, *U. S. Patent 3375135 A*, **1965**.

[70] B. Scrosati, J. Appl. Electrochem **1972**, *2*, 231-238.

[71] J. B. Bates, N. J. Dudney, G. R. Gruzalski, C. F. Luck, *U. S. Patent 5338625*, **1992**.

[72] J. B. Bates, N. J. Dudney, G. R. Gruzalski, R. A. Zuhr, A. Choudhury, C. F. Luck, J. D. Robertson, *J. Power Sources* **1993**, *43*, 103-110.

[73] J. B. Bates, N. J. Dudney, D. C. Lubben, G. R. Gruzalski, B. S. Kwak, X. H. Yu, R. A. Zuhr, *J. of Power Sources* **1995**, *54*, 58-62.

[74] J. B. Bates, G. R. Gruzalski, N. J. Dudney, C. F. Luck, X. H. Yu, *Solid State Ionics* **1994**, *70*, 619-629.

[75] N.J. Dudney*, Materials Science and Engineering B* **2005***, 116, 245–249.*

[76] S. H. Lee, P. Liu, C. E. Tracy, D. K. Benson, *Electrochem. Solid State Letters* **1999**, *2*, 425-427.

[77] N. J. Dudney, J. B. Bates, R. A. Zuhr, S. Young, J. D. Robertson, H. P. Jun, S. A. Hachney, *J. Electrochem. Soc.* **1999**, *146*, 2455-2464.

[78] J. B. Bates, N. J. Dudney, G. R. Gruzalski, R. A. Zuhr, A. Choudhury ,C. F. Luck, J. D. Robertson, *Solid State Ionics* **1992**, *53*, 647-654.

[79] X. Yu, J. B. Bates, G. E. Jellison, F. X. Hart, *J. Electrochem. Soc.* **1997**, *144*, 524-532.

[80] M. Ogawa, R. Kanada, K. Yoshida, T. Uemura, K. Harada, *Jornal of Power Sources* **2012**, 487-490.

[81] B. J. Neudecker, R. A. Ruhr, *Intercalation Compounds for Battery Materials*, Proceedings of the Electrochemical Society **2000.**

[82] N. J. Neudecker, N. J. Dudney, J. B. Bates, *J. Electrochem. Soc.* **2000**, *147*, 517-523.

[83] www.cymbet.com*,* **18.10.2017***.*

[84] http://www.frontedgetechnology.com/tech.htm, **18.10.2017***.*

[85] http://www.st.com/en/power-management/enfilm-thin-film-batteries.html, **18.10.2017***.*

[86] https://www.excellatron.com/advantage.htm, **18.10.2017***.*

[87] S.D. Jones, J. R. Akridge, *Solid State Ionics* **1996**, *86-88*, 1291-1294.

[88] B. J. Neudecker, R. A. Ruhr, J. B. Bates, *Jornal of Power Sources* **1999**, *81-82*, 27-32.

[89] J. Li, C. Ma, Mi.Chi , C. Liang, N. J. Dudney*, Adv. Energy Mater.* **2015**, *5*, 1401-1408.

[90] K. Kanehori, K. Matsumoto, K. Miyauchi, T. Kudo, *Solid State Ionics* **1983**, *9-10*, 1445-1448.

[91] S. -W. Song, K.-C. Lee, H.Y. Park, *Journal of Power Sources* **2016**, *328*, 311-317.

[92] J. B. Bates, D. Lubben, N.J. Dudney, *IEEE AESS Systems Magazine* **1995**, 30-32.

[93] M. Baba, N. Kumagai, H. Kobayashi, O. Nakano, K. Nishidate, *Electrochem. Solid State Letters* **1999**, *2*, 320-322.

[94] H. Ohtsuka, J.-i. Yamaki, *Solid State Ionics* **1989**, *35*, 201-206.

[95] J. Yamaki, H. Ohtsuka, T. Shodai, *Solid State Ionics* **1996**, *86-88*, 1279-1284.

[96] N. Kuwata, J. Kawamura, K. Toribami, T. Hattori, N. Sata, *Electrochemistry Communications* **2004**, *6*, 417-421.

[97] Y. S. Park, S. H. Lee, B. I. Lee, S. K. Joo, *Electrochem. Solid State Letters* **1999**, *2*, 58-59.

[98] C. Yada, A. Ohmori, K. Die, H. Yamasaki, T. Kato, T. Saito, F. Sagane, Y. Iriyama, *Adv. Energy Mater.* **2014**, *4*, 1301416.

[99] W. Nernst, *Zeitschrift für Elektrochemie* **1899**, *6*, 41-43.

[100] V. Thangadurai, W. Weppner, *Ionics* **2006**, *12*, 81-92.

[101] H. Rickert, *Angew. Chem.* **1978**, *90*, 38-48.

[102] P. G. Bruce, *Solid State Electrochemistry*, 1st ed., Cambridge University Press, Ney York, **1997**.

[103] P. E Stallworth, J. J. Fontanella, M. C Wintersgill, C. D. Scheidler, J J. Immel, S. G. Greenbaum, A. S. Gozdz, *J. Power Sources* **1999**, *81–82,* 739–747.

[104] L. Edman, A. Ferry, M. M. Doeff, *J. Mater. Res.* **2000**, *15*, 1950–1954.

[105] H. Buschmann, J. Dölle, S. Berendts, A. Kuhn, P. Bottke, M. Wilkening, P. Heitjans, A. Senyshyn, H. Ehrenberg, A. Lotnyk, V. Duppel, L. Kienlee J. Janek, *Phys. Chem. Chem. Phys.* **2011**, *13*, 19378-19392.

[106] B. E.Francisco, C. R. Stoldt, J.-C. M'Peko, *Chem. Mater.* **2014***, 26,* 4741–4749.

[107] J. A. Alonso, J. Sanz, J. Santamaria, C. Leon, A. Varez, M. T. Fernandez-Diaz, *Angew. Chem. Int. Ed.* **2000**, *39*, 619-621.

[108] M. Xu, M. S. Park, J. M. Lee, T. Y. Kim, Y. S. Park, E. Ma, *Phys Rev B* **2012**, *85* 052301-1-5.

[109] H. Y. P. Hong, *Mater. Res. Bull.* **1976**, *13*, 173-182.

[110] Y. Inaguma, C. Liquan, M. Itoh, T. Nakamura, *Solid State Commun.* **1993**, *86*, 689-693.

[111] R. Murugan, V. Thangadurai, W. Weppner*, Angew. Chem.* **2007**, *119*, 7925–7928.

[112] J. Awaka, N. Kijima, H. Hayakawa, J. Akimoto, *Journal of Solid State Chemistry* **2009**, *182*, 2046–2052.

[113] J. Kang, H. Chung, C. Doh, B. Kang, B. Han, *Journal of Power Sources* **2015**, 293, 11-16.

[114] H. Aono, E. Sugimoto, Y. Sadaoka, N. Imanaka, G.-y. Adachi*, Journal of the Electrochemical Society* **1989***, 136*, 590-591.

[115] J. S. Thokchom, N. Gupta, B. Kumar, *J. Electrochem. Soc.* **2008***, 155*, A915-A920.

[116] P. G. Bruce, A. R. West, *J. Solid State Chem.* **1982**, *44,* 354–365.

[117] R. Kanno, T. Hata, Y. Kawamoto, M. Irie, *Solid State Ionics* **2000**, *130*, 97–104.

[118] M. Murayama, R. Kanno, M. Irie*et al.*, *Journal of Solid State Chemistry* **2002**. *168*, 140-148.

[119] M. Murayama, N. Sonoyama, A. Yamada, R. Kanno, *Solid State Ionics,* **2004**. 170, 173-180.

[120] R. Kanno, M. Murayama, *J. Electrochem. Soc.* **2001**, *148*, A742-A746.

[121] D. Liu, W .Zhu, Z. Feng, A. Guerfi, A. Vijh, K.Zaghib, *Materials Science and Engineering B* **2016**, *213*, 169–176.

[122] S. Boulineau, M. Courty, J.-M. Tarascon, V. Viallet, *Solid State Ionics* **2012**, *221*, 1–5.

[123] Z. Liu, W. Fu, E. A. Payzant, X. Yu, Z. Wu, N. J. Dudney, J. Kiggans, K. Hong, A. J. Rondinone, C. Liang, *J. Am. Chem. Soc.* **2013**, *135*, 975−978.

[124] R. Mercier, J.-P. Malugani, B. Fahys, G. Robert, *Solid State Ionics* **1981**, *5*, 663-666.

[125] H. Wada, M. Menetrier, A. Levasseur, P. Hagenmuller, *Mater. Res. Bull.* **1983**, *18*, 189–193.

[126] Z. Zhang, J. H. Kennedy, *Solid State Ionics* **1990**, *38*, 217–224.

[127] A. Hayashi, S. Hama, H. Morimoto, M. Tatsumisago, T. Minami, *J. Am. Ceram. Soc.* **2001**, 84, 477–479.

[128] M. Tatsumisago, N. Machida, T. Minami, *J. Ceram. Soc. Jpn.* **1987**, *95*, 197–201.

[129] A. Yamauchi, A. Sakuda, A. Hayashi, M. Tatsumisago, *J. Power Sources* **2013**, *244*, 707-710.

[130] N. Aotani, K. Iwamoto, K. Takada, S. Kondo, *Solid State Ionics* **1994**, *68*, 35–39.

[131] A. Hayashi, K. Noi, A. Sakuda, M. Tatsumisago, *Nat. Commun.* **2012**, *3*, 856-891.

[132] H. Muramatsu, A. Hayashi, T. Ohtomo, *Solid State Ionics* **2011***, 182*, 116-119.

[133] J. B, Goodenough, *Pure & Appl. Chem* **1995**, *67*, 931-938.

[134] C. H. Chen, K. Amine, *Solid State Ionics* **2001**, *144*, 51−57.

[135] S. Stramare, V. Thangadurai, W. Weppner, *Chem. Mater.* **2003**, *15*, 3974−3990.

[136] J. K.Feng, L. Lu, M. O. Lai, *J. Alloys Compd.* **2010**, *501*, 255−258.

[137] U. v. Alpen, M. F. Bell, W. Wichelhaus, K. Y. Cheung, G. J. Dudley, *Electrochim. Acta* **1978**, *23*, 1395−1397.

[138] P. Knauth, *Solid State Ionics* **2009**, *180*, 911−916.

[139] A. Schwöbel, R. Hausbrand, W. Jaegermann, *Solid State Ionics* **2015**, *273*, 51-54.

[140] V. Thangadurai, D. Pinzaru, S. Narayanan, A. K. Baral, *J. Phys. Chem. Lett.* **2015**, *6*, 292−299.

[141] M. Kotobuki, H. Munakata, K. Kanamura, Y. Sato, T. Yoshida, *J. Electrochem. Soc.* **2010**, *157*, A1076–A1079.

[142] S. Wenzel, T. Leichtweiss, D. Krüger, J. Sann, J. Janek, *Solid State Ionics* **2015**, *278*, 98-105.

[143] N. D. Lepley, N. A. W. Holzwarth, Y. A. Du, Phys. Rev. B: Condens. Matter Mater. Phys. **2013**, *88*, 104103.

[144] E. Rangasamy, Z. Liu, M. Gobet, K. Pilar, G. Sahu, W. Zhou, H. Wu, S. Greenbaum, C. Liang, *J. Am. Chem. Soc.* **2015**, *137*, 1384–1387.

[145] A. Sakuda, A. Hayashi, M. Tatsumisago, *Chem. Mater.* **2010**, *22*, 949–956.

[146] S. Wenzel, D. A. Weber, T. Leichtweiss, M. R. Busche, J. Sann, J. Janek, *Solid State Ionics* **2016**, *286*, 24–33.

[147] S. Wenzel, S. Randau, T. Leichtweiß, D. A. Weber, J. Sann, W. G. Zeier, J. Janek, *Chem. Mater.* **2016**, *28*, 2400–2407.

[148] K. Takada, N. Ohta, L. Zhang, K. Fukuda, I. Sakaguchi, R. Ma, M. Osada, T. Sasaki, *Solid State Ionics* **2008**, *179*, 1333–1337.

[149] A. Sakuda, H. Kitaura, A. Hayashi, K. Tadanaga, M. Tatsumisago, *Electrochem. Solid-State Lett.* **2008**, *11*, A1–A3.

[150] Y. Jin, N. Li, C. H. Chen, S. Q. Wei, *Electrochem. Solid-State Lett.* **2006**, *9*, A273–A276.

[151] S. J. Visco;Y. S. Nimon, US 2007/0117007 A1, **2007**.

[152] H. Wan, G. Peng, X. Yao, J. Yang, P. Cui, X. Xu, *Energy Storage Materials* **2016**, 4, 59-65.

[153] X. Yao, D. Liu, C. Wang, P. Long, G. Peng, Y.-S. Hu, H. Li, L. Chen, X. Xu, *Nano Lett.* **2016**, *16*, 7148-7154.

[154] J. Reinacher, S. Berendts, J. Janek, *Solid State Ionics* **2014**, *258*, 1–7.

[155] S.-I. Furusawa, H. Tabuchi, T. Sugiyama, S. Tao, J. T. S. Irvine, *Solid State Ionics* **2005**, *176*, 553-558.

[156] Y. Ito, A. Sakuda, T. Ohtomo, A. Hayashi, M. Tatsumisago, *J. Ceramic Soc. Jpn.* **2014**, *122*, 349-345.

[157] D. J. Kalita, S. H. Lee, K. S. Lee, D. H. Ko, Y. S. Yoon, *Solid State Ionics* **2012**, *229*, 14-19.

[158] J. Z. Lee, Z. Wang, H. L. Xin, T. A. Wynn, Y. S. Meng, *J. Electrochem. Soc.* **2017**, *164*, A6268-A6273.

[159] K. H. Joo, H. J. Sohn, P. Vinatier, B. Pecquenard, A. Levasseur, *Electrochem. Solid State Letters* **2004**, *7*, A256-A258.

[160] S. Lobe, C. Dellen, M. Finsterbusch, H.-G. Gehrke, D. Sebold, C.-L. Tsai, S. Uhlenbruck, O. Guillon, J. *Power Sources* **2016**, *307*, 684-689.

[161] H. Chen, H. Tao, X. Zhao, Q. Wu, *Journal of Non-Crystalline Solids* **2011**, *357*, 3267-3271.

[162] Y. Xiong, H. Tao, J. Zhao, H. Chen, X. Zhao, Journal *of Alloys and Compounds* **2011**, *509*, 1910-1914.

[163] Y. Sakurai, A. Sakuda, A. Hayashi, M. Tatsumisago, *Solid State Ionics* **2011**, *182*, 59-63.

[164] A. Sakuda, A. Hayashi, S. Hama, M. Tatsumisago, *J. Am. Ceram. Soc.* **2010**, *93*, 765–768.

[165] Z. Quan, M. Hirayama, D. Sato, Y. Zheng, T.-a. Yano, K. Hara, K. Suzuki, M. Hara, R. Kanno, J. *Am. Ceramic Soc.* **2016**, *100*, 746-753.

[166] N. Ohta, K. Takada, M. Osada, L. Zhang, T. Sasaki, M. Watanabe, *Journal of Power Sources* **2005**, *146*, 707–710.

[167] S. Kim, M. Hirayama, S. Taminato, R. Kanno, *Dalton Trans.* **2013**, *42*, 13112-13117.

[168] J. S. Park, L. Cheng, V. Zorba, A. Mehta, J. Cabana, G. Chen, M. M. Doeff, T. J. Richardson, J. H. Park, J.-W. Song, W.-S. Hong, *Thin Solid Films* **2015**, *576,* 55–60.

[169] J. Tan, A. Tiwari, *ECS Solid State Letters* **2012**, *1*, Q57-Q60.

[170] F. Aguesse, V. Roddatis, J. Roqueta, P. Garia, D. Pergolesi, J. Santiso, J. A. Kilner, *Solid State Ionics* **2015**, *272*, 1-8.

[171] J.-K. Ahn, S.-G. Yoon, *Electrochimica Acta* **2004**, *50*, 371-374.

[172] O. Maqueda, F. Sauvage, L. Laffont, M- L- Martinez-Sarrion, L. Mestres, E. Baudrin, *Thin Solid Films* **2008**, *516*, 1651-1655.

[173] T. Ohnishi, K. Takada, *Solid State Ionics* **2012**, *228,* 80-82.

[174] C.-L. Lin, B. Zhang, Z.-W. Fu, *Solid Thin Films* **2006**, *515*, 1886-1892.

[175] C. Loho, R. Djenadic, M. Bruns, O. Clemens, H. Hahn, *Journal of the Electrochem. Soc.* **2017**, *164,*) A6131-A6139.

[176] H. Katsui, T. Goto, *Thin Solid Films* **2015**, *584,* 130–134.

[177] R.-J. Chen, M. Huang, W.-Z. Huang, Y. Shen, Y.-H. Lin, C.-W. Nan, *J. Mater. Chem. A* **2014**, *2*, 13277–13282.

[178] H. Matsuda, E. Hosono, H. Zhou, *MRS Proceedings* **2013**, *1496,* mrsf12-1496-j13-10. doi:10.

[179] K. Tadanaga, H. Egawa, A. Hayashi, M. Tatsumisago, J. Mosa, M. Aparicio, A. Duran, *J. Power Sources* **2015**, *273,* 844-847.

[180] Z. Zheng, H. Fang, F. Yang, Z.-K. Liu, Y. Wang, *Journal of the Electrochem. Soc.* **2014**, *161*, A473-A479.

[181] K. P. Abhilash, P- Sivaraj, P. C. Selvin, B. Nalini, K. Somasundaram, *Ceramics International* **2015**, 13823-13829.

[182] Z. Zheng, S. Song, Y. Wang, *Solid State Ionics* **2016**, *287*, 60-70.

[183] E.J. van den Ham, N. Peys, C. De Dobbelaere, J. D'Haen, F. Mattelaer, C. Detavernier, P.H.L. Notten, A.Hardy, M.K. Van Bael, *J. Sol-Gel Sci. Techn.* **2015**, *73*, 536-543.

[184] K. Takada, K. Fujimoto, T. Inada, A. Kajiyama, M. Kouguchi, S. Kondo, M. Watanabe, *Applied Surface Science* **2002**, *189*, 300-306.

[185] S. Arakawa, H. Nitta, S. Hayashi, Journal *of Crystal Growth* **200**1, *231*, 290–294.

[186] J. F. Ihlefeld , P. G. Clem , B. L. Doyle , P. G. Kotula , K. R. Fenton, C. A. Apblett*, Adv. Mater.* **2011**, *23*, 5663–5667.

[187] Y. Wang, Z. Liu, X. Zhu, Y. Tang, F. Huang, *J. Power Sources* **2013**, *224*, 225-229.

[188] C. Puscher, *Polytechn. J.* **1869**, *190*, 421-423.

[189] G. Rosenheim, W. Stadler, V. J. Mayer, *Z. Anorg. Allg. Chem.* **1906**, 49, 1-13.

[190] R. W. Birkmire, B. E. McCandless, W. N. Shafarman, R. D. Varrin, in *9th ECPV Solar Energy Conf.* **1989**, Freiberg, Germany, 134.

[191] H. Xin, J. K. Katahara, I. L. Braly, H. W. Hillhouse, *Adv. Energy Mater.* **2014**, *4*, 1301823-1-5.

[192] D. Lee, K. Yong, *Korean J. Chem. Eng.* **2013**, *30*, 1347-1358.

[193] M. Ebelmen, *C R Hebd Seances Acad Sci* **1844**, 19, 398-400.

[194] M. Ebelmen, *Ann Chim Phys* **1846**, *16*, 129-166.

[195] M. Ebelmen, *C R Hebd Seances Acad Sci* **1847**, *25*, 854-856.

[196] H. Dislich, *J Non-Cryst Sol* **1986**, *80*, 115-121.

[197] H. Schroeder, *Optica Acta: Intern. J. of Optics*, **1962**, 9, 249-254.

[198] W. Geffcken, *Glastech. Ber.* **1951**, *24*, 143-151.

[199] G. Frank, E. Kauer, H. Köstlin *Thin Solid Films* **1981**, *77*, 107-117.

[200] J. Fukushima, K. Kodaira, T. Matsushita *J Mater Sci* 1984, *19*, 595-598.

[201] K.D. Budd, S.K. Dey, D. A. Payne, Brit Ceram Soc Proc **1985**, *36,* 107-121.

[202] S.K. Dey, K.D. Budd, D.A. Payne *IEEE Trans UFFC* **1988**, *35*, 80-81.

[203] T. Schneller, R. Waser, M. Kosec, D.Payne, *Chemical Solution Deposition of Functional Oxide Thin Films*, Springer Verlag Wien **2013**, vii-ix.

[204] R. W. Schwartz, T. Schneller, R. Waser, *C. R. Chimie* **2004**, *7*, 433–461.

[205] G. Hodes, *Phys Chem Chem Phys* **2007**, *9*, 2181–2196.

[206] T. Schneller, D. Griesche, *Chemical Solution Deposition of Functional Oxide Thin Films*, Springer Verlag Wien, **2013**, 29-49.

[207] R. M. Pasquarelli, D. S. Ginley, R. O'Hayre, *Chem. Soc. Rev.* **2011**, 40, 5406–5441.

[208] S. Hoffmann-Eifert, T. Schneller, *Chemical Solution Deposition of Functional Oxide Thin Films*, Springer Verlag Wien **2013**, S. 407-429.

[209] T. Ye, Z. Sua, A. G. Evans, *Int. J. Solids Structures* **1992**, *29*, 2639-2648.

[210] O. Baldus, R. Waser *Appl Phys A* **2005***, 80*, 1553-1562.

[211] X. Chen, M. Yagi, Y. Akiyama, O. Machida, E. Ohta, M. Meixner, J. Stollenwerk, U. Boettger, T. Schneller . *Jpn. J. Appl. Phys.* **2013***, 52*, 09KA06.

[212] S. Teragawa, K. Aso, K. Tadanaga, A. Hayashi, M. Tatsumisago, *Chem. Lett.* **2013**, *42*, 1435-1437.

[213] X. Yao, D. Liu, C. Wang, P. Long, G. Peng, Y.-S. Hu, H. Li, L. Chen, X. Xu, *Nano Lett.* **2016**, *16*, 7148-7154.

[214] S. Ito, M. Nakakita, Y. Aihara, T. Uehara, N. Machida, *J. Power Sources* **2014**, *271*, 342-345.

[215] S. Yubuchi, S. Teragawa, K. Aso , K. Tadanaga, A. Hayashi, M. Tatsumisago , *J. Power Sources* **2015**, *293*, 941-945.

[216] K. H. Park, D. Y. Oh, Y. E. Choi, Y. J. Nam, L. Han, J.-Y. Kim, H. Xin, F. Lin , S. M. Oh, Y. S. Jung, *Adv. Mater.* **2016**, *28*, 1874-1883.

[217] S. Teragawa, K. Aso, K. Tadanaga, A. Hayashi, M. Tatsumisago, *J. Power Sources* **2014**, *248*, 939-942.

[218] D. H. Kim, D. Y. Oh, K. H. Park, Y. E. Choi, Y. J. Nam, H. A. Lee, S.-M. Lee, Y. S. Jung, *Nano Lett.* **2017**, *17*, 3013-3020.

[219] S. Wenzel, PhD thesis, *Thermodynamic and kinetic instability of inorganic solid electrolytes at lithium andsodium metal electrodes*, Universität Gießen **2016**.

[220] Safety data sheet, *Lithium titanate, spinel,* www.sigmaaldrich.com, accessed **19.10.2017**.

[221] C. Dietrich, D. A. Weber, S. Sedlmaier, S. Indris, S. P. Culver, D. Walter, J. Janek, W. G. Zeier, *J. Mater. Chem. A* **2017**, *5*, 18111-18118.

[222] K. Homma, M. Yonemura, T. Kobayashi, M. Nagao, M. Hirayama, R. Kanno, *Solid State Ionics* **2011**, *182*, 53–58.

[223] H. Yamane, M. Shibata, Y. Shimane, T. Junke, Y. Seino, S Adams, K. Minami, A. Hayashi, M. Tatsumisago, *Solid State Ionics* **2007**, *178*, 1163–1167.

[224] H. Eckert, Z. Zhang, J. H. Kennedy, *Chem. Mater.* **1990**. *2*, 273-279.

[225] C. Dietrich, D. A. Weber, S. P. Culver, A. Senyshyn, S. J. Sedlmaier, S. Indris, J. Janek, W. G. Zeier, *Inorg. Chem.* **2017**, *56*, 6681−6687.

[226] SDBS No. 324CDS-03-464 and SDBS No. 324HSP-04-529; http://sdbs.db.aist.go.jp/sdbs/cgi-bin/direct_frame_top.cgi, accessed **06.09.2017**.

[227] SDBS No. 15347CDS-09-399 and SDBS No. 15347HSP-06-128; http://sdbs.db.aist.go.jp/sdbs/cgi-bin/direct_frame_top.cgi, accessed **06.09.2017**.

[228] L. A. Laplanche, M. T. Rogers**,** *J. Am. Chem. Soc.* **1964***, 86,* 337-341*.*

[229] A. W. Hofmann, *Berichte der deutschen chemischen Gesellschaft* **1878**, *11*, 338-340.

[230] N. Muller, P. C. Lauterbur, J. Goldenson, *J. Am. Chem. Soc.* **1956**, *78*, 3557-3561.

[231] L. Maier, J. R. Van Wazer, *J. Am. Chem. Soc.* **1962**, *84*, 3054-3058.

[232] L. C. D. Groenweghe, J. H. Payne, J. R. Van Wazer, *J. Am. Chem. Soc.* **1960**, *82*, 5305-5311.

[233] Y. Seino, M. Nakagawa, M. Senga, H. Higuchi, K. Takada, T. Sasaki, *J. Mat. Chem. A* **2015**, *3*, 2756-2761.

[234] J. Schmedt auf der Günne, H. Eckert, *Chem. Eur. J.* **1998**, *4*, 1762-1767.

[235] H. Finegold, *Annals New York Academy of Science* **1958**, *70*, 875-889.

[236] F. Mizuno, T. Ohtomo, A. Hayashi, K. Tadanaga, T. Minami, M. Tatsumisago, *J. Ceram. Soc. Jpn.* **2004**, *112*, 709-712.

[237] E. K. Jaffe, M. Cohn, *Biochemistry* **1978**, *17*, 652-657.

[238] S. Oae, A. Nakanishi, N. Tsujimoto, *Chem, Ind.* **1972**, 575.

[239] Li_3PS_4: ICSD 180319; $Li_7P_3S_{11}$: ICSD 157654, $Li_4P_2S_6$: ICSD 242170; Li_7PS_6: ICSD 421130.

[240] Y. Wang, T. Matsuyama, M. Deguchi, A.Hayashi, A. Nakao, M. Tatsumisago, *JPS-Japan* **2016**, *124*, 597-601.

[241] A. Hayashi, M. Tatsumisago, T. Minami, Y. Miura, *Phys. Chem. Glasses* **1998**, *39*, 145-150.

[242] R. Koerver, I. Aygün, T. Leichtweiß, C. Dietrich, W. Zhang, J. O. Binder, P. Hartmann, W. G. Zeier, J. Janek, Chem. Mater. **2017**, *29*, 5574-5582.

[243] L. Le Van-Jodin, F. Ducroquet, F. Sabary, I. Chevalier, *Solid State Ionics* **2013**, *253*, 151-156.

[244] J. Zemek, O. A. Baschenko, M. A. Tyzykhov, *Thin Solid Films* **1993**, *224,* 141-147.

[245] S. Sicolo, M. Fingerle, R. Hausbrand, K. Albe, *J. Pow. Sources* **2017**, *354*, 124-133.

[246] P. Schichtel, M. Geiß, T. Leichtweiß, J. Sann, D. A. Weber, J. Janek, *J. Power Sources* **2017**, *360*, 593-604*.

[247] K. Minami, A. Hayashi, M. Tatsumisago, *Solid State Ionics* **2008**, *179*, 1282–1285.

[248] J. E. Trevey, J. R. Gilsdorf, S. W. Miller, S.-H. Lee, *Solid State Ionics* **2012**, *214*, 25–30.

[249] M. R. Zamfir, H. T. Nguyen, E. Moyen, Y. H. Lee, D. Pribat, *J. Mater. Chem* A **2013**, *1*, 9566-9586.

[250] B. R. Long, M. K. Y. Chan, J. P. Greeley, A. A. Gewirth, *J. Phys. Chem. C* **2011**, *115*, 18916-18921.

[251] L. Sang, R. T. Haasch, A. A. Gewirth, R. G. Nuzzo, *Chem. Mat.* **2017**, *29*, 3029-3037.

[252] J. Li, J. R. Dahn, *J. Electrochem. Soc.* **2007**, *154*, A156-A161.

[253] M. J.Chon, V. A. Sethuraman, A. McCormick, V. Srinivasan, P. R. Guduru, *Phys. Rev. Lett.* **2011**, *107*, 1-4.

[254] J. W. Wang, Y. He, F. Fan, X. H. Liu, S. Xia, Y. Liu, C. T. Harris, H. Li, J. Y. Huang, S. X. Mao, T. Zhu, *Nano Lett.* **2013**, *13*, 709-715.

[255] M. N. Obrovac, L. J. Krause, *J. Electrochem. Soc.* **2007**, *154*, A103-A108.

[256] M. Green, E. Fiedler, B. Scrosati, M. Wachtler, J. S. Moreno, *Electrochem. Solid-State Lett.* **2003**, *6*, A75-A79.

[257] J. Mosa, J. F. Vélez, I. Lorite, N. Arconada, M. Aparicio, *J. Power Sources* **2012**, *205*, 491-494.

[258] T. Ohzuku, A. Ueda, N. Yamamoto, *J. Electrochem. Soc.* **1995**, *142*, 1431-1435.

[259] Y. H. Rho, K. Kanamura, M. Fujisaki, J.-i. Hamagami, S.-i. Suda, T. Umegaki, *Solid State Ionics* **2002**, *151*, 151-157.

[260] J. Haetge, P. Hartmann, K. Brezesinski, J. Janek, T. Brezesinski, *Chem. Mater.* **2011**, *23*, 4384-4393.

[261] P. M. M. C. Bressers, E. A. Meulenkamp, *J. Electrochem. Soc.* **1998**, *145*, 2225-2230.

[262] J. Fu, *J. Am. Ceram. Soc.* **1997**, *80*, 1901-1903.